



HAL
open science

Grafting of salen complexes on silicon by means of Atom Transfer Radical Polymerization for applications in asymmetric catalysis

Rafaela Bechara

► **To cite this version:**

Rafaela Bechara. Grafting of salen complexes on silicon by means of Atom Transfer Radical Polymerization for applications in asymmetric catalysis. Organic chemistry. Institut Polytechnique de Paris, 2024. English. NNT: 2024IPPAX111 . tel-04862325

HAL Id: tel-04862325

<https://theses.hal.science/tel-04862325v1>

Submitted on 3 Jan 2025

HAL is a multi-disciplinary open access archive for the deposit and dissemination of scientific research documents, whether they are published or not. The documents may come from teaching and research institutions in France or abroad, or from public or private research centers.

L'archive ouverte pluridisciplinaire **HAL**, est destinée au dépôt et à la diffusion de documents scientifiques de niveau recherche, publiés ou non, émanant des établissements d'enseignement et de recherche français ou étrangers, des laboratoires publics ou privés.

GRAFTING OF SALEN COMPLEXES ON SILICON BY MEANS OF ATOM TRANSFER RADICAL POLYMERIZATION FOR APPLICATIONS IN ASYMMETRIC CATALYSIS

Thèse de doctorat de l'Institut Polytechnique de Paris
préparée à l'École Polytechnique

École doctorale n° 626 : Ecole Doctorale de l'Institut Polytechnique de
Paris (ED IP Paris)
Spécialité de doctorat: Chimie

Thèse présentée et soutenue à Palaiseau, 09 juillet 2024, par

Rafaela Bechara

Composition du Jury :

Olivier Riant

Professeur
Institute of Condensed Matter and Nanosciences
of Université Catholique de Louvain

President

Frédérique Cunin

Directrice de recherche, CNRS
Institut Charles Gerhardt de Montpellier

Rapporteuse

Daniel Grande

Directeur de recherche, CNRS
Institut Charles Sadron, Unistra

Rapporteur

Nadège Pantoustier

Maîtresse de conférences
ESPCI, Sorbonne Université

Examinatrice

Anne-Chantal Guoguet

Directrice de recherche, CNRS
Ecole Polytechnique

Directrice de thèse

Emmanuelle Schulz

Directrice de recherche, CNRS
ICMMO, Université Paris-Saclay

Co-Directrice de thèse

Philippe Roger

Professeur
ICMMO, Université Paris-Saclay

Invité

*To my dear parents,
fiancé João
& brother*

Acknowledgements

The last three years has been an incredible journey. Since I was very young, around the age of 10, I would say that I would become a scientist! I was also very specific saying I was going to do a PhD. I was already passionate about knowledge and I would read all kind of books about science, but specially, I would deeply observe the world around me. Well, 20 years later, here I am. I look back and feel proud of what I have achieved. However, I could not achieve any of that if it was not for some special people that came in my way. Specially during these last three years of my doctoral studies, I would like to express my sincere thanks for many incredible people I had the pleasure to encounter.

First and foremost, I would like to thank to Dr. Daniel Grande, Dr. Frédérique Cunin, Prof. Olivier Riant, and Dr. Nadège Pantoustier for accepting being part of the jury and evaluating my work. Your feedback and presence really honor me.

Then, my sincere appreciation for my supervisors Dr. Anne-Chantal Gouget, Dr. Emmanuelle Schulz, and Prof. Philippe Roger. I could not have been luckier than to have you three as my supervisors. You accepted me, taught me, treated me as equal and guided me throughout the whole process, not only for the scientific project, but also for my career. I thank each one of you for the time you dedicated to me, all the scientific discussions, but specially, the good humor and kindness.

I would like to thank as well Dr. François Ozanam, Dr. Mohamed Mellah, and Dr. Nadine Aubry-Barroca. Together with my supervisors, you were key for the success of this thesis. Countless times you helped me in the lab. I would like to thank you for the help you gave me during the correction of this manuscript, and for guiding me throughout the whole process of this thesis.

Then, I would like to extend my thanks to all personnel of the three labs I had the pleasure to work with: Lab PMC at Ecole Polytechnique, and Lab ECM and SM₂Vie at ICMMO, Université Paris-Saclay. I was so lucky because I got to work with amazing people in these three labs. My coworkers let the atmosphere of the lab much easier and they were always there to listen to me and help me when needed. Special thanks to Lilian, Tram, Syrine, Léa, Liangjing, Jospin, Qian, Antoine and Abdel.

I would also like to thank Ludovic Costa for the SEC-MALS analysis and treatments, Emilie Kolodziej for her help with GC and HPLC analysis, and Diana Dragoé and Damien Aureau for their immense help with the XPS data, scientific discussions and data analysis. Also, thanks to Catherine Henry-de-Villeneuve and Fouad Maroun for their help with AFM imaging.

My enormous appreciation and deepest acknowledgment to my parents and my brother, who always support and respect my decisions. Without their trust, encouragement, and support, I could never have come this far or accomplished this much. I am surely who I am because they were by my side, helping me to become the best version of myself. Thanks to them, I know that no matter how hard things can become, I will always overcome them because they are my fortress.

And finally, my endless gratitude goes to the love of my life, my fiancé, João. We met in France in September 2020, and since then, we have supported one another during M2 and thesis. I am so thankful to have you by my side and for the strength you give me, but most importantly, for the joy you bring. Thank you for the countless times you listened to me and discussed the results of the thesis with me—even when you didn't understand much. Thank you for being patient, for providing the support I needed, and for being the best partner I could ever have.

At last, this has been a joyful and enriching journey. Regardless of where life takes me next, I will always take pride in my path to France and the pursuit of this PhD.

Table of Contents

PROLOGUE	1
i. Context	1
ii. Contributions	5
iii. Organization of the manuscript	6
CHAPTER 1: Bibliography	7
PART A: CHEMISTRY OF SILICON SURFACES	8
1.1. Silicon surface: choice of material and properties.....	8
1.2. Modification of surfaces with organic molecules	12
1.2.1. General methods	12
1.2.2. Microwave grafting	14
1.2.3. Grafting from an oxidized surface	16
1.2.4. Grafting from a silicon-hydrogenated surface	17
1.3. Fourier Transform Infrared Spectroscopy: the experimental principle	20
PART B: ATRP OF METHACRYLATES	22
1.4. A perspective of Atom Transfer Radical Polymerization	22
1.4.1. Influence of ligands	24
1.4.2. Influence of initiators.....	26
1.4.3. Influence of solvents.....	27
1.5. Cu(0) mediated supplemental activator and reducing agent (SARA) ATRP.....	28
1.6. Surface Initiated (SI)-ATRP.....	30
1.7. SI-ATRP from flat surfaces.....	33
1.8. Functionalization of polymers	34
PART C: SUPPORTED ASYMMETRIC SALEN CATALYSIS	38
1.9. Homogenous salen catalysts and their reactivity	39
1.9.1. Cobalt salen complexes	39
1.9.2. Chromium salen complexes.....	40
1.10. Immobilization of salen catalysts to develop supported catalysts	43
1.10.1. On organic supports	44
1.10.2. On inorganic supports	47
1.11. Towards the future of supported salen catalysis	58
PART D: CONCLUSIONS AND GOALS FOR THIS PROJECT	59
CHAPTER 2: Preparation of a surface-initiated layer on silicon	61
2.1. Preparation of an oxidized and a hydrogenated surface.....	62
2.2. Grafting of initiator 1 on surface for SI-ATRP	64
2.3. Quantification of the grafted initiator 1 on Si-H _x surface.....	67
2.4. Optimization of the initiator 1 MW grafting	68
2.5. Calculation of error in the grafting of initiator 1	71
2.6. Grafting of other initiators for SI-ATRP	71
2.7. Study on macroporous silicon (100).....	84
2.8. Conclusions	87
CHAPTER 3: ATRP of methacrylates in solution and on surface	88
3.1. Polymerization of MEMA in solution	89
3.2. Polymerization of MEMA on surface	91
3.3.1. Developing longer polymer brushes	94
3.3.2. X-ray photoelectron spectroscopy	95
3.3.3. Atomic Force Microscopy	99

3.3.	Polymerization of MEMA on macroporous silicon	101
3.4.	Copolymerization of MEMA/AZMA in solution	103
3.4.1.	Synthesis of AZMA.....	103
3.4.2.	Classical copolymerization of AZMA and MEMA.....	103
3.5.	Copolymerization of MEMA/AZMA on surface	109
3.5.1.	In the case of a crystalline silicon surface	109
3.5.2.	X-ray photoelectron spectroscopy	112
3.5.3.	In the case of a macroporous silicon surface	114
3.6.	Supplemental activator and reducing agent (SARA) polymerization	117
3.6.1.	Influence of zero valent copper	117
3.6.2.	Copolymerization of MEMA/AZMA and kinetics of Cu(0)-mediated SARA ATRP.....	118
3.6.3.	Influence of the temperature.....	121
3.7.	Developing more complex structures using SARA ATRP	122
3.7.1.	HEMA homopolymerization	123
3.7.2.	MEMA/HEMA copolymerization	124
3.8.	Conclusions	126

CHAPTER 4: Synthesis of salen catalysts and post-functionalization of copolymers ..128

4.1.	Contextualization	129
4.1.1.	Synthesis of salen ligands.....	129
4.1.2.	Sonogashira Pd/Cu cross-coupling reactions.....	130
4.1.3.	Functionalization using click chemistry	131
4.2.	Synthesis of enantiopure salen ligands	132
4.3.	Synthesis of salen complexes	135
4.3.1.	Chromium-salen complexes	135
4.3.2.	Cobalt-salen complexes	136
4.3.3.	Characterization of metal-salen complexes	136
4.4.	Synthesis of FTIR markers for click chemistry	138
4.4.1.	Synthesis of aryl-1	139
4.4.2.	Synthesis of aryl-2.....	140
4.4.3.	Synthesis of aryl-4.....	140
4.4.4.	Characterization of aryl products by ATR-FTIR.....	141
4.5.	Click chemistry with copolymers in solution	142
4.5.1.	Using FTIR markers	142
4.5.2.	Using salen complexes	145
4.6.	Click chemistry with copolymers on surface	149
4.6.1.	Using FTIR markers on crystalline silicon.....	149
4.6.2.	Using salen complexes on macroporous silicon	153
4.7.	Conclusions	156

CHAPTER 5: Supported asymmetric catalysis

5.1.	Contextualization	158
5.1.1.	Homogenous salen catalysis	158
5.1.2.	Supported salen catalysis	159
5.2.	Homogenous Catalysis	161
5.2.1.	Asymmetric ring opening (ARO) of epoxides.....	161
5.2.2.	Henry reaction	162
5.2.3.	Hydrolytic Kinetic Resolution (HKR) of epibromohydrin	163
5.3.	Multipurpose supported catalysis	164
5.4.	Silicon supported monocatalysis	169
5.4.1.	ARO of cyclohexene oxide.....	169
5.4.2.	Henry reaction	171
5.5.	Conclusions	172

CHAPTER 6: General conclusions and perspectives	173
6.1. General conclusions.....	173
6.2. Perspectives.....	175
6.2.1. Copolymers of MEMA/HEMA/AZMA	175
6.2.2. Supported catalysis	176
CHAPTER 7: Experimental section.....	179
APPENDIX A	217
APPENDIX B	224
APPENDIX C	234
APPENDIX D	242
SYNTHÈSE DE THÈSE DE DOCTORAT EN FRANÇAIS	244
REFERENCES.....	251

Abbreviations and acronyms

AFM	Atomic Force Microscopy
APTES	(3-aminopropyl)triethoxysilane
ARO	Asymmetric Ring Opening
ATR-FTIR	Attenuated Total Reflectance-Fourier Transform Infrared
ATRP	Atom Transfer Radical Polymerization
AZMA	azido-3-propyl methacrylate
bpy	2,2'-bipyridine
BrIBx	10-undecylenic-2-bromoisobutyrate
Cat*	Catalyst
CDCl₃	deuterated chloroform
CRP	controlled/living radical polymerization
Cyclam	1,4,8,11-tetraazacyclotetradecane
DCM	dichloromethane
dNbp	4,4'-dinonyl-2,2'-dipyridyl
D	dispersity
DMAP	4- <i>N,N</i> -dimethylaminopyridine
DMF	<i>N,N</i> -dimethylformamide
dn/dc	refractive index increment
DP	degree of polymerization
eBiB	ethyl- α -bromoisobutyrate
Ee	enantioselectivity
Eq.	equivalent
FWHM	full width half maxima
GC	Gas Chromatography
HEMA	hydroxyethylmethacrylate
HKR	hydrolytic kinetic resolution
HMTETA	1,1,4,7,10,10-hexamethyltriethylenetetramine
IUPAC	International Union of Pure and Applied Chemistry
K_{act}	activation constant
K_{ATRP}	(ATRP) equilibrium constant
K_{deact}	deactivation constant
K_p	propagation constant
MALS	multi-angle light scattering
MBPA	methyl α -bromophenylacetate
MCM-41	Mobil Composition of Matter No. 41
MCM-48	Mobil Composition of Matter No. 48
MCT	mercury-cadmium-tellurium
MEMA	2-methoxyethyl methacrylate
Me₆TREN	tris[2-(dimethylamino)ethyl]amine
MHz	Mega Hertz
M_n	Number average molar mass
M_n calc	Calculated average molar mass
M_n SEC	Experimental average molar mass
M_w	Mass average molar mass
NMR	Nuclear Magnetic Resonance

p	conversion
PAZMA	polymer of AZMA
PHEMA	polymer of HEMA
PMDETA	<i>N,N,N',N'',N'''</i> -pentamethyldiethylenetriamine
PMEMA	polymer of MEMA
PSi	porous silicon
RAFT	Reversible Addition-Fragmentation chain-Transfer
RDRP	Reversible Deactivation Radical Polymerization
r.t.	room temperature
SAM	Self-Assembled Monolayer
SARA ATRP	Supplemental Activator and Reducing Agent Atom Transfer Radical Polymerization
SEC	Size Exclusion Chromatography
SEM	scanning electron microscopy
SET-LRP	Single-Electron-Transfer-Living Radical Polymerization
SI-ATRP	Surface-Initiated Atom Transfer Radical Polymerization
TBME	<i>tert</i> -butyl methyl ether
TFAAD	trifluoroacetamide-protected 10-aminodec-1-ene
TGA	Thermal Gravimetric Analysis
THF	tetrahydrofuran
TOF	turnover frequency
TON	turnover number
TPEDA	<i>N,N,N',N'</i> -tetrakis(2-pyridylmethyl)ethylenediamine
TPMA	tris(2-pyridylmethyl)amine
UV	Ultra-Violet
UV-vis	Ultra-Violet visible
XPS	X-ray Photoelectron Spectroscopy

PROLOGUE

General project background

“Nothing in life is to be feared, it is only to be understood. Now is the time to understand more, so that we may fear less.”

Marie Curie

SUMMARY

i.	Context	1
ii.	Contributions	5
iii.	Organization of the manuscript	6

i. Context

Catalysis is at the core of fundamental and applied research and it is one of the most important aspects in industrial processes. The efficiency of catalysis is also a pillar in green chemistry as it allows chemical transformations to achieve their optimal having lower environmental impact. Although homogenous catalysts have usually higher activity, their huge disadvantage is the complicated removal from reaction mixture and reuse.¹ Supported catalysts is the solution for this problematic, in which the catalyst can be incorporated in insoluble solid supports, such as fine particles, powders, granules or films, and then be recovered and reused very easily. Silicon substrates are strategic candidates for developing supported catalysts due to their well-known and robust chemistry.

This project aims at the preparation of macroporous silicon functionalized by enantiopure metallic complexes of salen type, following robust, multi-step grafting processes. Salen type ligands, whose structure is shown in **Figure 1**, associated with metals can form chiral salen-metal complexes that are known for their catalytic activity allowing the preparation of scalemic synthons.²

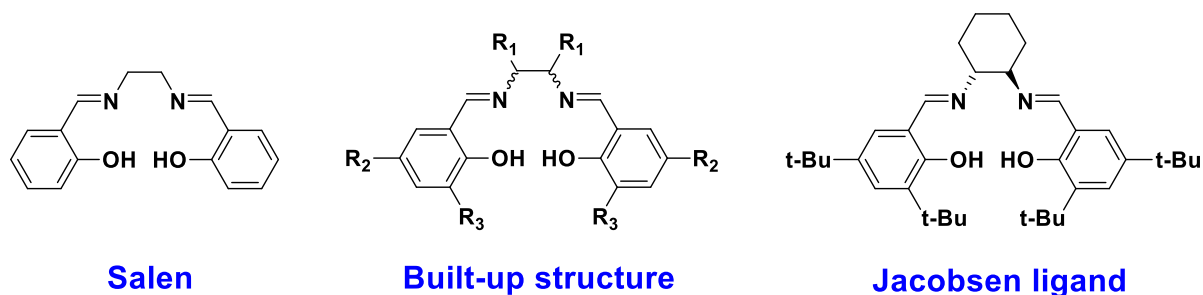
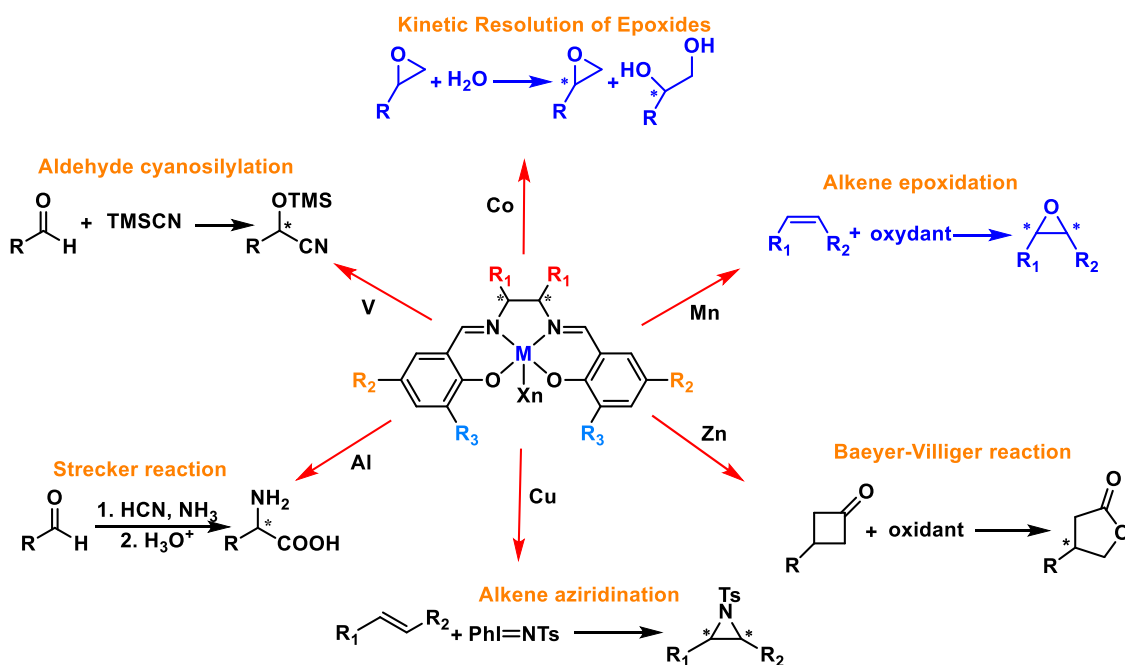
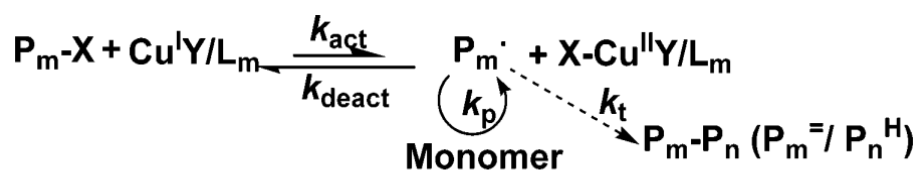


Figure 1: Salen type ligands.

Besides, salen ligands are easily modified (R_1 , R_2 and R_3 in **Figure 1**), and associated with many metals of transition, they allow the enantioselective catalytic formation of carbon-carbon or carbon-heteroatom bonds with excellent efficiencies both in terms of activity and selectivity. Their catalytic spectrum is quite large, comprising many different catalytic reactions, from cyanosilylation of aldehydes to sulfoxidation, as example (**Scheme 1**).



The immobilization of salen catalysts is performed by macromolecular engineering to control the composition of the grafted chains.⁴ The strategy relies on the copolymerization, by atom transfer radical polymerization (ATRP),⁵ of functionalized methacrylate-type monomers. Atom transfer radical polymerization (ATRP) mediated by a metal (very frequently copper) complexes is a powerful technique for preparing polymers with precisely controlled architecture. The control depends on an appropriate equilibrium between an activation process (the formation of radicals, k_{act}) and a deactivation process (the formation of alkyl halides, k_{deact}) (**Scheme 2**).⁶ ATRP is a catalytic process that uses copper complex in which copper can exist in two different oxidation states. The lower oxidation state of copper ($Cu^I Y/L_m$), where Y is a halide and L is a ligand, reacts with the initiator (alkyl halide P_m-X) generating a radical $P_m\cdot$ that reacts with the monomer at a constant k_p to form the polymer. The radicals can also react with each other which will terminate the reaction with a constant k_t , or back with the $X-Cu^{II} Y/L_m$ which leads to the deactivation of the reaction with a constant k_{deact} . Such approach can also be performed on surface by first grafting an initiator on surface and then carrying out the further surface initiated (SI)-ATRP to yield polymer brushes on surfaces.

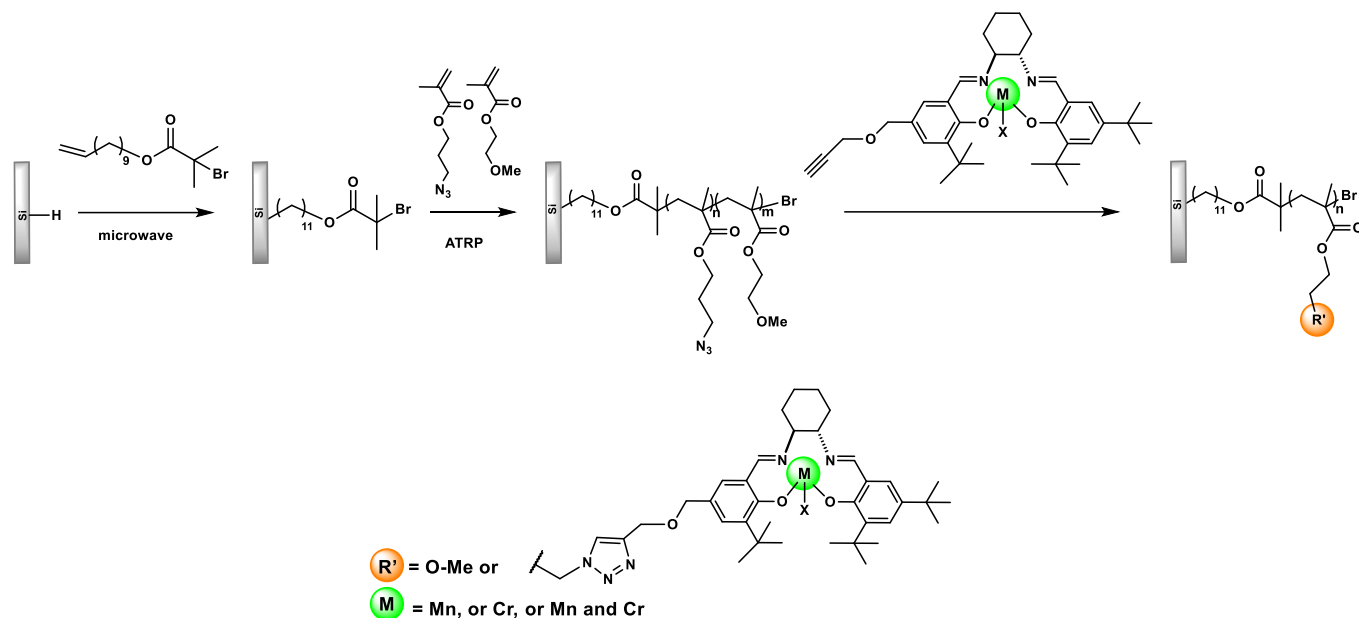


Scheme 2: Proposed mechanism for ATRP.⁶

Later, these polymers synthesized by ATRP are modified by post-functionalization with salen complexes of identical or different metallic salts (such as Mn and Cr) to be tested in asymmetric catalysis. To the best of our knowledge, no grafting of these types of monomers has been performed on silicon in order to obtain catalytic activity. However, the use of silicon as a substrate is particularly interesting because its hydrogenated surface allows the grafting of organic species via extremely robust Si-C covalent bonds, in addition to enabling the control of the grafted species by quantitative FTIR spectroscopy in ATR (Attenuated Total Reflection) geometry.⁷ Besides, macroporous silicon substrates were chosen because of its high surface area can increase the catalyst loading.

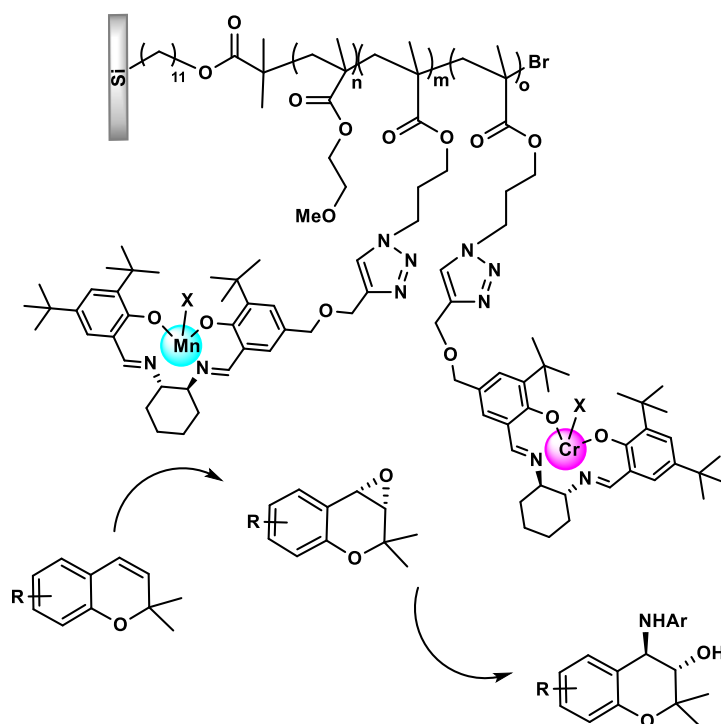
Therefore, this project has as objectives the preparation of porous silicon functionalized by enantiopure metallic complexes of salen type (**Scheme 3**) by means of ATRP to control the

composition of the grafted chains.⁴ Therefore, first an initiator is grafted on the surface of silicon, then by SI-ATRP, methacrylate copolymers are grown on surface, which are finally reacted with salen catalysts via click chemistry reaction to afford the supported catalyst.



Scheme 3: Proposed multi-step grafting starting from a hydrogenated silicon surface.

The ultimate objective of this project is to test these modified catalysts in asymmetric catalysis aiming the sequential catalysis by first converting a chromene into an epoxide catalyzed by a manganese salen complex, and later have its epoxide ring opened forming an amino alcohol catalyzed by a chromium salen complex in a one pot reaction, as shown in **Scheme 4**.



Scheme 4: Sequential multi-step asymmetric catalysis using Mn/Cr salen complexes grafted on silicon.

ii. Contributions

The ECM team at PMC has been working on this project for over 9 years through a collaboration between two teams from ICMMO (Institut de Chimie Moléculaire et des Matériaux d'Orsay), at Université Paris-Saclay: “Catalyse Moléculaire” with Dr. Emmanuelle Schulz and “Synthèse de Molécules et de Macromolécules · pour le Vivant et l'Environnement” with Prof. Philippe Roger. Before this thesis, the project has received two contributions: one from the PhD work of Dr. Nacim Zidmal (thesis from 2015 – 2018) and the other from the post-doc Dr. Erigene Bakangura (researcher from 2020 – 2021). The consortium worked on the development of ATRP conditions in solution for different monomers, and on the design of catalysts, to perform supported catalysis.^{4, 8}

Thus, the objective of this thesis is to apply these methodologies developed in solution into silicon surface, besides developing multipurpose catalysis. In parallel, these concepts were transferred to macroporous silicon surface to develop the envisioned supported monocatalysts. In this project, the macroporous silicon samples were prepared through a special collaboration with Dr. Gaël Gautier and Dr. Thomas Defforge from Université de Tours.

iii. Organization of the manuscript

The thesis manuscript is divided in 7 chapters and it is organized as follows:

Chapter 1 contains the state of the art and bibliography of the chemistry of silicon surfaces, ATRP polymerization of methacrylates, and supported salen-metal catalysis.

Chapter 2 is devoted to the functionalization of silicon surfaces (oxidized and hydrogenated surface) with ATRP initiators by means of micro-wave grafting. It discusses the quantification of the prepared monolayers by ATR-FTIR and its characterization by XPS, AFM, and contact angle. It also develops the grafting methodology for macroporous silicon.

Chapter 3 deals with the ATRP polymerization of methacrylates in solution and on silicon surfaces. It discusses classical and SARA ATRP methodologies of three methacrylate monomers. In addition, it demonstrates direct quantitative characterization of polymer brushes obtained on silicon, and their characterization by XPS, AFM and ellipsometry.

Chapter 4 describes the synthesis of salen catalysts and the post-functionalization of copolymers by means of click chemistry. The post-functionalization of copolymers was done first with FTIR markers and then with salen catalysts, both in solution and on surface.

Chapter 5 encompasses the results obtained using supported asymmetric catalysis, using either the silicon copolymers anchored on silicon substrates or free copolymers, for monocatalysis or dual catalysis.

Chapter 6 is the general conclusions of this work and the perspectives.

Chapter 7 is the experimental section.

CHAPTER 1

Bibliography

“Science is not just a body of facts, but a way of thinking critically and objectively about the world around us.”

Marie Curie

SUMMARY

PART A: CHEMISTRY OF SILICON SURFACES	8
1.1. Silicon surface: choice of material and properties.....	8
1.2. Modification of surfaces with organic molecules	12
1.2.1. General methods.....	12
1.2.2. Microwave grafting	14
1.2.3. Grafting from an oxidized surface	16
1.2.4. Grafting from a silicon-hydrogenated surface	17
1.3. Fourier Transform Infrared Spectroscopy: the experimental principle	20
PART B: ATRP OF METHACRYLATES	22
1.4. A perspective of Atom Transfer Radical Polymerization	22
1.4.1. Influence of ligands	24
1.4.2. Influence of initiators.....	26
1.4.3. Influence of solvents.....	27
1.5. Cu(0) mediated supplemental activator and reducing agent (SARA) ATRP.....	28
1.6. Surface Initiated (SI)-ATRP.....	30

1.7.	SI-ATRP from flat surfaces	33
1.8.	Functionalization of polymers	34
PART C: SUPPORTED ASYMMETRIC SALEN CATALYSIS		38
1.9.	Homogenous salen catalysts and their reactivity	39
1.9.1.	Cobalt salen complexes	39
1.9.2.	Chromium salen complexes.....	40
1.10.	Immobilization of salen catalysts to develop supported catalysts	43
1.10.1.	On organic supports	44
1.10.2.	On inorganic supports	47
1.11.	Towards the future of supported salen catalysis	58
PART D: CONCLUSIONS AND GOALS FOR THIS PROJECT		59

This chapter will give an overview of the state of the art of the main topics of this thesis, ranging from chemistry on surface, to polymerization and then to catalysis. It is separated in three main parts with the first one discussing the chemistry of silicon surfaces, from the basic properties until the grafting from oxidized and hydrogenated surfaces. Part two deals with the state of the art for ATRP polymerization considering two main types of ATRP: classical and the supplemental activator and reducing agent (SARA) ATRP mediated by Cu(0). It also discusses the advancements of SI-ATRP either on silicon or other surfaces, and the further post-modification of polymers. Part three reports on the developments of supported homogenous catalysis using salen complexes for the asymmetric catalysis of various reactions.

Part A: Chemistry of silicon surfaces

1.1. Silicon surface: choice of material and properties

Silicon substrates are essential in both scientific research and technological advancements, due to their unique properties. Since mid-1990s, the modification of silicon substrates has been widely studied for their various applications such as microelectronics and biosensors.⁹ The development of integrated circuits, microprocessors, and other electronic components has been made possible by the widespread use of silicon (100), which serves as the foundation of many different electronic components.¹⁰

Silicon's crystalline structure also allows for the precise control of the grafting of molecules on its surface, making it an interesting material for the development of layers with different properties.⁹ It also exhibits excellent thermal conductivity and stability, thus rendering it a robust substrate for applications such as catalysis. Finally, by using HF etching, it is possible to obtain a grafting via Si-C bonds, which are quite inert turning the developed structures less prone to leaching and hydrolysis.¹¹ Silicon has also a low cost, and it is very abundant, which makes it a practical choice for scaling up the procedures. Finally, silicon was chosen for this project as the substrate because we are able to precisely quantify the molecules by ATR-FTIR since crystalline silicon is used as the ATR crystal during the analysis. Besides, it allows the easy characterization of the modified surface by XPS and AFM.

Monocrystalline silicon has a face centered cubic Bravais lattice (FCC) called diamond structure where each atom is positioned in the center of a tetrahedron and attached to its four neighboring atoms by covalent bonds (**Figure 2**). In a general production process, the silicon wafers are cut from a single crystal silicon ingot using a rotating diamond inner peripheral blade. This process makes it able to cut silicon plates along any crystal plane, the (100) and the (111) being the most widely used. In this project, we have used (111)-oriented crystalline silicon wafers. An ideal (111) plane is shown in **Figure 2b** at the atomic scale. Each silicon atom of the surface (111) plane has a bond perpendicular to the plane of the surface, which is a favorable configuration for the grafting of molecules on the surface.⁷

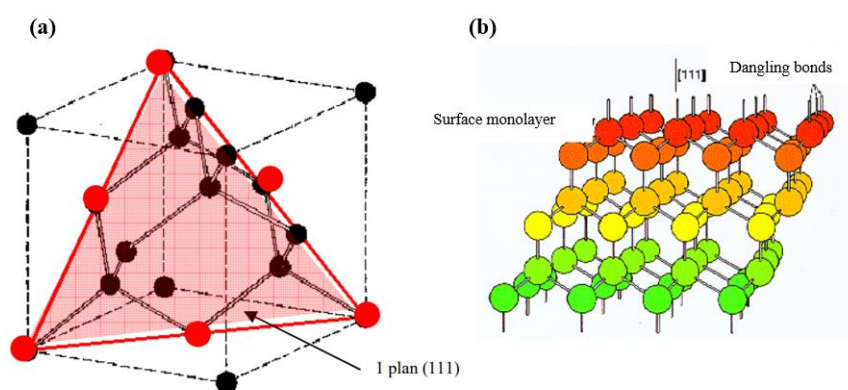


Figure 2: (a) Diamond cubic crystal structure, (b) arrangement of atoms near a (111) surface. Figure adapted from Aureau thesis.¹²

A network of regular steps has a height of 3.14 \AA , which corresponds exactly to the distance between two atomic bilayers along the [111] direction of the Si crystal. In order to obtain such network, it is advantageous to cut the wafer with a slight miscut (term used to

address the disorientation of the cut of the wafer with respect to the crystalline axes) relative to an ideal (111) plane. The amplitude of the miscut will determine the width of the obtained atomic terraces and the direction of its projection on the (111) plane will affect the rectilinearity of the steps. **Figure 3** shows a schematic diagram of a miscut yielding a (111) vicinal stepped surface. The miscut is defined by 2 angles, α (the amplitude) and θ (the direction of the projection). In this project, the samples used have an α of 0.2° and θ of 180° , with a thickness average of $500\ \mu\text{m}$. In order to reveal the terraced structure of the vicinal surface, it is necessary to remove the oxide layer that naturally forms on the silicon surface.¹³

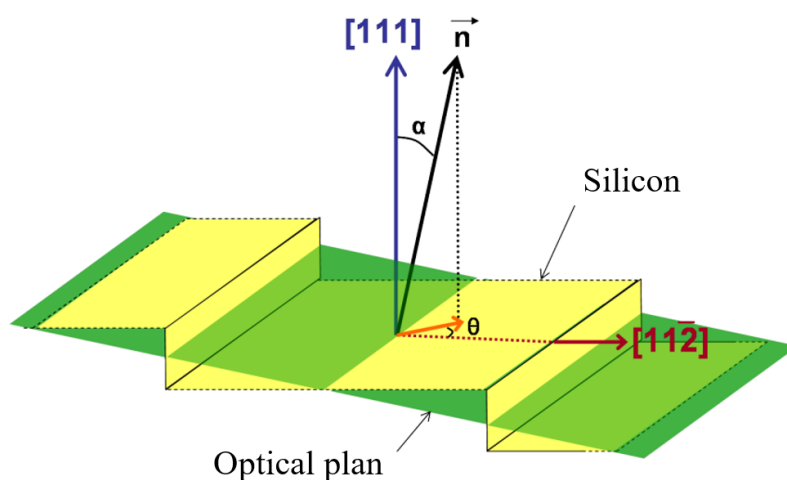


Figure 3: Diagram of a vicinal surface of silicon (111). α is the angle of the miscut with respect to the normal to the surface and θ is the direction of the miscut in the plane of the surface. Figure adapted from Douarche thesis.¹³

The functionalization of silicon surfaces is usually performed through two main approaches, either directly on native oxidized silicon surfaces (SiO_x), or on hydrogen-terminated silicon surfaces (SiH_x). The latter is formed by etching the silicon surface either in basic or acidic media, such as NH_4F or HF solutions, for instance. The crystallographic face (111) of silicon is a dense plane of the crystal. The step-and-terrace structure of the vicinal surface is revealed at the atomic scale if an anisotropic etching of silicon is performed (using a solution of NH_4F for instance). These flat surfaces constitute an ideal substrate for well-controlled surface chemistry.

However, the isotropic etching, with HF solution, provides a rough surface as the material is etched evenly in all directions from the silicon substrate. **Figure 4** shows the mechanism of HF etching. In this mechanism, the removal of the oxidized surface overlayer leads to the

formation of Si–F, which is highly polar. Therefore, the strong static charge polarizes the Si–Si back-bond of SiSi–F, making it vulnerable to attack by HF.¹⁴ In fact, theoretical calculations by Trucks and coworkers¹⁵, showed that the barrier to attach a hydrogen atom to the back Si of SiSi–F and release surface Si as SiF₄ is around 1 eV. The resulting hydrogenated surface is non-polar and hydrophobic, besides being highly resistant to chemical attack by HF, which means that no further etching occurs,¹⁴ therefore not damaging the silicon structure.

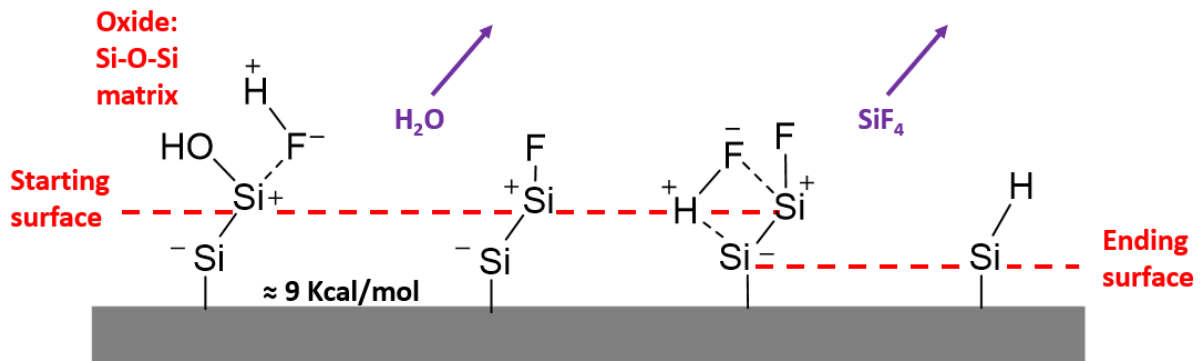


Figure 4: Mechanism leading to the formation of hydrogenated silicon surface after HF etching. The last step of oxygen removal from SiO₂ involves HF attack on the Si–O bond, with removal of OH as H₂O and termination of the surface Si atom with fluorine. Further attack of the polarized Si^{δ-}–Si^{δ+} bond leads to H termination. Image reconstructed from Peng and coworkers.¹⁴

In more details, HF aqueous solution yields an isotropic etching of the Si(111) surface by etching the material in all directions, bringing it a roughness on surface that is not present when an anisotropic etching is performed. In fact, anisotropic etching removes the material from a silicon substrate in only one direction; thus, creating well-defined features (**Figure 5**).

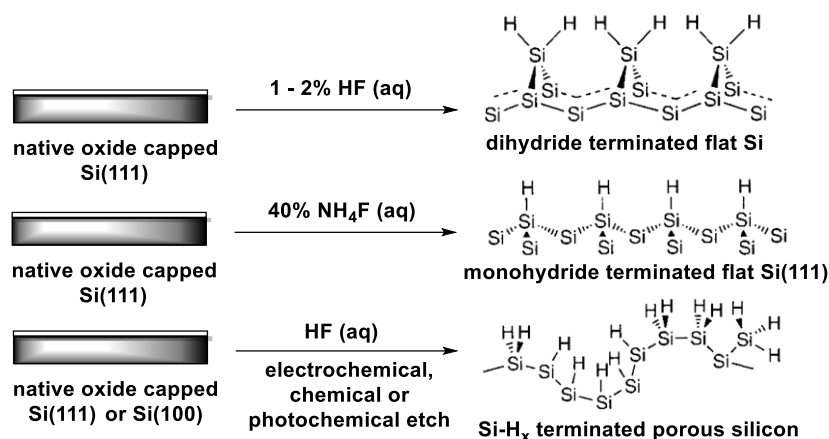


Figure 5: Preparation of hydride-terminated Si(100) and Si(111) surfaces by chemical etching in fluoride-containing solutions. Alternative etchants (e.g. KOH, NaOH) have also been reported for the isotropic etching of Si. HF etching on Si(111) also yields a di or trihydride-terminated silicon surface.¹⁶ Image reconstructed from Buriak's work.⁹

1.2. Modification of surfaces with organic molecules

1.2.1. General methods

The reaction of 1-alkenes and 1-alkynes at hydride-terminated silicon surfaces is one of the strategies to graft organic molecules on silicon. This reaction is called hydrosilylation and it was first reported by Linford and coworkers in 1993.¹⁷ This monolayer was obtained from a reaction between an alkyne and hydrogenated silicon surface in the presence of diacetyl peroxide at 100 °C for one hour. The hydrosilylation reaction consists in inserting a C–C unsaturated bond into a Si–H bond.

It can be activated by various forms, such as heat, UV and catalysts. In the case of hydrosilylation reactions activated by heat, the alkene reacts directly with the Si–H bond forming a Si–C bond that is highly stable due to its nonpolar covalent nature.¹⁸ Two possible mechanisms are proposed for the case of thermal activation for the hydrosilylation (radical or concerted), as it is shown in **Figure 6**. The radical mechanism consists in assuming a thermally-induced homolytic cleavage of the Si–H bond (by analogy of the reaction using a radical formed from the homolytic cleavage of a peroxide molecule, which attacks the Si–H bond on the surface of silicon to form a radical Si•). The surface silyl radical then reacts with the unsaturated bond from the alkene to form the covalent Si–C bond between silicon and the terminal carbon from the alkene. This radical moves to β position of the alkene, and it then attacks a nearby Si–H bond to form yet another silyl radical. This new silyl radical attacks

another alkene molecule and this process is repeated over and over again until the whole hydrogenated silicon surface is grafted. This reaction should be carried out at high temperature ($\geq 150^\circ\text{C}$), in order to initiate the homolytic breakage of the Si–H bond and create the radical silyl on surface (**Figure 6**).¹⁹ This initial Si–H cleavage step can also be achieved by UV irradiation,^{18,20} thus initiating the chain process.

The concerted mechanism is much simpler, in which the Si–H and the carbon-carbon double or triple bond approach in a parallel fashion and pass through a four-center transition state which yield to the final product. Coletti and coworkers²¹ performed a density functional calculations on this proposed mechanisms of ethylene and acetylene as models of the thermal functionalization of SiH_x surfaces and they found that the activation energy for the concerted pathway of around 60 kcal/mol for both molecules is low enough to suggest that the concerted mechanism is a viable pathway for the hydrosilylation of alkenes by thermal activation.

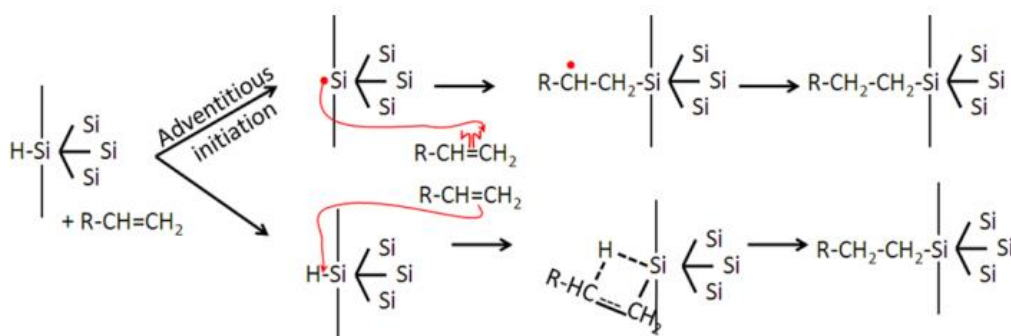


Figure 6: Possible reaction pathways for the thermal hydrosilylation: radical-based (top) and concerted (bottom) mechanism. Retrieved from Peng's review.¹⁴

The alkyl-SAM (self-assembled monolayer)-passivated surfaces are more stable than hydrogenated surfaces even though the alkene can only replace less than 50% of the surface hydrogen due to steric hindrance.¹⁴ The functionalized monolayer can later be reacted with other chemicals for further post modifications allowing the development of complex structures on surface. There are other pathways for the surface functionalization, such as by using catalysts²² or electrochemical processes.²³

All these techniques make it possible to obtain silicon surfaces functionalized by organic molecules, with a more or less dense and ordered monolayer. In the simplest cases, alkenes are used for grafting through the hydrosilylation reaction; however, the grafting of more complicated molecules is also possible. Considering molecules with functional groups such as

alcohols, amines and aldehydes, it is possible that the functional group also reacts with the hydrogenated silicon surface, in competition with the hydrosilylation reaction if the functional molecule also bears a terminal unsaturated C–C bond. Therefore, they could eventually form a Si–O–C or Si–N–C bond, making their grafting more complicated than simple alkenes.²⁴

A recent methodology for grafting of alkenes on silicon surface has emerged in the last years,²⁵ but it is still scarcely used for the grafting of molecules on silicon: microwave grafting. In this project, we have chosen to use microwave grafting because the UV grafting brings low stability for the initiator molecules for ATRP, which have a labile C–Br bond,²⁶ and thermal grafting has demonstrated not to be a good procedure in view of the degradation of the initiator solution after thermal treatment.^{8a} Therefore, microwave grafting appears to be a good alternative for this work, which could also bring the extra advantage of simplifying the reaction conditions with lower reaction time, for instance.

1.2.2. Microwave grafting

Microwave activation is still a growing branch in respect to grafting on silicon with approximately 35 documents for the keywords “silicon”, “grafting” and “microwave” between the year of 1999 to 2024 under Scopus database. Among these documents, only some are found in the desired intersection. For instance, Shou-Jun Xiao and coworkers have used a diazirine compound as a stable carbene precursor to react with Si–H terminated porous silicon (PSi) under microwave irradiation.^{25a} They have also used a series of azides to be covalently link Si–H terminated PSi by microwave in the presence of a peroxide initiator.^{25d} In 2003, Boukherroub and coworkers showed the chemical functionalization of hydrogen-terminated PSi surfaces with 1-alkenes under microwave irradiation to yield organic monolayers covalently attached to the surface through Si–C bonds.^{25b} Later in 2006, Boukherroub and coworkers also showed the functionalization of bifunctional molecules onto hydrogen-terminated porous silicon using microwave activation, and it was showed that the reaction takes place at both the carbon-carbon and the carbon-oxygen double bonds.²⁷ Betancourt-Mendiola and coworkers also studied the microwave grafting and optimized the reaction conditions for the chemical functionalization of porous silicon particles (PSip) using 3-aminopropyl triethoxysilane (APTES). They observed a higher grafting density of APTES when using microwave that obtained using other strategies, even using shorter reaction times and lower temperatures.^{25c}

Gates and coworkers²⁸ demonstrated a rapid covalent modification using silicon oxide surfaces with alcohol-containing compounds via a microwave-assisted grafting. They proposed a kinetic study for the formation of SAMs on SiO_x using microwave in which the radiation can induce the substrate heating yielding in high temperatures at the SiO_x surfaces, where the condensation of 1-octanol takes place (**Figure 7**). The molecules need to interact with surface-bound silanol groups for the reaction to occur. So, in step 1, before the microwave reaction, a layer of water molecules is adsorbed on the substrate surface, separating the surface from the solution of aliphatic alcohols. In step 2, microwave radiation accelerates the heating of silicon and then there is a molecular transport at the interface. Finally, in step 3, the alcohols form SAMs by a condensation reaction.

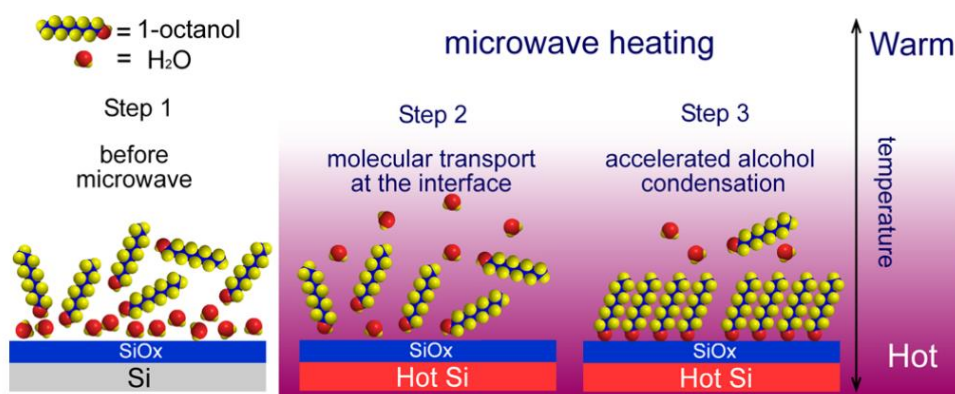


Figure 7: Depiction of the formation of self-assembled monolayers (SAMs) by microwave-assisted reaction of aliphatic alcohols with silicon oxide surfaces.²⁸

All in all, the use of microwave as a source of energy for the grafting of molecules leads to an increase in the rate of the grafting and a higher surface coverage. Though local surface heating certainly plays a major role, the details of the grafting mechanism are not yet fully understood and the few examples in the literature are still too scarce for reaching a better understanding. Noticeably, Tiemblo and coworkers performed in 2009 a comparative study between microwave and conventional heating grafting of alkyltrimethoxysilanes onto silica particles.²⁹ They found that solid-state NMR suggests structural differences in the grafted layers obtained by the two grafting methods, with a much higher loading of grafted molecules by microwave activation due to a great acceleration of the siloxane autocondensation.

Therefore, using microwave-assisted grafting and the possible structure of the layer is yet a vast area for study in surface chemistry. One of the goals of this thesis is to advance one step towards a better comprehension of microwave grafting on silicon surfaces. An example

by Lu and coworkers showed the grafting of an initiator, 10-undecenyl 2-bromoisobutyrate, on silicon using microwave,³⁰ however, a detailed study of the microwave parameters and grafting density and structure of the layer is lacking. Therefore, this was a starting point in our investigation of the initiator grafting on surface using microwave activation.

1.2.3. Grafting from an oxidized surface

Oxides are appealing materials as they are typically very accessible and also thermodynamically stable. They are usually easy to prepare, and their surface functionalization is possible owing to the reactivity of surface-bound -OH groups as anchoring points for a packed monolayer. The activation of the OH groups on different surfaces, such as textiles, silica, silicon, and other metals, are usually obtained by various methods: wet-etching, dry etching and plasma activation. In the case of silicon substrates, the most common form is the wet-etching using piranha solution, a mixture of hydrogen peroxide (H₂O₂) and sulfuric acid (H₂SO₄). The piranha solution removes surface organic matter and oxidizes the surface, yielding a SiO_x surface.

The attachment of organic monolayer onto oxide silicon surface is made through a covalent Si–O bond that is quite strong and efficient for the development of monolayers. It is however less inert than a Si–C bond in view of the polarity of the Si–O–C link which is somewhat prone to hydrolysis. The attachment of the molecules are mostly obtained from reactions with silanes, phosphonates, carboxylates, catechols, alkenes/alkynes and amines.³¹ Surface modification using alkylsilanes is one of the most common used methods to prepare monolayers on oxide surfaces. The reaction of organosilanes (RSiX₃, R₂SiX₃, R₃SiX, in which X is a leaving group), with an OH surface allows these species to be grafted via a Si–O–Si bond. This method has been used in many areas.³² The other aforementioned techniques for grafting molecules onto SiO_x surfaces are also very interesting, but the one of our particular study is the case of alkenes/alkynes, as the initiator molecule used in this work has a double bond available for the grafting onto silicon surfaces.

The attachment of alkynes on oxides available in the literature has been discussed mainly in the cases of photochemical or thermal activation. One of the first examples was described by Zuilhof and coworkers in which the modification of an oxidized silicon carbide was obtained upon irradiation of alkenes at room temperature with UV light at 254 nm.³³ The surface of silicon carbide is terminated with hydroxy groups such as Si–OH and C–OH upon wet-etching with diluted HF solution.³⁴ The irradiation of the substrate in an alkene solution

yielded the covalent attachment of the molecule onto the surface. They proposed that the reaction seems to proceed by a Markovnikov-type β -addition as the irradiation of an alkyne containing no methyl group, such as CH_2F -terminated alkyne, yields a clear CH_3 signal in the IR spectra.³³ Other examples using SiO_x surfaces, such as glass or synthetic fused silica and UV irradiation for the grafting of terminal alkenes also suggests a mode of reaction following a Markovnikov addition.³⁵

Hamers and coworkers also demonstrated an analogous surface chemistry using TiO_2 , in which thin films of trifluoroacetamide-protected 10-aminodec-1-ene (TFAAD) was obtained on TiO_2 via UV irradiation.³⁶ However, no CH_3 signal was observed in the IR spectrum of the obtained surfaces, suggesting that the layer was covalently bound through the terminal carbon of the olefin group. Regarding the mechanisms, it is likely controlled by the fact that the surface hydroxyl groups are good hole (h^+) scavengers, and Ti^{4+} are electron (e^-) scavengers. Then, it is thought that the irradiation provides a positively charged hydroxyl radicals that form a weak complex with the organic alkene, and induce the nucleophilic attack facilitating the hydrogen transfer to saturated the carbon atoms, therefore grafting the monolayer.³⁷

These examples using photochemical activation have also a thermal analogue reaction on these oxide surfaces. For instance, Mischki and coworkers described the grafting of 1-decene with thermal heating at $150\text{ }^\circ\text{C}$ for 16h, in which once more a Markovnikov addition was proposed.³⁸ Another example by Zuilhof and coworkers shows the grafting of 1-octadecene at $130\text{ }^\circ\text{C}$ for 6h from a hydroxyl-terminated SiC surface.³⁹

To the best of our knowledge, there is no example of microwave-assisted grafting using oxide silicon surfaces, but we believe that the grafting pathway should follow a similar pathway as the ones aforementioned in this section.

1.2.4. Grafting from a silicon-hydrogenated surface

The grafting of organic molecules on a hydrogenated silicon surface is advantageous since it allows for a better control of the reactivity and surface chemistry than starting from oxidized surfaces. As mentioned before, the SiH_x surface can be obtained by various forms, such as wet-etching using fluorinated compounds. When the etching is performed in NH_4F , a staircase structure with monoatomic steps is obtained. These monoatomic steps are easily observed by Atomic Force Microscopy (AFM), which makes it a valuable pathway for following the modifications on surface. **Figure 8** shows the AFM images of a hydrogenated

silicon surface using isotropic (a) and anisotropic etching (b). Then, following for the grafting of molecules from an anisotropic etching, it is still possible to observe the atomic steps on surface. This is usually an indirect proof of the formation of a monolayer (c).

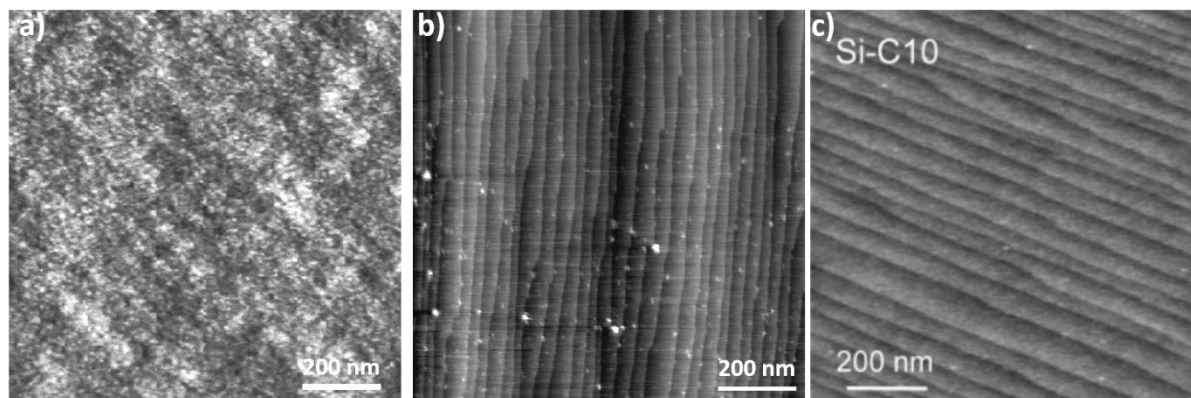


Figure 8: AFM images of (a) SiH_x surface from an isotropic etching (from ECM group), (b) SiH surface from an anisotropic etching (presented later in this thesis) and (c) staircase structure of the Si(111) surface after the organic modification with an alkyl monolayer.⁴⁰

Hydrogenated silicon surfaces are attractive to work because of their easy preparation, the possibility of forming robust Si–C bonds after grafting, and their relative stability in air. In fact, the Si–H bonds are somewhat stable during a few hours. However, prolonged exposure to air results in the re-oxidation of the surface.¹³

As briefly introduced in **section 1.2.1**, the main pathway for the grafting of molecules on hydrogenated silicon surface is through the hydrosilylation reaction. Many types of activation are possible, as already discussed, for instance, the thermal and UV activation or Lewis acid-catalyzed activation of unsaturated molecules. An extensive review from Gooding about these reactions is available.¹⁶ In this manuscript, a highlight in the developments from ECM group is given.

For instance, in 2006 with the work of Faucheux, we have shown that the *direct* photochemical reaction of undecylenic acid on Si–H (111) surface leads to monolayers terminated with intact carboxylic acid end groups. The methodology for grafting was successful in only one end of the molecule, and no reaction occurs between the carboxyl group and the silicon surface. The quantitative analysis of the grafted chains showed that the acid monolayers are quite dense with a surface coverage (scaled to the number of surface Si atoms) between 0.32 to 0.39.⁴¹ A year later, a complete study on the thermal stability of different

organic layers on silicon was investigated using Attenuated Total Reflection (ATR)-FTIR. These monolayers were covalently bound onto an atomically flat Si-H surface through the hydrosilylation of 1-decene, heptadecafluoro-1-decene or undecylenic acid. It was observed that the carboxylic acid terminal group undergoes successive chemical transformations forming anhydrides, which later (>250 °C) losses its functional group. Interestingly, the elimination of the functional group may lead to an end pairing of the grafted chains, which could result in an improved thermal stability.⁴²

Chazalviel and coworkers studied the grafting of mixed carboxyl-terminated monolayers on Si(111) through photochemical hydrosilylation of undecylenic acid/1-decene mixtures. The later attachment of a simple primary amine to the mixed-acid-terminated monolayers were achieved in a physiological buffer in a two-step process to activate the carboxyl terminations using the well-known coupling reagent EDC/NHS.⁴³

Another interesting example is the work of Gouget-Laemmel and coworkers that used multi-step amidation to develop azide-terminated silicon surfaces for the further functionalization of biological probes for biosensing applications.⁷ The highly dense monolayers containing terminal azide groups are prone to bioconjugation with alkynyl glycans compounds via a copper-catalyzed azide-alkyne cycloaddition, therefore developing glycan-type biosensors for the selective detection of proteins.

In 2015 our group started to work on the development of initiators monolayers for application in surface-initiated atom transfer radical polymerization (SI-ATRP). From the work of Zidelmal and coworkers, three different initiators for ATRP were grafted on Si-H surface by means of either UV or thermal activation, yielding monolayers of around 0.9 to 1.7 molecules·nm⁻².^{8a} Although the grafted monolayers were able to perform SI-ATRP of styrene, the direct grafting of 10-undecenyl 2-bromoisobutyrate via thermal activation showed a chemical degradation of the initiator in which the solution turned from transparent to black during experiment.

Therefore, following this progress, we aimed at developing the protocol and understanding the grafting mechanism and behavior of the microwave-assisted grafting of ATRP initiators on silicon for the further SI-ATRP and its post-functionalization for application in catalysis.

1.3. Fourier Transform Infrared Spectroscopy: the experimental principle

In the context of this thesis, ATR-FTIR spectroscopy is used throughout the whole process because it is the simplest analysis that makes it possible to follow the chemical modifications on surface and to quantify the materials on surface. In fact, our group has been used this technique for years, and has developed a special ATR compartment in which the crystalline silicon is used as the ATR crystal.

Molecular assemblies exhibit vibration frequencies which can often be analyzed as stretching and bending modes of specific molecular sub-units. The resonant vibrational energies are specific from these sub-units and vary depending on their environment. They fall in the infrared range (between 0 and 4000 cm^{-1}). The basic principle of vibrational infrared spectroscopy is based on the excitation of these vibrations by a polychromatic electromagnetic wave in the infrared range. Resonant absorption of radiation by molecules at specific frequencies leads to a decrease in the intensity of the measured signal and allows for identifying the molecular sub-units responsible for this absorption.

In this project, the spectrometer was used in ATR geometry. This technique has the advantage of increasing the sensitivity of the signal. The principle consists in propagating the infrared beam inside the silicon whose refractive index is higher than the adjacent medium. Multiple reflections take place on the internal walls of the crystal. The silicon samples used for this geometry are beveled at around 45° on both edges and their sizes (17.5 mm width, 500 μm thickness) are optimized to reduce the optical path length in silicon. A typical silicon prism gives about 20 – 30 reflections. This methodology is very sensitive and allows us to analyze samples in the range of 10^{+13} molecules per cm^2 .

Therefore, it is a very practical methodology, which after, can be used for the quantification of the molecules on surface through a correlation with the absorption of a similar molecule in solution (calibration experiment). Details of this calibration methodology is given in **Appendix C**. Using a wire-gride polarize, the infrared beam is *s*- or *p*- polarized, according to the direction of the electric field, perpendicular or parallel to the plane of incidence. **Figure 9** shows a scheme in which the Si-H bonds are only in perpendicular position to the surface, which then would be detectable in polarization *p* only (since *s*-polarized radiation has no electric-field component perpendicular to the surface, i.e., in the direction of the dipole induced

by the stretching motion of the Si-H unit). Since the molecules on surface are tilted from the surface normal by $30 - 40^\circ$, the contributions from both *s*- and *p*- polarization should be accounted for the correct quantification of molecules on surface.

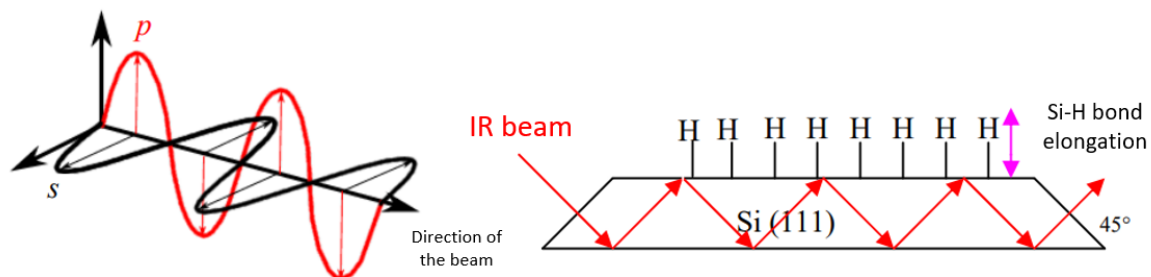


Figure 9: Scheme of the polarization of the infrared beam and of the probing of the Si-H bonds orthogonal to the (111) silicon surface.¹²

Part B: ATRP of methacrylates

1.4. A perspective of Atom Transfer Radical Polymerization

Atom transfer radical polymerization has been used to make polymers with controlled molar mass for over 25 years. In terms of mechanisms, ATRP is rooted in atom transfer radical addition (ATRA) and inspired by metal catalyzed telomerizations and redox initiated polymerizations.⁴⁴ However, contrary to telomerizations, in which the molar mass of the polymer does not increase with the monomer conversion, in ATRP the polymer molar mass increases linearly with the conversion, therefore, maintaining a low dispersity, which indicates that all chains grow together.⁴⁵ The kinetics of ATRP follows the principle of persistent radical effect (PRE), and it is an oxidized metal catalyst that is the deactivator, whereas it is the corresponding reduced metal catalyst that is the activator of the radical reaction.⁴⁴

This concept of activation and deactivation is the core of ATRP. Copper complexes are the most common catalysts for ATRP and it involves the halogen atom abstraction from an alkyl halide (initiator) by a copper(I)/ligand complex. During the activation, the copper(I) species undergoes an inner sphere electron transfer (ISET), which results into the halogenated X-copper(II)/ligand complex and the corresponding transient radical.⁴⁶ **Figure 10** shows the scheme for both ATRA and ATRP copper-catalyzed mechanisms.

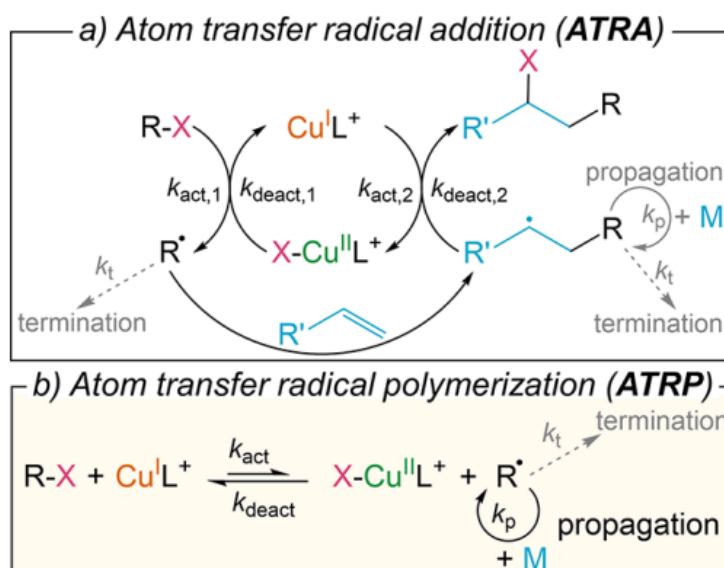


Figure 10: General mechanisms of copper-catalyzed (a) ATRA and (b) normal ATRP.

The main components of ATRP are the monomer, an initiator with a transferable (pseudo)halogen, a catalyst, the solvent. Temperature, reaction times, and additives can also influence ATRP. First, the typical monomers for ATRP includes styrenes, methacrylates, methacrylamides and acrylonitrile. All of those examples contain substituents that are able to stabilize the transient radicals during propagation.⁴⁷ Even under the same conditions, each monomer has its own equilibrium constant between active and dormant species. Therefore, the concentration of propagating radicals and the rate of radical deactivation need to be adjusted to maintain the control of the polymerization. However, since ATRP is a catalytic process, the equilibrium also depends on the amount and reactivity of the transition-metal catalyst present in the reaction.⁴⁸ The initiator determines the number of growing chains, and if initiation is fast but termination is negligible, then the number of growing chains is constant and equal to the initial initiator concentration. Therefore, the degree of polymerization (DP) increases with the initiator concentration in a way that $DP = [M]_0/[initiator]_0 \times conversion$.⁴⁸

The catalyst is also an important parameter in ATRP processes, and the effectiveness of the catalyst depends on the ability of the transition metal to expand its coordination sphere to accommodate the halogen atom from the initiator. The most widely used catalyst system is based on copper. The catalytic system is composed not only of the transition metal, but also of a ligand, which role is to stabilize the different oxidation states of the metal; therefore, adjusting the redox potential, it also helps in the solubility of the catalyst in the reaction media.⁴⁶ The most common ligands used for the catalyst system are based on nitrogen or phosphorus, although the latter is generally employed with iron or ruthenium metals, whereas nitrogen-based ligands are mostly employed with copper catalysts. The activity of the ligands depends on various points, such as the nature of the ligand (cyclic, linear or branched) or the nature of the substituent (aryl amine, aryl imine, alkyl amine or pyridine).⁴⁹

Solvents can also play a role in the ATRP process since it can be carried out either in bulk or in solution, or even in heterogenous systems, such as emulsions or suspensions. When a solvent is used, it is necessary that the transfer constant of this solvent is low and that it does not cause side reactions with other system components, such as the catalyst. The solvents used are either non-polar solvents, such as *p*-xylene, or polar solvents such as acetone or DMF.⁴⁸

With the possibility of controlling size and composition of polymers, ATRP enables the development of various compositions and architectures for copolymers with less or more complicated structures (**Figure 11**).

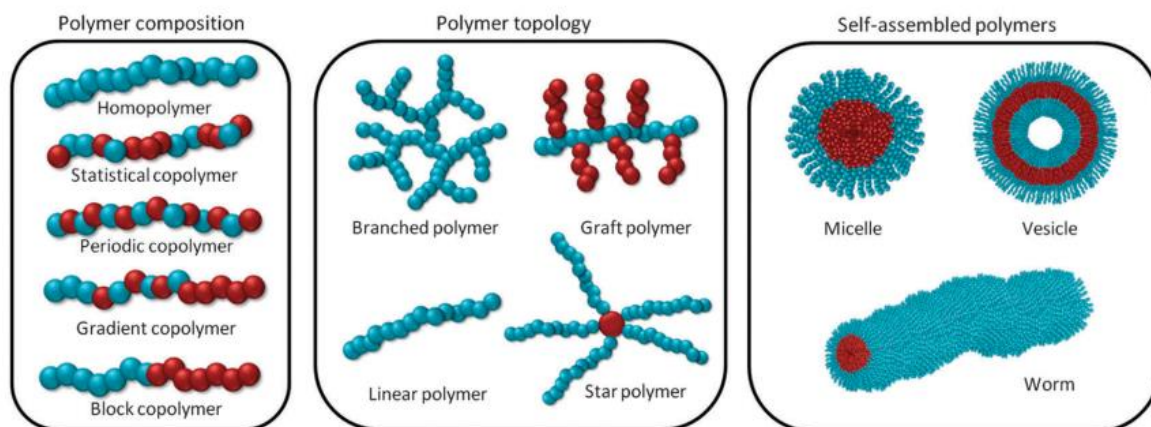


Figure 11: Different polymer compositions, morphologies and architectures that can be achieved using ATRP.⁵⁰

In these next sections, we will delve into the details of ATRP and the elements that influence the kinetics and control of the polymerization.

1.4.1. Influence of ligands

The ligand has an important role for solubilizing the copper salts and tuning the copper catalyst activity. Therefore, the choice of ligand for ATRP greatly influences the effectiveness of the catalyst, and the redox potential of the copper complex serves as a guide parameter for designing the catalyst.⁶ Aliphatic amines are more electron rich and generally better σ donors than pyridines or imines, therefore, their copper complexes usually have lower redox potentials and favor the formation of copper(II) species. This results in a faster polymerization rate using aliphatic amines as ligands than with pyridine or imine analogs.⁵¹ Nitrogen based ligands are usually chosen for Cu-mediated ATRP as they provide good k_{act}/k_{deact} . Furthermore, ligands based on sulfur, oxygen, or phosphorus are less effective due to different electronic effects and/or unfavorable binding constants.⁵² Monodentate nitrogen ligands do not promote successful ATRP, and the general order of Cu complex activity for ligands is tetradentate (cyclic-bridged) > tetradentate (branched) > tetradentate (cyclic) > tetradentate (linear) > tridentate > bidentate ligands.⁵³

Figure 12 presents all values of k_{act} with ethyl 2-bromoisobutyrate (eBiB) that were directly measured or extrapolated, arranged in a logarithmic scale for a better comparison of activities of Cu complexes with ligands. In short, the nature of nitrogen atoms is also important

and follows the order pyridine \geq aliphatic amine $>$ imine, also, the ethylene bridge is a better linkage for N atoms in the ligand than propylene.

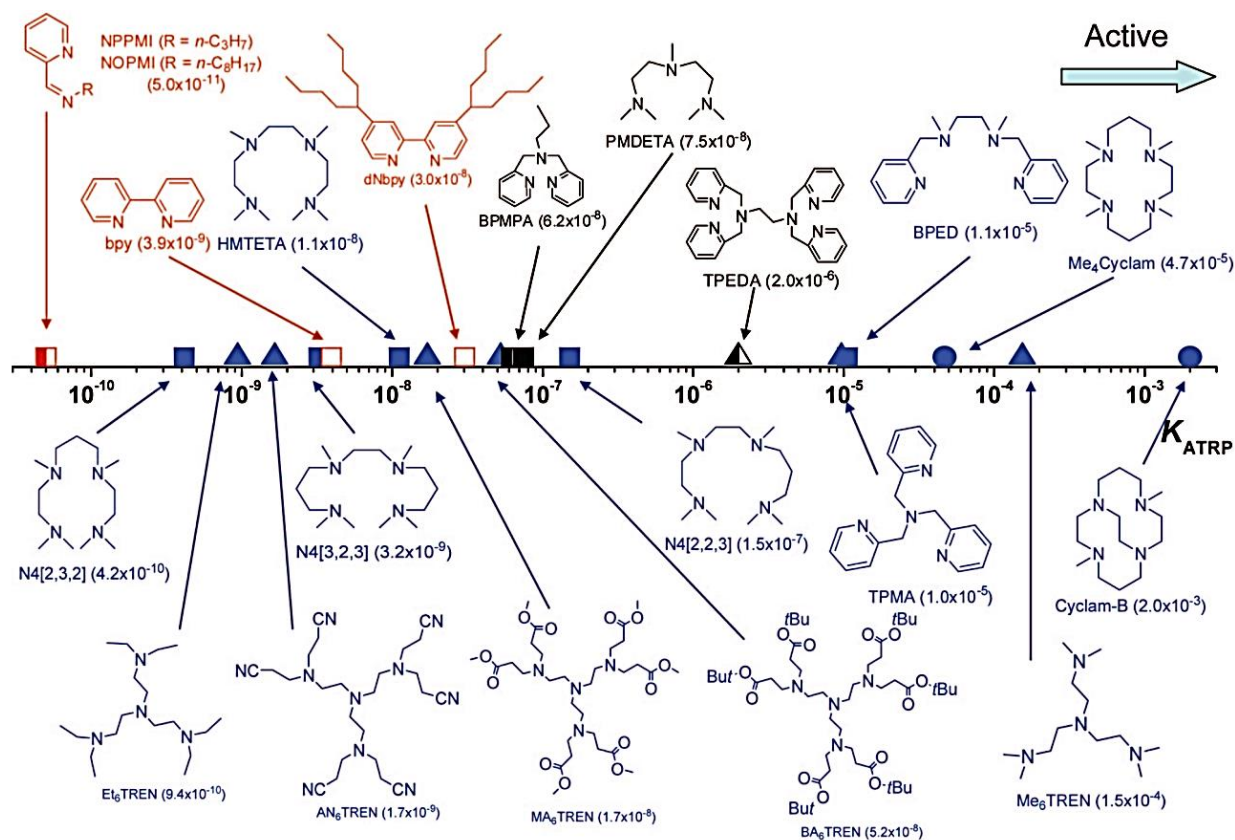


Figure 12: ATRP equilibrium constants K_{ATRP} for various N-based ligands with the initiator eBiB in the presence of Cu^IBr in MeCN at 22 °C. Color key: (red) N2; (black) N3 and N6; (blue) N4. Symbol key: (solid) amine/imine; (open) pyridine; (left-half-solid) mixed; (\square) linear; (Δ) branched; (\circ) cyclic.⁵³

Figure 13 brings the correlation between the ATRP equilibrium constant and activation and deactivation equilibrium constants for different catalysts using 12 different nitrogen-based ligands and copper. It clearly shows that K_{ATRP} increases as a result of both increase in k_{act} and decrease of k_{deact} , and that the k_{act} has a bigger influence than k_{deact} on the K_{ATRP} . The best catalyst should have a large value of K_{ATRP} so it can be used in lower concentrations, but also a large k_{deact} so to provide good control of the polymerization. The most traditional ATRP ligands, such as bpy, dNbpy, PMDETA and HMTETA, falls into this category, having a somewhat large K_{ATRP} but also good control due to sufficiently large k_{deact} values.

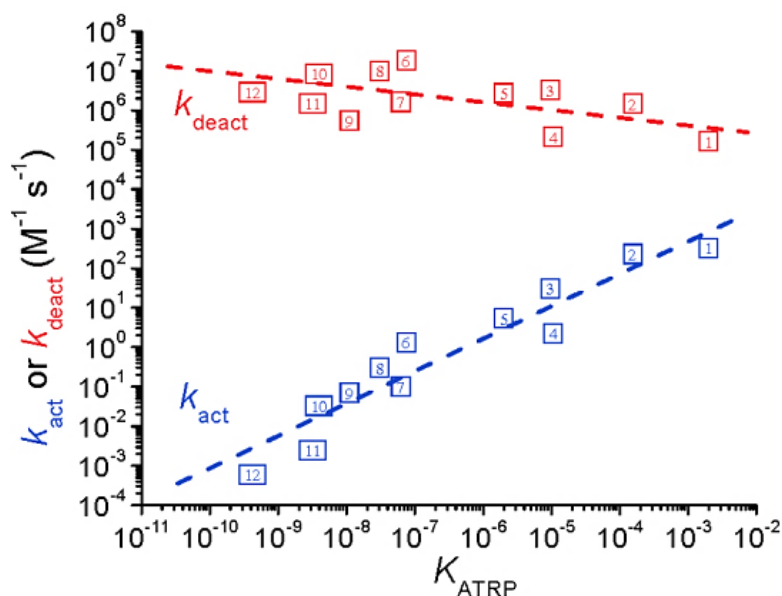


Figure 13: Correlation of k_{act} and k_{deact} with K_{ATRP} for various $\text{Cu}^{\text{I}}\text{Br}/\text{ligand}$ catalysts with eBiB at 22 °C in MeCN. Ligand number key: (1) Cyclam-B; (2) Me_6TREN ; (3) TPMA; (4) BPED; (5) TPEDA; (6) PMDETA; (7) BPMPA; (8) dNbpy; (9) HMTETA; (10) bpy; (11) $\text{N}4[3,2,3]$; (12) $\text{N}4[2,3,2]$. Abbreviations: cf **Figure 12**.⁵³

1.4.2. Influence of initiators

Many studies have demonstrated that the initiator structure influences the control and kinetics of ATRP, as it defines the radical formed during initiation, therefore altering the activation constant and kinetic equilibrium.^{6, 53-54} Studies have shown that alkyl bromides are several times more active than the corresponding alkyl chlorides, for instance, eBiB > EtClIB, BrPN > ClPN, PEBr > PECl, and MBrP > MCIP (cf **Figure 14**). The difference in the K_{ATRP} values for eBiB and EtClIB facilitates the halogen exchange required to synthesize well-defined polymers.⁵³

Figure 14 shows the K_{ATRP} of various initiators with $\text{Cu}^{\text{I}}\text{X}/\text{TPMA}$ ($\text{X} = \text{Br}, \text{Cl}$) in MeCN at 22 °C, and it can be clearly seen that the modification of the initiator structure affects greatly the activation rate constants. It basically depends on the nature of the leaving group, the substitution degree of the initiator and the activity of the alkyl group. For instance, increased activation rate constants are observed as the initiator substitution increases. Therefore, tertiary R-bromoesters have higher activation rate constants than secondary and primary. In fact, the ratios are $\sim 1:10:80$ for primary, secondary, and tertiary α -bromoesters, respectively. This is due by the better stabilization of the radical with more substituted carbon. The environment of

the α -substituent is also important for the stabilization of the radical, for example, alkyl bromides with $-\text{C}(\text{O})\text{NEt}_2$, $-\text{Ph}$, $-\text{C}(\text{O})\text{OMe}$, and $-\text{CN}$ groups ratios are $\sim 1:4:8:600$.⁵⁵ The differences in the equilibrium constants are explained in terms of the competing effects of the substituents on the stability of the alkyl halide bond, i.e., with the increase of the electron-donating ability of the substituent (i.e., cyano < ester < phenyl), and the effects on the stabilities of the alkyl radical formed (ester < cyano < phenyl).⁵³

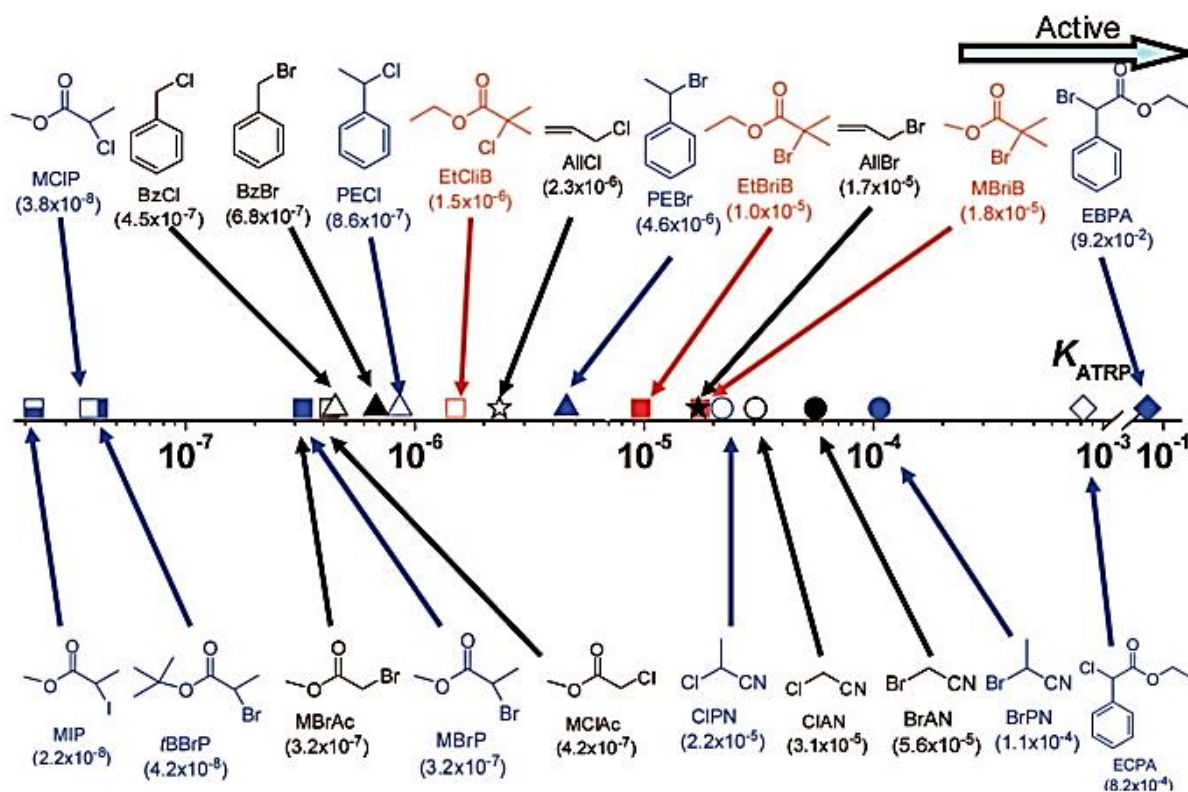


Figure 14: ATRP equilibrium constants for various initiators with $\text{Cu}^{\text{I}}\text{X}/\text{TPMA}$ ($\text{X} = \text{Br}, \text{Cl}$) in MeCN at 22 °C. Color key: (red) 3°; (blue) 2°; (black) 1°. Symbol key: (solid) R-Br; (open) R-Cl; (bottom-half-solid) R-I; (Δ) phenyl; (\square) ester; (\circ) nitrile; (\diamond) phenyl ester; (\star) allyl.⁵³

In short, the activity of the alkyl group for the initiators follows i) degree of substitution in which $3^\circ > 2^\circ > 1^\circ$, ii) stabilization of radical with phenyl ester > cyanide > ester > benzyl > amide, and iii) leaving group effect with $\text{I} > \text{Br} > \text{Cl} \gg \text{SCN} \approx \text{NCS}$.

1.4.3. Influence of solvents

The kinetics of Atom Transfer Radical Polymerization is also influenced by the type of solvent used for polymerization. In fact, the reaction can proceed in bulk conditions (with only the monomers), but also in diluted systems using different solvents. Using solvatochromic

parameters, the K_{ATRP} values were measured and predicted for a $\text{Cu}^{\text{I}}\text{Br}/\text{HMTETA}$ system by Braunecker *et al.*⁵⁶ These findings are summarized in **Figure 15**. In general, K_{ATRP} ranges between 10^{-9} and 10^{-10} in aromatic hydrocarbons, between 10^{-8} and 10^{-9} in ethers, ketones, and nitriles, is $\sim 10^{-8}$ in most alcohols, and is between 10^{-7} and 10^{-8} for most amides. There are two exceptions in which the K_{ATRP} is quite high, when using water and formamide, which could be of interest for the ATRP of less reactive monomers.

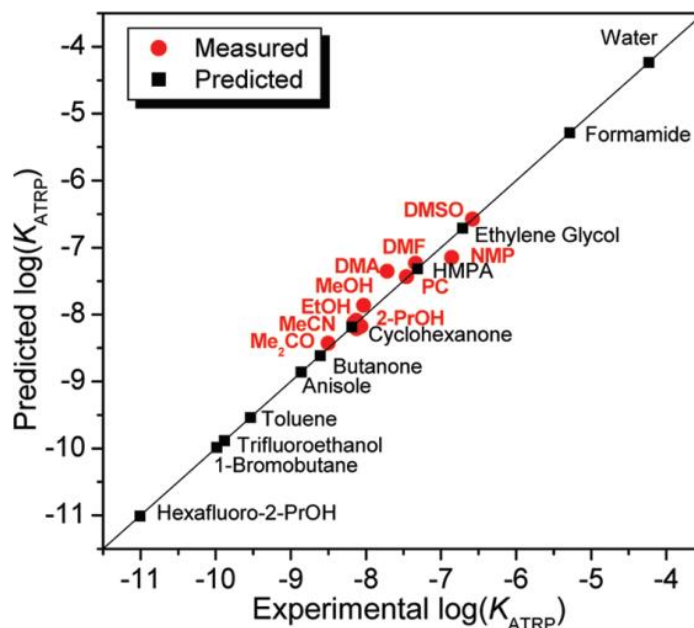


Figure 15: $\log(K_{\text{ATRP}})$ values measured for $\text{Cu}^{\text{I}}\text{Br}/\text{HMTETA}$ with methyl α -bromoisobutyrate as initiator plotted against predicted values.⁵⁶

1.5. $\text{Cu}(0)$ mediated supplemental activator and reducing agent (SARA) ATRP.

The timeline shown in **Figure 16** summarizes the evolution of the procedure named Supplemental Activation Reducing Agent (SARA) ATRP, which is based on the roles of $\text{Cu}(0)$ in the overall activation and reactivation mechanism. It indicates that $\text{Cu}(0)$ and $\text{Fe}(0)$ were first used in an ATRP in 1997.⁵⁷ They were used to directly activate the alkyl halide initiators as a supplemental activator (SA) and to reduce $\text{Cu}(\text{II})$ catalyst complexes to form $\text{Cu}(\text{I})$ catalyst *in situ* in a comproportionation reaction (**Figure 17**). The zero oxidation state metal remained in the reaction to reduce the concentration of $\text{Cu}(\text{II})$ formed by termination reactions.

Some developments in the SARA procedure was followed with the use of tris[2-(dimethylamino)ethyl]amine (Me_6TREN) as ligand, which allowed the ATRP to be conducted

at room temperature,⁵⁸ besides as other developments using polar solvents.⁵⁹ In 2006, Percerc and coworkers⁶⁰ described an ultrafast procedure with a proposed mechanism consisting of an activation step proceeding by a low activation energy outer-sphere single-electron-transfer (SET). The resulting Single-Electron-Transfer Living Radical Polymerization (SET-LRP) process was activated by a catalytic amount of the electron-donor Cu(0), Cu₂Se, Cu₂Te, Cu₂S, or Cu₂O species, but not by Cu(I) species. Since then, the mechanistic aspects of atom transfer radical polymerization in the presence of zero-valent copper and polar media have been under discussion since 2006.⁶¹

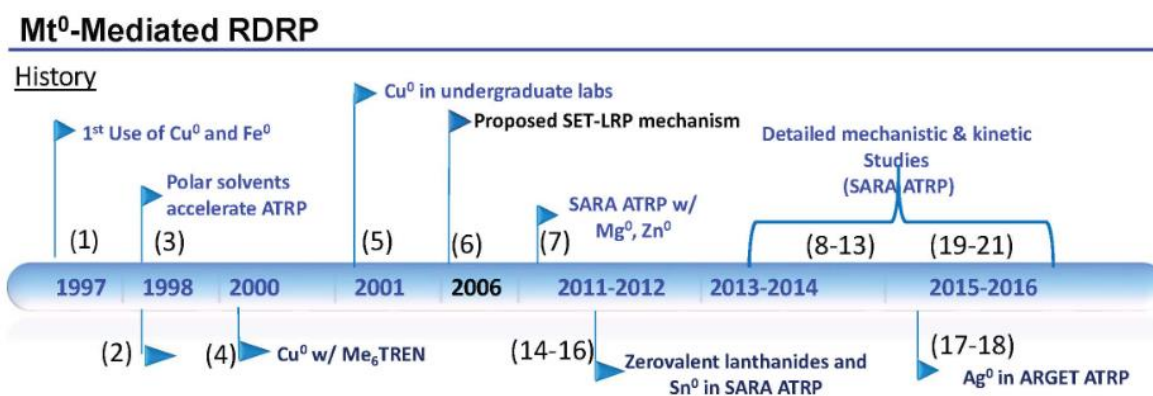


Figure 16: Evolution of the procedure named Supplemental Activation Reducing Agent (SARA) ATRP.⁶²

Some works by K. Matyjaszewski and colleagues describe the basics of SARA ATRP,⁶³ and the experimental evidence supports the SARA ATRP mechanism. Cu(0) functions as a supplementary activator and reducing agent through an inner-sphere electron transfer process that takes place during a slow activation step. Cu(I) is the main activator of dormant alkyl halides. This process involves an even slower disproportionation of Cu(I) to Cu(II) and a rather sluggish comproportionation reaction between Cu(0) and Cu(I). (**Figure 17**).

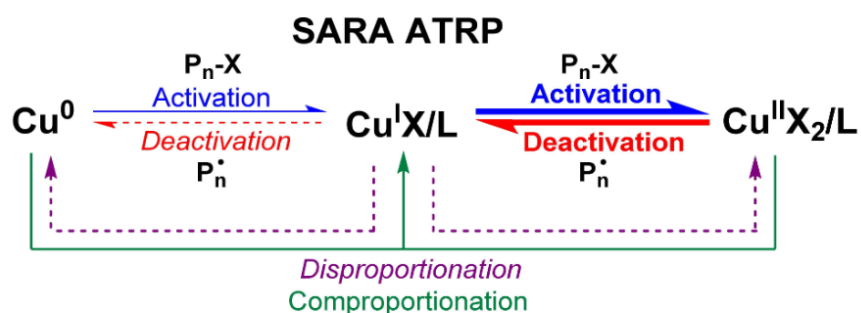


Figure 17: General mechanism of comproportionation for SARA ATRP.⁶²

However, Cu(0)-mediated polymerization is a complex system, with several components including monomer, ligand, solvent, initiator and copper with different oxidation states, in addition to various equilibrium reactions that includes disproportionation and comproportionation.⁶⁴ There are a few reviews available on the details on the mechanisms for both SARA ATRP and SET-LRP.^{61, 65} Regardless, Cu(0)-mediated polymerizations enable significant reduction in termination reactions, enabling the convenient and facile synthesis of polymer materials.⁶⁴

These new methodologies for ATRP were created in an effort to overcome the problems associated with classical ATRP. For instance, classical ATRP has complication with the initiation and air sensitivity of Cu(I). In fact, during initiation of classical ATRP, the alkyl halide initiator and activator species rapidly react and force the reaction in the forward direction to obtain a dynamic equilibrium. However, this results in the production of radicals that outrun the number of deactivators, which could result in undesirable bimolecular terminations.⁶⁴ Cu(0)-mediated reactions slowly removes the deactivator at a sufficient concentration that maintain the control of polymerization, while also providing an air-stable system.

In summary, Cu(0)-mediated reversible deactivation radical polymerization (RDRP) is a versatile method that is used to create controlled polymers with complex architectures,^{63a} while exhibiting various advantages such as very low concentration of copper (ppm), simple set up and deoxygenation procedures, and narrow molar mass distributions.⁶⁶

1.6. Surface Initiated (SI)-ATRP

Surface-initiated atom transfer radical polymerization (SI-ATRP) is a powerful tool that allows for the synthesis of organic–inorganic hybrid materials.⁶⁷ In fact, SI-ATRP is

particularly appealing to graft large amounts of chemicals, such as catalysts, biological probes biofouling agents etc. The polymers can be immobilized on surfaces by both physical or chemical methods. Considering physical methods, a preformed polymer in solution can be physisorbed on the surface yielding these modified surfaces (**Figure 18**).

However, covalent bonding of polymer chains onto surface has received greater attention because this methodology allows the construction of relative stable polymer layers. In general, these covalently attached polymer layers can be prepared by either the “grafting-to” or “grafting-from” method (**Figure 18**). The “grafting-to” involves the chemical reaction of a preformed polymer with a surface containing a functional group for attachment. Its main advantage is the simplicity of the methodology and the possibility of well characterizing the polymer chains before attachment on surface.⁶⁸

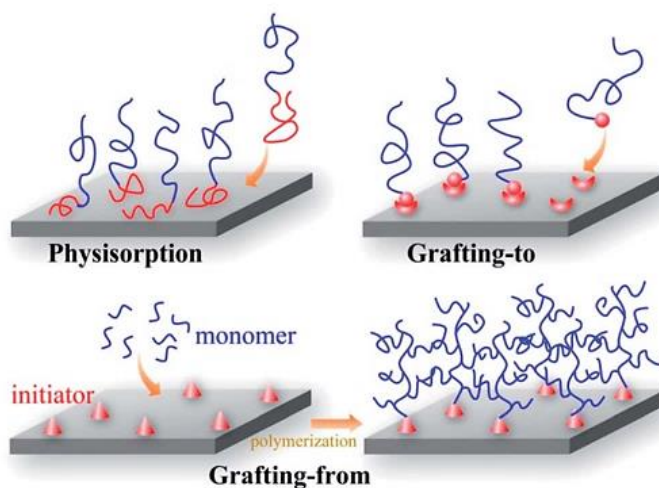


Figure 18: Schematic illustration of different methods for immobilizing polymer chains on solid surfaces: physisorption, “grafting-to” and “grafting-from” (surface initiated polymerization).⁶⁸

Using the “grafting-from” method allows the polymerization of the monomer on an initiator functionalized surface *in situ*. Usually the grafting density is determined by the initiator density. Unlike the “grafting to” technique, this method is not limited by steric hindrance of the preformed polymer chains, which normally yields higher grafting densities. The characterization of the polymer chains grown by the “grafting from” technique is usually made by the detachment of the polymer from the surface to obtain information on molar mass distribution. Occasionally, the “grafting from” technique can suffer from low initiator

efficiency and different rates of diffusion of monomers to the active sites, which would potentially lead to higher chain length distribution.⁶⁸

The properties of grafted polymers on surface might change depending on the grafting density and wettability,⁶⁹ thus yielding various conformations of polymer chains on surface. Considering the swollen state, if a grafting density is < 0.01 chains/nm², a mushroom conformation is obtained (**Figure 19**); however, if the grafting density is in the range of $0.01 - 0.7$ chains/nm² a semi-dilute brush regime is obtained. Finally, a high-density brush regime can be obtained when the grafting density is superior to 0.7 chain/nm².

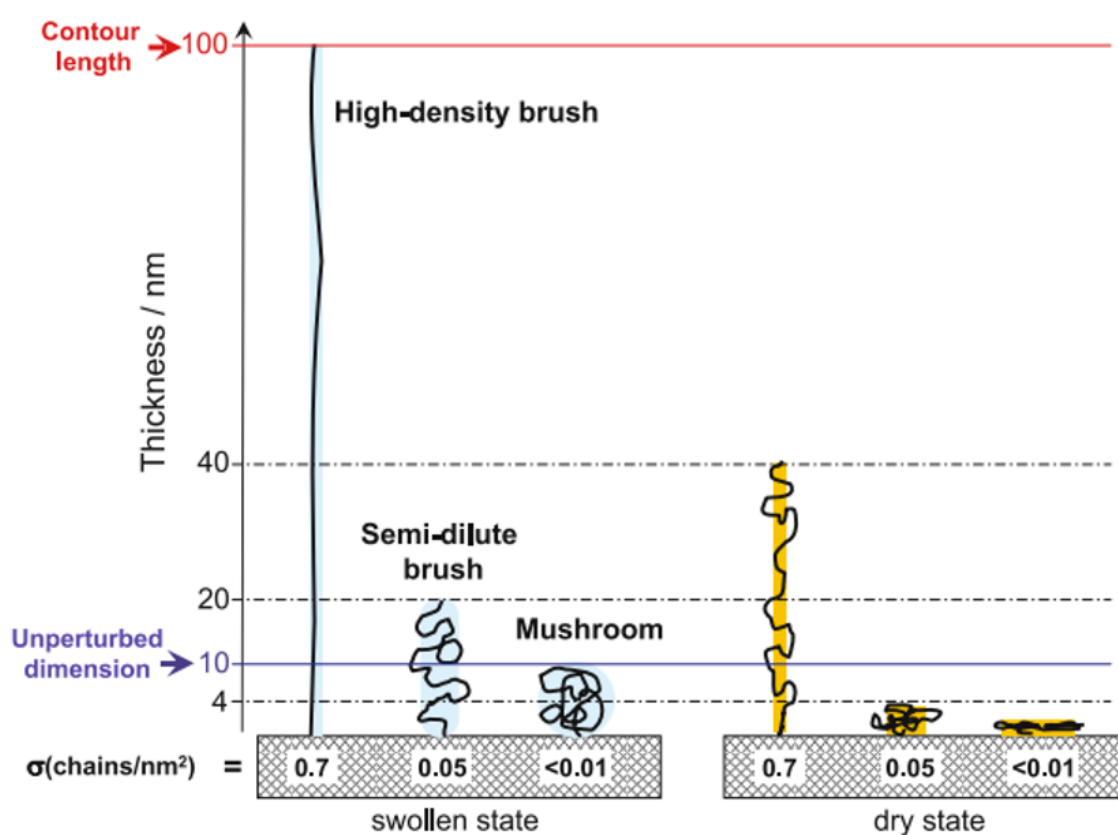


Figure 19: Schematic illustration of conformations of end-grafted polymer chains in wet and dry states as a function of graft density.⁷⁰

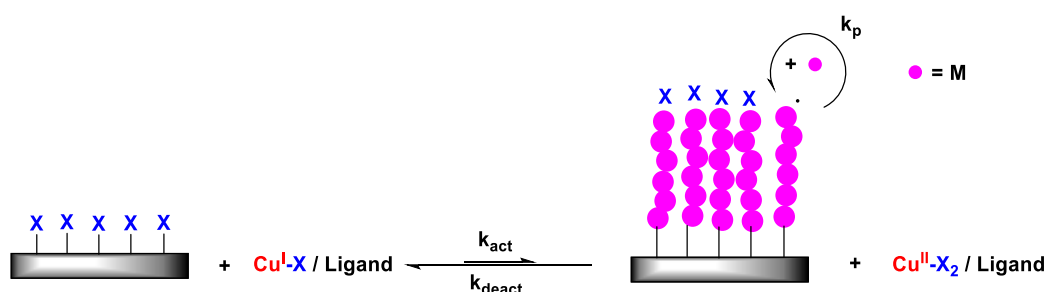
Polymer brushes on surfaces via controlled polymerization techniques has become a powerful method to tailor the chemical and physical properties of interfaces and has helped the development of surface and interface engineering. In the last decades, many developments have emerged including the application of polymer brushes in catalysis, electronics and biosensing, for instance. An extensive review on SI-ATRP describing the state-of-the-art, the opportunities

and challenges of generating polymer brushes from surfaces is available from Klok and coworkers.⁷¹

Our group has successfully demonstrated the SI-ATRP of styrene on silicon surface from a “grafting-from” methodology and the direct quantification of polymer brushes without the need of detaching the polymer brushes from the surface; therefore contributing to the advancements on the characterization of polymers on surface.^{8a} In this manuscript, polymers grafted on surface were obtained in the brush conformation regime.

1.7. SI-ATRP from flat surfaces

Modification of flat surfaces with polymeric films are particularly interesting because these materials allow the design of surfaces with properties such as wettability, biocompatibility, biocidal activity, adhesion, adsorption, among others. As already described, the graft density of the initiator affects the morphology of the tethered (co)polymer chains. An important point to obtain brush polymers on surface is to control the grafting of the initiator to induce the polymerization of monomers and their density. Grafting densities have to be higher than 0.01 nm^{-2} to reach the brush-like regime.⁷⁰ **Scheme 5** shows a schematic representation of SI-ATRP from a flat surface.



Scheme 5: Illustration for “grafting-from” approach employed to introduce polymer brushes onto the surface of flat materials via SI-ATRP.

There are many examples on the literature describing the SI-ATRP from flat surfaces, specially from polyethylene terephthalate (PET),^{5, 72} cellulose,⁷³ poly(lactic acid) (PLA)⁷⁴ and silicon.^{8a, 75} In fact, the use of polymers attached to solid supports helps the development of smart surfaces, which can be tunable through conformational changes of the polymer chains in response to external inputs (for example, pH, temperature and solvent).⁷⁶

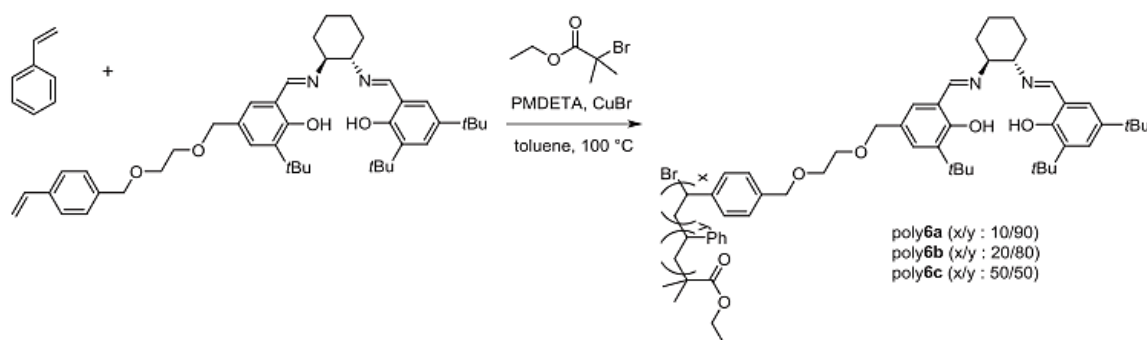
In the context of this thesis and with the objective in mind to be able to recycle and reuse catalysts, the choice of the substrates is also important. We believe that silicon substrates fulfill the requirements for a robust supported catalyst: starting from its hydrogenated surface, dense and functional organic layers can be grafted through highly resistant covalent Si–C bonds over a large pH range (from acidic to pH=9). SI-ATRP can be then performed to grow copolymers with adjustable thicknesses; and their subsequent post-functionalization with catalysts together with the high specific area of macroporous silicon should allow the high loading of catalysts for an efficient activation of chemical reactions in liquid phase. In fact, Riant and coworkers have demonstrated the applicability of SI-ATRP on silicon substrates for applications in catalysis where they have attached palladium catalysts on polymer brushes grown on silicon substrates and further evaluated them in a reaction based on the palladium(0)-mediated deprotection of a coumarin type compound.⁷⁷ This example demonstrates the applicability of polymer brushes in catalysis, together with the use of silicon substrates.

1.8. Functionalization of polymers

The post-modification of polymers dates as early as 1840 when Hancock and Ludersdorf reported the transformation of natural rubber into a tough and elastic material upon treatment with sulfur.⁷⁸ Since then, functional polymers have been studied to develop materials with different properties. In fact, polymers with atomic groups with higher polarity or reactivity than traditional hydrocarbon chains are classified as functional polymers. They display improved properties compared to their non-functional counterparts. The functionalization of polymers can be obtained by various methodologies, such as by chain extension, branching or cross-linking reactions.⁷⁹ Polymer functionalization is defined by a functional polymer synthesis process consisting of three main approaches: direct-functional polymer synthesis, post-functionalization of polymers, and functional group transformation.⁸⁰

Obtaining functionalized polymers containing catalysts sites are possible by either the post-functionalization or the direct polymerization approach. In fact, our consortium successfully demonstrated the synthesis of salen based copolymers by the direct polymerization of the catalyst with a modified styrene in its backbone (**Scheme 6**).⁴ The modified polymers were later complexed with the desired metal to undergo asymmetric catalysis, which yielded good reactivity and selectivity. However, this approach has some disadvantages, such as the

control of the polymerization with such bulky monomers, and the possible complexation of the ligand with copper metals during polymerization.



Scheme 6: Functionalized monomer and styrene copolymerization by ATRP to obtain polymeric salen ligands.⁴

Therefore, to overcome these disadvantages, this thesis focuses on using functionalized polymers for further post-functionalization with salen catalysts. Therefore, this section will mainly focus on the various methods for the post-functionalization of polymers.

The main reactions used for the post modification of polymers include addition, substitution, elimination and isomerization reactions. For the addition reaction, the post-polymerization modification is often identical to their small molecule counterparts. Therefore, the functional group on the polymer reacts with a small molecule in an addition reaction.⁸¹ This is the case of hydrogenation of unsaturated polymers,⁸² or the epoxidation of unsaturated bonds,⁸³ for instance. However, the most common reaction for post-functionalization of polymers is the substitution reaction. It includes reactions such as esterification, amidation, hydrolysis, etc. For example, the esterification reaction is highly important for the modification of cellulose,⁸⁴ and the hydrolysis of poly(vinyl acetate) represents the most suitable synthesis for poly(vinyl alcohol).⁸⁵

Elimination and isomerization reactions are less common but also very useful for the development of new polymers. Considering elimination reactions, dehydrochlorinations, dehydrogenations and dehydrations result in unsaturated polymers.⁸¹

In view of these four main reactions, it englobes eight main types of chemical transformations, which are the post-polymerization modification via 1) thiol-ene addition; 2) reaction with epoxides, anhydrides, oxazolines and isocyanates; 3) active esters; 4) thiol-

disulfide exchange; 5) Diels-Alder reactions; 6) Michael-type addition; 7) azide alkyne cycloaddition reactions; and 8) ketones and aldehydes. Other reactions are also possible such as Pd-catalyzed couplings and thiol-yne additions.⁸¹ **Figure 20** shows these main types of reactions, and it highlights the azide alkyne cycloaddition reactions since it is the main focus of this thesis.

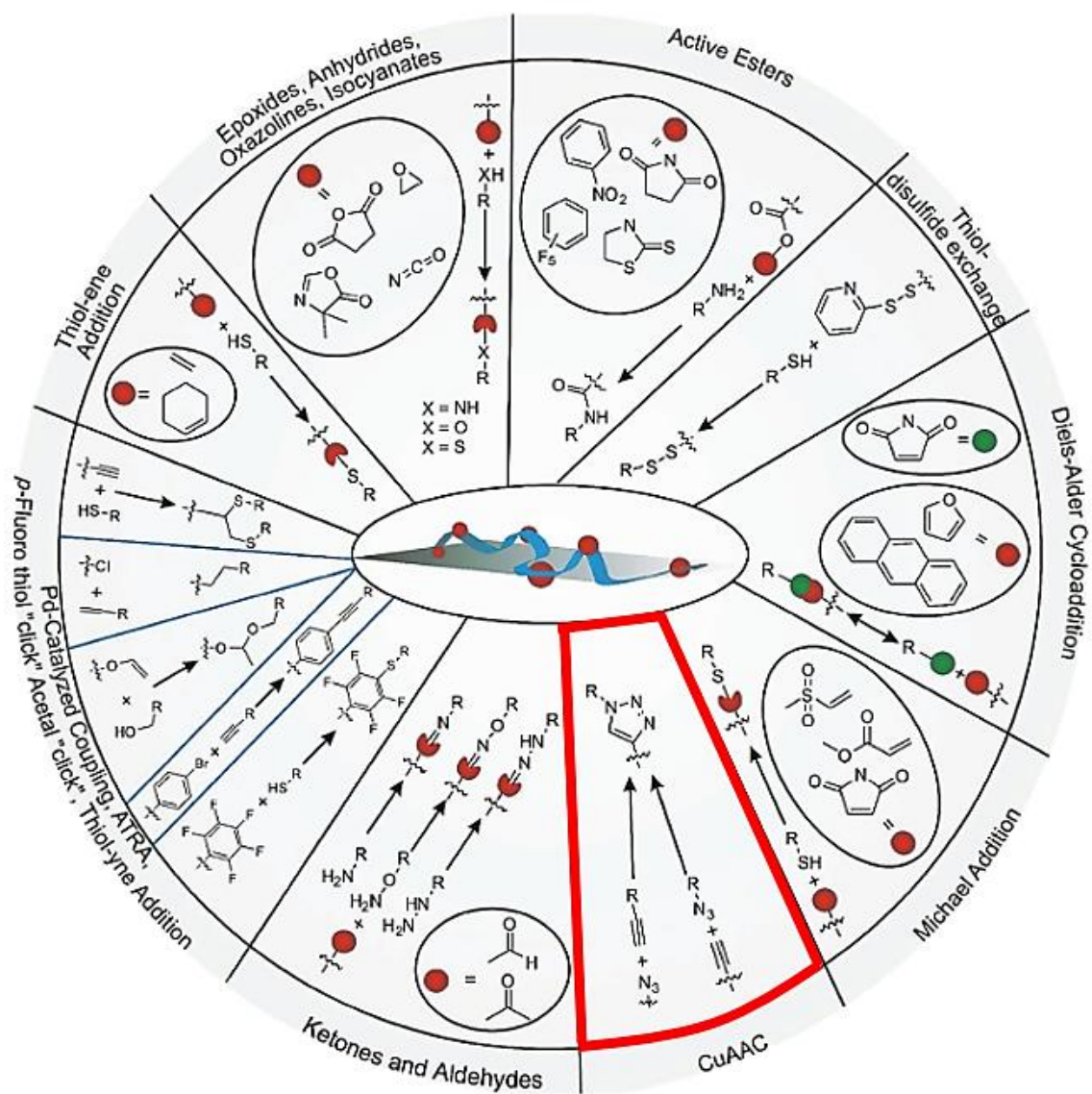


Figure 20: Schematic illustration of the main classes of reactions that can be used for the preparation of functionalized polymers via post-polymerization modification.⁸¹ Highlight in red for the post functionalization using click chemistry, the pathway used in this thesis.

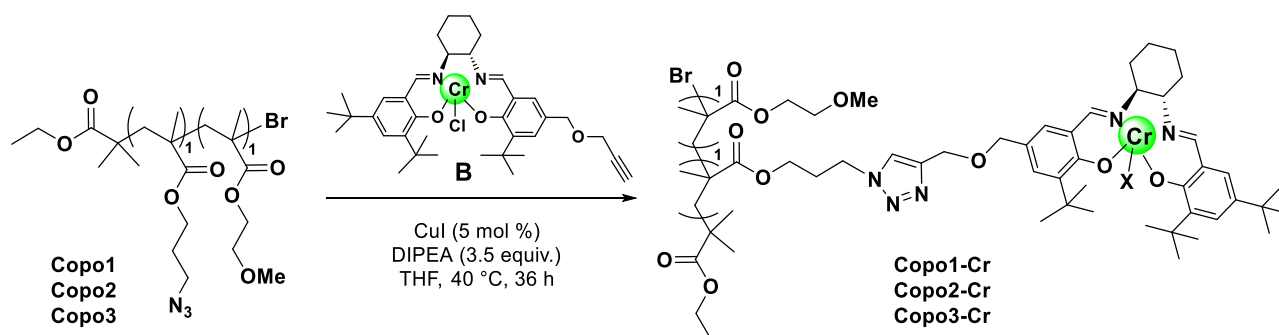
The Huisgen 1,3-dipolar cycloaddition (CuAAC) reaction between azides and alkynes, commonly named “click chemistry reaction”, can be carried out at mild conditions using Cu(I) salts. The strategy involving click chemistry for the post-modification of polymers have

demonstrated its efficiency for the modification of various monomers containing either the azide function,⁸⁶ or the alkyne function,⁸⁷ with most of the times 90 – 100 % conversion of the functional group in both aqueous and organic media under mild conditions.⁸¹

The best example from the literature for this thesis is the work by Summerlin *et al.* in which they showed the polymerization of azido-3-propyl methacrylate (AZMA) and then functionalized the PAZMA via click chemistry with various alkynes under mild conditions and with a yield > 95%, showing an attractive alternative for preparing polymers with high degrees of functionalization.⁸⁸

One of the major drawbacks of this approach is the possible contamination of copper on the polymers, making it necessary the further purification of the modified polymer. The remaining copper could potentially be a problem considering biomedical applications because of copper's toxicity.⁸⁹ However, considering that the application envisioned in this thesis is in asymmetric catalysis, this is not a concern and makes the strategy for functionalization of polymers via click chemistry a very attractive and efficient methodology.

Therefore, to overcome these disadvantages, this thesis focuses on using functionalized polymers for further post-functionalization with salen catalysts. Thus, first a functional copolymer is synthesized, which contains the AZMA comonomer. Then, this copolymer is post functionalized with a salen catalyst by means of click chemistry (**Scheme 7**). This is the strategy applied in this manuscript and it allows the better control of the polymers and the correct complexation of metals to obtain the supported catalysts.



Scheme 7: Post-modification strategy applied in this thesis to obtain supported salen catalysts. Copo1, Copo2 and Copo3 has different loadings of AZMA comonomer: 10, 30 and 50% respectively.^{8b}

Part C: Supported asymmetric salen catalysis

In the catalysis community, the urge to develop more efficient, selective, and environmentally friendly catalysts is one of the main challenges for scientists. The immobilization of catalysts on supports has been an attractive approach to design catalysts that have enhanced properties, such as better thermal/chemical resistance. Also, supported catalysts have the major advantage of being easily separated from the reaction mixture by simple centrifugation and/or filtration.⁹⁰ This allows the reuse of such catalysts, thus enabling the development of procedures that are in accordance with green chemistry.

Figure 21 shows a schematic representation of homogenous catalysis, in which all reagents and catalysts are present in the same media, and the supported catalysis. In the homogenous pathway, the reagents react with the catalyst in the same reaction media, forming an intermediate, which later forms the product. The catalyst remains soluble in the solution and therefore needs to be removed from the reaction media usually by tedious and time demanding procedures, such as column chromatography. In most cases, the catalyst cannot be re-engaged in another reaction because of its complicated recovery. On the contrary, if a supported catalyst is used, the reagents react with the catalyst supported on a substrate to form the desired product. In this way, the supported catalyst and product remained separated and the catalyst can be easily recovered from the medium and no further purification is necessary.⁹¹

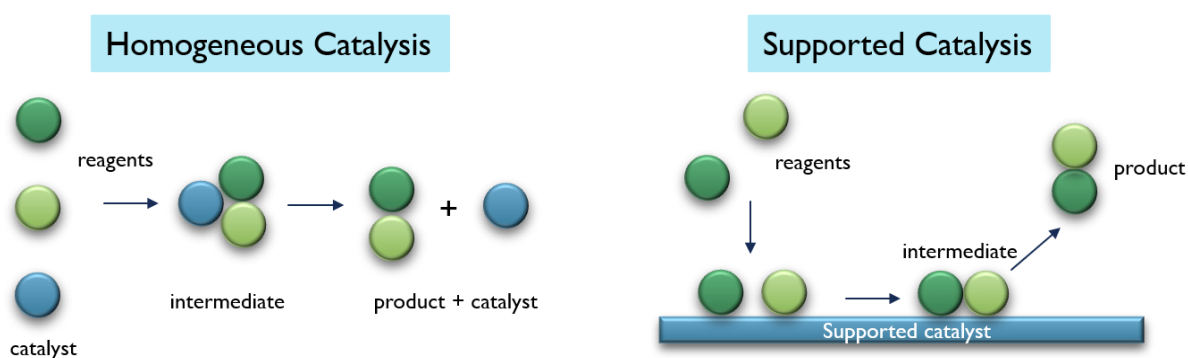


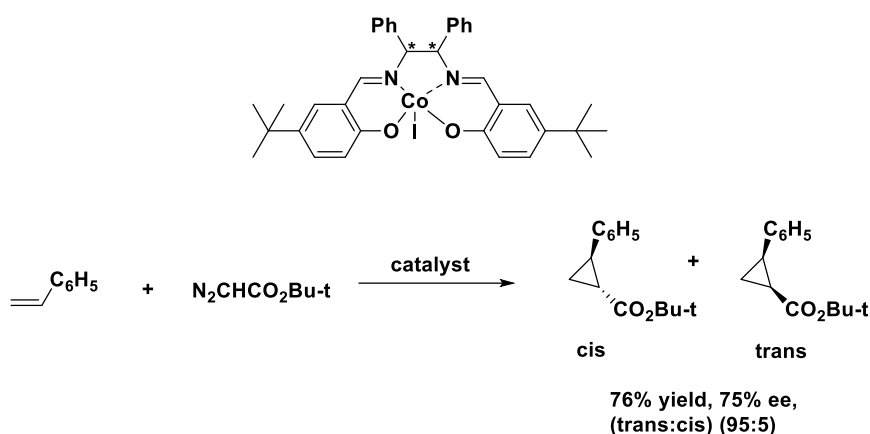
Figure 21: Representation of homogenous catalysis and supported catalysis.

In this part, an overview of the main achievements using supported salen complexes is given, with first the contextualization of key reactions using chromium and cobalt metals in homogenous catalysis, and then with supported catalysis.

1.9. Homogenous salen catalysts and their reactivity

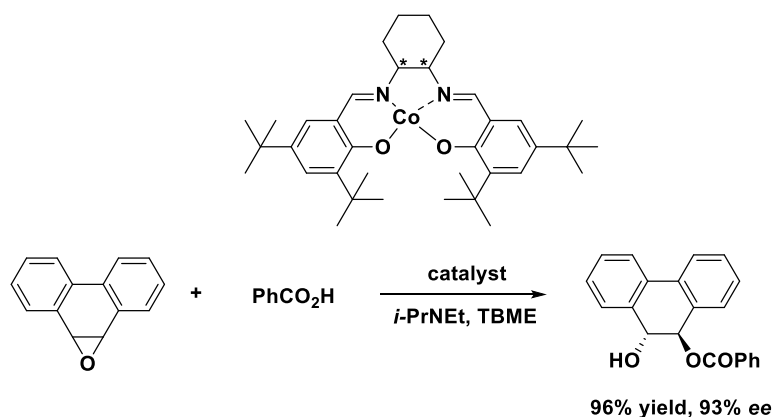
1.9.1. Cobalt salen complexes

Cobalt-salen complexes are usually associated with their extraordinary activity in kinetic resolutions. However, they also promote many other asymmetric reactions because of their pronounced Lewis acid character.⁹² For instance, Katsuki and coworkers used Co(salen) complex to catalyze the cyclopropanation of styrene with *tert*-butyl diazoacetate (**Scheme 8**). The reaction showed overall high trans-selectivity (trans : cis = 95 : 5).⁹³



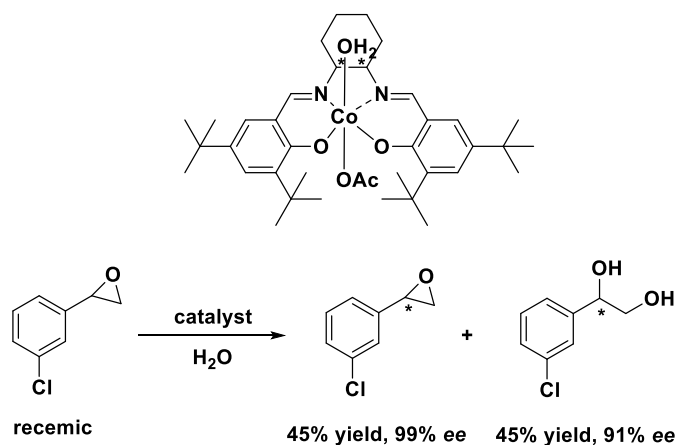
Scheme 8: Asymmetric cyclopropanation of styrene using cobalt salen complexes.

Although not very common as chromium salen complexes, Co(salen) catalysts can also be applied for the ring opening of *meso* epoxides. Jacobsen *et al.* described⁹⁴ the asymmetric nucleophilic ring opening of *meso* epoxides using benzoic acid in the presence of a cobalt salen catalyst giving good yields and enantioselectivity (**Scheme 9**).



Scheme 9: Asymmetric ring-opening of a *meso* epoxide using cobalt salen complexes.

As a last example to describe the reactivity of cobalt salen complexes, there is the famous hydrolytic kinetic resolution (HKR) of terminal epoxides. This reaction was first demonstrated by Jacobsen *et. al* in 1997,⁹⁵ in which Co(salen) complexes are able to promote the hydrolytic kinetic resolution of racemic epoxides enabling the access to terminal epoxides and diols in high enantioselectivity. **Scheme 10** shows an example of the HKR of 2-(3-chlorophenyl)oxirane demonstrated by Jacobsen *et. al.* in 1997 obtaining the desired diol product with enantioselectivity higher than 90%.⁹⁶



Scheme 10: Hydrolytic kinetic resolution of racemic epoxides using cobalt salen complexes.

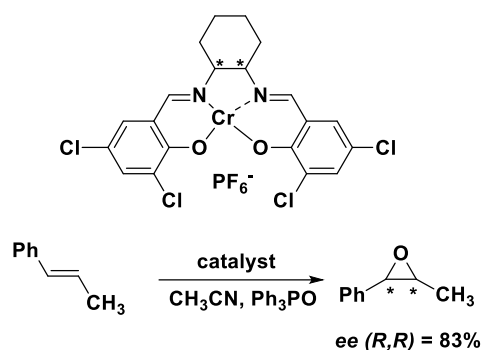
This reactivity is further evaluated in this thesis with the HKR of epibromohydrin using Co-OAc salen catalysts.

1.9.2. Chromium salen complexes

Chromium salen complexes have gained significant attention in catalysis because of their versatile reactivity allowing their employment in the promotion of various reactions. One of the hallmark reactions catalyzed by Cr(salen) complexes is the asymmetric epoxidation from olefins. This is an important reaction for the development of building blocks in pharmaceuticals, agrochemical and fine chemicals industry.

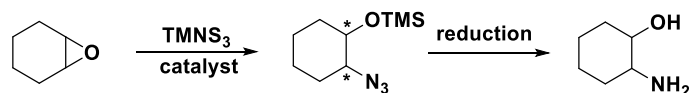
In 1995 Bousquet and Gilheany⁹⁷ first reported the asymmetric epoxidation of alkenes promoted by chromium salen complexes (**Scheme 11**). The catalysts successfully catalyzed the reaction for β -methylstyrene up to 83% enantioselectivity, however, they noticed that *trans*-alkenes were epoxidized at higher rates and greater enantioselectivity than their analogous *cis*-alkenes. McGarrigle and Gilheany wrote a comprehensive review regarding the epoxidation of

alkenes promoted by chromium (and manganese) salen catalysts in case the reader would like more details in this type of reactivity.⁹⁸



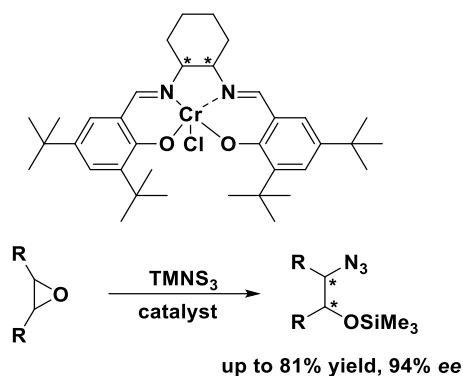
Scheme 11: Asymmetric epoxidation of (*E*)- β -methylstyrene.

Another important reactivity of chromium salen catalysts is the asymmetric ring opening (ARO) of *meso* epoxides. In fact, when this reaction is employed using azides as nucleophiles it brings an easy pathway for the conversion of products into valuable vicinal amino alcohols with high optical purity (**Scheme 12**).⁹⁹



Scheme 12: The asymmetric ring-opening of cyclohexene oxide with TMSN_3 followed by reduction to synthesize the corresponding *trans*-1,2-amino alcohol with high enantioselectivity.⁹⁹

The first use of a metal-salen catalyst for the ARO of epoxides was done by Jacobsen and coworkers in 1995 with the use of chromium (III) salen complexes for the ARO of various epoxides using trimethylsilylazide (TMSN_3) as nucleophile.¹⁰⁰ The catalyst promotes the reaction with good yields (up to 91% of isolated yield) and excellent enantioselectivity (up to 94%) depending on the employed epoxide.



Scheme 13: Asymmetric ring-opening of epoxides using chromium salen catalysts.

Considering the mechanistic aspects of this reaction, kinetic studies revealed a second-order dependence of the reaction rate on the catalyst which suggests that it plays a dual role in the mechanism by activating both the electrophile and the nucleophile in a bimetallic rate determining step (**Figure 22**).¹⁰¹

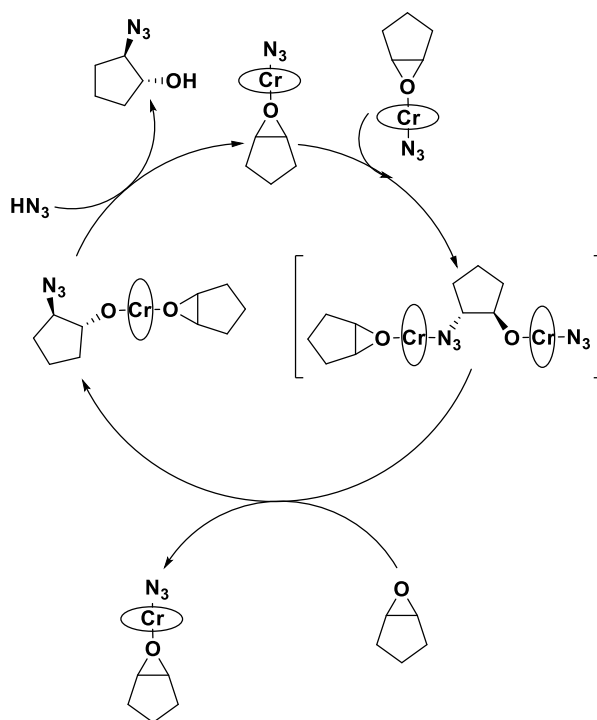
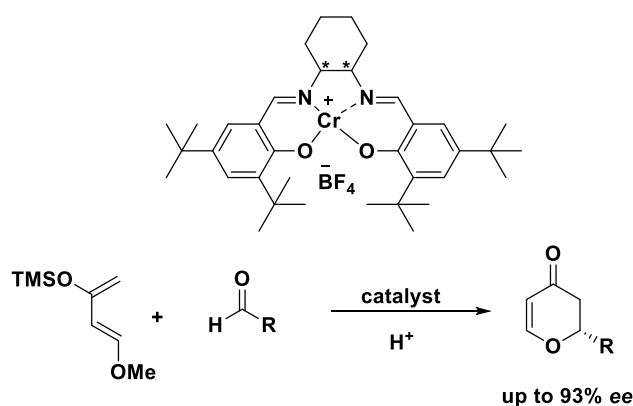


Figure 22: The mechanism for the ARO of cyclopentene oxide with TMSN_3 catalyzed by Cr-salen complexes as proposed by Jacobsen *et al.*¹⁰¹

The mechanistic insights considering a bimetallic rate-determining step led to further development of catalysts with more complex structures, such as in dimeric form, to study in greater detail the bimetallic cooperativity in vision of obtaining higher selectivity and activity. Jacobsen *et al.* designed and studied these dimeric catalysts in the ARO of cyclopentene oxide

and they observed that the covalent linkage of the (salen)Cr units provided the catalysts 1-2 orders of magnitude times more reactive than the monomeric analogues, with no loss in enantioselectivity.¹⁰² The ARO of epoxides is studied in this thesis and further discussed in **Chapter 5**.

As a final example of reactivity of Cr(salen) complexes, there is also the Hetero-Diels–Alder reactions. In Jacobsen's group, they also demonstrated the asymmetric hetero-Diels–Alder reaction of an aldehyde with the Danishefsky's diene using 2 mol% of a Cr(salen) catalyst.¹⁰³ The catalysts provided good reactivity and enantioselectivity, with the counterion of the metal affecting both the reactivity and selectivity of the reaction.



Scheme 14: Asymmetric hetero-Diels–Alder reaction using Cr(salen) catalyst.

1.10. Immobilization of salen catalysts to develop supported catalysts

The field of asymmetric catalysis has been dominated by homogenous catalysts in spite of their difficult separation and reuse as well as their elevated cost because they give excellent selectivities and activities. However, in the last few decades, significant development has been made in the area of solid-phase chemistry which contributed to the progress on stereoselective heterogeneous catalysis.¹⁰⁴ The heterogeneous asymmetric catalysts can be divided into mostly two classes: 1) application of immobilized homogeneous catalysts, commonly called supported catalysts, and 2) catalysis on surfaces that are chiral themselves or with chiral modifiers.^{90b} In this thesis, we will mainly focus on the class 1, but an extensive review on asymmetric heterogeneous catalysis englobing the three categories is provided by Escher *et. al.*^{90b}

The advantages of immobilizing catalysts on supports are tremendous, being the first and foremost the easy separation and efficient recycling of the catalyst. Besides, metal traces may be minimized in the final products if no leaching occurs, and the handling of procedure is

usually much simpler. Considering the supported catalysts, there are various supports to choose from, and a variety of linking techniques possible.^{90b} The immobilization can occur via covalent or non-covalent linkage between the chiral catalyst and the support. **Figure 23** brings the various modes of immobilization of catalysts to achieve supported catalysis.

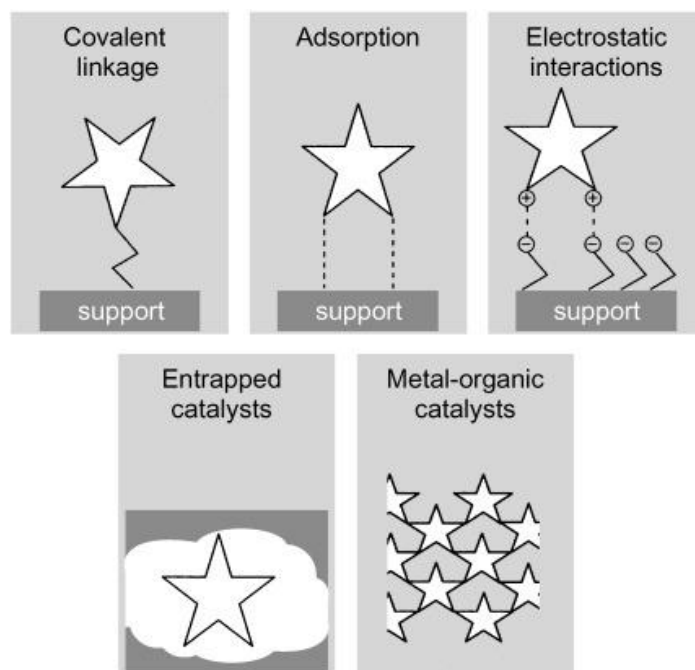


Figure 23: Strategies for the immobilization of chiral homogeneous catalysts (symbolized by stars).^{90b}

However, there are certain constraints with the immobilization of catalysts on supports, such as the undesired interactions between the support and the metal complex, the optimal geometry of the catalyst that can be disturbed by the support but is essential for high enantioinduction, limited access to the active sites and possible leaching of the catalysts.^{90b}

In the next sections, a main focus on the two main different supports is given: organic and inorganic supports. An overview of the developed salen supported catalysts on these classes of materials is investigated for a summary of the main achievements in this area.

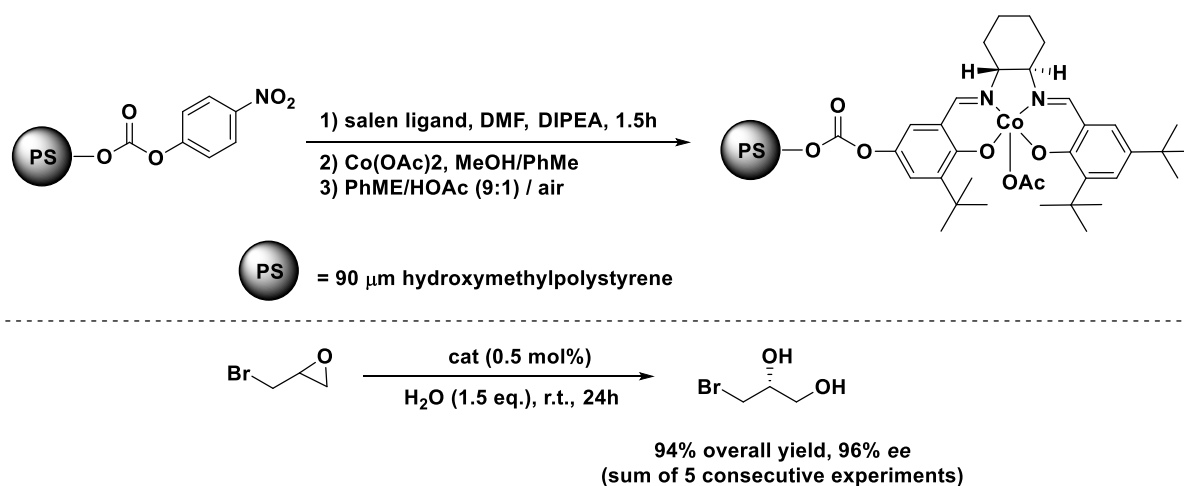
1.10.1. On organic supports

1.10.1.1. Cross-linked polymers

The combination of polymers and homogeneous catalysts to develop supported catalysts has been a strategic solution for developing supported catalysts. In fact, polymers offer an

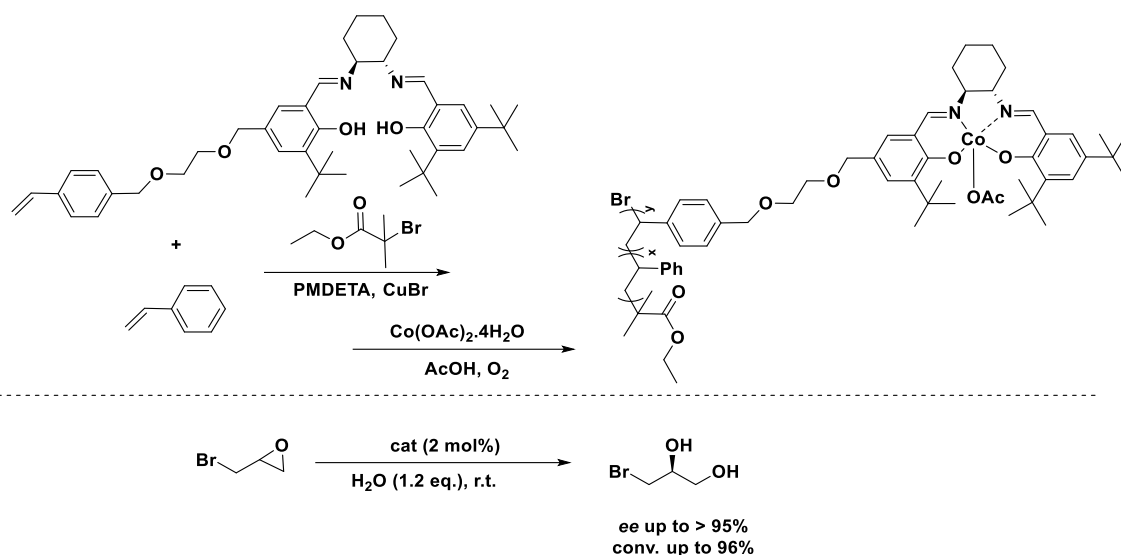
attractive pathway for designing supported catalysts due to their ease of post functionalization, besides providing stability and recyclability to the anchored catalyst. One well-known and easy methodology for post-functionalization of polymers is click chemistry.¹⁰⁵ Together, they can design complex structures and obtain supported catalysts with quite robust chemistry, which are unlikely to leaching and prone to reuse many times.^{8b} With this technique, it is possible to click different types of catalysts on polymers, and therefore design different supported catalysts.

One of the earliest examples of salen catalysts based on polymers is from Jacobsen and coworkers in 1999.¹⁰⁶ They described the synthesis of polystyrene and silica-bound chiral Co(salen) complexes, and they showed that the catalysts are efficient with high enantioselectivity (> 90%) for the HKR of terminal epoxides (**Scheme 15**).



Scheme 15: Synthetic approach for the development of polymer based salen(Co) complexes, and an example for the dynamic HKR of epibromohydrin.¹⁰⁶

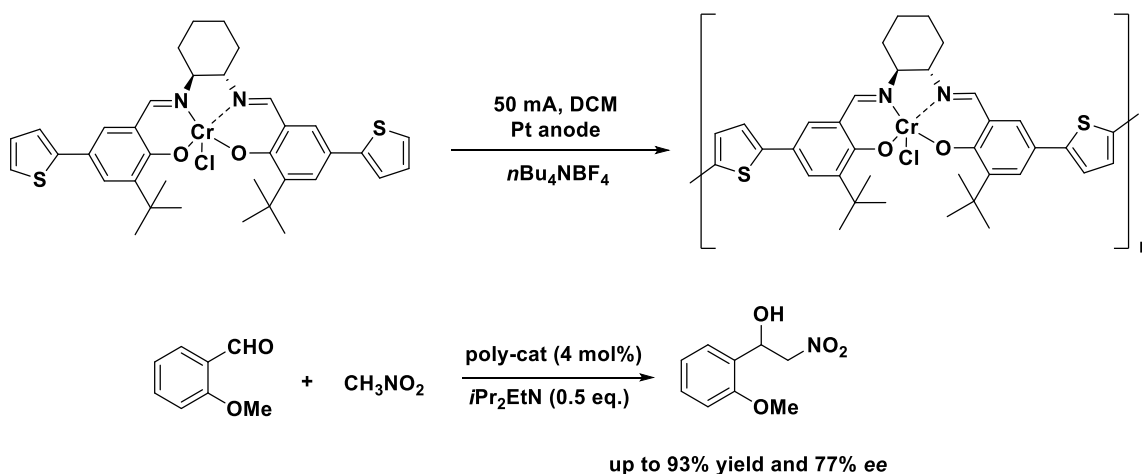
Our consortium has already synthesized salen supported catalysts based on polymers. There are certainly two examples highly cited in this thesis, the first from Zidelmal and coworkers,⁴ and the second from Bakangura and coworkers.^{8b} **Scheme 16** shows the example of Zidelmal and coworkers, in which supported salen was developed by the ATRP of a modified salen monomer containing styrene group. The corresponding Co-catalyst was efficient in the HKR of epibromohydrin with a enantioselectivity up to 95% and conversion up to 96%.



Scheme 16: ATRP of salen monomers for HKR and their catalytic evaluation.⁴

1.10.1.2. Electropolymerization

Schulz's group also worked on the electropolymerization of salen monomers to develop supported salen catalysts. These salen monomers are based on chiral thiophene-salen ligands and they have shown to be efficient for promoting different asymmetric reactions, such as hetero-Diels-Alder, HKR of terminal epoxides, and Henry reaction.¹⁰⁷ These complexes were electropolymerized to give chiral polymers as insoluble powders and they were used up to 15 cycles with no significant loss in their reactivity.



Scheme 17: Electropolymerization of Co-thiophene salen complexes described by Zulauf and coworkers.^{107b}

1.10.2. On inorganic supports

Inorganic solids have been commonly used as supports for chiral salen complexes.^{3, 108} There have been great advancements on the strategies for immobilization of salen complexes in inorganic supports, from encapsulation within cavities of porous materials, such as zeolites and MOFs, to covalent immobilization on the support on silica, for instance. One of the main advantages of immobilization of catalysts on inorganic solids is the high chemical and thermal stability of the inorganic support which turns the supported catalyst stable in various reactions conditions.^{108a}

There are three main strategies for immobilization of catalysts on inorganic supports: i) encapsulation within the cages of large pores; ii) immobilization by weak dipolar or strong coulombic interactions, in which the salen complex is adsorbed onto the support by ion-pairing with an ionic solid and iii) by covalent bond between the support and salen complex.^{108a} In the next subsections these types of immobilization will be further discussed considering the main inorganic supports used.

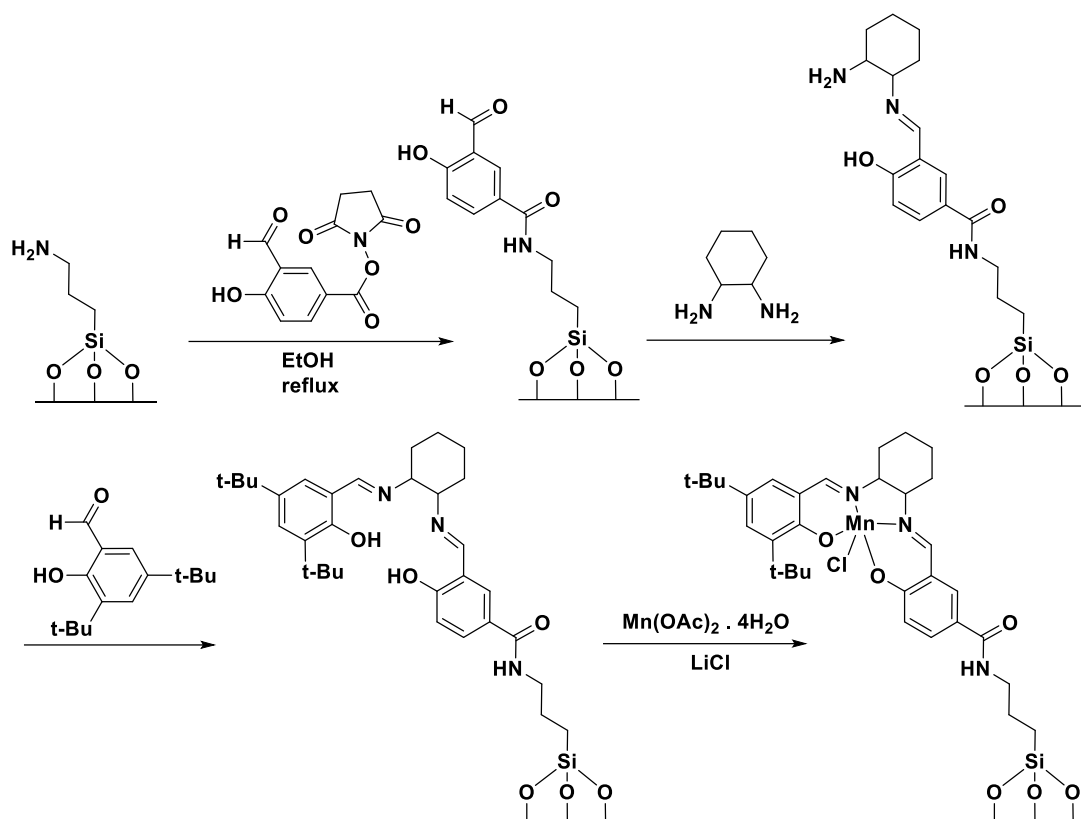
1.10.2.1. Silica

In order to maintain the reactivity and stereoselectivity of the immobilized catalyst, it is key to preserve the microenvironment of the catalyst on the support material so to allow the suitable site isolation and access to the catalytic sites.¹⁰⁹ The encapsulation of catalysts into the pore system of molecular sieves via host-guest interaction may provide such environment. In fact, as early as 1997, Frunza *et. al.*¹¹⁰ reported the embedding of chiral Mn(II) cationic complex of salen type into the pores of mesoporous substituted silicates (MCM-41 like). They tested the epoxidation of olefin and showed the fully maintenance of the catalytic activity and stereoselectivity of the salen complex. Besides, due to strong host-guest interaction, mainly between the aromatic rings of the complex and the internal surface silanol groups of the mesopores, the catalyst is stable and not prone to leaching. The maintenance of the enantioselectivity compared with the homogenous analogue shows that the encapsulation of the complex inside the pores of MCM-41-type materials preserves the desired geometry of the catalyst for an effective catalysis. There are many other examples in the literature showing the effective methodology of encapsulating salen complex in the pores of silica materials while maintaining good reactivity and selectivity.¹¹¹

However, the main approach to use silica as inorganic support for the asymmetric catalysis with salen complexes is by the covalent anchoring of the salen complex through the direct condensation of the silanol groups on the silica surface with the catalyst to form a Si-O-C bond. There are many examples in the literature of the attachment of salen complexes to silica. A literature search in April 2024 on SciFinder database shows 41 examples of works with the intersection of the keywords “asymmetric”, “salen”, “silica” and “support” which includes supports such as MCM-41, MCM-48, SBA-15, SBA-16, and amorphous SiO₂. From those 41 examples, around 30 examples are in regard to the covalent attachment of salen catalysts on silica materials.

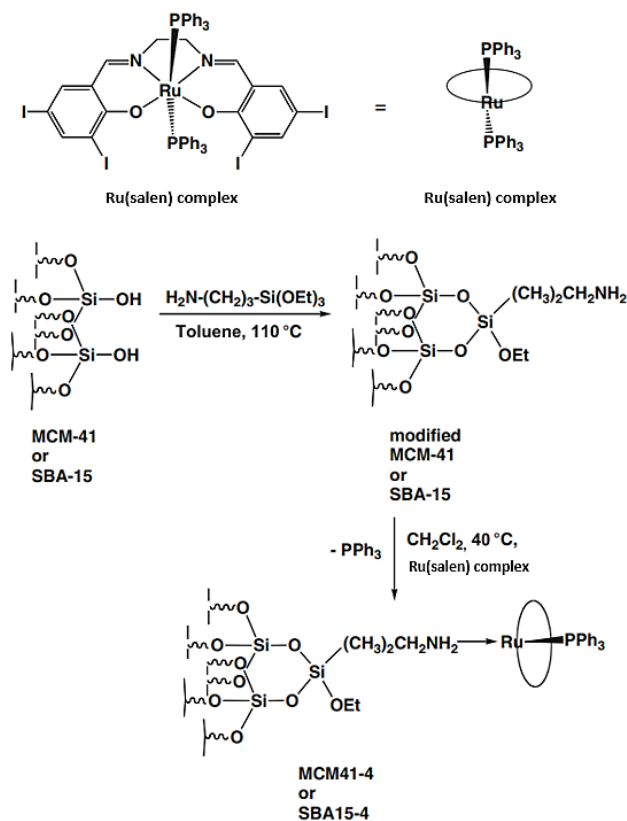
A common strategy for grafting molecules on silica is to first react the silanol on surface with aminopropyl triethoxysilane (APTES) to act as linker, since many other reactions are possible with a terminal amine. Using this strategy, there are two main possibilities for the design of supported catalysts on silica, which is 1) the multi-step grafting and build-up of the catalyst on the material, and 2) the direct attachment of the catalyst via the reaction with the NH₂ functional group.

Zhang and coworkers¹¹² used the first methodology to design an unsymmetrical manganese (III) salen complex on MCM-41 (**Scheme 18**), which was tested in the aerobic epoxidation of olefins, and showed relatively high activity and epoxide selectivity. The catalyst could be reused six times, although a decrease in activity was observed from more than 99% in the first run to around 74% in the sixth round.



Scheme 18: Multi-step grafting on silica to design supported salen catalysts described by Zhang and coworkers.¹¹²

The direct functionalization method is more straightforward and guarantee the quality of the catalyst being anchored. Kühn and coworkers described the anchoring of Ru(II)(salen)(PPh₃)₂ on the surface of MCM-41 and SBA-15 using APTES as linker (**Scheme 19**). The supported catalyst retained the activity and high selectivity towards the olefination of various aldehydes, although they noticed that the supported catalyst was less effective than its homogenous analogue due to difficult accessibility of the active site inside the pores.



Scheme 19: Strategy for grafting salen complex on mesoporous silica described by Kühn *et al.*¹¹³

The aminopropyl triethoxysilane (APTES) can also be used as linker through the aminopropyl tethers by complexation with the metal, as described by Garcia and coworkers.¹¹⁴ They designed the supported catalysts either by covalent bonding through the reaction of APTES and the salen catalyst, or by a non-covalent bonding (**Figure 24**). The supported catalyst developed through coordination to the metal center catalyzed the ARO of cyclohexene oxide with high yield ($> 93\%$) and moderate enantioselectivity ($50 - 70\%$), but it was found to undergo extensive leaching of the complex during catalysis. However, the covalently anchored catalyst showed no leaching, but a lower activity and selectivity ($43 - 66\%$ yield and $8 - 18\%$ *ee*), which was attributed to a likely change in the reaction mechanism when the catalyst is anchored.

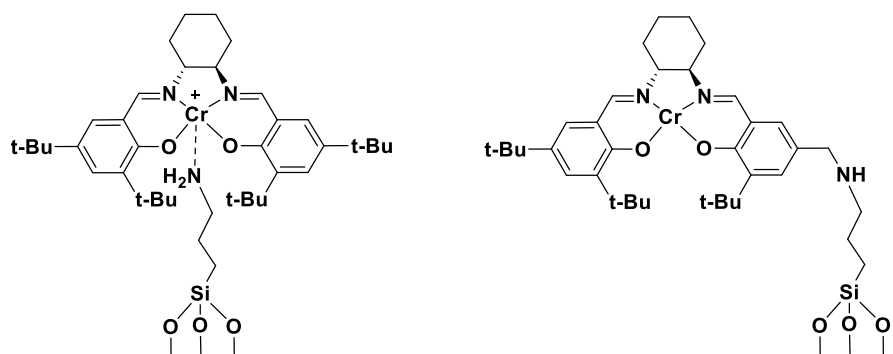
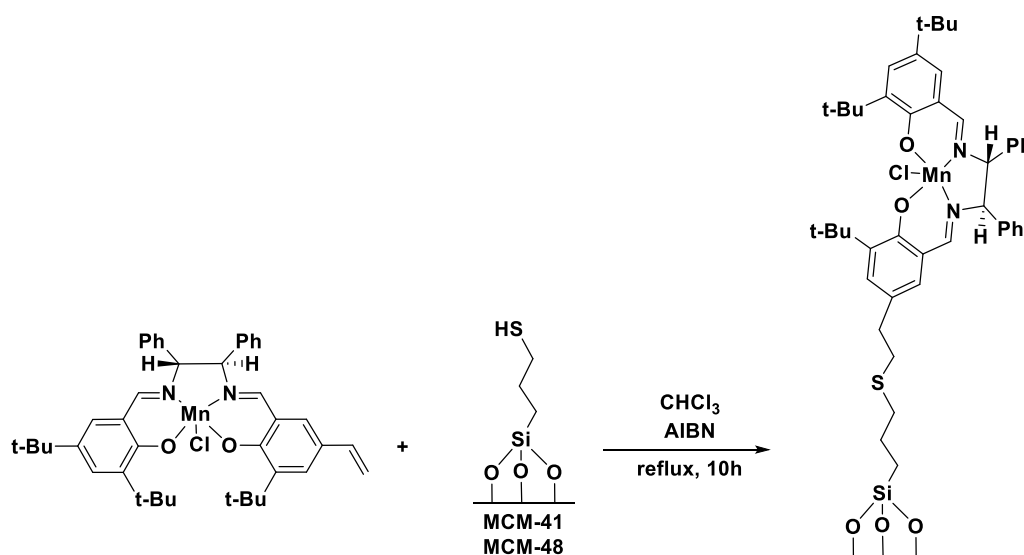


Figure 24: Cr–salen complexes anchored to functionalized silicates as described by Garcia and coworkers.¹¹⁴

Another study investigated the influence of the pore size of the mesoporous silica materials on the catalytic efficiency of the supported catalysts. Ji and coworkers¹¹⁵ described an unsymmetrical chiral Mn(III) salen complex immobilized onto a series of MCM-41 and MCM-48 mesoporous materials with different pore sizes. The strategy for immobilization was via a thiol-ene reaction of the modified support containing a thiol group and the alkene moiety from the salen catalyst (**Scheme 20**). They tested the catalysts in the asymmetric epoxidation of styrene, indene, and 1-phenylcyclohexene, and they observed that the activity and enantioselectivity were closely related to the pore size of the supports, in which the larger pores lead to higher conversions and *ee* values.



Scheme 20: The synthesis of supported chiral Mn(III) salen catalysts described by Ji *et al.*¹¹⁵

As a last example, ATRP has been investigated by the group of Jones for preparing polystyrene brushes containing cobalt-salen complexes grafted on silica.¹¹⁶ They reported the first use of pendant Co(III)-salen catalyst on silica supported polymer brushes for enhancing cooperative catalysis in the HKR of epichlorohydrin. The polymer brushes architecture provided a unique framework for promoting site to site interactions which is required in the proposed bimetallic transition state of the HKR mechanism. The supported catalyst displayed increased activities and retained high enantioselectivities (>99%) after reuse. This work provides us insights for the use of ATRP and solid supports for salen catalysis.

There are also other examples considering the immobilization of salen catalysts via non-covalent bonding, such as ionic bonding¹¹⁷ and impregnation,¹¹⁸ that also yields good enantioselective and reactivity, but they are not going to be discussed further in this manuscript.

1.10.2.2. Zeolite

Zeolites are typically crystalline porous tectosilicates composed of corner-shared metal tetrahedral oxide structures. As silica, they are also commonly employed in supported asymmetric catalysis due to their stable physical properties and tunable pore sizes,^{90a} however, there are far less examples using salen complexes. One of the earliest examples of encapsulation of salen complexes within zeolites was that of Sabater and coworkers,¹¹⁹ whose synthesis involved the condensation of optically active trans-(*R,R*)-1,2-diaminocyclohexane and salicylaldehyde around Mn^{II} metal ions resident in the supercages (1 Mn²⁺ every 5 supercages) and a final oxidation step (**Figure 25**). However, the selectivities and reaction rates so far reported are lower than those obtained with the analogous homogeneous catalysts.

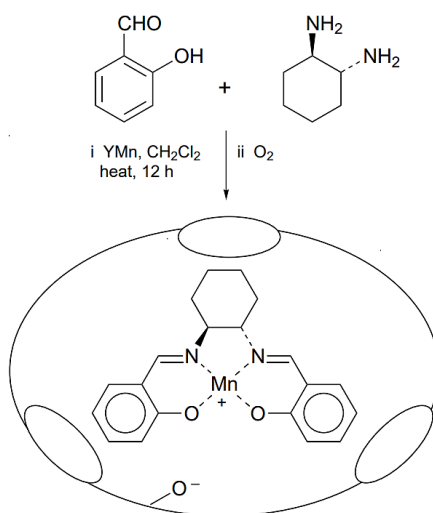


Figure 25: Immobilisation of (salen)Mn(III) complex in zeolite Y by encapsulation described by Sabater et. al.¹¹⁹

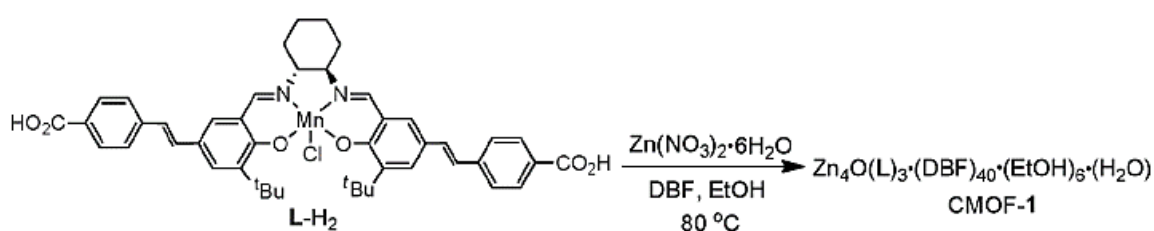
Hölderich and coworkers later extended this study to other salen type ligands with a variety of transition metals as the active center.¹²⁰ They were synthesized with the “ship-in-a-bottle” method, in which the main feature is the host-guest interaction that is neither covalent nor ionic, but rather by restrictive pore openings which in principle retain all properties of the homogenous complex. The immobilized catalysts were tested in the diastereoselective epoxidation of (–)- α -pinene, and a 100% conversion was achieved in most cases, with the best result resulting in 100% conversion, 96% epoxide chemoselectivity and 91% diastereomeric excess with the cobalt(salen) entrapped catalyst.

In a significantly more recent development, Modi and coworkers,¹²¹ in 2023, described a Cu(II)-salen complex encapsulated in MWW-zeolite as an efficient chiral catalyst for the synthesis of 3,4-dihydropyrimidin-2-(1H)-one (DHPMs) derivatives. DFT studies helped to fine tune the catalyst to fit into the pocket of the porous MWW support while keeping its chirality. The supported catalyst proved a potent catalyst under short reaction times, and it allows the rapid and simple isolation of the active MWW-trapped Cu(salen) catalyst to be reused in at least five consecutive runs.

Nonetheless, the confinement effect on porous materials like zeolites may influence the enantioselectivity and reactivity of the catalysts. Because the zeolite has a rigid structure and the catalyst is firmly fitted in the supercage, this may affect the conformation of the ligand and reaction intermediates by avoiding changes in ligand geometry during the reaction, which could ultimately damage the *ee* compared to the homogenous counterparts.^{108b}

1.10.2.3. Metal Organic Framework (MOFs)

Metal-organic frameworks (MOFs) have gained popularity for their high permanent porosity and structural tunability, as well as their potential for catalysis.¹²² Metallosalen derivatives provide the basis for one of the most effective chiral MOF catalysts among those that have been described.¹²³ As example, Song and coworkers^{123b} developed a chiral MOF (1cy topology) from the Mn–Salen derived dicarboxylic acid and the $[\text{Zn}(\text{NO}_3)_2 \cdot 6\text{H}_2\text{O}]$ secondary building unit (**Scheme 21**). They were then used in highly regio- and stereo-selective sequential alkene epoxidation and epoxide ring-opening reactions, with a yield of 60% and enantioselectivity of 81% for the ring opening and 82% for the epoxidation.



Scheme 21: Synthesis of salen(Mn) MOFs proposed by Song *et.al.*^{123b}

As a last example, the very interesting example in the literature of supported salen catalysts using MOFs is the work by Xia and coworkers¹²⁴ in 2017, and it also served us as insight for the development of multifunctional catalysts in this thesis. They designed multivariate metal-organic frameworks (MTV-MOFs) based on salen catalysts to produce multiple and cooperative active sites (**Figure 26**). The catalysts, containing up to three different chiral metallosalen catalysts, were used in various asymmetric sequential alkene and epoxide ring-opening reactions, which allowed cooperative activation resulting in improved efficiency of the catalysts. Many examples show high enantioselectivity (>90%), demonstrating the efficacy of the developed catalysts.

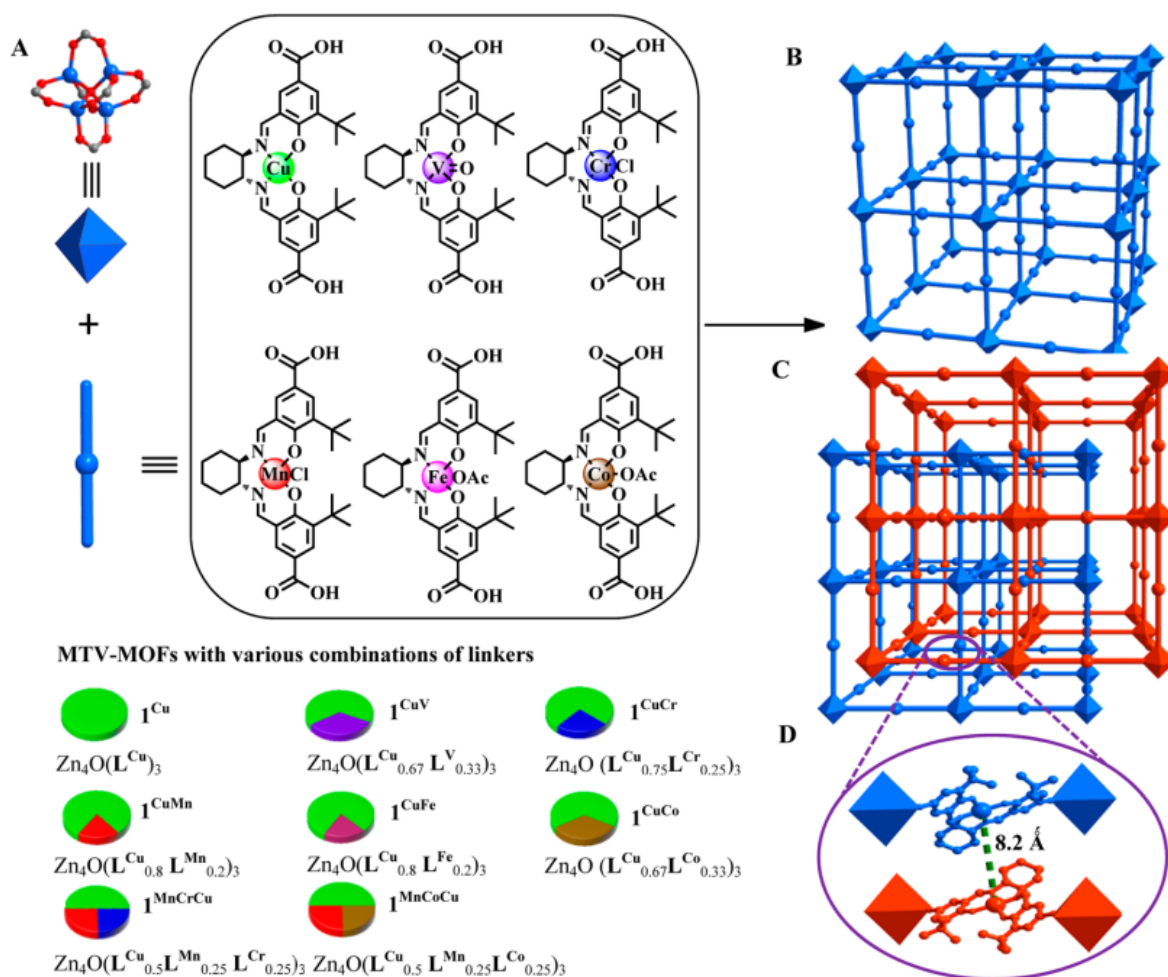


Figure 26: (A) Construction of MOF 1^{Cu} and corresponding MTV-MOFs 1^{CuM} and $1^{\text{CuMM}'}$ with different metallosalen linkers. (B) One 3D unit of MOF 1^{CuM} . (C) Two-fold interpenetrating 1^{Cu} (red indicates the interpenetrated 3D network). (D) Close-up view of two L^{Cu} units brought into proximity to each other by 2-fold interpenetration.¹²⁴

1.10.2.4. Magnetic nanoparticles

Magnetic nanomaterials are advantageous for preparing supported salen catalysts due to their good chemical stability and easy functionalization. Although most inorganic supports require different separation techniques, magnetic materials can be readily separated from the reaction mixture using an external magnet; therefore, they offer high reusability and accessibility. Magnetic alloy nanoparticles of Fe-Co, Co-Ni, and Fe-Ni are superior catalyst supports for various chemical reactions, making them excellent supports for recyclable metal salen-type catalysts.¹²⁵

There are many examples with the use of magnetite nanoparticles immobilized salen-metal catalysts, and most of them uses SiO_2 to cap the magnetic nanoparticle.¹²⁶ As one example, Su and coworkers¹²⁷ reported a magnetic Co(III) salen supported catalyst with uniform spherical core-shell structure synthesized by a microemulsion method to catalyze the CO_2 fixation into cyclic carbonates. The catalysts exhibited 99% yield with 100% selectivity for the ring-opening addition reaction of CO_2 and epoxide, and they were later reused up to 5 times with no substantial leaching (**Figure 27**).

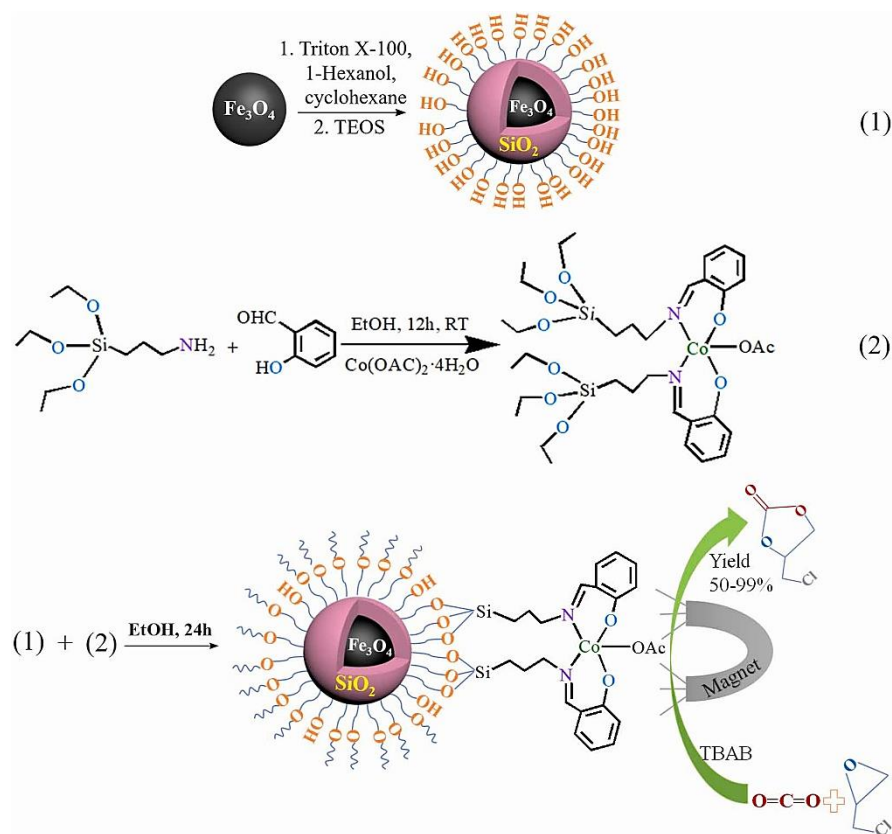
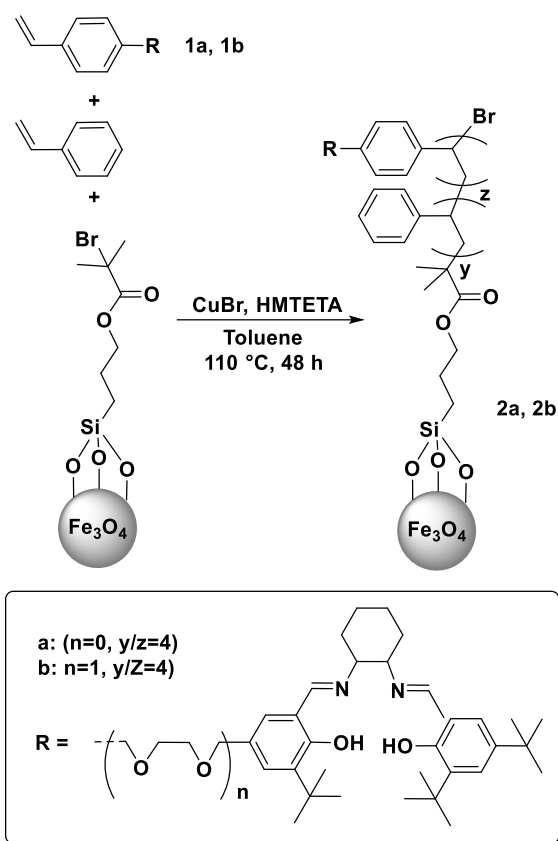


Figure 27: Schematic illustration of the synthesis of magnetic $\text{Fe}_3\text{O}_4@\text{SiO}_2/\text{Co(III)-Salen}$ nanocomposite and its application for the chemical fixation of CO_2 into cyclic carbonates. Work developed by Su and coworkers.¹²⁷

Another example is from Jones and coworkers,¹²⁸ where they demonstrated the combined use of ATRP and magnetic particles to design supported salen catalysts (**Scheme 22**). Polystyrene brushes containing Co(III)-salen were prepared via ATRP from Fe_3O_4 nanoparticles modified with an initiator molecule. Once more, the polymer brushes architecture promotes the cooperative interactions necessary for Co-salen catalyzed ring-opening of epoxides. The magnetic nanoparticle-based polymer brushes were easily recovered from the solution using a magnetic field.



Scheme 22: Synthesis of non-metallated salen functionalized MPB (2a and 2b). Modified from the work of Jones and coworkers.¹²⁸

1.10.2.5. Silicon

Silicon is by far the least common support used to develop salen supported catalysts. In fact, for the best of our knowledge, no salen complexes have been attached on the surface of silicon for the purpose of catalysis. The example found for the functionalization of silicon using salen is the work of Condorelli and coworkers¹²⁹ in which they used a cavitand modified salen to be grafted on the surface of Si (100) by photochemical hydrosilylation, and by thermal hydrosilylation onto porous silicon. These cavitands are used as organic receptors, and they discovered that the salen molecules remained intact and retained their unique features following silicon anchoring.

Although silicon has not yet been employed as a support in asymmetric catalysis, as explained in part 1 of this chapter, silicon has many advantages as support to perform asymmetric catalysis: 1) robust Si-C grafting via a SiH_x pathway, 2) robust and well-known chemistry, and 3) possible direct quantification of salen catalysts on surface by ATR-FTIR and X-ray photoelectron spectroscopy (XPS) technique. Therefore, this thesis is on the edge of a

breakthrough considering salen catalysts on silicon surface for the design of supported asymmetric catalysts.

1.11. Towards the future of supported salen catalysis

Supported chiral salen complexes are stable and recyclable catalysts that efficiently catalyze asymmetric reactions. This section brought a small overview of the advancements on supported catalysis using salen complexes, but there are still many examples of supports and strategies that were not discussed in this manuscript. More complete works discussing the details of immobilization of catalysts and design of heterogenous and/or supported salen catalysts are available in the literature.^{3, 90b, 108a, 108b, 109, 114, 130} These procedures are robust, easy to implement and very efficient for recycling, and they usually have low metal leaching; however, they still lack the control over the location of catalytic sites on the support, which could easily manage their cooperativity.¹³⁰

Therefore, the future for supported salen catalysis lays on the better control over the location of active sites to improve the cooperative behavior of such catalysts. Besides, the immobilization of catalysts can also enable the discovery of new reactivities using multicatalysis.

Part D: Conclusions and goals for this project

This chapter gave an overview of the three main pillars studied in this thesis: 1) silicon surface chemistry, 2) Atom Transfer Radical Polymerization and 3) salen-supported asymmetric catalysis. Considering the last pillar, there are many techniques used by the academic community to develop such catalysts, and they consist mostly by either modifying these complexes, for instance with a polymerizable unit, so to recover them by simple precipitation, or by attaching them on different solid substrates.

Controlled radical polymerization has attracted much attention for the grafting of these complexes so to obtain polymer brushes with well-defined macromolecular architectures while still maintaining activity and enantioselectivity. Polymer brushes can also facilitate the better control of the catalytic sites by selectively functionalizing the desired polymer. Given these advantages, controlled polymerization techniques have been chosen to develop such catalysts for this thesis.

Then, silicon has been selected in this thesis because of its well-known surface chemistry and the possibility of forming robust Si–C bonds, which improves the stability of the grafted catalyst and avoid metal leaching to the reaction mixture. Besides, polymer brushes developed by SI-ATRP on silicon surface are well-organized and provides an interesting platform for the further functionalization with catalysts.

Therefore, this thesis' objectives are to develop salen supported catalysts on silicon by first studying the hydrosilylation of different initiators for ATRP on silicon surface by microwave-assisted reaction, and then the further SI-ATRP of methacrylates on surface. Thanks to the developed techniques in our laboratory, we are able to make the direct quantification of polymer brushes on surface without their detachment from the surface. Then, click chemistry is employed to functionalize these polymers brushes on surface with the salen catalysts to obtain the desired supported catalysts. The supported catalyst based on silicon has yet another advantage considering the other common supports because it can be removed from the reaction media simply with a tweezer, and not even a filtration is necessary.

Formerly, all these concepts are applied to macroporous silicon as it is a support with a higher surface area compared to crystalline silicon. Thus, the ultimate goal of this thesis is to obtain good reactivity and selectivity using these supported salen catalysts based on

macroporous silicon. If such objective is achieved, this marks the first contribution of salen catalysts supported on silicon.

CHAPTER 2

Preparation of a surface-initiated layer on silicon

“The only source of knowledge is experience.”

Albert Einstein

SUMMARY

2.1.	Preparation of an oxidized and a hydrogenated surface.....	62
2.2.	Grafting of initiator 1 on surface for SI-ATRP	64
2.3.	Quantification of the grafted initiator 1 on Si-H _x surface.....	67
2.4.	Optimization of the initiator 1 MW grafting	68
2.5.	Calculation of error in the grafting of initiator 1	71
2.6.	Grafting of other initiators for SI-ATRP	71
2.7.	Study on macroporous silicon (100).....	84
2.8.	Conclusions	87

This part of the thesis work consists in preparing solid substrates functionalized with initiators as SI-ATRP starters for further applications in catalysis. Silicon was chosen to be the solid material for this project since silicon has a controllable and robust chemistry, as well as well-known surface topography. Therefore, this chapter will focus on the grafting of different molecules for SI-ATRP and the quantification of the grafted layers by using ATR-FTIR. It will describe the successive chemical steps to achieve a surface with a desired chemical functionality. The techniques used to characterize and study the surface monolayers are atomic

force microscopy (AFM), infrared spectroscopy (ATR-FTIR), X-ray Photoelectron Spectroscopy (XPS), ellipsometry, and contact-angle measurements.

2.1. Preparation of an oxidized and a hydrogenated surface

The silicon wafer used for this project (Siltronix, France) is a (111)-oriented single crystal. It was chosen over (100) for crystalline silicon because its denser plan of silicon dangling bonds pointing normal to the surface allows a well-controlled chemistry by AFM and IR. The oxidized silicon surface (SiO_x) is obtained by first cleaning the silicon surface with a piranha solution to remove organic physisorbed and chemisorbed molecules and dust. Therefore, when performing grafting on an oxidized surface, the silicon prism is then used directly after the piranha treatment.

For the preparation of a hydrogenated silicon surface, a HF solution was used for an isotropic etching, yielding a rough silicon surface as the isotropic etching removes the silicon of the surface in all crystallographic directions.¹³¹ After the treatment in piranha solution, the prism is treated with concentrated or diluted solutions of HF that etch the native silicon oxide layer yielding a hydrogen-terminated Si-H_x monolayer on the surface.

This Si-H_x monolayer has a chemical stability of approximately 2 hours¹³, and prolonged exposure to air causes the surface to be oxidized again. Therefore, it is important to etch the surface always prior to the grafting and/or chemical analysis. Oxidized and hydrogenated surfaces are always analyzed in order to access the chemical modifications on surface. **Figure 28** shows an example of a spectrum of a freshly hydrogenated silicon surface after the removal of the native oxide layer of Si(111) using 50% HF, the reference being the oxidized surface. The negative bands correspond to a loss, whereas the positive bands indicate the gain of vibration modes, meaning chemical compounds on surface. Therefore, the positive SiH_x bands in the region of $2079 - 2130 \text{ cm}^{-1}$ correspond to the formation of hydride bonds after the etching. The Si-H stretching vibration modes are seen as three peaks of increasing intensity at 2083 , 2107 and 2136 cm^{-1} , which are attributed to Si-H monohydride, Si-H₂ dihydride and Si-H₃ trihydride, highlighting the roughness of the surface at the atomic scale. The negative bands around 1058 and 1237 cm^{-1} are associated to the Si-O-Si vibration modes. The transverse optical (TO) Si-O-Si is at 1058 cm^{-1} and is visible for both *p*- and *s*-polarization. The one at 1237 cm^{-1} corresponds to the longitudinal optical (LO) Si-O-Si, and is only visible for *p*-polarization.¹³² The intense negative Si-O-Si bands and the positive Si-H_x bands indicate that the etching using HF (50%) successfully removes the native oxide layer and forms a

hydrogenated silicon surface. From the intensity of the transverse optical phonon vibration in *s*-polarization at 1060 cm^{-1} it is possible to estimate the oxide thickness removed from the surface, knowing that 1 mAbs corresponds to a thickness of $\sim 1.5\text{ \AA}$ of oxide.¹³³ In this particular case (7.4 mAbs, data not shown), a 11 \AA oxide film thickness is estimated. This example is especially more oxidized, but samples in this manuscript usually varies from 3 – 7 mAbs, i.e $\sim 4.5 - 11\text{ \AA}$ oxide film thickness.

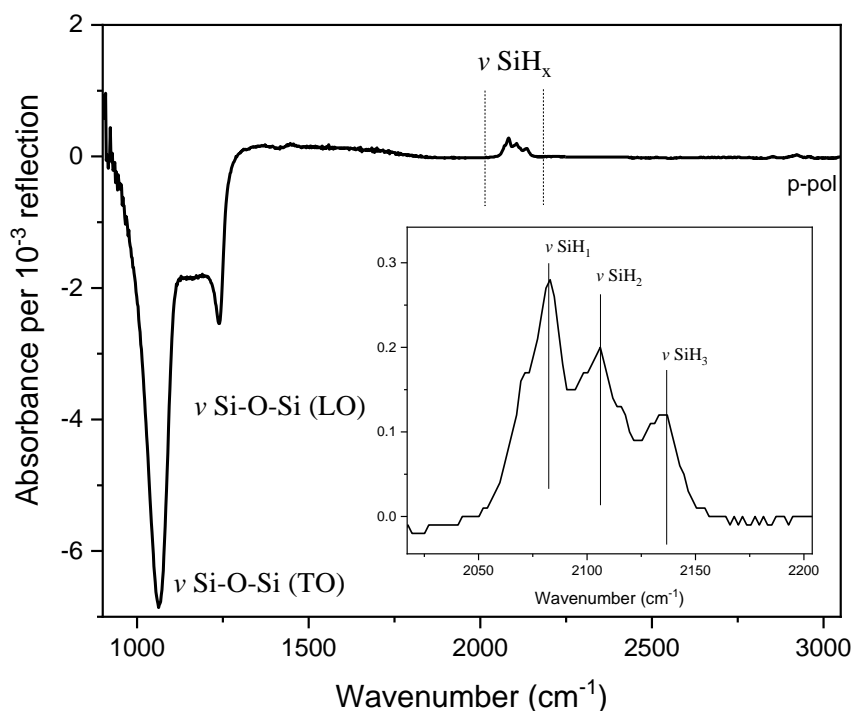


Figure 28: ATR-FTIR spectrum (*p*-polarization) of a hydrogenated silicon using an oxidized silicon surface as reference. Etching conditions: HF (50%) for 5 seconds.

The HF etching of the surface using various HF concentrations was successful, and etching with a HF concentration of 2% for four minutes also yielded perfectly etched surface as shown in **Figure 28**. The tested conditions are summarized in **Table 1**. It includes the HF treatment for both crystalline and macroporous silicon. Macroporous silicon has to be etched in an ethanolic solution as the water's surface tension does not allow the solution to enter the pores for a perfect etching of the pore walls. Therefore, alcohol is used as its surface tension is much lower than water's (21.6 mN/m as compared to 72.8 mN/m).¹³⁴ In all cases, after immersion of the sample in DI water or ethanol, it is also rinsed for another 5 seconds under running DI water. Then the sample is dried under N_2 stream and used directly for the desired grafting.

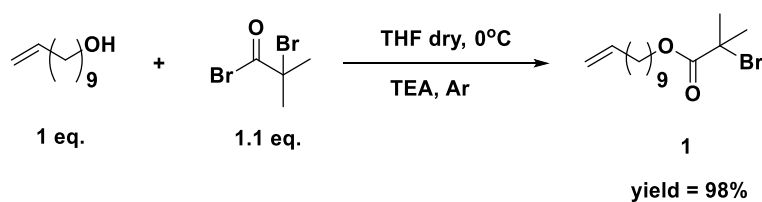
Table 1: Various conditions for HF etching on crystalline or macroporous silicon that yields an etched SiH_x surface. After the last step, all samples are always rinsed for a further 5 seconds under running water.

Type of silicon structure	HF aqueous solution concentration (%)	Time of immersion in HF solution or exposure to HF vapor (s)	Time of immersion in DI water or ethanol (s)
Crystalline (111)	50	5	5
Crystalline (111)	5	180	5
Crystalline (111)	2	240	5
Crystalline (111)	Vapor of 50% solution	45*	N/A
Macroporous (100)	25	120	5
Macroporous (100)	Vapor of 50% solution	45*	N/A

* for each side of the silicon sample.

2.2. Grafting of initiator 1 on surface for SI-ATRP

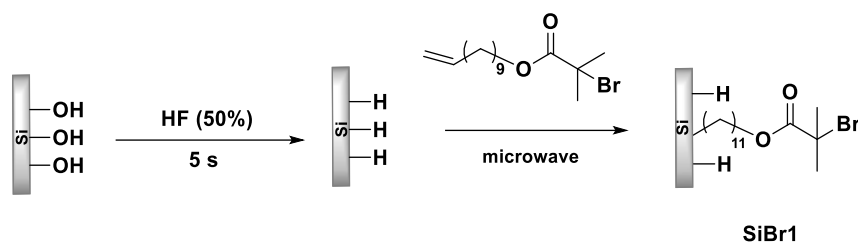
The initiator, 10-undecylenic-2-bromoisobutyrate, here called initiator 1, was obtained from the esterification between 10-undecen-1-yl and α -bromoisobutyrate bromide in dried THF at 0 °C in 3 h using triethylamine as catalyst (**Scheme 23**). The product is obtained after simple workup as a colorless liquid in 98% yield.



Scheme 23: Synthesis of 10-undecen-1-yl 2-bromo-2-methylpropanoate, initiator 1.

The strategy for the grafting of the initiator for polymerization relies on first producing a hydrogenated surface to later react it with the bromo initiating molecule, as shown in **Scheme 24**. It is known that the grafting of 1-alkenes can be achieved by either heat or UV.¹⁸ Our team has already worked on the grafting of initiator 1 by means of thermal activation,^{8a, 135} however, it has been shown that the initiator decomposes after 16h with a thermal activation at 180 °C ,

and it cannot be reused afterwards. Nevertheless, recently, Lu and coworkers have successfully grafted the alkyl initiator used in this project by means of microwave (MW) grafting.³⁰ The microwave radiation substantially decreases the reaction time as compared to a normal heating activation using oil bath. In fact, the latter has usually 16 to 20h reaction time, while for microwave, it can be performed in one hour. Therefore, inspired by this work, we used the same approach to graft the organic molecules on silicon surface.



Scheme 24: General scheme for the grafting of 10-undecylenic-2-bromoisobutyrate on Si in microwave assisted synthesis (SiBr1).

The grafting of 10-undecylenic-2-bromoisobutyrate on silicon (111) using microwave-assisted activation has been studied. The main motivation for this first step of the project is to obtain a better understanding of the grafting of initiator 1 on silicon surface by studying the microwave parameters (temperature, pressure and time of reaction), as well as the concentration of the initiator solution, and the rinsing protocol. The first trials were performed using the optimized conditions for the grafting of 1-decene on Si(111)-H developed by Irma Liascukiene, postdoc researcher in our group from 2020 to 2021 (unpublished results). The conditions were: 125 °C (target temperature), 50 or 30 W (maximum microwave power), for 50 min reaction. However, for the grafting of initiator 1 the power was set to 50W because preliminary data between 50W and 30W showed that the temperature fluctuations using 50W were lower than when using 30W, as shown in **Figure 29**. Concerning the concentration of the initiator solution, a concentration of 10 vol% in mesitylene yields satisfactory results with similar densities than using the neat initiator, *i.e.*, without diluents/solvent;^{8a} therefore, there is no need to use it at high concentration avoiding the waste of high quantities of initiator.

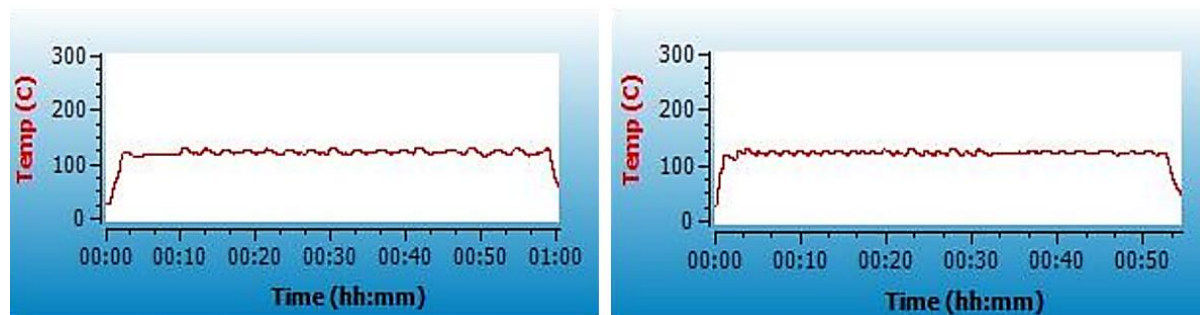


Figure 29: Temperature over time graphs of the microwave experiments using 30W (left) and 50W (right) power.

As an example, **Figure 30** shows a spectrum of a grafted surface. If successful grafting is obtained, the spectrum is quite simple to analyze, with only two main bands originating from C=O and CH₂ vibrations. The band at 1730 cm⁻¹ is characteristic of the stretching vibration mode of the C=O bond of an ester, and the bands at 2858 and 2931 cm⁻¹ correspond to symmetric and antisymmetric stretching vibration modes of CH₂ groups. A smaller band at 2967 cm⁻¹ can also be observed, assigned to a CH₃ vibration mode. Because the spectrum of a freshly hydrogenated surface is used as the reference, we observe a negative peak from SiH_x, consistent with the assumption that initiator 1 is grafted through a Si–C bond (**Figure 30**).

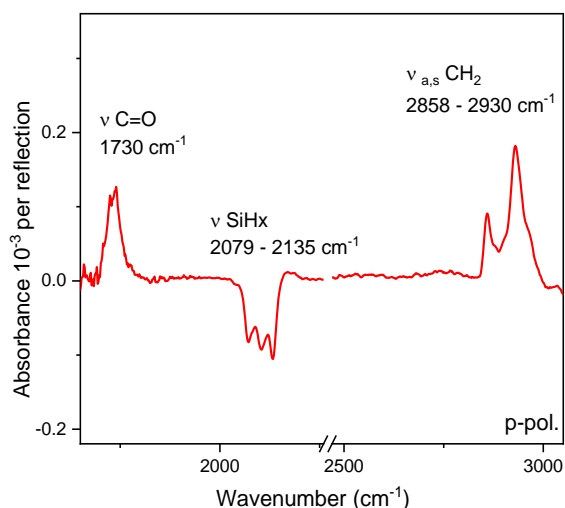


Figure 30: ATR-FTIR spectrum of the surface layer obtained after grafting initiator 1 on c-Si(111). The reference spectrum is that of SiH_x surface (etching conditions: HF (50%) for 5 s). Grafting conditions: MW 125 °C, 50 min, 50 W, 10 vol%. The data from this spectrum corresponds to entry 2 in **Table 2**.

2.3. Quantification of the grafted initiator 1 on Si-H_x surface.

ATR-FTIR using the silicon prisms as the crystal element enables the quantification of the molecules grafted on surface. We have developed quantitative tools for analyzing the carbonyl peaks. The integrated absorbances A_s and A_p of this peak is computed from the spectra recorded in *p*- and *s*-polarization of the IR beam, respectively.⁴¹ An IR calibration using initiator 1 is performed at different concentrations in CDCl₃ to determine the corresponding Abs_s^0 of the carbonyl mode of the initiator (further details are given in **Appendix C**). A spectrum of the pristine SiO_x surface was used as a reference for computing absorbances. The C=O ester band at 1730 cm⁻¹ was integrated using Origin software from 1698 to 1765 cm⁻¹ for *s*-polarization, and a linear baseline was adjusted between the extremities. The integration values were taken as a quantitative reference of the absorption of the stretching vibration mode of C=O to build the regression line shown in **Figure 31**, which slope $\frac{\text{Abs}_s^0}{C}$ was of 0.8092.

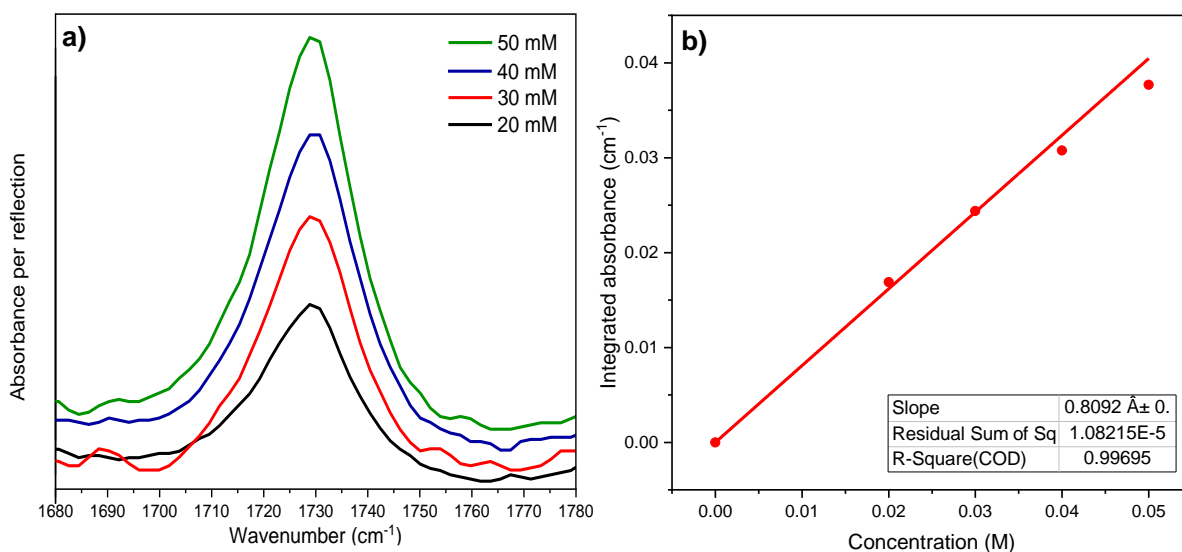


Figure 31: a) ATR-FTIR spectra in *s*-polarization of a solution of initiator 1 from 1680-1780 cm⁻¹ at different concentrations in CDCl₃, b) Calibration curve of initiator 1 using the integrated absorbance of each spectrum in different concentrations.

Then, it is possible to translate the magnitude of the C=O peak of the spectra of the grafted surfaces into a surface concentration of molecules using the slope obtained with the calibration. Specifically, the values of the integrations in both *s*- and *p*-polarizations of the grafted surface enable the determination of two characteristic quantities $N_{//}$ and N_{\perp} (**Figure 32**). They are equivalent to a surface concentration of molecules corresponding to the projection of the

dynamic dipole of the considered mode on the surface and its normal, respectively. The sum of these two values gives the total number of molecules grafted on the surface per cm^2 . A silicon (111) surface has a density of 7.8×10^{14} atoms/ cm^2 , and considering the value obtained for the case shown in **Figure 30** which is 8.0×10^{13} molecules/ cm^2 (entry 2, **Table 2**), the coverage percentage of ester molecules is approximately 10%. In fact, the maximum of surface coverage we can obtain is 50% due to steric hindrance of the alkyl chains on surface considering a SiH formed by anisotropic etching.¹³⁶ Usually, the hydrosilylation reaction using thermal or UV activation leads to 20 to 30% of surface coverage,^{13, 40-41} However, the obtained density of the initiated layer grafted via thermal activation^{8a} is around the same value as those obtained by microwave activation.

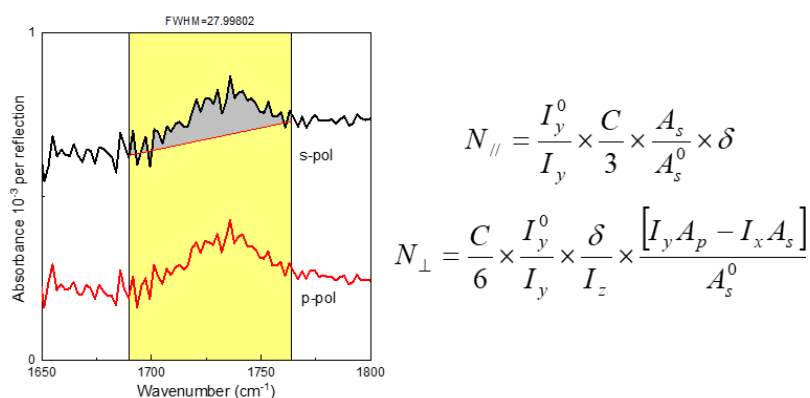


Figure 32: Example of C=O peak integration (A_s and A_p) of the spectrum in s - and p -pol (entry 2 in **Table 2**), and the corresponding N_{\perp} and N_{\parallel} formulas in which δ is penetration depth, I is the intensity of the IR field in the vicinity of Si and I_y^0 is the field intensity in the calibration solution.

2.4. Optimization of the initiator 1 MW grafting

The grafting of initiator 1 on silicon surface by microwave-assisted reaction is fairly new, and there are not many reports on it available in the literature. To better understand the surface grafting of the initiator, it was decided to perform a statistical study. The parameters of grafting, such as the temperature of the reaction, time and volume concentration of initiator 1, were studied using chemometrics. The experimental design was a full factorial design of 3 factors of 2 levels, leading to 8 main experiments. The three factors were: temperature (125 and 170°C), time (20 and 50 min) and concentration (10 and 50 % v/v). To calculate the errors, 2 central-points experiments were also performed. **Table 2** shows the results from this design of experiments.

Table 2: Full factorial design of 3 factors of 2 levels for the grafting of 10-undecylenic-2-bromoisobutyrate on silicon (111) from a solution in mesitylene.

Entry	Temp. (°C)	Time (min)	Conc. (vol/vol, %)	Intensity C=O <i>p</i> -pol (mAbs),	Density of grafted chains (nm ⁻²)
1	125	20	10	0.13	0.67
2	125	50	10	0.16	0.80
3	125	20	50	0.08	0.67^a
4	125	50	50	0.07	0.24
5	170	20	10	0.16	0.97
6	170	50	10	0.18	0.63
7	170	20	50	Not clear	-
8	170	50	50	0.17	0.88
9	147.5	35	30	0.14	0.69
10	147.5	35	30	≈0.13 ^b	-

* Power: 50 W. Power is applied at the beginning of the heating and then it is varied through the experiment in order to maintain the temperature constant. Usually it varies from 2 to 25 W after reaching the target temperature. The integration ranges from 1698 to 1765 cm⁻¹ except in a) where it ranges from 1663 to 1754 cm⁻¹ as the peak is broader. All surfaces were rinsed with toluene, and then twice in toluene (US bath), and a final rinse with dichloromethane except b) with was further rinsed with Soxhlet using DCM as solvent (24h). Approximate number because of lack of quality of spectrum. All samples were etched using HF (50%) for 5s, except entry 9 which was used vapor HF (50%) for both faces.

The quantification of the grafting density was not reliable for entry #10 because a broad peak at 1618 cm⁻¹ appears, which can be attributed to absorbed water, but it made the analysis of the peak at 1730 cm⁻¹ much harder and therefore was not attempted. The same peak was also observed in entry #3, but the quantification was possible. For entry #7, although a peak at 1730 cm⁻¹ is observed, it is very small, and due to the water vapor in the spectrum, the quantification of the peak was not possible. Because of these constrains, no statistical analysis could be computed as these missing points unable the correct analysis of the data.

However, there is still important information that can be retrieved from these experiments. For instance, increasing the concentration of initiator 1 does not improve the grafting of the molecule on silicon at temperature 125 °C in the two concentrations analyzed (entry #1 to #4). In fact, it worsens the grafting, diminishing the density grafting from ≈ 0.8 / nm² to 0.2 / nm². The second block considering 170 °C is more complicated to analyze because there is no clear trend between entries #5 to #8. In all investigated cases, no change was

observed in the $^1\text{H-NMR}$ of the reaction mixture (**Figure 97, Appendix B**); therefore, some kind of degradation/reaction must happen only on surface which makes the initiator grafting very sensitive to the analyzed parameters.

Nevertheless, it is clear that no higher concentration of initiator was needed for the grafting of this molecule. Therefore, new tests using only 5% vol/vol of initiator in mesitylene were performed in higher and lower temperature during longer time (2h) (entries # 1 and #2 in **Table 3**) to investigate whether even lower concentrations would yield better initiated surfaces. Together with these, 3 replicates of the conditions using higher temperature during 50 min (170°C, 10% vol/vol) were also performed to assess the error bar when working in harsher conditions. The values extracted from these experiments are found in **Table 3**.

Table 3: Further studies of the grafting behavior of 10-undecylenic-2-bromoisobutyrate on silicon (111).

Entry	Temp. (°C)	Time (min)	Conc. (vol/vol, %)	Intensity C=O (mAbs), <i>p-pol</i>	Density of grafted chains (nm ⁻²)
1	125	120	5	0.07	0.19
2	170	120	5	0.08	0.20
3	170	50	10	0.10	0.55
4	170	50	10	0.08	0.28
5	170	50	10	0.23	0.89

* All samples were etched using HF (50%) for 5s.

These results show that decreasing the concentration to 5% does not improve the grafting even at higher reaction time, yielding lower grafting density (0.2 nm⁻²) than using 10% v/v (0.8 nm⁻²). The replicate tests at higher temperature proved that the grafting of initiator is not well controlled in these conditions with a variation range quite broad from 0.3 to 0.9 nm⁻².

This section showed that the grafting density of the initiator on SiH_x surface significantly varies when using different conditions, such as temperature and time. In **Table 3**, it was also seen that the grafting at higher temperatures yields surfaces with different densities, even if all parameters remains the same. Thus, it seems that the grafting at higher temperatures suffers from a poor control of the process. However, if the grafting of initiator 1 is performed at 125 °C, in a 10% v/v in mesitylene, with 50W as power during 50 min, it is possible to obtain a grafting density with around the same value, which is discussed in the next section.

2.5. Calculation of error in the grafting of initiator 1

Table 4 shows four examples of the grafting of initiator 1 in the conditions aforementioned. The average number is $0.71 \text{ molecules}\cdot\text{nm}^{-2}$ with a standard deviation of 0.06. The error can be calculated by considering the average number as the expected value. In any case, the error falls in the range of 15%, which is a value considered within the experimental error of the density calculation. Therefore, these conditions were validated as the conditions for the grafting of the initiator 1 providing the best control, and thus, used for the next parts of this manuscript.

Table 4: Quantification of grafting density (from $\nu \text{ C=O}$) and the error calculation for the microwave grafting using $125 \text{ }^\circ\text{C}$, 50W and 50 min of reaction in a 10% v/v of the initiator 1 in mesitylene.

Entry #	Abs _{s,p} (area)	N _{//}	N _⊥	N total (nm ²)	Error (%)*
1	0.00458, 0.00477	0.64	0.15	0.80	11
2	0.00408, 0.00427	0.56	0.15	0.71	≈ 0
3	0.00330, 0.00349	0.48	0.14	0.62	15
4	0.00397, 0.00411	0.57	0.15	0.72	1
			Average	0.71	
			Standard deviation	0.06	

*error considering the average value as the calculated value, and each value as the experimental value.
Error = (calculated value – experimental value)/experimental value.

2.6. Grafting of other initiators for SI-ATRP

This part the manuscript has been inspired by the article by [Rafaela Bechara](#), [Philippe Roger](#), [Mohamed Mellah](#), [Nadine Barroca-Aubry](#), [Emmanuelle Schulz](#), [Thomas Defforge](#), [Gaël Gautier](#), [François Ozanam](#), [Anne-Chantal Gouget-Laemmel](#). Microwave-assisted grafting of an ATRP initiator on crystalline and macroporous silicon and subsequent polymerization. Manuscript in preparation.

After studying the grafting of initiator 1 under different microwave conditions, we wanted to analyze the behavior of two other different initiators for ATRP grafted on silicon surface by microwave activation, in both oxidized and hydrogenated surface. The synthesis of initiator 1

was described, but the other two initiators are commercial and were used without modifications.

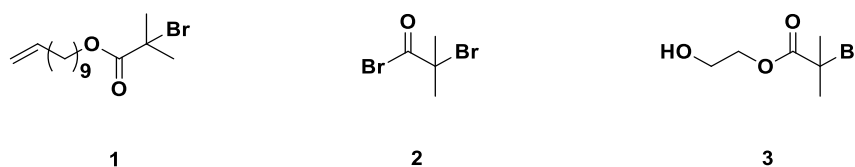


Figure 33: Representation of the three initiators used for SI-ATRP processes. 1) 10-undecenyl-2-bromo-2-methylpropionate, 2) α -bromoisobutyryl bromide, 3) 2-hydroxyethyl 2-bromoisobutyrate.

The grafting of the three initiators, both on oxidized and hydrogenated surface, was performed using microwave activation in a dynamic mode to achieve 125 °C during 50 min with 50W as maximum power. Etching was performed using either 5 or 2 % HF solution. The characterization of the obtained structures was performed by ATR-FTIR spectroscopy using the grafted silicon prism as ATR element, and the grafting density was determined using the ν C=O vibration of each initiator as explained in the **section 2.3**. The grafted surfaces are named as SiOBr1, SiOBr2 and SiOBr3 if the grafting is performed from an oxidized surface using initiator 1, 2 and 3, respectively. Similarly, the grafted surface obtained from the grafting of initiator 1 and 3 on a hydrogenated surface is named SiBr1 and SiBr3, respectively.

Figure 34 shows the ATR-FTIR spectra of the silicon surface after grafting of initiator 1, 2 and 3 on oxidized surface, in which the reference spectrum is that of a freshly oxidized Si(111) surface (SiO_x). The spectrum of SiOBr1 (**Figure 34a**) is similar to those obtained for SiBr1 showed in the last sections, however with a higher grafting density of 1.7 nm^{-2} . Surprisingly, we expected the opposite since the hydrosilylation with alkenes from a hydrogenated surface is well-known to obtain dense layers; however, the grafting density of initiator 1 on oxidized surface was approximately 2 times higher than compared to the hydrogenated surface. The grafting is obtained from the reaction of SiOH with C=C as explained in the review of Zuilhof and coworkers on the covalent surface modification of oxide surfaces.³¹ The ν C=O peak is observed at 1732 cm^{-1} , and the contribution of the CH_2 symmetric and asymmetric bands in the region of $2835 - 2950 \text{ cm}^{-1}$, besides the stretching of CH_3 bond at 2965 cm^{-1} .

The grafting of initiator 2 was performed using a protocol inspired from Bech and coworkers.⁵ The reaction involves a nucleophilic substitution of hydroxyl groups with the Br moiety linked to the carbonyl. As expected, initiator 2 does not graft on a hydrogenated surface, but only on an OH terminated surface with a density of 2.8 nm^{-2} . The SiOBr2 spectrum (**Figure 34b**) shows a broader peak as compared to the other initiators which also appears at a lower wavenumber, at 1713 cm^{-1} . This corresponds to the siloxane ester Si-O-C=O ,¹⁹ which is in accordance with the structure of initiator 2. Finally, initiator 3 yields high grafting densities for both oxidized and hydrogenated silicon surfaces with values of 3.6 and 2.5 nm^{-2} , respectively. Those values of several grafted molecule/ nm^2 reach those of the densest nonfunctional alkyl chains grafted on silicon.¹³⁷ The FTIR spectrum for both SiOBr3 and SiBr3 has another contribution at 1600 cm^{-1} , which can be attributed to a carbonate stretching vibration,¹³⁸ suggesting that a bilayer has been formed as sketched in **Scheme 25**.

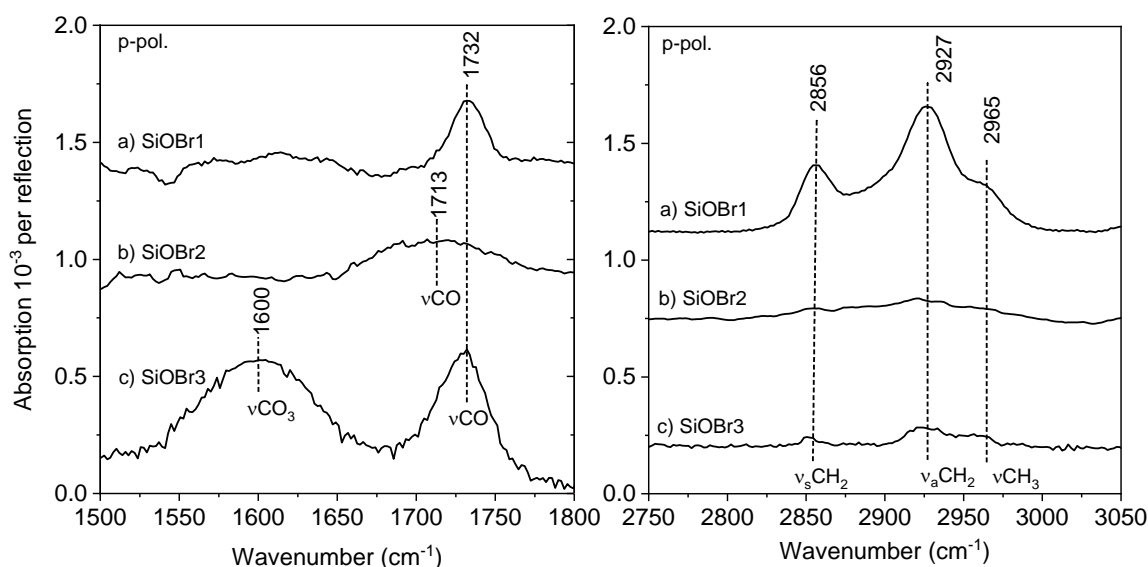
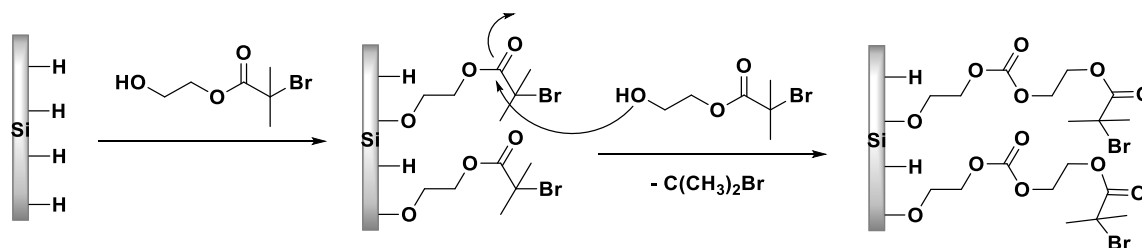


Figure 34: ATR-FTIR spectrum in *p*-polarization of the grafting of initiator 1 (a), 2 (b) and 3 (c) on SiOx surface. The reference spectrum is the oxidized SiOx surface.



Scheme 25: Proposed reaction on surface for initiator 3 to form a bilayer with a carbonate linkage.

Figure 35 shows the ATR-FTIR spectra of only initiator 1 and 3 after grafting on hydrogenated since no grafting of initiator 2 was observed on a hydrogenated silicon surface, as expected. The reference spectrum is that of a freshly hydrogenated Si(111) surface (SiH_x). In both cases, we observe the disappearance of the SiH_x bands from 2079 – 2135 cm⁻¹ (not shown). SiBr1 and SiBr3 show the same features as those discussed for their counterparts obtained from an oxidized surface, however, the carbonate stretching band at 1600 cm⁻¹ in SiBr3 is smaller than the one observed in SiOBr3, which indicates a lower formation of the bilayer depicted in **Scheme 25** when starting from a hydrogenated silicon surface. This is also evidenced by the lower grafting density of SiBr3 (2.5 nm⁻²) compared to SiOBr3 (3.6 nm⁻²).

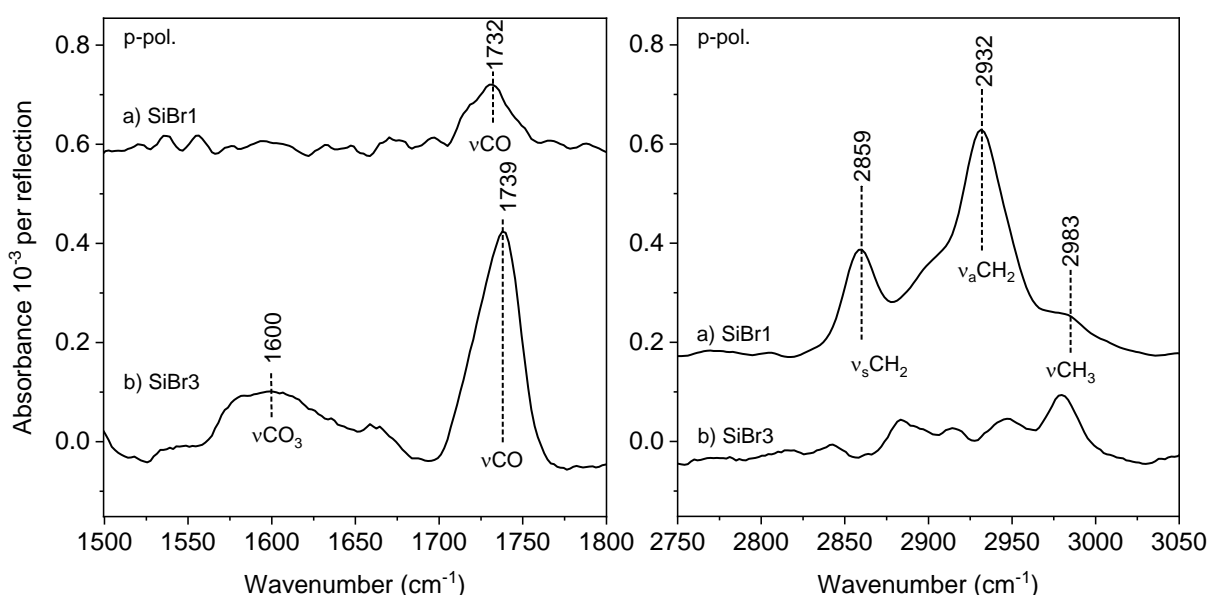
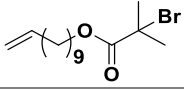
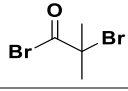
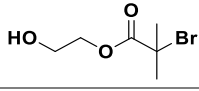


Figure 35: ATR-FTIR spectra in *p*-polarization of the grafting of initiator 1 (a) and 3 (b) on SiH_x surface. The reference spectrum is the hydrogenated SiH_x surface.

The quantification of the initiator density on surface was performed as shown in the work of Gouget-Laemmel and coworkers^{8a}, as well as in **section 3** of this chapter. The grafting densities obtained using this method are summarized in **Table 5**.

Table 5: Density of C=O functions (nm⁻²) of initiator 1, 2 and 3 grafted on SiO_x and SiH_x using the following MW conditions: 125 °C, 50 W, 50 min, 10% v/v of the initiator in mesitylene.

			
SiO _x	1.7	2.8	3.6
SiH _x	0.7	No grafting	2.5

The water contact angle was measured for the surfaces grafted using initiator 1 and 3 (**Figure 36**). The obtained values for SiOBr1 and SiBr1 were very similar, with an approximate value of around $73 - 75^\circ$, which demonstrates a balance in hydrophilicity and hydrophobicity of the initiator layer with a median value. However, SiOBr3 and SiBr3 have both a much lower values of around $41 - 46^\circ$, characteristic of hydrophilic surfaces, which is consistent with the various oxygen present in these surfaces.

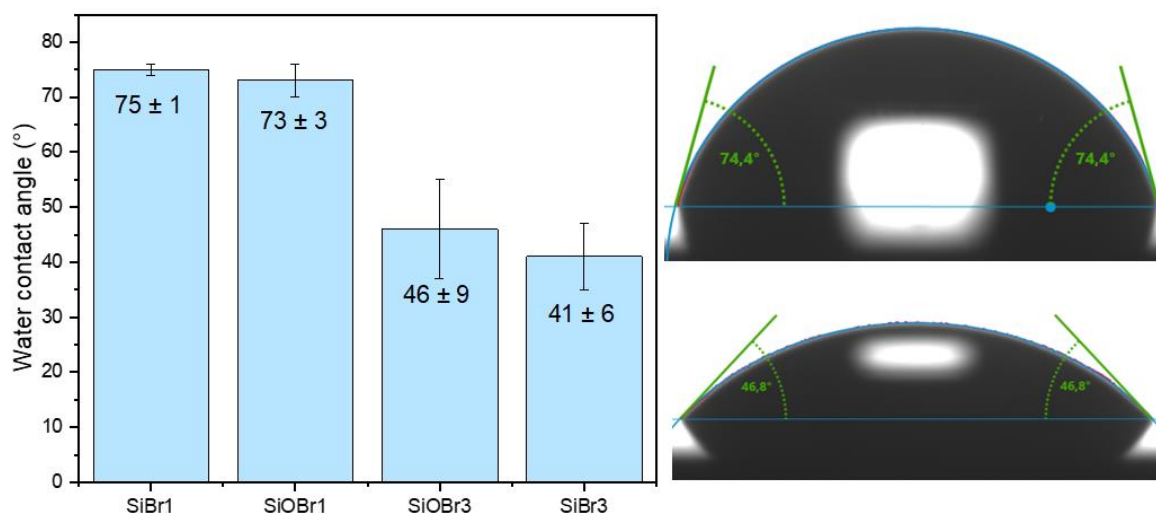


Figure 36: Static water contact angle of the initiator terminated surfaces using initiator 1 and initiator 3, and the images of the water droplets on the surface as example for SiOBr1 and SiOBr3.

The Br3d core level spectra of the prepared surfaces using initiator 1 and initiator 3 are shown in **Figure 37** and they split into two contributions, the first one being a doublet at ~ 69.4 eV (Br $3d_{5/2}$) and ~ 70.4 eV (Br $3d_{3/2}$), attributed to Br–C bond and second doublet at ~ 70.5 eV (Br $3d_{5/2}$) and ~ 71.4 eV (Br $3d_{3/2}$) corresponding to another Br moiety probably linked to oxygen due to its higher binding energy. This other contribution is not observed when initiator 1 is coated on a surface of silver using a drop coating technique (**Figure 98** in **Appendix B**). Therefore, the results suggest that the doublet observed at 70.5 eV is formed during the grafting of the initiator on surface, and it can be a form of O–Br. In fact, the shape these doublets changes from one surface another one, which suggests that it could be linked differently on surface, and/or interact with the XPS beam differently.

Surprisingly, no Br peak was observed for SiOBr2 surface (**Figure 96** in **Appendix B**), but the C/Si ratio of this surface provides a thickness of 0.36 nm (**Table 7**), which compares to

the expected thickness of this molecule, approximately 0.5 nm (obtained by 3D ChemDraw). As initiator 2 is very reactive, we propose that it reacts with the surface with both ends, bridging on the surface and therefore losing its Br atoms which become unavailable for further polymerization. Therefore, this surface was not considered for polymerization any further, and it will not be discussed in this manuscript.

Regarding initiator 3, the Br/C=O values are much higher than expected – 1 – with a value of 12 for SiOBr₃ and 3.6 for SiBr₃, once more indicating the formation of multilayers on the grafting of initiator 3 on surface, and in a higher degree considering SiOBr₃.

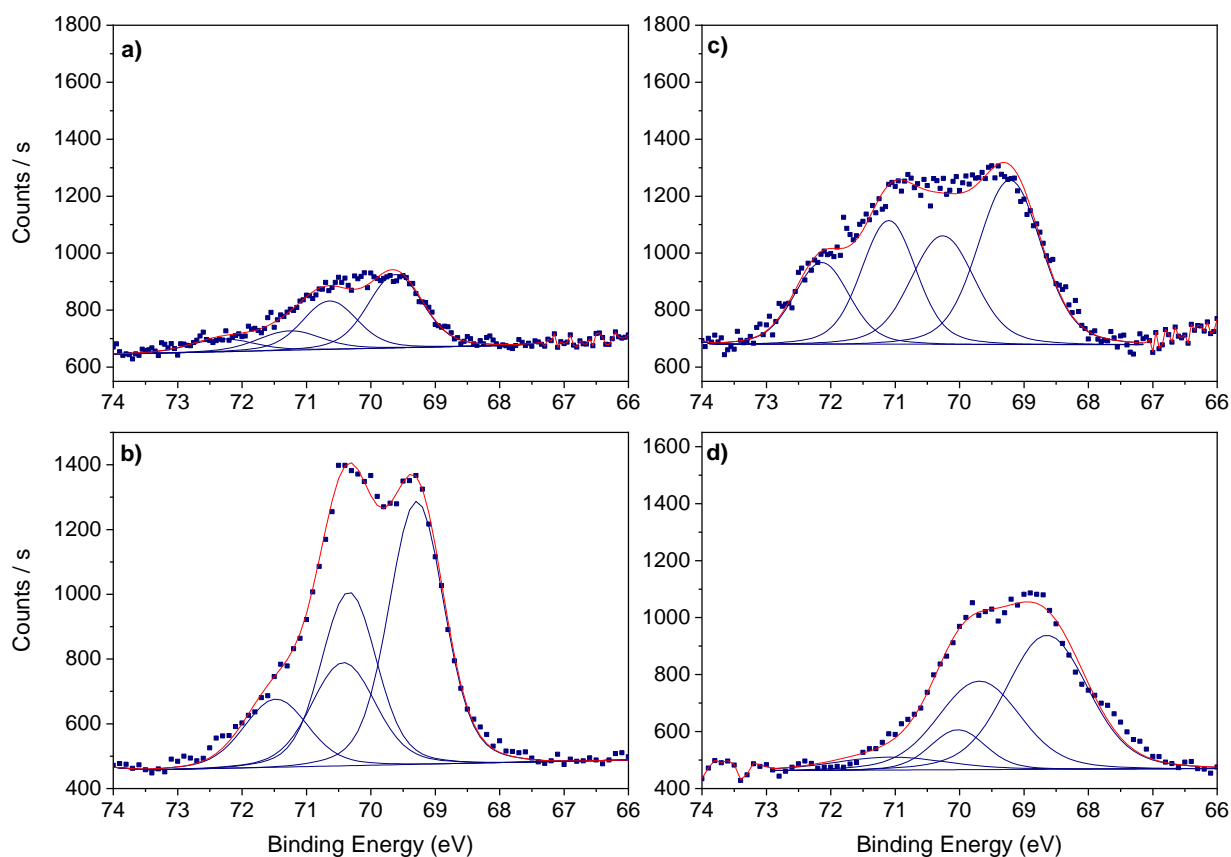


Figure 37: XPS spectra of Brd₃ core level region for the grafted surfaces using initiator 1 and initiator 3 on SiO_x and SiH_x surfaces. a) SiOBr₁, b) SiBr₁, c) SiOBr₃ and d) SiBr₃.

C1s XPS peak (**Figure 38**) recorded after grafting of initiators 1 and 3 shows the three main contributions: C–C, C–O/C–Br and C=O. However, the grafting of initiator 3 exhibits a higher contribution at high eV which is absent in the case of initiator 1. It points to the existence of highly oxidized carbon contribution compatible with the structure proposed for the grafting of initiator 3 in **Scheme 25**. Qualitatively, the peak C–C at 285 eV is dominant in the spectra of SiBr₁ and SiOBr₁ as compared to SiOBr₃ and SiBr₃, which makes sense since a long alkyl

chain is grafted on the surface. However, the ratios of the various components deduced from the fit are not always in agreement with the expected ones.

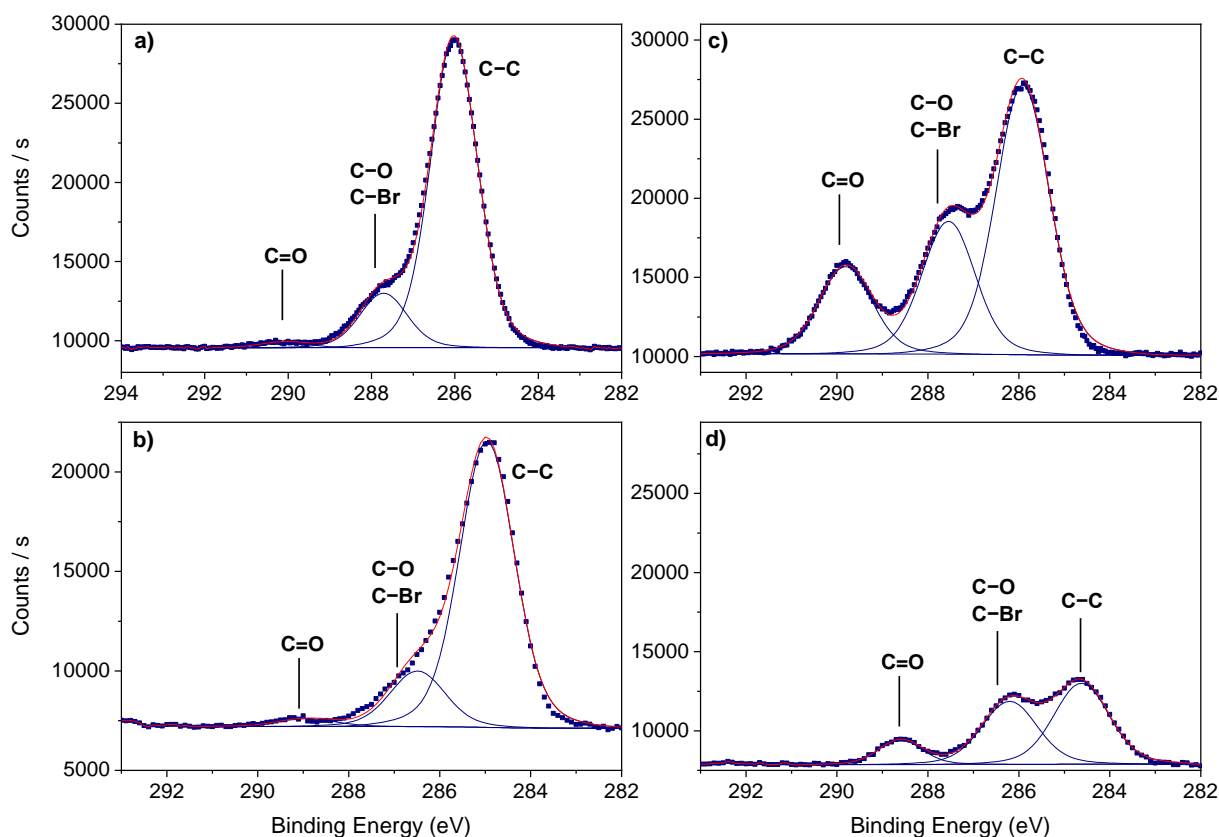


Figure 38: XPS spectra of C1s region for the grafted surfaces using initiator 1 and initiator 3 on SiO_x and SiH_x surfaces. a) SiOBr_1 , b) SiBr_1 , c) SiOBr_3 and d) SiBr_3 . C-C at ~ 285 eV, C-O+C-Br at ~ 286 eV and C=O ~ 289 eV. The spectra are not normalized.

The ratios of C=O/C-O, (C-O + C-Br)/C-C and C-C/C=O of SiOBr_1 are different from the expected ones (**Table 6**). In fact, the C=O has a much lower contribution than anticipated. Other SiOBr_1 surface showed higher contribution of C=O and better ratio of the C1s elements, but other inconsistencies were also observed. These contradictions make it hard the analysis of SiOBr_1 and the understanding of the possible mechanisms involved in the microwave grafting of initiator 1 from an oxidized surface. For the case of SiBr_1 , the C=O/Br ratio is ~ 0.9 , a very close value than expected. However, when analyzing the ratio of C=O/(C-O + C-Br) and C-C/C=O, a lower contribution of C=O is observed, but the ratio (C-O + C-Br)/C-C is as expected, which could indicate a partial degradation of the ester bond. There is also no clear evidence of Si-C contribution for the C1s of SiBr_1 , which could suggest a grafting via Si-O-C bond.

For the grafting using initiator 3, the analysis of the ratios is more complicated since a bilayer of the initiator is formed in both cases. If we imagine the case in which only one layer of the initiator 3 is grafted we expect the ratios of $C=O/(C-O + C-Br) = 0.33$, $(C-O + C-Br)/C-C = 1.5$ and $C-C/C=O = 2$. However, if a bilayer is formed, these values are 0.4, 2.5 and 1 respectively. Therefore, since we do not know the extent of the bilayer, the obtained values should fall between the theoretical values calculated above. Arbitrarily, the theoretical values provided on the **Table 6** for SiOBr3 is the one considering a 100% bilayer, and for SiBr3 a 100% monolayer, although we know it is not the case for both surfaces. Nevertheless, the obtained values for SiOBr3 are very different from the expected ones. A high contribution of C-C is found, which could come from contamination, but it has also a lower value of C-O. Finally, for SiBr3, the $C=O/(C-O + C-Br)$ ratio falls in the expected range, but it a higher contribution of C-C is also found. The C=O/Br values are much higher than expected, which indicated once more the formation of multilayers on these surfaces. These values are summarized in **Table 6**. Thus, it is difficult to correctly quantify these layers since they are quite thin and they are prone to possible contamination which increases the C-C contribution. The complicated XPS spectra suggests a disorganized grafting of these molecules, and therefore no clear proof of forming a perfect monolayer.

Table 6: Expected and experimental values of C1s contribution ratios obtained for SiOBr1, SiBr1, SiOBr3 and SiBr3.

Sample	$C=O/(C-O + C-Br)$ expected, experimental	$(C-O + C-Br)/C-C$ expected, experimental	$C-C/C=O$ expected, experimental	$C=O/Br$ expected, experimental
SiOBr1	0.33, 0.11	0.27, 0.17	11, 53	1, 2.4
SiBr1	0.5, 0.15	0.16, 0.19	12, 35	1, 0.9
SiOBr3	0.4, 0.65	2.5, 0.5	1, 3.1	2, 12
SiBr3	0.33, 0.31	1.5, 0.77	2, 4.1	1, 3.6

Nonetheless, the surface-layer thickness can be deduced by the ratio of C/Si as proposed by Zuilhof and coworkers.¹³⁹ In short, the atomic C/Si ratios were converted in layer thickness (d_{ML}) using the following relationship:

$$d_{ML} (\text{\AA}) = \lambda_{ML}^{Si} \times \sin(\varphi) \times \ln(1 + C/Si)$$

Where $\lambda_{\text{ML}}^{\text{Si}}$ is the attenuation length of Si2p photoelectrons in the organic monolayer ($\lambda_{\text{ML}}^{\text{Si}} = 39.5 \text{ \AA}$)⁴⁰ and φ is the angle between the surface plane and the detector (takeoff or polar angle; $\varphi = 90^\circ$). For the calculation, the whole area of C1s was considered and also the whole area of Si2p. The obtained values and the corresponding thickness layer are found in **Table 7**, and it shows a good correlation to the thereafter discussed results. For SiOBr1 and SiBr1, a value of $\sim 17 \text{ \AA}$ is obtained, which is in accordance with the expected value for initiator 1. In fact, considering a tilt angle of 30° , and the length of initiator 1 of 18.7 \AA (determined by Chemdraw3D software), the calculated thickness is $d = \sin(60^\circ) \times 18.7$, which gives $\sim 16 \text{ \AA}$.^{8a} For SiOBr2, the obtained value was of 4.3 \AA , lower than that expected (around 5 \AA), once more suggesting the bridging of the initiator on surface. For SiOBr3 over twice the expected value – around 7.1 \AA – is found, yet again corroborating with the proposed formation of a bilayer. Finally, SiBr3 is only slightly higher than an expected single layer for initiator 3, which advocates for a preferential formation of single layer over a bilayer.

Table 7: Thickness values found for the grafted initiating surfaces by using the C/Si ratio obtained by XPS.

Type of terminated initiator surface	C/Si	Layer thickness (\AA)
SiOBr1	0.50	16.2
SiBr1	0.56	17.7
SiOBr2	0.12	4.3
SiOBr3	0.70	20.9
SiBr3	0.24	8.5

Even if there is no degradation observed in the solution proved by NMR analysis, by analyzing the XPS data, as well as the statistical study in **section 2.4**, we consider that the grafting of the initiators by microwave are done in a somewhat disorganized manner, which may come from the local superheating on silicon caused by the micro waves. In fact, when observing by camera the grafting of the initiators using the conditions previously mentioned, we could clearly see the formation of bubbles (**Figure 39**), which is an indication of the solvent reaching its boiling point (165.7°C for mesitylene). Therefore, the temperature reached during grafting is higher than the set temperature at 125°C , at least locally. Since the microwave machine measures the temperature only at the bottom of the reactor flask, and not the solution itself, the temperature control might not be so efficient for this type of experiments.

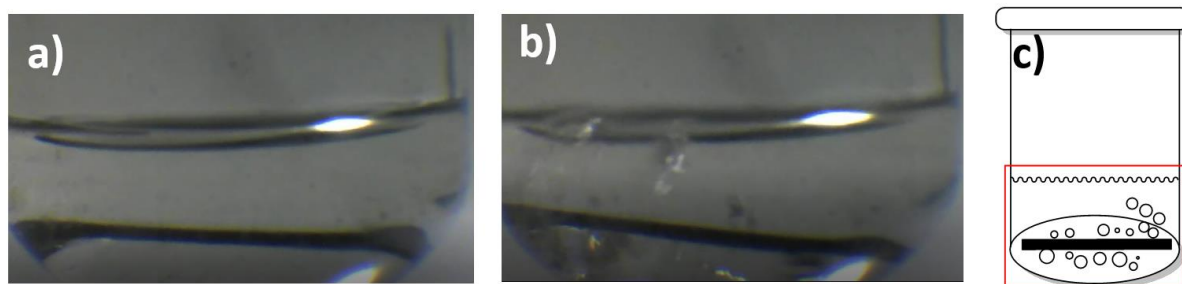


Figure 39: Images taken from the microwave machine during the grafting of initiator 1 on silicon surface showing the formation of bubbles. a) when no bubbles are formed; b) right after the release of bubbles from the heating of silicon; c) schematic representation of the microwave reactor containing the silicon prism and the bubbles formed. Red square represents the area viewed on the photos a and b.

Therefore, to understand more the characteristics of the grafted surface obtained by microwave assisted grafting, AFM technique was performed on SiBr1 by starting from a SiH surface obtained by the anisotropic dissolution in a solution of NH_4F . Notably, this enables the study the grafting of molecules on these surfaces as to prove the homogeneity of the grafting. In fact, the further grafting should respect the structure and maintain the steps-like aspect of the surface if i) only one layer of the molecule is chemisorbed grafted; ii) if the grafting is homogenous.

Thus, hydrogenated silicon surfaces was prepared by means of anisotropic etching in 40% NH_4F solution⁴¹ and analyzed by AFM images in tapping mode. The images (**Figure 40a**) shows a surface exhibiting atomically flat terraces separated by monoatomic steps confirming the correct anisotropic etching. Then the initiator 1 was grafted on a freshly hydrogenated surface using the microwave parameters given in **section 2.4**. If a well-organized and homogeneous layer is grafted, the staircase structure should remain after grafting. However, we observed the disappearance of the steps yielding a rough surface (**Figure 40b**), and also the presence of white spots on surface.

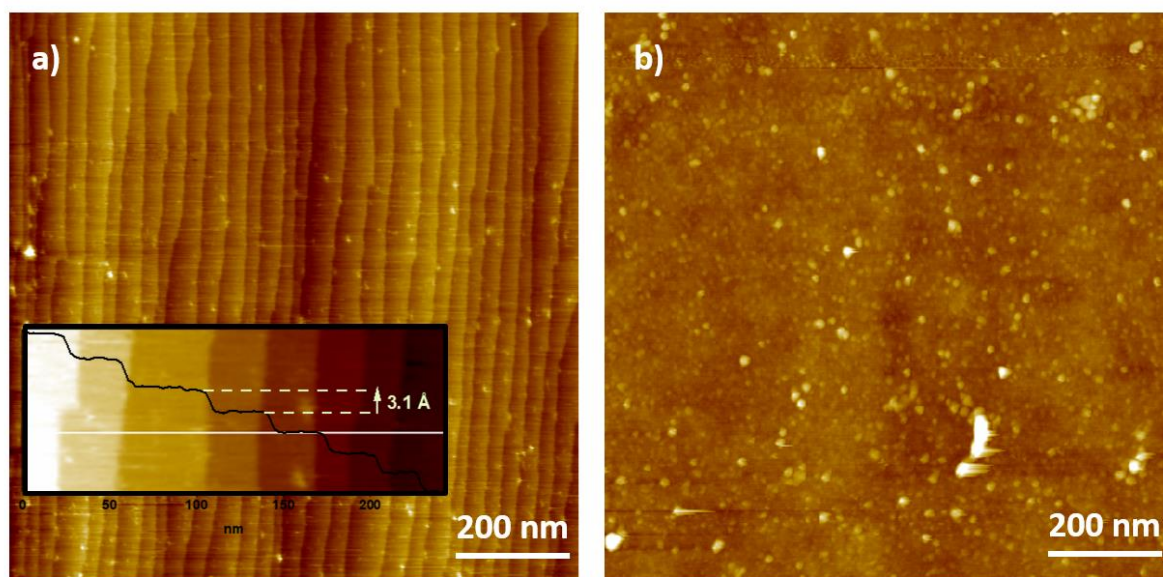


Figure 40: AFM images obtained in tapping mode. (a) hydrogenated H-Si(111) prepared in NH_4F exhibiting flat atomic steps; (b) after grafting of initiator 1 (SiBr1) exhibiting a rough surface using the following MW conditions: 125 °C, 50 min, 50W, 10% v/v (initiator/mesitylene).

By analyzing the grafted images, it is clear that no monolayer of the initiator is formed. Either the layer is too dense, and therefore the monoatomic steps disappeared, or the surface gets oxidized once again during the microwave activation, which could explain why no Si-C was observed in the XPS of these surfaces. In addition, we observe many white spots that ranges from 1 to 10 nm in the z axis. By performing a quantification of grains observed on the images (**Figure 41**), we observe, for two different images taken from the same sample, that the grains represent a total surface coverage of 5.2 and 8.8%. The total volume of grains was also calculated and then correlated with the volume of the molecule of initiator 1.

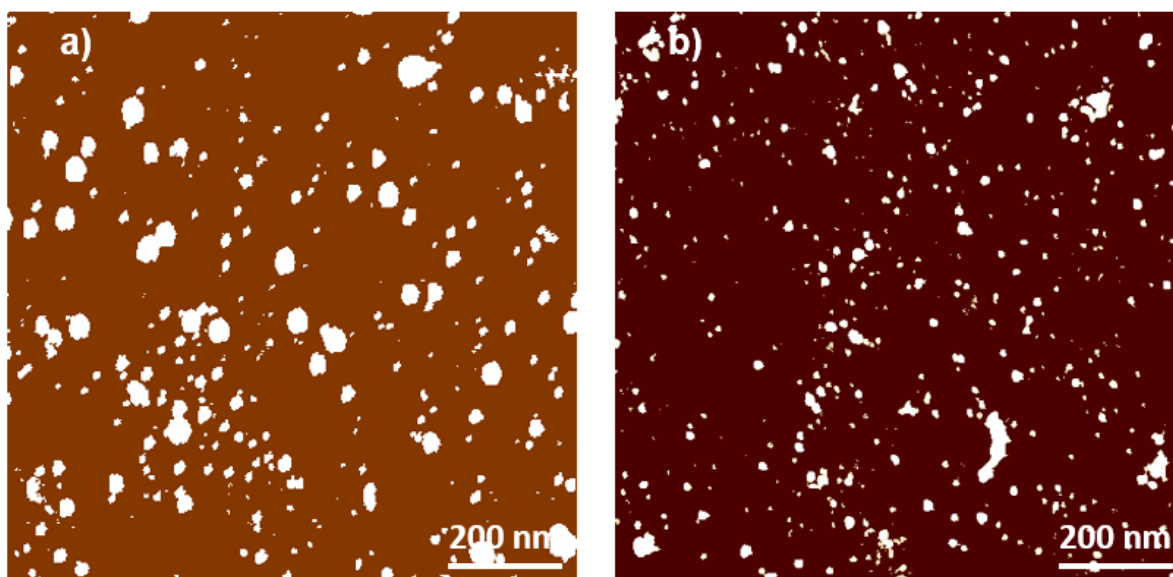


Figure 41: AFM images examples for the calculation of percentage of grains on surface for SiBr1 with a) 1.109 value of detection level. # detected grains = 353; # mean area = 2.5×10^2 nm²; # grains per μm^2 = 3.5×10^2 ; # coverage = 8.8 %; b) 0.8168 value of detection level. # detected grains = 477; # mean area = 1.1×10^2 nm²; # grains per μm^2 = 4.8×10^2 ; # coverage = 5.2 %.

For the estimation of the volume of molecule of initiator 1, as a rough estimation, the molecule is assimilated to a cylinder, as shown in **Figure 42**, which provides a molecule volume of around 165 Å³.

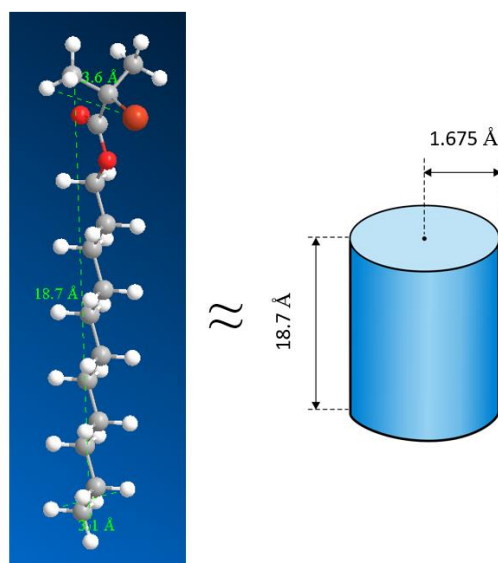


Figure 42: ChemDraw3D of initiator 1 and its rough approximation to a cylinder to calculate its volume.

Then, by correlating the volume of the molecule to the total volume of grains, the number of molecules per nm^2 is obtained. These values are shown in **Table 8**. From two images obtained from the same sample, the number of molecules $\cdot \text{nm}^{-2}$ ranged from 0.3 to 1.1. This range falls within the obtained values for the quantification of molecules by ATR-FTIR, which indicates that the grains observed on the images could be in fact agglomerates of the initiator molecule.

Table 8: Estimation of volume of grains and correlation to the number of molecules per nm^2 considering that the grains are consisted of the molecule of initiator 1.

	Image 41a	Image 41b
Volume of one molecule of initiator 1 (nm^3)*	0.1648	0.1648
Total volume of grains (nm^3) per μm^2	180521	47927
# of molecules/ μm^2	1.10×10^6	2.91×10^5
# of molecules/ nm^2	1.1	0.3

*using a rough estimation by calculating the volume of a cylinder with the distances between atoms in the extremities for height and for diameter.

From this study using XPS and AFM techniques, it appears that the microwave grafting, although very practical, fast and efficient, does not yield to a homogenous monolayer of the initiator on surface, but instead, contributes to a disorganized grafting of the molecule. This disorganization of molecules grafted on surface could explain why it is difficult to control and obtain good reproducibility for grafting of these molecules on surface.

2.7. Study on macroporous silicon (100)

One of the biggest advantages of turning a material into a porous one is the increase of its surface area. It is particularly interesting in supported catalysis because a higher catalyst loading can be obtained using less material. Therefore, it is our interest to work with such materials. Based on IUPAC classification¹⁴⁰, macroporous materials have pores higher than 50 nm and this value is high enough for the modification of the surface to yield the catalysts envisioned, plus having space for the reaction to occur inside the pores.

Using macroporous silicon as substrate has many advantages, such as the large surface area, making it suitable for various applications; tunable pore size, which can be controlled during fabrication process; besides it exhibits low cost and scalability, and many other advantages related to optics and electronics that are not specifically relevant for the envisioned application in this thesis, but interesting to mention.

The macroporous samples were prepared by electrochemical etching and provided by our collaborators in Université de Tours. They had approximately 70% porosity in the porous layer, with a pore depth of $\sim 7.5 \mu\text{m}$ and pore diameter of 150 – 275 nm. The top and cross section view of the samples are shown in **Figure 43**.

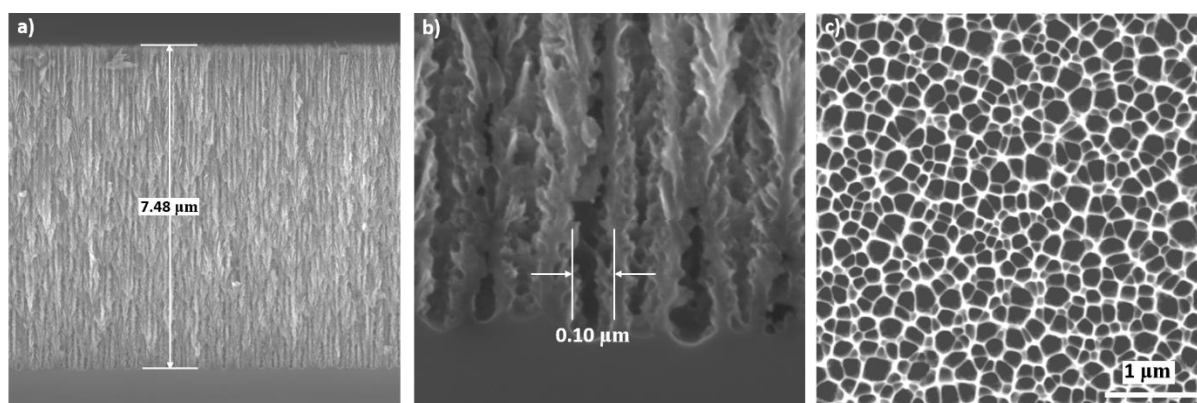


Figure 43: SEM images of the macroporous samples, a) cross section view, b) zoom in the cross section view and c) top view.

The etching of the macroporous silicon was performed by immersing the sample in 25% ethanolic HF and a clear hydrophobic layer is observed. The FTIR spectrum of the SiH_x surface in transmission mode in relation to the SiO_x surface is shown in **Figure 44** and the peaks associated to the SiH_x bands are clearly seen between 2079 to 2139 cm^{-1} . The oscillations

found in the FTIR spectrum of macroporous silicon are associated to optical interferences effects arising from the low refractivity index and homogeneity of the porous layer.

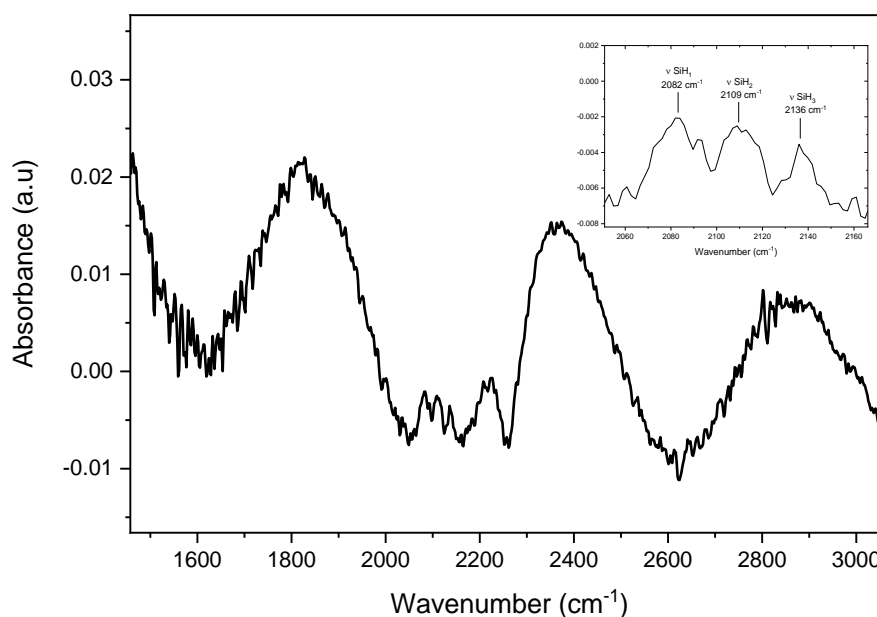


Figure 44: FTIR spectrum of a SiH_x surface on macroporous silicon (100).

By performing the grafting of initiator 1 on the hydrogenated macroporous silicon surface, it is seen the SiH_x peaks in negative, suggesting that the grafting was done through a Si–C or Si–O–C bond, besides other expected bands in positive, such as the stretching mode of CH_2 from the alkyl chain from $2845 - 2983 \text{ cm}^{-1}$, the scissors deformation band of CH_2 at 1465 cm^{-1} and the stretching mode of C=O from the ester at 1715 cm^{-1} , shown in **Figure 45**. The positive band at 2250 cm^{-1} is associated to the stretching mode of H–Si–O backbone indicating a level of oxidation of the surface during the grafting. Most interestingly, the C=O band is approximately 100 times more intense than that obtained for crystalline silicon (around 0.1 to 0.2 mAbs). This increase in value is expected since in macroporous structure we have an increase in the materials' surface area. This sample was later engaged in the polymerization of 2-methyl methoxy methacrylate (MEMA), a result shown in **Chapter 3**.

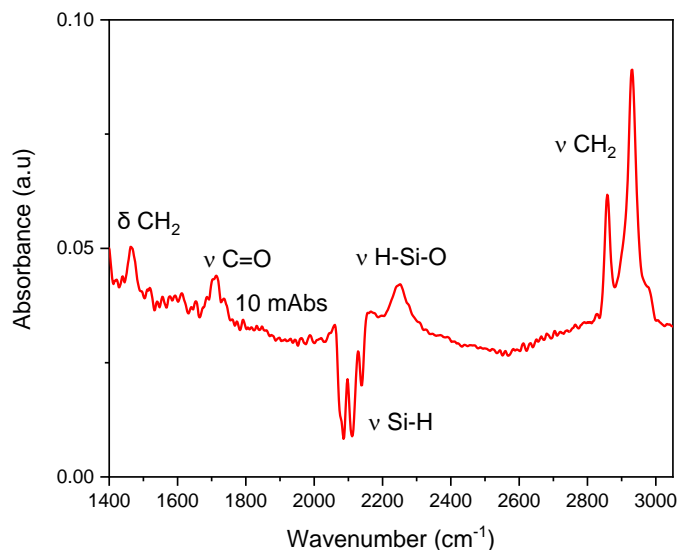


Figure 45: FTIR spectrum of initiated surface monolayer on macroporous silicon (100), the reference spectrum is the hydrogenated surface. Grafting conditions: 10% vol/vol initiator 1/mesitylene, MW: 125 °C, 50 W, 50 min.

The XPS analysis of the grafted surface of macroporous silicon is shown in **Figure 46** with the fits for the Br3d, C1s and Si2p region. The Br3d region (**Figure 46a**) shows 4 components as seen before in the case of crystalline silicon in **section 2.6**. The Si2p (**Figure 46c**) has 6 components, the Si2p_{3/2} Si-Si at 99.59 eV and its doublet at 100.21 eV, and the SiO₂ and its doublet at 103.00 and 103.64 eV, and finally the interfacial Si peaks at 100.45 and 101.07 eV. The C1s region (**Figure 46b**) shows a huge contribution of C-C peak at 285.18 eV in comparison to the C-O and C=O peaks. In fact, the ratio of C=O/C-C ~ 0.015 is much lower than the expected ratio of 0.076 (1 C=O for 13 C-C). The Br/C=O ratio is found to be approximately 0.3, whereas a value of 1 was expected. However, quantification of layers on macroporous silicon by XPS is usually more complicated than compared to crystalline silicon.

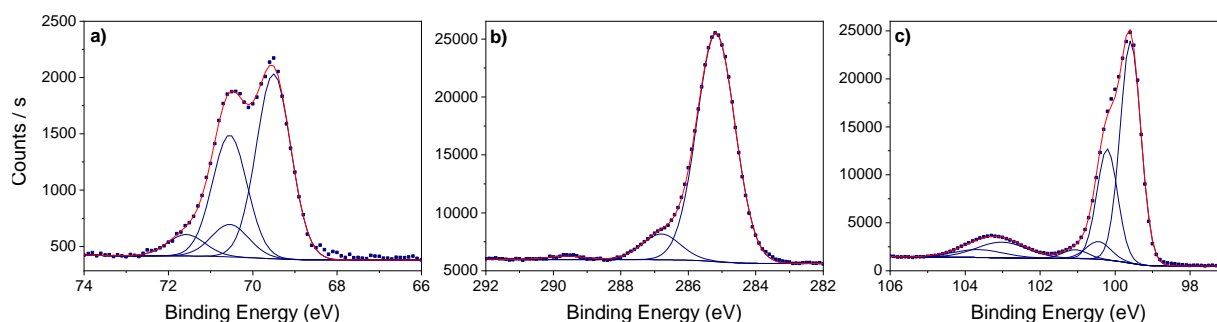


Figure 46: XPS spectrum of Br3d (a), C1s (b) and Si2p (c) region for the grafted surface using initiator 1 on SiH_x surface on macroporous silicon.

For the moment, Brunauer-Emmett-Teller (BET) and thermogravimetric analysis (TGA) analysis are not possible for these macroporous silicon samples since their porous layer is thin, and thus, no difference of mass (TGA) or gas adsorption (BET) is observed. Therefore, FTIR and XPS are the main techniques to analyze the surface modification on these supports.

2.8. Conclusions

This chapter has effectively shown the grafting of several initiators on a crystalline and macroporous silicon surface by means of microwave activation. The modified surfaces were investigated by ATR-FTIR, XPS, AFM and contact angle. Three different initiators were grafted on a hydrogenated and oxidized silicon surfaces, and they were later studied by ATR-FTIR to obtain the layer densities. The grafted surface using initiator 1 on a hydrogenated surface gives a density of 0.7 nm^{-2} , whereas the same initiator on an oxidized surface gives a density of 1.7 nm^{-2} . However, no clear evidence of Si–C bond formation is observed for SiBr1. Initiator 2 loses its bromine, evidenced by XPS, which suggests a bridging of the initiator on surface. The initiator 3 gave high densities (2.5 and 3.6 nm^{-2}) in both oxidized and hydrogenated surfaces, but a tendency to form bilayers or agglomerates.

The XPS and AFM analysis of SiBr1 suggests that the MW grafting yields a disorganized grafting of molecules on surface, together with the formation of aggregates. However, MW activation still shows to be an efficient pathway for the formation of initiated-layer for SI-ATRP as it is very a practical methodology, besides, the grafting of initiator 1 could be reproducible in the conditions analyzed.

CHAPTER 3

ATRP of methacrylates in solution and on surface

“On fait la science avec des faits, comme ont fait une maison avec des pierres : mais une accumulation de faits n’est pas plus une science qu’un tas de pierres n’est une maison.”

Henri Poincaré

SUMMARY

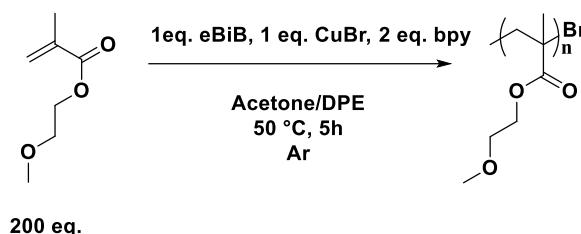
3.1. Polymerization of MEMA in solution.....	89
3.2. Polymerization of MEMA on surface	91
3.3.1. Developing longer polymer brushes	94
3.3.2. X-ray photoelectron spectroscopy	95
3.3.3. Atomic Force Microscopy	99
3.3. Polymerization of MEMA on macroporous silicon.	101
3.4. Copolymerization of MEMA/AZMA in solution	103
3.4.1. Synthesis of AZMA.....	103
3.4.2. Classical copolymerization of AZMA and MEMA.....	103
3.5. Copolymerization of MEMA/AZMA on surface	109
3.5.1. In the case of a crystalline silicon surface	109
3.5.2. X-ray photoelectron spectroscopy	112
3.5.3. In the case of a macroporous silicon surface	114
3.6. Supplemental activator and reducing agent (SARA) polymerization	117
3.6.1. Influence of zero valent copper	117
3.6.2. Copolymerization of MEMA/AZMA and kinetics of Cu(0)-mediated SARA ATRP.....	118
3.6.3. Influence of the temperature	121
3.7. Developing more complex structures using SARA ATRP	122

3.7.1.	HEMA homopolymerization	123
3.7.2.	MEMA/HEMA copolymerization	124
3.8.	Conclusions	126

This chapter consists of developing the copolymerization of methacrylates in solution and on surface. The polymerization of methacrylates was studied by means of classical ATRP and SARA ATRP. Therefore, this chapter focus on the copolymerization of MEMA/AZMA in solution to understand its characteristics, and then, the application on surface to develop copolymer brushes on silicon, which are later quantified by ATR-FTIR. The techniques used to characterize the copolymers obtained in solution are $^1\text{H-NMR}$ and Size Exclusion Chromatography (SEC); and the techniques to characterize the polymer brushes are ATR-FITR, AFM, XPS, ellipsometry and water contact angle measurements.

3.1. Polymerization of MEMA in solution

The polymerization of MEMA (2-methoxyethyl methacrylate) was studied using the reaction conditions chosen used by Sumerlin *et al.*⁸⁸ for the polymerization of AZMA, which uses ethyl 2-bromoisobutyrate (eBiB) as initiator and anhydrous acetone containing 5 vol% diphenyl ether (DPE) as solvent at 50°C with $[\text{MEMA}]:[\text{eBiB}]:[\text{CuBr}]:[\text{bpy}] = 200:1:1:2$ (Scheme 26).



Scheme 26: Conditions for homopolymerization of MEMA.

A kinetic study of the ATRP synthesis of PMEMA was performed, and the results indicates that the polymerization satisfies all the criteria of a controlled polymerization in molar mass for polymerization times ranging from 1 to 5 hours up to a monomer conversion of 60%. The conversion calculation is made by considering the integral of the methylene hydrogens in the monomer (a1 and a2) in comparison to the new hydrogens in the polymer (6), as shown in the **Figure 47** and the formula below.

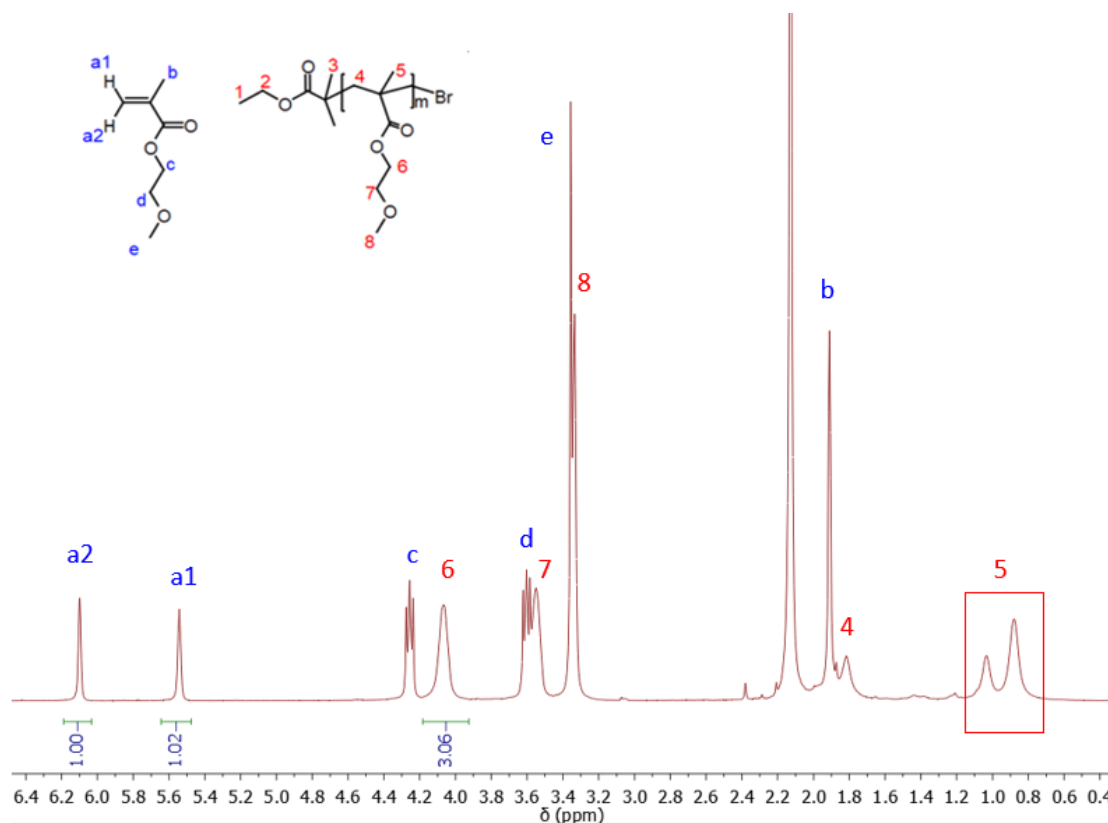


Figure 47: ^1H NMR of the polymerization of MEMA (reaction mixture) after 5h.

$$\text{Conv}_{\text{MEMA}} = \frac{\text{Integral H6}}{(\text{integral H}_a + \text{integral H}_6)}$$

By calculating the conversion hour by hour, it is possible to plot the semi-logarithmic kinetic representation, which in this case indicates an increase in $\text{Ln} [M]_0/[M] = -\text{Ln}(1-p)$ as a function of time with a rate constant of 0.19 h^{-1} (**Figure 48**).

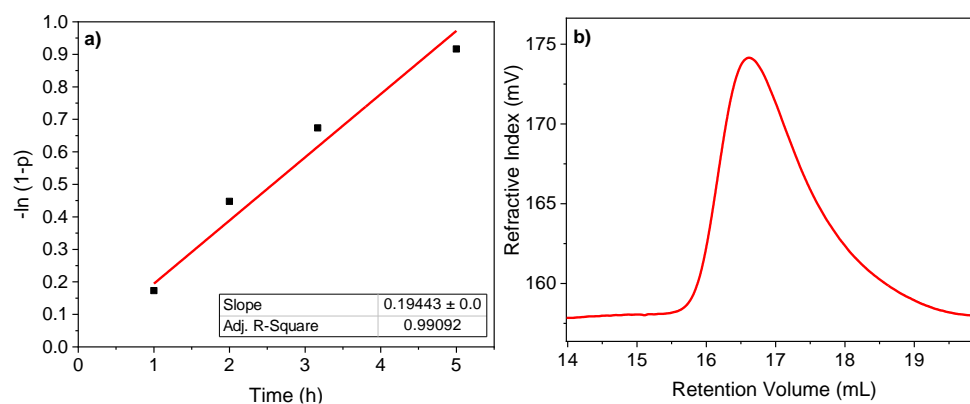


Figure 48: a) semilogarithmic kinetic plot for the ATRP of MEMA, b) SEC-MALS profile for the precipitated polymer of MEMA at 5h reaction.

The absolute number-average molar mass M_n obtained by SEC-MALS only at the end of the reaction (13 800 g/mol) is close to the theoretical M_n calculated through the NMR conversion (17 300 g/mol). Samples at other time of reaction were not analyzed, however, the dispersity \mathcal{D} after 5 hours of reaction is found with a value of 1.2, which is consistent with controlled polymerizations. These results are summarized in **Table 9**.

Table 9: Summary of results obtained by SEC-MALS and ^1H NMR for the homopolymerization of MEMA.

Time (min)	Conversion (%)	$-\ln(1 - p)$	M_n^a (g/mol)	M_n^b (g/mol)	\mathcal{D}^b
60	16	0.17	-	-	-
120	36	0.45	-	-	-
190	49	0.67	-	-	-
300	60	0.92	17 300	13800	1.23

^a Calculated by ^1H -NMR ^b Obtained from SEC-MALS analysis

The polymerization of MEMA was also observed with no addition of initiator in solution, since the temperature itself can start the polymerization going up to 60% conversion checked by NMR after 6 hours; however, as expected, the polymerization is not controlled (as proved by SEC-MALS with a \mathcal{D} value of 6.4). In any case, this does not affect the polymerization on surface, since the ATRP initiator is grafted on surface and the polymerization will start growing from the surface to form polymers brushes. Even if polymer chains with no control are formed in solution, they would not be anchored on surface, therefore not interfering in the final result.

3.2. Polymerization of MEMA on surface

This part has been inspired by the article by [Rafaela Bechara](#), Philippe Roger, Mohamed Mellah, Nadine Barroca-Aubry, Emmanuelle Schulz, Thomas Defforge, Gaël Gautier, François Ozanam, Anne-Chantal Gouget-Laemmel. Microwave-assisted grafting of an ATRP initiator on crystalline and macroporous silicon and subsequent polymerization. Manuscript in preparation.

The same conditions as detailed later are applied on the surface of SiBr1, SiOBr1, SiBr3 and SiOBr3, except that no initiator was added on solution but CuBr_2 was added as a deactivating agent.¹⁴¹ The SI-ATRP on SiOBr2 was performed, but as expected, it did not work since no Br function was observed by XPS for this surface. **Figure 49** shows the ATR-FTIR spectra in p -polarization of the four polymerized surfaces (SiOBr1-PMEMA, SiBr1-PMEMA,

SiOBr3-PMEMA and SiBr3-PMEMA). The quantification of the density of monomer units grown on surface was performed by using a calibration of MEMA in solution, as explained in **Appendix C**. SiOBr3 has the highest density with a value of 62 monomer units·nm⁻², while the others are roughly the same with densities from 9 to 14 monomer units·nm⁻². These values are shown in **Table 10**. In all cases, the main peaks related to the polymer are the C=O stretching mode at 1730 cm⁻¹ and the CH₂ stretching modes between 2770 to 3050 cm⁻¹. By comparing the four spectra, the infrared intensities for the polymerization from SiOBr3 are much larger than that for SiOBr1, SiBr1 and SiBr3.

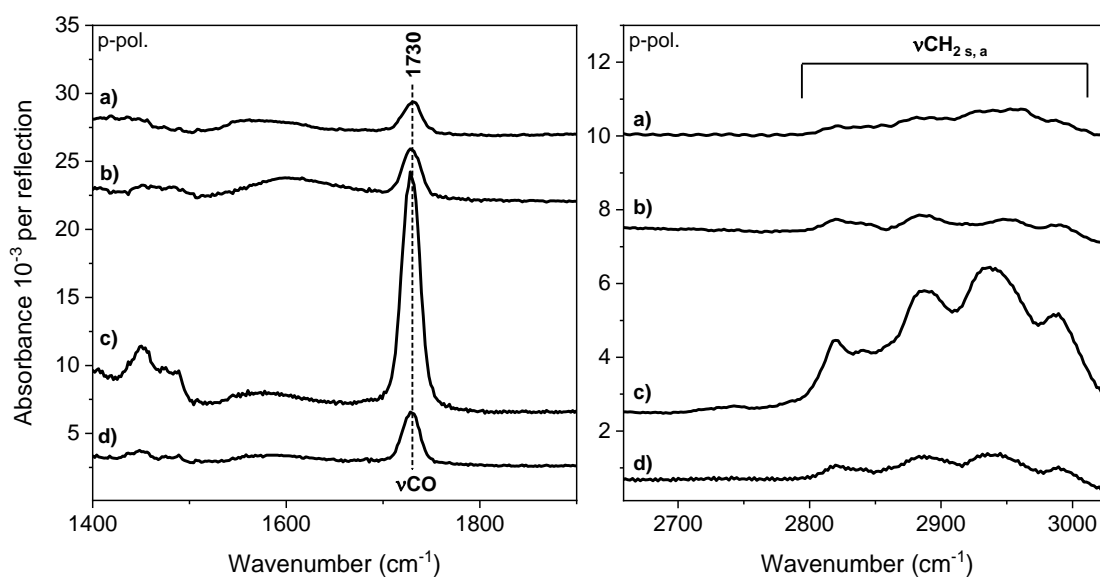


Figure 49: ATR-FTR spectra of PMEMA on surface. a) SiOBr1-PMEMA b) SiBr1-PMEMA c) SiOBr3-PMEMA and d) SiBr3-PMEMA. Spectra in the range of 1400 – 1900 cm⁻¹ and 2660 – 3030 cm⁻¹.

Table 10: Density (from vCO), nm⁻² of initiator molecules and of monomer units after polymerization of MEMA on SiBr1, SiOBr1, SiBr3 and SiOBr3.

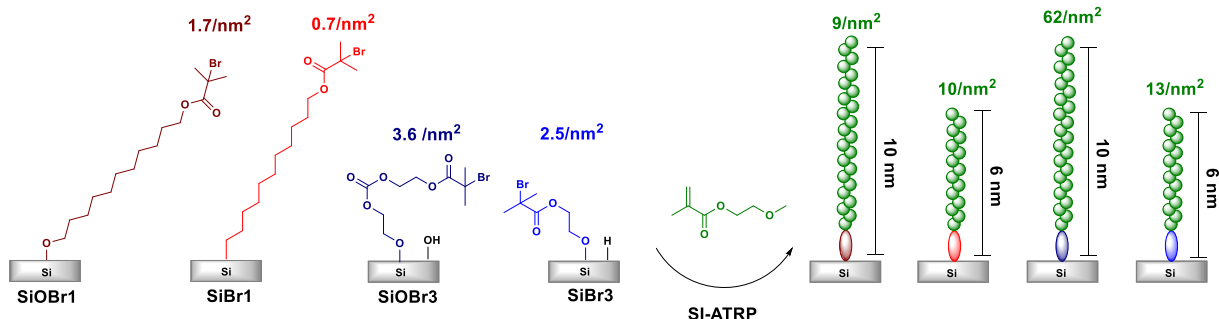
Type of surface	Br1	Br1-PMEMA	Br3	Br3-PMEMA
SiOx	1.7	9.1	3.6	61.8
SiHx	0.7	10.1	2.5	13.4

Ellipsometry measurements for the samples showed a value of around 6 to 10 nm of polymer brush thickness, value in accordance with similar methacrylate-type polymers brushes found in the literature.¹⁴² These values are shown in **Table 11**.

Table 11: Thickness of polymerized surfaces obtained by ellipsometry fixing the refractive index of the polymer layer at 1.6.

SiOBr1-PMEMA	SiBr1-PMEMA	SiOBr3-PMEMA	SiBr3-PMEMA
10.5 ± 0.5 nm	5.8 ± 0.3 nm	10 ± 0.2 nm	6.4 ± 0.4 nm

The degree of polymerization (DP) can also be deduced from the scaling law applicable for dry polymers, i.e., $L/a = DP^{2/3}$.¹⁴³ In this equation, the thickness of the brushes (L) is normalized to the distance (a) between two monomers, which is around 0.25 nm in this case (provided by 3D ChemDraw). For instance, considering the thickness obtained by ellipsometry of SiBr1-PMEMA minus the thickness of the initiator layer deduced by XPS (**Table 7**), a polymer thickness of ~4 nm is obtained, which in turn gives a DP of ≈ 65 . For both SiOBr1-PMEMA and SiOBr3-PMEMA, for which the thickness is around 10 nm, DP is $\approx 180 - 210$. Finally, for Si-Br3PMEMA a DP of ≈ 105 is found. From these DP, it is possible to obtain the fraction of active initiators in each case, which are 2%, 22%, 10% and 5% for SiOBr1-PMEMA, SiBr1-PMEMA, SiOBr3-PMEMA and SiBr3-PMEMA, respectively. These values are detailed in **Table 12**. **Scheme 27** resumes the polymerization of MEMA on the four surfaces studied.

**Scheme 27:** Polymerization of MEMA from different surfaces.

Considering the case of grafting initiator 1, the % of active initiator sites is lower as the density of initiator molecules is higher comparing SiOBr1 and SiBr1 (1.7 nm^{-2} with 2% active sites vs. 0.7 nm^{-2} with 22% active sites, respectively). Since the polymerization reaction was performed using the same methodology, we hypothesize that this trend is due to steric hindrance present in highly dense initiator layers, *i.e.*, highly dense initiator layers hinder the number of sites engaged in polymerization. In fact, SiBr1 shows to be the most active surface for polymerization of MEMA with a percentage of active sites of 22, ~10 times higher than its counterpart SiOBr1. However, this was not observed using initiator 3, but this case is more

complicated due to the formation of a bilayer of initiator. Still, SiOBr3 has the highest number of active initiating molecules, *i.e.* 0.3 nm^{-2} , due to its high grafting density. In all cases, a brush regime is obtained since the grafting density is $> 0.01 \text{ nm}^{-2}$.

Table 12: Calculated DP from the scaling law ($L/a = DP^{2/3}$), the density of molecules for each polymer chain and the % of initiator active sites.

Type of surface	L (nm) ^a	L/a	DP	σ of polymer chain (nm^{-2}) ^b	% of active sites
SiOBr1-PMEMA	8.9	35.6	212	0.04	2
SiBr1-PMEMA	4.0	16.1	65	0.16	22
SiOBr3- PMEMA	7.9	31.6	178	0.35	10
SiBr3- PMEMA	5.6	22.2	105	0.13	5

^a Thickness value from ellipsometry minus the thickness of initiator given by XPS. ^b Obtained by dividing the density of monomer units shown in **Table 10** by the calculated DP, in which σ means density.

The water contact angle (WCA) of all modified surfaces after polymerization of MEMA were measured. The WCA gives the information of hydrophobicity of the surface and help to understand the possible conformations of the molecules on surface. For instance, it is expected to have around the same value of contact angle for all four cases since all of them bear the same polymer on surface. From **Table 13**, all values are close, except SiOBr1-PMEMA which is slightly higher than the others.

Table 13: Static water contact angle of the MEMA polymer brushes on surface

SiOBr1-PMEMA	SiBr1-PMEMA	SiOBr3-PMEMA	SiBr3-PMEMA
81 ± 1	71 ± 1	70 ± 2	68 ± 2

3.3.1. Developing longer polymer brushes

The elongation of polymer chains can be achieved by prolonged reaction time. This elongation is characterized by an increase in the number of molecules $\cdot \text{nm}^{-2}$ with respect to the reaction time. This increase of density of monomer units with the increase of reaction time offers insights for the development of polymer brushes with different thicknesses for various applications. For instance, SiOBr1 surface was engaged for the polymerization of MEMA over 15 h yielding a surface with a polymer brush density of 42 nm^{-2} , much higher than those obtained at 5 h reaction with a density of around 9 nm^{-2} (**Table 10**), also accompanied with a higher polymer brush thickness (21.9 nm vs 8.9 nm for the case of 5h reaction). The DP is also higher with a factor of 3.8, a similar value of the time ratio (5/15), suggesting that the

polymerization has a linear correlation in respect to time of reaction, although more points at various times should be performed to confirm this trend. Besides, the percentage of active sites remains roughly the same in both cases, which also proposes a good reproducibility of these reactions. **Table 14** summarizes the discussed results, and **Figure 50** shows the ATR-FTIR spectra of these two examples.

Table 14: Calculated DP from the scaling law, the density of molecules for each polymer chain and the % of initiator active sites for the case of SiOBr1 under 5 h or 15 h reaction.

Time of reaction	L ^a	L/a	DP	σ of polymer chain (nm ⁻²) ^b	% of active sites
5h	8.9	35.6	212	0.04	2
15h	21.9	87.5	819	0.05	3

^a Thickness value from ellipsometry minus the thickness of initiator given by XPS (1.6 nm). ^b Obtained by dividing the density of monomer units by the calculated DP, in which σ means density. Initiator density for experiment at 15h is 1.7 nm⁻².

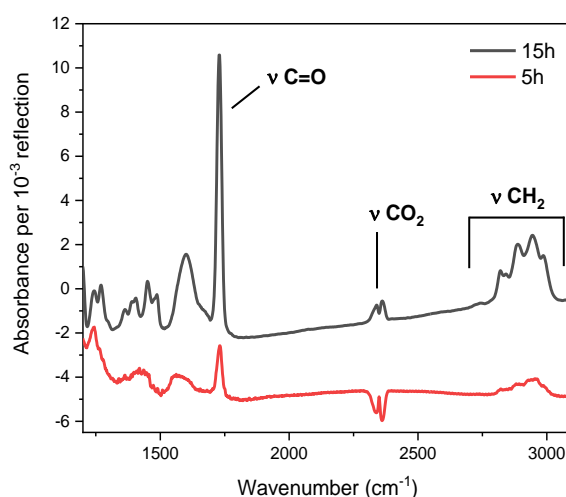


Figure 50: ATR-FTIR spectra in *p*-polarization of polymer brushes of MEMA on SiOBr1 surface in 5h and 15h reaction time. The reference spectra are the SiOBr1 before polymerization reaction.

3.3.2. X-ray photoelectron spectroscopy

XPS can provide a somewhat more detailed insight into the polymer structure by analyzing the decomposition of the C1s peak (**Figure 51**). After polymerization of MEMA on surface, each unit of the polymer backbone includes 3 C–C, 3 C–O and 1 C=O bonds. Therefore, when analyzing the C=O/C–O and C=O/C–C intensity ratios, a value of 0.33 for both ratios is expected. For SiOBr1, the C=O/C–O ratio is of 0.38, whereas the C=O/C–C = 0.2, showing more C–C bonds than expected. This higher contribution of C–C may come from

the grafted initiators molecules. However, the C1s/Si2p ratio is ~ 3.4 , suggesting that the thickness of the polymer brush is somewhat high and should significantly attenuate the contribution from the grafted initiator molecules. It then appears that the polymer layer has not a homogeneous thickness over the surface: the layer is not enough dense for efficiently covering the surface, which leaves part of the initiator molecules easily accessible to XPS analysis and accounts for an increase of the C–C contribution. It makes sense to observe this behavior on the SiOBr1 surface where the fraction of active initiator molecules is only 2%. For the SiBr1 surface, the C=O/C–C and C–O/C–C ratios are 0.34 and 0.31, respectively, close to the expected value. On this surface the C1s/Si2p ratio is of 2.8, pointing to a thinner but homogeneously denser polymer layer than on SiOBr1, that corroborates with a higher 20% fraction of active initiating molecules.

When using initiator 3, the polymer layer appears also homogeneous. On SiOBr3, the trend is as expected, with ratio values of 0.35 and 0.34 for C=O/C–C and C–O/C–C respectively, on a thick layer evidenced by a C1s/Si2p ratio of ~ 12 (in agreement with ATR-FTIR and ellipsometry data). In the case of SiBr3, the amount of C–O appears somewhat smaller than expected (C=O/C–O ratio of 0.44), but the ratio C=O/C–C = 0.33 is as expected. The thickness of the polymer layer appears the thinnest (C1s/Si2p ratio of 1.5), *i.e.*, thinner than that found on SiOBr3. The XPS data containing all atomic percentage are available in **Appendix A**.

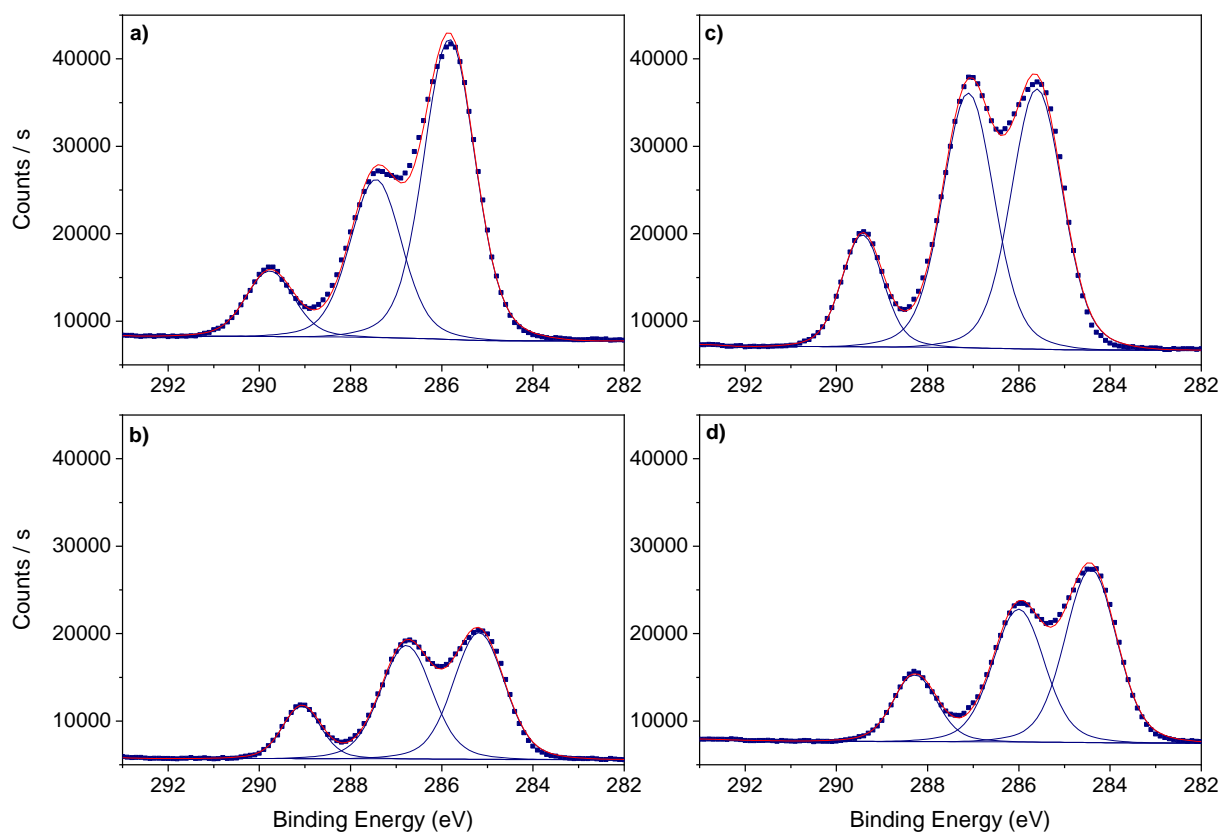


Figure 51: XPS spectra for C1s region of a) SiOBr1-PMEMA, b) SiBr1-PMEMA, c) SiOBr3-PMEMA, d) SiBr3-PMEMA. Peak C–C at 285.6 eV, C–O at 287.1 and C=O at 289.4 eV. The spectra are not normalized.

When comparing the spectra of Si2p of all four polymerized surfaces (**Figure 52**), only SiOBr1 has a strictly different shape from the others, having a higher SiOx contribution. This could come from the low fraction of active initiator molecules, therefore leaving parts of the surface more vulnerable to unwanted oxidation during the sample manipulation.

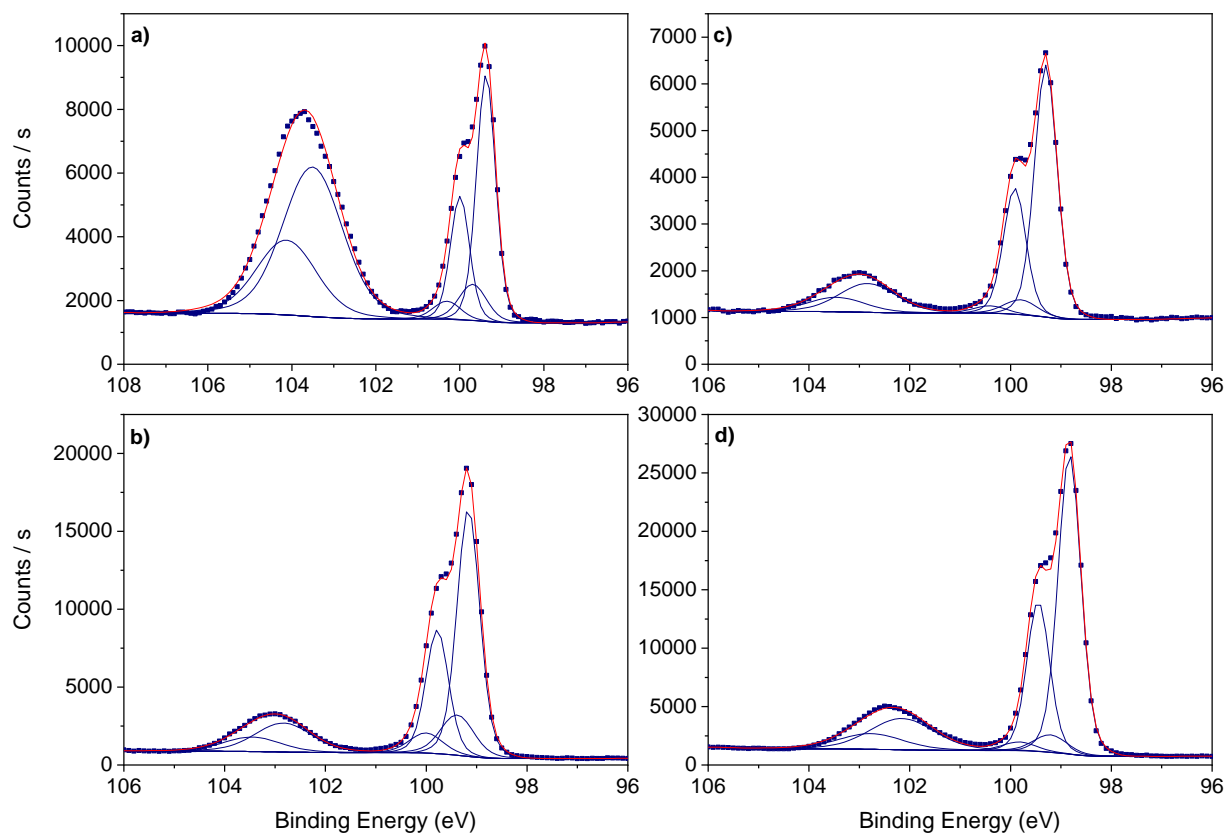


Figure 52: Si_{2p} XPS spectra for polymerized surfaces, a) SiOBr1-PMEMA, b) SiBr1-PMEMA, c) SiOBr3-PMEMA, d) SiBr3-PMEMA. Peak Si–Si at 99.38 eV, interfacial Si at 99.7 eV and C=O at 103.5 eV. The spectra are not normalized.

As a matter of visual conceptualization of the thickness enlargement after polymerization, **Figure 53** shows the XPS survey spectra of the terminated initiator surface and its polymerized surface afterwards for the case of SiBr₃. There is a clear gap between surveys being the polymerized surface in higher counts/s because of its denser layer. Analogy, the carbon and oxygen peaks are clearly much higher in intensity in the polymerized surface compared to the terminated initiator surface when both silicon peaks are normalized.

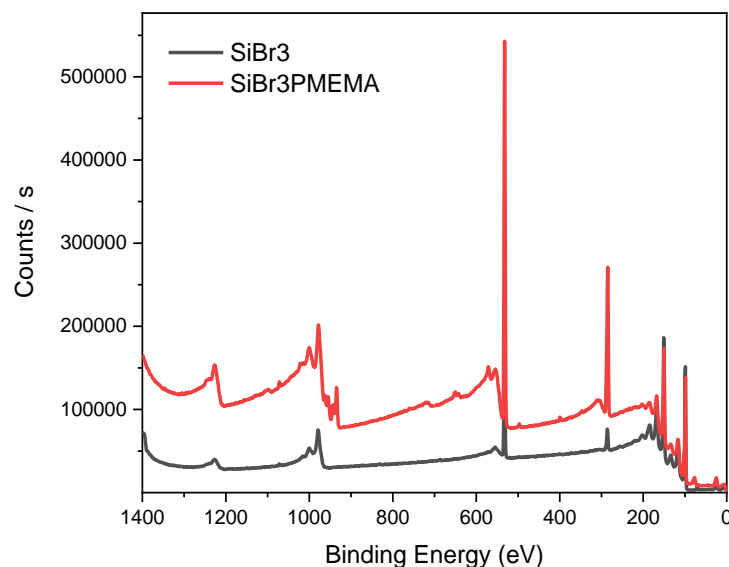


Figure 53: XPS survey of SiBr₃ (red) and SiBr₃-PMEMA (black).

3.3.3. Atomic Force Microscopy

AFM (Atomic Force Microscopy) gives valuable information about the chemical and mechanical properties of the surfaces, as well of course, the general topography of the surface. When discussing SI-ATRP or even other types of polymerization on surface, it is always interesting to also obtain the thickness value by a mechanically afforded scratch on surface to remove the polymer layer and then measuring the step, *i.e.*, the height of the polymer layer compared to the silicon bulk. The AFM topography image of the prepared brushes of MEMA on surface of SiOBr₁ (**Figure 54**) confirms the formation of a continuous and homogenous film of polymer, with a layer rugosity of around 1 – 2 nm. The bright spots observed on the image indicate the deposition of adsorbed macromolecules, or even covalently linked chains from solution via locally recombination reactions. These patterns were also observed by Slowikowska and coworkers¹⁴² for the SI photoinduced ATRP of poly(methyl methacrylate). These agglomerates have on average 5 to 10 nm height, and even though the prepared surfaces are cleaned and well rinsed many times, including using a Soxhlet for 8h with THF as solvent, the agglomerates were observed in all cases. However, SiBr₃-PMEMA and SiBr₁-PMEMA show less homogeneity of the polymer layer, *i.e.* polymer islands were observed instead of a homogenous layer as compared to SiOBr₁-PMEMA and SiOBr₃-PMEMA. This lack of homogeneity can be related to a thinner thickness of the polymer layer on surface (see **Table 11**). Other AMF images are shown as supporting information in **Appendix B**.

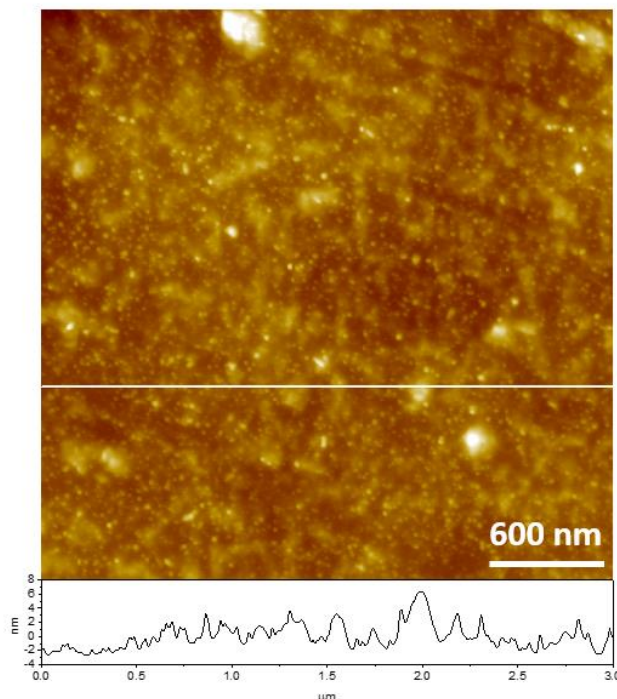


Figure 54: AFM image of SiOBr1-PMEMA layer showing the homogenous polymer brush layer as well as agglomerates of polymers on surface. The profile is shown below the image and corresponds to the line traced over it with an agglomerate of around 8 nm and layer rugosity of $\sim 1 - 2$ nm.

Besides, when measuring the thickness of the layer as show in **Figure 55** for the case of SiOBr1-PMEMA, a thickness of around 8 nm is obtained. Likewise, the polymer brushes on the surface of SiBr1-PMEMA and SiOBr3-PMEMA were evaluated of around 4-5 nm and 9 nm respectively. Unfortunately, it was not possible to measure the thickness of the polymer brush by AFM and by surface scratches for SiBr3-PMEMA, as these thin layer polymer brushes (from 5 to 10 nm) are quite hard to be measured by AFM since they give minimal optical difference between the silicon bulk and the polymer brush, thus complicating the detection of the scratches. Still, thickness values found for the studied surfaces are in accordance with those values obtained by ellipsometry (**Table 11**), with slight changes of 1 to 2 nm between the two measurements. Therefore, the AFM validates the accuracy of the model and methodology of the ellipsometry measurements. Since ellipsometry is a faster and easier analysis compared to AFM, this technique was preferred over AFM for the quantification of the polymer brushes thickness for all the prepared polymers on surface in this manuscript.

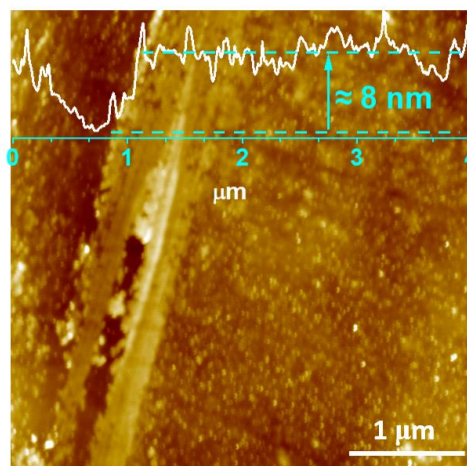


Figure 55: Top-view images and cross sections at the frontier between the silicon substrate and the PMEMA layer on SiOBr1-PMEMA showing a thickness layer of around 8 nm.

3.3. Polymerization of MEMA on macroporous silicon.

The simplest case of grafting the initiator on surface is the using initiator 1 on hydrogenated silicon surface as demonstrated in **Chapter 2**. The other cases could be of practical interest, but offer less straightforward avenues for quantitative analysis. As an illustration, the application to other type of surface, a macroporous silicon surface, is presented for the SiBr1 case. Therefore, the same methodology was also applied to a macroporous surface, containing pore size of 150 – 275 nm and pore thickness of 7.5 μm, with an approximate porosity of 70% for the porous layer. **Figure 56** shows the results initiator grafting (already presented in **Chapter 2**) and then its further polymerization of MEMA. As expected, the intensities of the peaks, in special regard to the C=O vibration mode, is much more intense than the ones observed in crystalline silicon (approximately 100 times more).

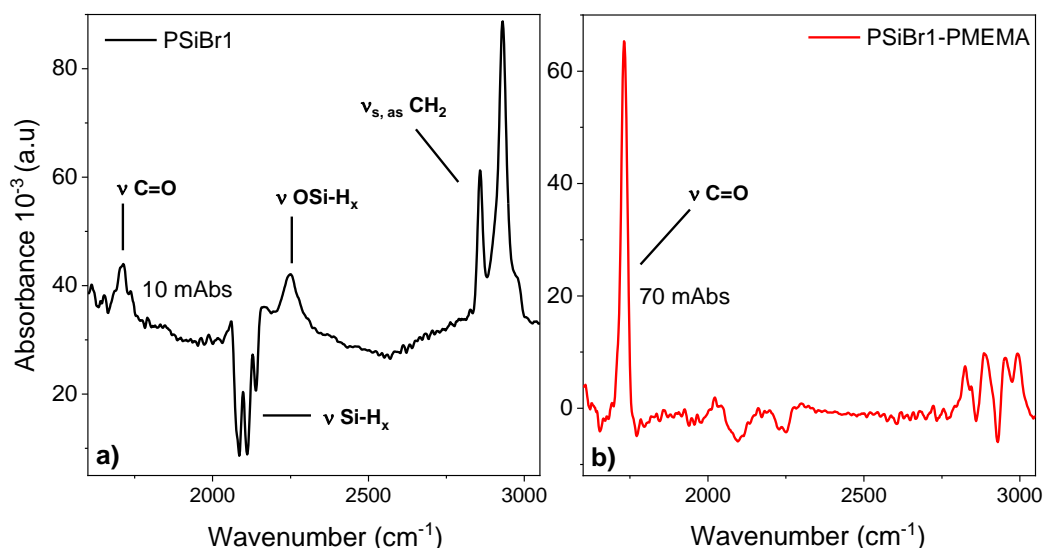


Figure 56: Macroporous-Si(100) with pore size of 150 – 275 nm and pore thickness of 7.5 μ m. a) grafted surface using initiator 1 from a SiH_x surface, b) polymerized surface using the following conditions [MEMA]:[CuBr]:[CuBr₂]:[bpy]) 200:1:0.05:2, plus initiated surface; in acetone/DPE (5%) at 50 °C, 5h in argon atmosphere.

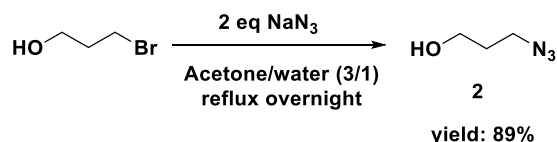
Since the analysis of the macroporous is done by normal transmittance and not by ATR, the quantification of density is not possible as done for crystalline silicon. However, a correlation slope can be envisioned between the molecules/nm² to mAbs of the associated peak when using crystalline silicon. Taking the examples of polymer brushes of MEMA on surface presented in **section 3.2**, a slope of 3.5 is obtained (**Table 29**, in **Appendix B**).

From this slope, it is possible to correlate the mAbs obtained from the transmission FTIR of macroporous silicon (70 mAbs) would give an average value of 247 monomer units/nm² if ATR calibration procedure would apply. However, transmission FTIR is known to be about twice less sensitive than ATR FTIR spectroscopy.¹⁴⁴ Thus, a value of \sim 500 monomer units/nm² has been used. Although rudimentary, this method gives an approximative value of molecules on surface.

3.4. Copolymerization of MEMA/AZMA in solution

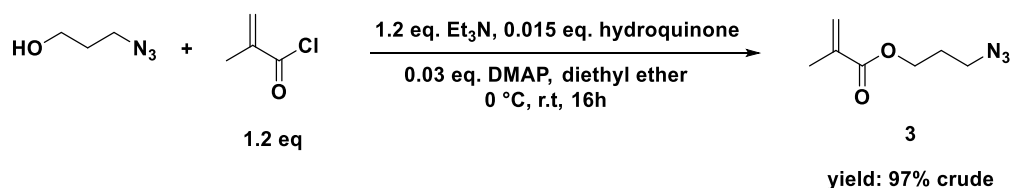
3.4.1. Synthesis of AZMA

The synthesis of AZMA starts with the synthesis of 3-azido propanol, with the nucleophilic substitution of bromo propanol with sodium azide (**Scheme 28**) yielding compound **2** with 89%.



Scheme 28: Synthesis of azido propanol.

The next step of the synthesis of AZMA was based on the work of Sumerlin and coworkers⁸⁸, but optimized to provide better yield (**Scheme 29**).



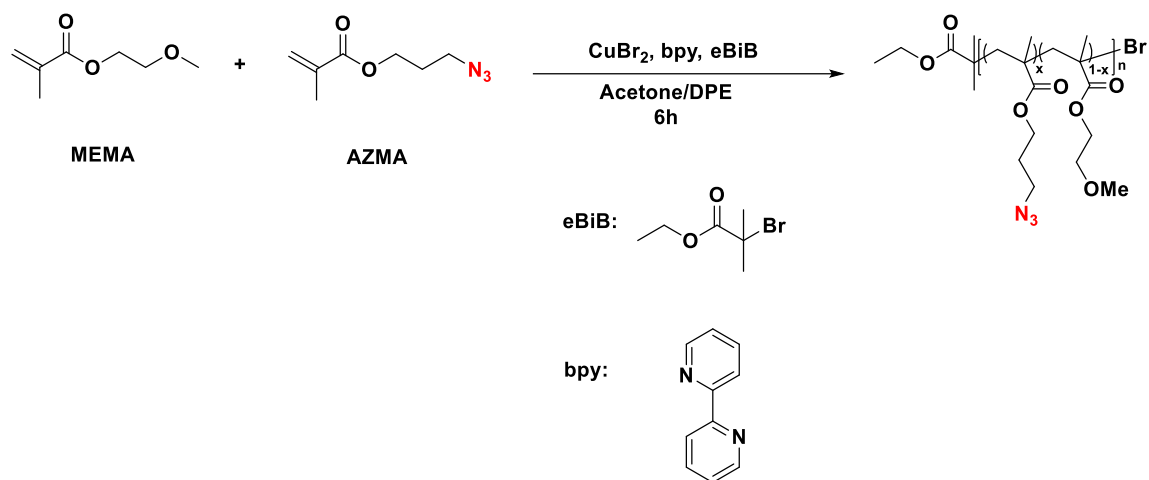
Scheme 29: Synthesis of AZMA (3-azidopropyl methacrylate).

The original procedure, Sumerlin and coworkers used vacuum distillation to purify AZMA, unfortunately in our hands the distillation meant many losses of product. Other attempts, using horizontal distillation were also performed, but still, with no success. The product can be also purified using column chromatography with silica as the stationary phase and gradual increase in polarity of petroleum ether : triethylamine as the eluent, however, this pathway is not adequate for large batches of product.

Finally, with many optimizations of the procedure vacuum distillation, the purification yield has been greatly improved.

3.4.2. Classical copolymerization of AZMA and MEMA

Polymerization of AZMA was described by Sumerlin *et al.*⁸⁸, and was already reproduced by our consortium, together with the copolymerization of MEMA and AZMA.^{8b} **Scheme 30** shows the general conditions for this copolymerization.



Scheme 30: Copolymerization conditions for MEMA and AZMA.

The first attempts to reproduce these results showed that small quantities of impurities in the AZMA product affects the copolymerization of MEMA/AZMA, resulting in the formation of largely dispersed copolymers.

Some of these attempts are summarized in **Table 15**, showing the obtained results for the copolymers under different conditions (ligand, time or temperature). These results show no control of the copolymerization reaction in these conditions with large dispersities measured by SEC-MALS. In some cases (entries 3 and 4) the copolymers were not soluble in THF indicating possible reticulation of the copolymers. Later, it was highlighted that the quality and purity of AZMA are the main responsible for the lack of control of the copolymerization reaction, thus making the purification process of AZMA extremely important. Thus, AZMA should be used freshly distilled and no later than 2 weeks even if stored at -5°C .

Table 15: Results of copolymerization of ([MEMA]:[AZMA]:[CuBr]:[ligand]:[eBiB]) x:200-x:1:2:1 in acetone/DPE (5%), with envisioned DP of 200.

Entry	T (°C)	Time (h)	Ligand	Loading M/A	Conversion M/A (%) ^a	Ratio M/A ^a	Mn ^b (g/mol)	Mn ^c (g/mol)	D ^c
1	65	6	dNbpy	50/50	61/62	61/39	18 800	12 630	5.97
2	65	20	dNbpy	50/50	93/93	66/34	28 400	11 720	2.87
3	50	6	dNbpy	50/50	65/58	68/32	19 000	-	-
4	50	6	bpy	50/50	44/44	66/34	13 420	-	-
5	50	6	bpy	25/75	35/20	55/45	8 500	5 730	1.52

^a Calculated from $^1\text{H-NMR}$ ^b with $M_{n, \text{calc}} = M_{\text{eBiB}} + p_{\text{MEMA}} \times M_0_{\text{MEMA}} \times \text{DP}_{\text{target(MEMA)}} + p_{\text{AZMA}} \times M_0_{\text{AZMA}} \times \text{DP}_{\text{target(AZMA)}}$. ^c Obtained from SEC-MALS analysis. M/A means MEMA/AZMA.

The conversion and ratio of the copolymers are calculated by NMR. **Figure 57** shows an example of the $^1\text{H-NMR}$ mixture during copolymerization for the calculation of ratio and conversion of polymers. The conversion is calculated by comparing the peaks of monomers to polymers, as explained in **section 3.1**. Since the monomers are very alike and many peaks appear in the same region, the easiest way to calculate the conversion and ratio of polymers is by using the peaks in the region of 3.9 to 4.4 ppm (magnified region in **Figure 57**). Therefore, the conversion of MEMA is obtained with $\text{Conv}_{\text{MEMA}} = \frac{\text{Integral Hi}}{\text{Integral Hi} + \text{integral H4}}$. The same is applied for AZMA, with $\text{Conv}_{\text{AZMA}} = \frac{\text{Integral Hc}}{\text{Integral Hc} + \text{integral H10}}$.

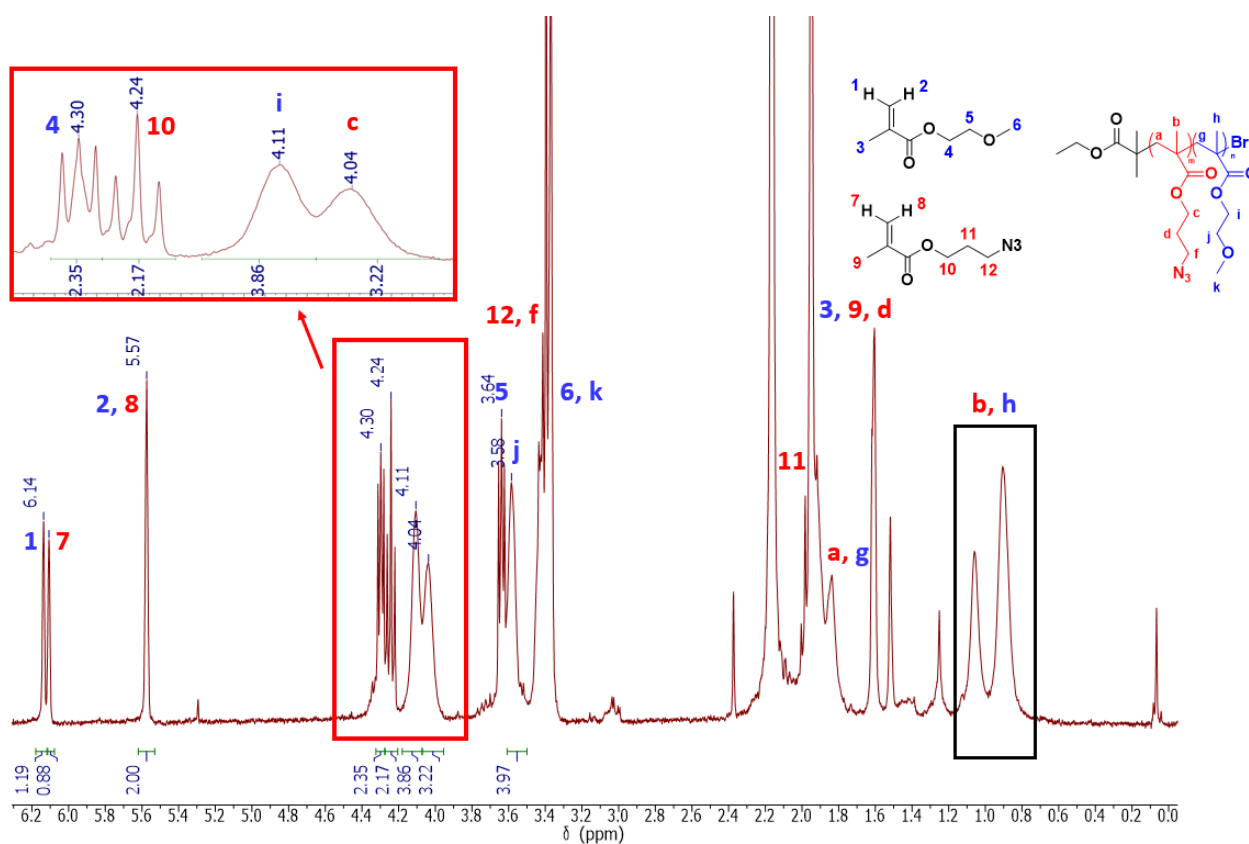


Figure 57: $^1\text{H-NMR}$ of the reaction mixture of the copolymerization of MEMA/AZMA 50/50 after 6h, and its corresponding peaks for the monomers and copolymer. Inset shows a higher magnification of the region between 3.9 to 4.4 ppm, the region used for the calculation of conversion and ratio of polymers.

The ratio of copolymers is calculated by the difference of the integral of the polymer MEMA at 3.6 ppm to the integral of both MEMA and AZMA from 4 – 4.2 ppm. Then, the same is done for AZMA.

$$\text{Ratio}_{\text{PMEMA}} = \frac{\text{Integral } H_{i(\text{PMEMA})}}{(\text{Integral } H_{i(\text{PMEMA})} + \text{Integral } H_{c(\text{PAZMA})})} = \frac{3.86}{7.08} = 0.54.$$

With right conditions, *i.e.* meaning extremely pure reagents and correct degassing of liquids, it was possible to obtain copolymers with better control, although some were still with somewhat large dispersities (around 1.6, for instance). As observed in **Table 16**, the composition obtained by NMR of the copolymers agrees with the initial comonomer feed. The copolymerization of MEMA/AZMA in a 50/50 initial feed was performed at 50 and 65 °C. The kinetics of the copolymerization at 65 °C is faster, with a conversion of the monomers of around 62 to 65%, compared to 47 – 48% at 50 °C; however, the obtained M_n provided by SEC is much higher than expected. In all cases, the copolymerization reaction is indeed less controlled than the homopolymerization of MEMA, with experimental M_n values systematically higher than the theoretical M_n data. This can be explained by a possible side chain reaction of the azide function, giving rise to a wider distribution of molar masses, corroborating with the increased dispersity of the synthesized copolymers.

In the case of entry 2 of the **Table 16**, a difference in the shape of the SEC chromatogram of a replicate from the same precipitated copolymer was observed (**Figure 58**). The other replicates for other synthesized copolymers did not show difference in the curve shape and SEC-MALS results. This could indicate a lack of homogeneity of the prepared copolymers containing high amounts of AZMA comonomer, most probably due to the interaction of its reactive azide group forming branched and/or reticulated copolymers.

Table 16: Results of copolymerization of ([MEMA]:[AZMA]:[CuBr]:[bpy]:[eBib]) X:200-X:1:2:1 in acetone/DPE (5%), with envisioned DP of 200, during 6h.

Entry	T (°C)	Loading M/A	Conversion M/A (%) ^a	Ratio M/A (%) ^a	M_n ^a (g/mol)	M_n ^c (g/mol)	\mathbf{D}^c
1	65	50/50	62/65	54/46	19 600	32 800	1.31
2a	50	50/50	48/47	54/46	13 700	12 800	1.39
2b	-	-	-	-	-	18 700	1.42
3	50	70/30	52/52	66/33	15 600	27 500	1.43

^a Calculated from ¹H-NMR ^b with $M_{n \text{ calc}} = M_{\text{eBib}} + p_{\text{MEMA}} \times M_0_{\text{MEMA}} \times \text{DP}_{\text{target(MEMA)}} + p_{\text{AZMA}} \times M_0_{\text{AZMA}} \times \text{DP}_{\text{target(AZMA)}}$. ^c Obtained from SEC-MALS analysis. M/A means MEMA/AZMA.

Previously, E. Bakangura *et al.*^{8b} have demonstrated that catalysts supported on copolymers of MEMA and AZMA that has higher AZMA proportion gives better catalytic

results, probably due to better bimetallic cooperation obtained with a polymer matrix denser in catalytic sites. Therefore, feeds higher than 30% of AZMA were preferred in this thesis.

SEC profiles (**Figure 58**) of the copolymers presented in **Table 16** were unimodal, assessing the efficiency of the copolymerization versus homopolymerization.

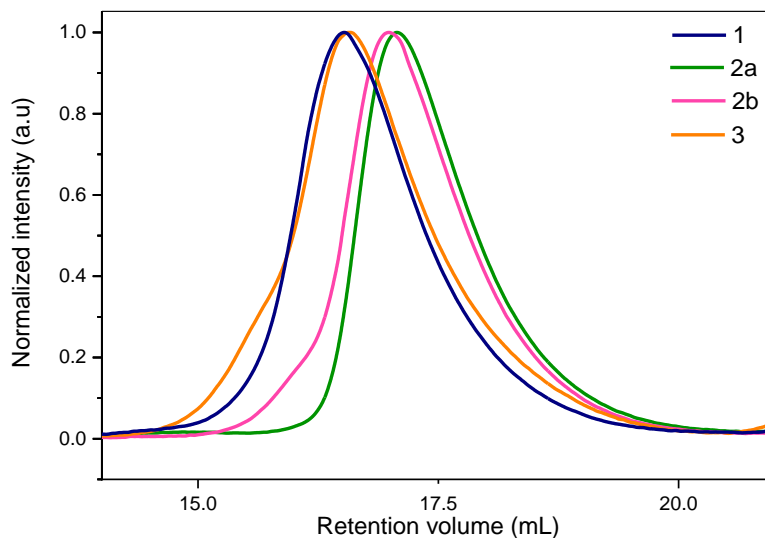


Figure 58: SEC chromatograms of MEMA/AZMA copolymer obtained by classical ATRP. Entries from **Table 16**.

No copolymers with higher ratio of AZMA (> 50%) was obtained in a sufficient controlled dispersity using classical ATRP and optimized conditions.

As the copolymers will be used for further post-modification either in bulk or after being grown from surface (“grafting-from” methodology), other characterization techniques are important to access the chemical modifications after post-functionalization.

The chemical composition of the synthesized copolymer can be assessed by ATR-FTIR spectroscopy in the range of 3500 to 600 cm^{-1} (**Figure 59**). Mainly, the bands at 2950 and 2900 cm^{-1} are associated with the stretching vibration modes of the CH_2 from aliphatic moieties. A strong azide stretching mode is observed at 2100 cm^{-1} , and the $\text{C}=\text{O}$ stretching mode is observed at 1725 cm^{-1} and $\text{C}-\text{O}$ at 1130 cm^{-1} . The azide peak is the most important peak to be observed in the copolymers since it is the function which will be modified after click reaction, making it possible to follow and assess the modified copolymers. The fingerprint region is harder to analyze, but has bands related to the carbon backbone structure of the copolymers.

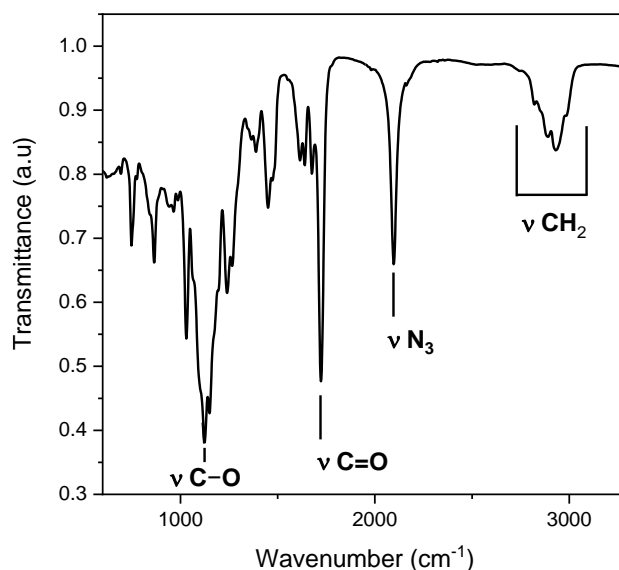


Figure 59: ATR-FTIR spectrum of the copolymer of MEMA/AZMA with an initial feed of 50/50 (entry 2 of **Table 16**)

XPS can also give important information regarding the synthesized copolymers. **Figure 60** shows the N1s and C1s region for the copolymer of MEMA/AZMA with an initial feed of 50/50 (entry 2 of **Table 16**). For N1s, the expected ratio of $\text{N}=\underline{\text{N}}=\text{N}/\underline{\text{N}}=\text{N}=\underline{\text{N}}$ is 0.5 if we consider that the $\text{C}-\underline{\text{N}}=\text{N}=\text{N}$ has its most contribution as $\underline{\text{N}}=\text{N}=\underline{\text{N}}$. The obtained ratio is of 0.45, a very proximate value of those expected. We also observe a small contribution of C–N at 398.5 eV which could be formed from the azide exposure with the electron beam during XPS analysis. This interaction is further discussed in the next section. Whereas for the C1s, there are 8 C–C, 2 C=O and 4 C–O expected for the copolymer if disregarding the initiator contribution. Therefore, the expected ratio of C=O/C–C and C=O/C–O is 0.25 and 0.5 respectively. The obtained ratio C=O/C–C is 0.2 which is in good agreement with the expected ones. Nevertheless, the obtained value for C=O/C–O is 0.34, showing a higher contribution of C–O than expected. Since the MEMA comonomer has more C–O than AZMA comonomer (3 vs 1, respectively), it could be hypothesized that the higher ratio of MEMA comonomer in the copolymer results in a higher contribution of C–O. This higher ratio of MEMA is confirmed by NMR (**Table 16**).

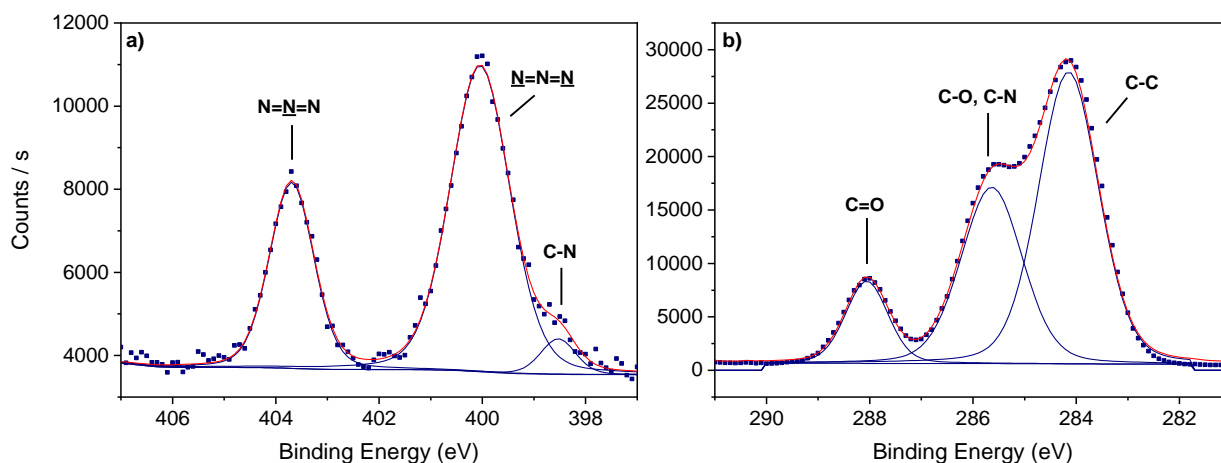


Figure 60: N1s (a) and C1s (b) XPS spectra for copolymer of MEMA/AZMA in a 50/50 initial feed (entry 2 of **Table 16**). N1s region: peak $\text{N}=\text{N}=\text{N}$ at 403.7 eV and $\text{N}=\text{N}=\text{N}$ at 400 eV and C-N at 398.5 eV. C1s region: peak C-C at 284 eV, C-O at 285.6 and C=O at 289 eV.

The Br3d region was also analyzed (**Figure 100** in **Appendix B**) and it is present with around 0.2 atomic percentage in the sample, showing that the atom is still preserved and further polymerization with these copolymers could also be possible.

3.5. Copolymerization of MEMA/AZMA on surface

3.5.1. In the case of a crystalline silicon surface

The copolymerization of MEMA and AZMA on surface has been performed using the optimized conditions found in solution with no addition of sacrificial initiator, and with special attention to the use of purified AZMA. At the end of the reaction, the modified prism was cleaned with conventional techniques and further with Soxhlet purification.

The general conditions were $[\text{MEMA}]_0:[\text{AZMA}]_0:[\text{CuBr}]_0:[\text{CuBr}_2]_0:[\text{bpy}]_0 = \text{X}:200\text{-X}:1:0.05:2$. The ATR-FTIR spectra of the copolymers on surface in a ratio of MEMA/AZMA of 90/10, 70/30 and 50/50 initial feed are shown in **Figure 61**, which are named SiBr1-Copo1, SiBr1-Copo2, and SiBr1-Copo3, respectively. The reference spectrum for each case is their grafted surface before polymerization. The C=O stretching mode at 1730 cm^{-1} and the azide stretching mode at 2100 cm^{-1} are observed, besides the C-O stretching mode at 1130 cm^{-1} .

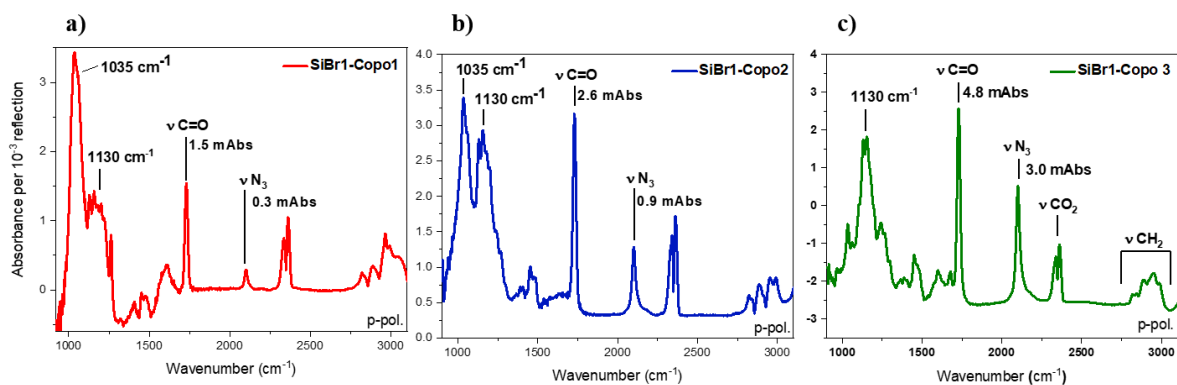


Figure 61: ATR-FTIR spectrum of the copolymers on surface using [MEMA]:[AZMA]:[CuBr]:[CuBr₂]:[bpy] = X:200-X:1:0.05:2 in acetone and DPE (5%) for 6h at 50 °C where a) SiBr1-Copo 1 with X = 180 b) SiBr1-Copo2 with X = 140 and c) SiBr1-Copo 3 with X = 100. For all cases, the reference spectrum is of their grafted surface before polymerization.

However, a level of surface oxidation is present in the case of SiBr1-Copo1 and SiBr1-Copo2 as unveiled on the IR spectrum with a peak at around 1035 cm⁻¹ corresponding to the silicon oxide vibrations. This peak is stronger as the density of comonomer units are lower (**Table 17**), thus suggesting that the polymerization suffered from oxidation, hindering the growth of thicker copolymer chains in the case of SiBr1-Copo1 and SiBr1-Copo2.

The ratio between the absorbance intensity of the azide (at 2100 cm⁻¹) in proportion to the carbonyl peak (at 1730 cm⁻¹) gives an increasing value from SiBr1-Copo1 to the SiBr1-Copo3 copolymers, with an azide ratio of 0.2 for SiBr1-Copo1, 0.34 for SiBr1-Copo2 and 0.62 for SiBr1-Copo3. These ratios give an overview of the comonomers proportions on surface; however, it is only an estimation since the absorption cross-section of the azide stretching modes and the carbonyl stretching modes are not necessarily the same.

A better quantification of the comonomers proportion is possible through the quantification of polymer chains considering the azide peak (from AZMA) or the carbonyl peak (from MEMA). An IR calibration for AZMA monomer was performed (see **Appendix C** for further information) by recording the spectra of different known concentrations of AZMA in CDCl₃. These spectra were treated using the oxidized SiO_x surface spectrum as a reference to obtain the peaks associated to AZMA. The N₃ azide band at 2100 cm⁻¹ was integrated from 2051 – 2179 cm⁻¹ for *s*-polarization and a linear baseline was adjusted between the extremities. The integration values were taken as a quantitative reference of the absorption of the stretching

vibration mode N_3 to build the regression line which the slope $\frac{\text{Abs}_s^0}{C}$ is 1.17 for the calibration of AZMA.

Then, it is possible to correlate the integrations in both *s*- and *p*-polarizations of the polymer brushes with the obtained slope to obtain the polymer density in terms of C=O or N_3 stretching bands. **Table 17** shows the total number *N* of monomer units on three surfaces studied, using both the νCO and νN_3 . Finally, the ratio determined for the copolymers on surface are 0.22 for SiBr1-Copo1, 0.33 for SiBr1-Copo2 and 0.56 for SiBr1-Copo3. These values are similar to those found by calculating the ratio of the stretching intensities of the peaks because the absorption cross-section of both functional groups is close to each other. For the copolymer 90/10, a higher insertion of AZMA is observed in the comonomer composition than expected; however, the other two copolymers respect the initial loading.

Table 17: Density of molecules from νCO and from νN_3 in nm^{-2} in the copolymers on surface. M/A means MEMA/AZMA.

Type of surface	Initial loading (M/A)	σ of monomer units (νCO , nm^{-2})	σ of monomer units (νN_3 , nm^{-2})	Ratio of σ $N_3/\text{C=O}$ (%)
SiBr1-Copo1	90/10	6.06	1.30	22
SiBr1-Copo2	70/30	8.62	2.81	33
SiBr1-Copo3	50/50	16.28	9.08	56

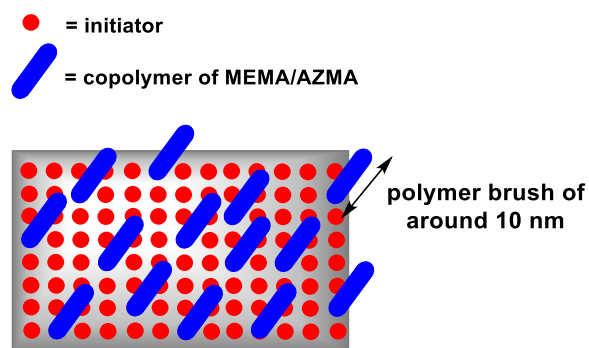
For SiBr1-Copo3, which is the scenario of great interest of this thesis as it has higher AZMA content – and therefore higher catalyst loading/g of copolymer – the polymer brushes thickness of ~ 9 nm was measured by ellipsometry using 1.6 as refractive index. After subtracting the thickness of SiBr1 (initiated surface of around 1.8 nm), a thickness of 7.1 nm is obtained (**Table 18**). The degree of polymerization (DP) obtained by the scaling law, as shown in **section 3.2**, provides a similar value of ~ 150 , similar to those obtained for the polymer brushes of PMEMA. The calculated SiBr1 density for this surface is of 0.72 nm^{-2} . The density of monomer units per active site is obtained with a value of 0.1 nm^{-2} . Finally, the percentage of active sites (15%) for the copolymerization of MEMA/AZMA on this surface also gives similar values than the ones presented for the homopolymerization of MEMA on surface from the same initiated surface. These results are summarized below.

Table 18: Calculated DP from the scaling law, the density of molecules for each copolymer chain and the % of initiator active sites.

Type of surface	L ^a	L/a	DP	SiBr1 density	σ for 1 polymer chain (nm ⁻²) ^b	% of active sites
SiBr1- Copo3	7.1	28.5	152	0.72	0.1	15

^a Thickness value from ellipsometry minus the thickness of initiator given by XPS (1.77 nm).^b obtained by dividing the total density of comonomer units (16.3 nm⁻²) by the obtained DP (157).

Figure 62 shows a schematic representation of the obtained polymer brushes on surface. The silicon surface has a quantity of initiating molecules grafted on surface that 15% are active, in this particular case. From these active sites, statistical copolymers of MEMA/AZMA with a DP of ~ 150 and a thickness of around 10 nm in dry stated were grown.

**Figure 62:** Schematic representation of the polymer brushes on surface.

3.5.2. X-ray photoelectron spectroscopy

To study the polymer structure on surface, the SiBr1-Copo3 was analyzed by XPS. The 50/50 ratio copolymer backbone should include 8 C–C, 2 C=O, 4 C–O, 2 $\underline{\text{N}}=\text{N}=\underline{\text{N}}$ and 1 $\text{N}=\underline{\text{N}}=\text{N}$ (disregarding the initiator molecules). Therefore, when analyzing the ratios of C=O/C–O, C=O/C–C, C=O/N= $\underline{\text{N}}=\underline{\text{N}}$ and $\underline{\text{N}}=\text{N}=\underline{\text{N}}/\text{N}=\underline{\text{N}}=\text{N}$, values of 0.5, 0.25, 2 and 2, respectively, are expected. In the N1s spectra, the nitrogen $\underline{\text{N}}=\text{N}=\underline{\text{N}}$ were fitted in the same peak, as the difference in binding energy is small. **Figure 63** shows the fits for the N1s and C1s core levels. The experimental ratios give approximate values with 0.34, 0.23, 2.5 and 2.2 for C=O/C–O, C=O/C–C, C=O/N= $\underline{\text{N}}=\underline{\text{N}}$ and $\underline{\text{N}}=\text{N}=\underline{\text{N}}/\text{N}=\underline{\text{N}}=\text{N}$ respectively, demonstrating a good correlation between the expected and obtained copolymer structure on surface.

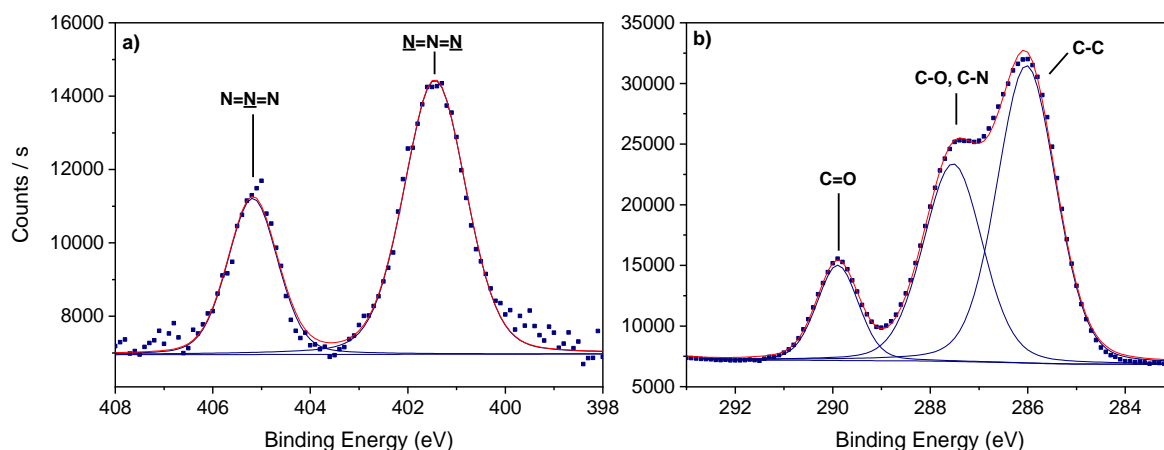


Figure 63: N1s (a) and C1s (b) XPS peaks for SiBr1-Copo3. N1s region: peak $\text{N}=\underline{\text{N}}=\text{N}$ at 405.2 eV and $\underline{\text{N}}=\text{N}=\underline{\text{N}}$ at 401.4 eV. C1s region: peak C-C at 286 eV, C-O at 287.5 eV, C=O at 289.8 eV.

As the azide function is a very reactive group, it is important to observe their stability over time under electron beam. Thus, the N1s core level was analyzed during 2h40 min with over 149 spectra consisting of 4 scans each to evaluate the chemical stability of the N_3 function. **Figure 64** shows this iteration, and it is observed that the $\text{N}=\underline{\text{N}}=\text{N}$ peak at 405.2 eV transforms to the peak C-N at 400.6 eV over time, clearly demonstrating the low stability of the reactive N_3 group during the analysis. At iteration 1, a small peak for the C-N bond is already observed, probably indicating the rapid degradation of the functional group. At iteration 149, almost no $\text{N}=\underline{\text{N}}=\text{N}$ is observed, and therefore, the peak remaining at 401 eV can be attributed to quaternary nitrogen formed on surface.¹⁴⁵ Consequently, XPS measurements of the copolymers before and after post-modification should start with the N1s region in order to obtain correct atomic information of the structures.

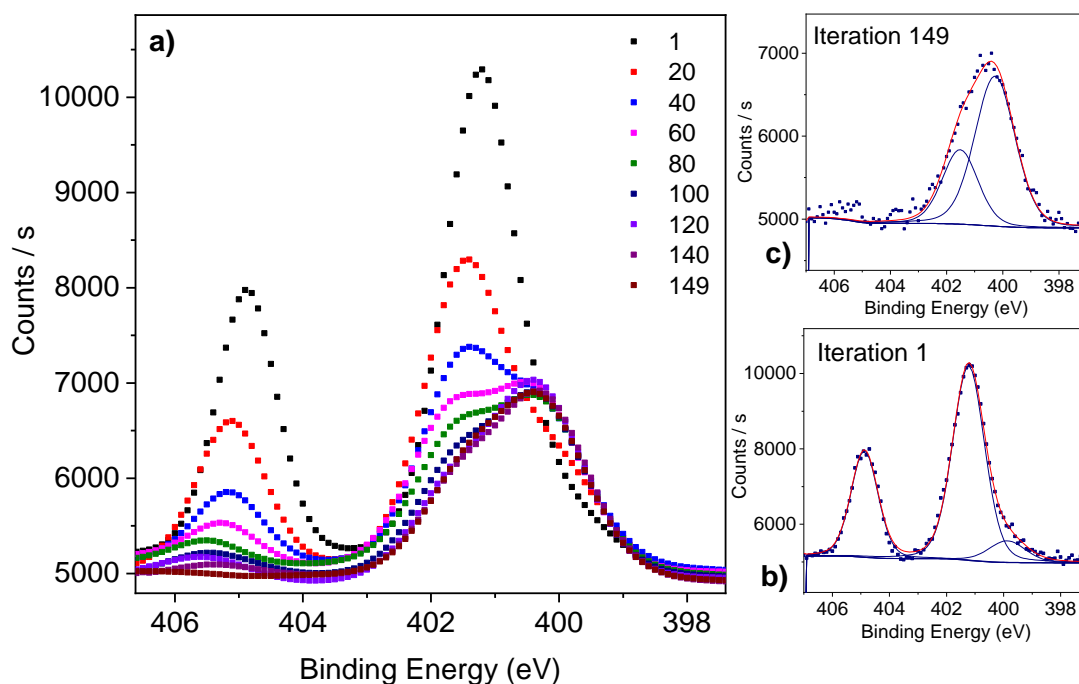


Figure 64: N1s core level iteration over time. a) N1s spectra at iterations numbers 1, 20, 40, 60, 80, 100, 120, 140 and 149 showing the evolution from N=N=N to C-N during the exposure of the surface to electrons. b) Fit for the iteration 1, and c) fit for the iteration 149.

3.5.3. In the case of a macroporous silicon surface

The final goal of this thesis is to develop supported catalysts on surface of silicon to undergo either monocatalysis at a first glance, and then multi-catalysis in a further step. As explained in **Chapter 2**, crystalline silicon is not an ideal surface for this application since its crystalline structure has a definite area that is not enough large when discussing catalysis. Nevertheless, macroporous silicon presents a significantly more compelling substrate because its higher surface area can accommodate more polymers and catalysts. The crystalline silicon is used as a model structure, since the characterization analysis in this substrate has already been well-developed.

Figure 65 shows the grafted surface using initiator 1 in the conditions exposed in **Chapter 2 (section 2.7)**, and the copolymerized surface using the same conditions as SiBr1-Copo3 in **section 3.5.1**. The mAbs of the azide peak (2100 cm^{-1}) is around 77 mAbs, more intense than observed for the case of crystalline silicon (about 3.0 mAbs).

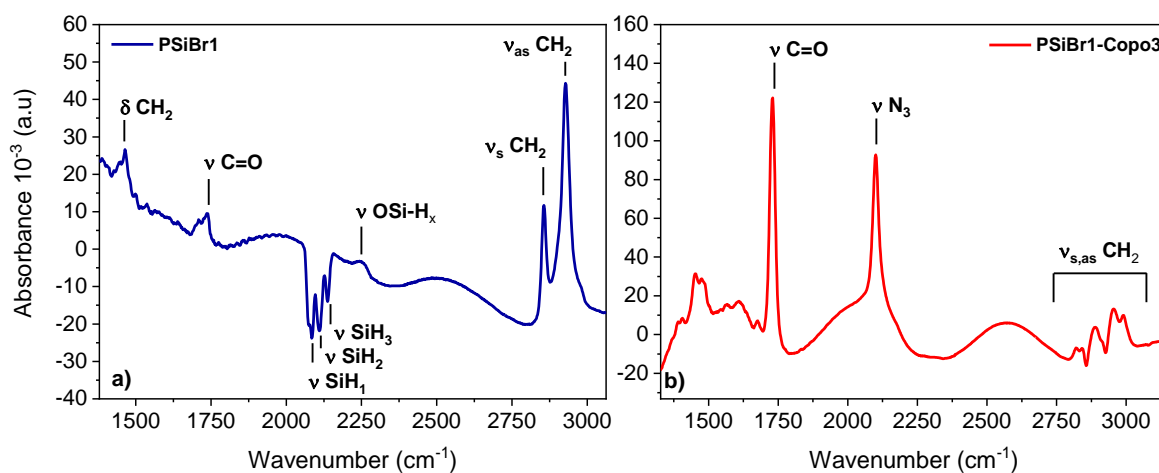


Figure 65: Macroporous-Si(100) with pore size of 150 – 275 nm and pore thickness of 7.5 μ m. FTIR spectra of a) grafted surface using initiator 1 from a SiH_x surface, b) polymerized surface using the following condition [MEMA]₀:[AZMA]₀:[CuBr]₀:[CuBr₂]₀:[bpy]₀ = 100:100:1:0.05:2, plus initiated surface in acetone/DPE (5%) at 50 °C, 6 h in argon atmosphere.

Similar to the previous XPS spectra for SiBr1-Copo3, PSiBr1-Copo3 has also the same main contributions, as expected. In the N1s region (**Figure 66a**), the N=N=N contribution is seen at 405.2 eV and N=N=N at 401.7 eV. The peak at 400.3 eV is attributed to C-N, which is formed during analysis, once more demonstrating the low stability of the azide group under beam of electrons. The C1s region is shown in **Figure 66b** and shows the main contributions: C-C at 286 eV, C-O at 287.5 eV, C=O at 289.9 eV.

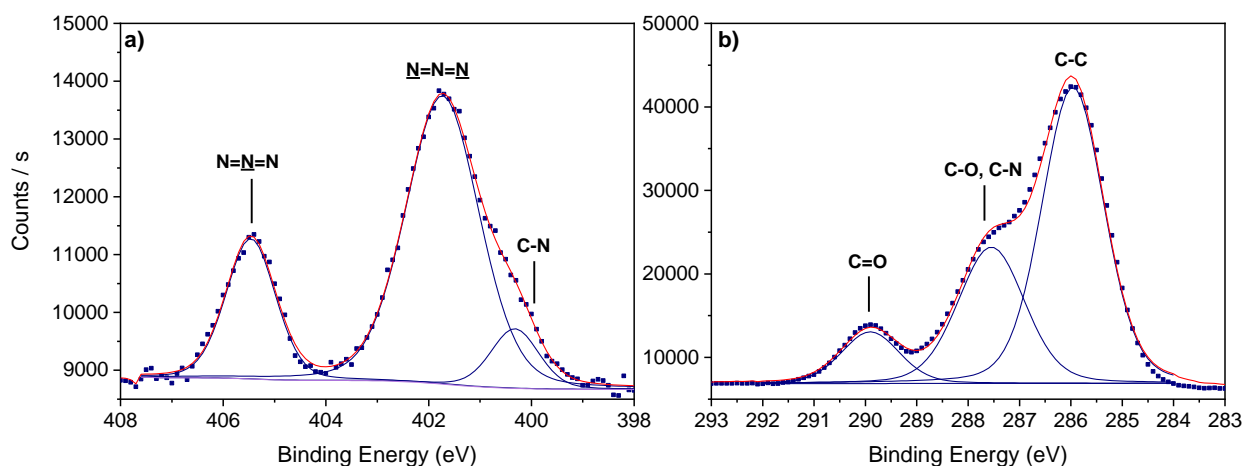


Figure 66: N1s (a) and C1s (b) XPS peaks for PSiBr1-Copo3. C1s region: peak C-C at 286 eV, C-O at 287.5 eV, C=O at 289.9 eV. N1s region: peak N=N=N at 405.2 eV and N=N=N at 401.7 eV.

The macroporous silicon used in this study have thin pore depth of 7.5 μm and its estimated surface area is approximately 10 to 20 m^2/g considering a pore size of around 200 nm (250 nm near the surface and 150 at the interface).¹⁴⁶ Therefore, its surface area is still small for detecting differences in mass by using thermogravimetric analysis (TGA) or gas adsorption in the pores by using Brunauer-Emmett-Teller (BET) analysis, which makes its quantitative analysis quite complicated.

In fact, considering a pore thickness of around 7.5 μm , the real volume of the macroporous silicon sample in 1 cm^2 can be estimated with the formula (1):

$$v = e \times 1 \text{ cm}^2 \quad (1)$$

Where e is the pore depth, a volume of $7.5 \times 10^{-4} \text{ cm}^3$ is obtained. Then, considering the silicon density (ρ) of 2.3 g/cm^3 , the corresponding mass of silicon related to the real volume is obtained with:

$$m = v \times (1 - p) \times \rho \quad (2)$$

Where p is the porosity of the porous layer ($\sim 70\%$). Therefore, the corresponding mass is $\sim 5.2 \times 10^{-4} \text{ g}$. Then, by multiplying this value by the approximate average pore size of 15 g/m^2 , the real area of the macroporous silicon is 78 cm^2 for every 1 cm^2 of crystalline silicon. Therefore, an increase of around 80 times in area compared to crystalline silicon is obtained using macroporous silicon.

Nevertheless, it is important to quantify the density of azide units in the copolymer structure on surface in order to calculate the number of moles of salen complex to be engaged in the click reaction, and later, to calculate the right amounts of reagents in the catalysis trials. Therefore, the same correlation between the mAbs and the density of molecules as seen in **section 3.3** can be performed to quantify the approximate density of comonomer units on surface. Using the mAbs of νN_3 shown in **Figure 65b** and the density of νN_3 shown in **Table 17** for the case of crystalline silicon, a slope of ~ 3 is obtained for the linear regression obtained for the correlation of molecules/ nm^2 to mAbs (**Table 30, Appendix B**). Thus, using the same procedure as **section 3.3**, a value of 460 monomer units of AZMA / nm^2 is estimated.

3.6. Supplemental activator and reducing agent (SARA) polymerization

This part has been inspired by the article by [Rafaela Bechara](#), Philippe Roger, Mohamed Mellah, Nadine Barroca-Aubry, François Ozanam, Anne-Chantal Gouget-Laemmel, Emmanuelle Schulz. Development of multipurpose supported asymmetric salen catalysts by SARA copolymerization. Manuscript in preparation.

It has been shown in this chapter the difficulty of inserting AZMA into the MEMA/AZMA copolymer matrix by classical ATRP. No copolymers with higher AZMA content were obtained using classical ATRP with good dispersities. It was often seen as well that for an envisioned loading of 50/50 copolymer, usually it has 60/40 MEMA/AZMA content in the end showing the lower kinetics of AZMA in relation to MEMA.^{8b} In order to bypass this difficulty, a type of Reversible Deactivation Radical Polymerization (RDRP), called supplemental activator and reducing agent (SARA) polymerization was employed. It consists in a strictly simpler and faster procedure, with less complicated degassing of liquids, and use of lower quantities of copper.

3.6.1. Influence of zero valent copper

Before copolymerization trials, first the influence of the amount of zero valent copper was observed for the homopolymerization of MEMA. The amount of zero valent copper also contributes to the kinetics of zero valent-mediated RDRP.¹⁴⁷ **Figure 67** shows the dependence of the polymerization kinetics on the Cu(0) wire length (1 and 2 cm). Under the same reaction conditions, the variation of Cu(0) wire length mildly affects the kinetics of the polymerization with an increase of the apparent kinetic rate (k_{app}) from 0.31 h^{-1} to 0.45 h^{-1} when using the 2 cm wire copper.

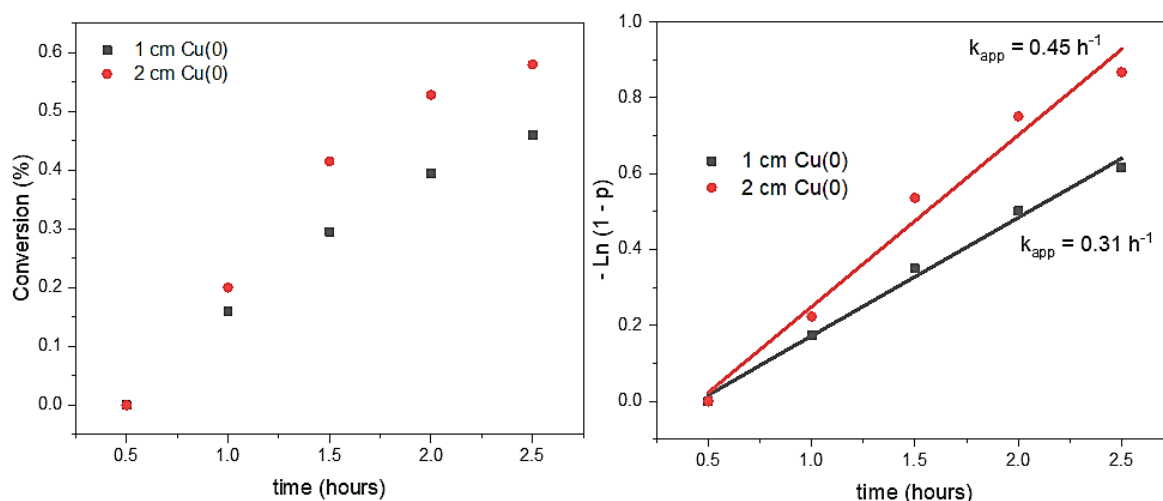
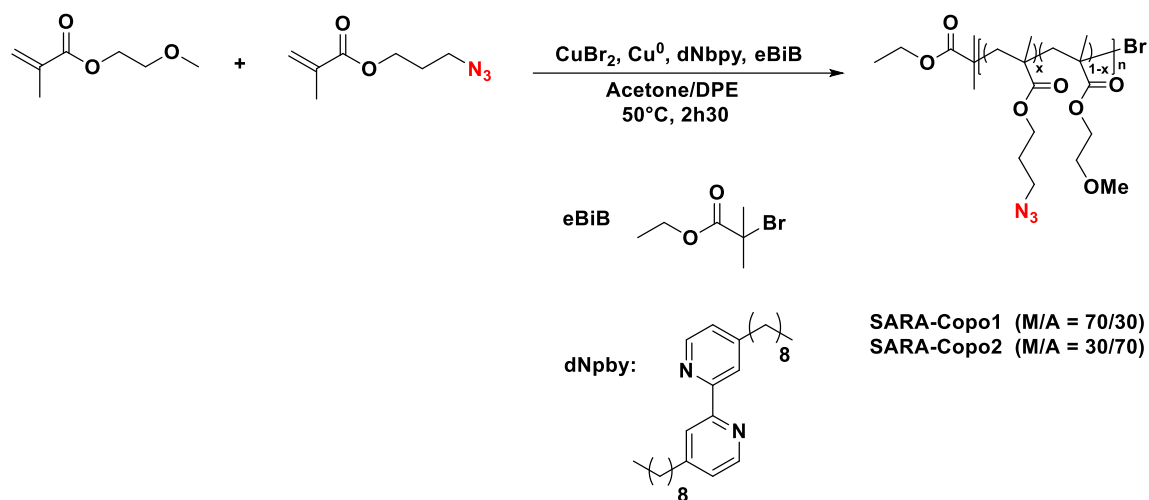


Figure 67: Kinetics of Cu(0)-mediated SARA ATRP of MEMA with varying Cu(0)-length between 1 and 2 cm. Polymerization conditions: $[\text{MEMA}]_0:[\text{CuBr}_2]_0:[\text{dNbpy}]_0:[\text{eBiB}]_0 = 200:0.1:0.4:1$, $T = 50\text{ }^\circ\text{C}$, in acetone.

The induction period – time for the polymerization reaction to start – is not greatly affected by the wire length of Cu(0) with both cases having an induction of around 30 min. The SEC analysis of the obtained polymers showed a narrower dispersity in the case of 2 cm wire Cu(0) giving a value of 1.28 vs. 1.95 for 1 cm Cu(0). Therefore, 2 cm wire Cu(0) was chosen for the following experiments.

3.6.2. Copolymerization of MEMA/AZMA and kinetics of Cu(0)-mediated SARA ATRP

The copolymerization conditions found for the successful synthesis of copolymers of MEMA and AZMA using Cu(0)-mediated SARA ATRP includes acetone/DPE (50:5 %v/v considering total volume of reaction) as solvent, dNbpy as ligand, eBiB as initiator and 2 cm of Cu(0) wire and $[\text{MEMA}]_0:[\text{AZMA}]_0:[\text{CuBr}_2]_0:[\text{dNbpy}]_0:[\text{eBiB}]_0 = X:200-X:0.1:0.4:1$, $T = 50\text{ }^\circ\text{C}$ during 2.5 hours (**Scheme 31**). The ligand dNbpy was preferred for this study because it was shown to yield polymers with better dispersities compared to bpy, as demonstrated by Nguyen and coworkers.¹⁴⁸



Scheme 31: Reactions conditions for the SARA ATRP of MEMA and AZMA, M/A means MEMA/AZMA.

The copolymers containing higher amount of AZMA were successfully synthesized, and therefore, two copolymers with two contrasting compositions, one having 30% of AZMA and the other containing 70% were studied. These copolymers will later be post-functionalized and engaged in catalysis trials to act as multipurpose catalysts, and thus, contrasting loads of AZMA is an interesting manner of evaluate the catalysts efficiency.

The conversion of the monomers was checked by $^1\text{H-NMR}$ and ranged up to 52 to 60%. The semilogarithmic kinetic plot for both polymerization reaction is shown in **Figure 68**. In both cases, the kinetics of the monomers are similar ranging from 0.34 to 0.46 h^{-1} . The copolymers were analyzed by SEC-MALS in THF.

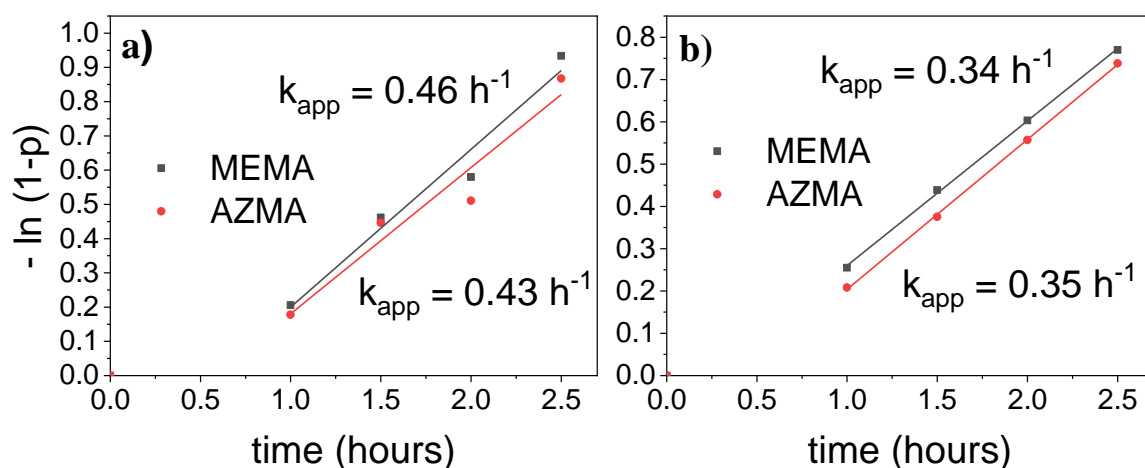


Figure 68: Semilogarithmic kinetic plot for the copolymers of MEMA/AZMA in a loading of a) 70/30 and b) 30/70 using SARA ATRP in the proportion of $[\text{monomers}]_0/[\text{eBiB}]_0/[\text{dNpby}]_0/[\text{CuBr}_2]_0 = 200/1/0.4/0.1$ at 50 °C for 2h30.

Table 19 shows the calculated and experimental molar masses of the copolymers. For simplification, the copolymer of MEMA/AZMA in a 70/30 loading is called SARA-Copo1 and the copolymer in a 30/70 loading is called SARA-Copo2. The dispersity of SARA-Copo1 ($\mathcal{D} = 1.32$) is lower than that of SARA-Copo2 ($\mathcal{D} = 1.54$), as expected since the increase in AZMA content showed an increase of the dispersity of the copolymers in solution.^{8b} eBiB is a widely used initiator for Cu(0)-mediated RDRP, and although this initiator provides good conversion for the MEMA and AZMA monomers, the obtained dispersity remained relatively high ($\mathcal{D} = 1.3 - 1.5$). A higher experimental M_n value than the calculated one was also observed, which was attributed to the lower initiation rate of eBiB.¹⁴⁸ However, this has no impact on the final application of the copolymers, making this SARA ATRP a very attractive technique for the development of supported catalysts.

Table 19: Calculated molar mass and SEC-MALS data for the obtained copolymers by SARA copolymerization.

Sample	Conversion M/A (%) ^a	Ratio M/A (%) ^a	M_n^b (g/mol)	$M_{n\text{SEC}}^c$ (g/mol)	\mathcal{D}^c
SARA-Copo1	61/58	70/30	18 220	35 340	1.32
SARA-Copo2	54/52	33/67	16 900	41 500	1.54

^a Calculated from ¹H-NMR b) with $M_{n\text{calc}} = M_{\text{eBiB}} + p_{\text{MEMA}} \times M_0_{\text{MEMA}} \times \text{DP}_{\text{target(MEMA)}} + p_{\text{AZMA}} \times M_0_{\text{AZMA}} \times \text{DP}_{\text{target(AZMA)}}$. ^b Obtained from SEC-MALS analysis. M/A means MEMA/AZMA.

The broader molar mass distribution of SARA-Copo2 is compared to the narrower molar mass distributions of SARA-Copo1, as observed by the SEC profiles in **Figure 69**. The SEC profiles of both copolymers were unimodal, validating the efficiency of the copolymerization versus homopolymerization.

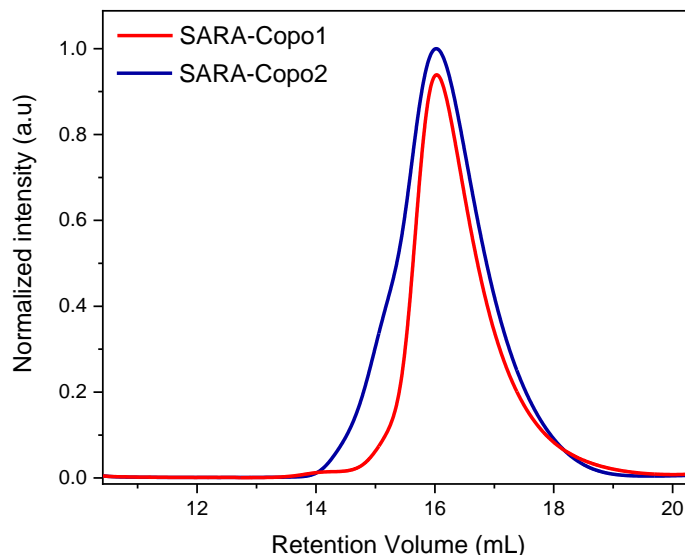


Figure 69: Evolution of SEC profiles of copolymers obtained by SARA copolymerization, entries from **Table 19**.

3.6.3. Influence of the temperature

SARA ATRP aims to overcome some limitations in classical ATRP, such as slow polymerization rates or strict reaction conditions. It can be conducted under milder conditions, such as at room temperature. This is particularly interesting because it offers advantages such as reduced energy consumption and stability for temperature-sensitive monomers. There are few examples in the literature of successful polymerization of acrylates and/or methacrylates at room temperature.^{58, 149} Thus, the copolymerization of MEMA/AZMA was tested at room temperature with the aim of narrowing the monodispersity of the copolymers.

Table 20 shows some examples of the copolymers at room temperature. The kinetics is much lower, with a conversion of around 50% after 6 hours of reaction. The induction period is higher than observed at 50 °C, with the start of polymerization (observed by the change of color of the solution from green to amber) after 1h30 approximately. The obtained polymers have roughly the same dispersity than those obtained at 50 °C even when using lower amounts of AZMA in the reaction initial feed. Therefore, performing the SARA copolymerization at 50 °C is more advantageous: a faster kinetics, and the average dispersity still remaining around

1.5. Thus, the best reactions conditions for the SARA ATRP of MEMA/AZMA is the one presented in **section 3.6.2**, meaning $[\text{monomers}]_0/[\text{eBiB}]_0/[\text{dNpby}]_0/[\text{CuBr}_2]_0 = 200/1/0.4/0.1$ at 50 °C for 2h30 using acetone and DPE (5%) as solvents.

Table 20: Calculated molar mass and SEC-MALS data for the obtained copolymers by SARA copolymerization at room temperature. Conditions for polymerization: $[\text{monomers}]_0/[\text{eBiB}]_0/[\text{dNpby}]_0/[\text{CuBr}_2]_0 = 200/1/0.4/0.1$ at r.t for 6h in acetone and DPE (5% v/v).

Trial	Loading M/A ^a	Conversion M/A (%) ^b	Ratio M/A (%) ^b	M _n (g/mol) ^c	M _n SEC (g/mol) ^d	Đ ^c
1	90/10	48/50	88/12	14 193	28 800	1.54
2	70/30	46/46	70/30	13 857	22 400	1.46

^a Initial loading ^b Calculated from ¹H-NMR ^c with $M_{n \text{ calc}} = M_{\text{eBiB}} + p_{\text{MEMA}} \times M_0_{\text{MEMA}} \times \text{DP}_{\text{target(MEMA)}} + p_{\text{AZMA}} \times M_0_{\text{AZMA}} \times \text{DP}_{\text{target(AZMA)}}$. ^d Obtained from SEC-MALS analysis. M/A means MEMA/AZMA.

The SEC chromatograms of the obtained copolymers are shown in **Figure 70**. Both are unimodal with Đ in the order of 1.5.

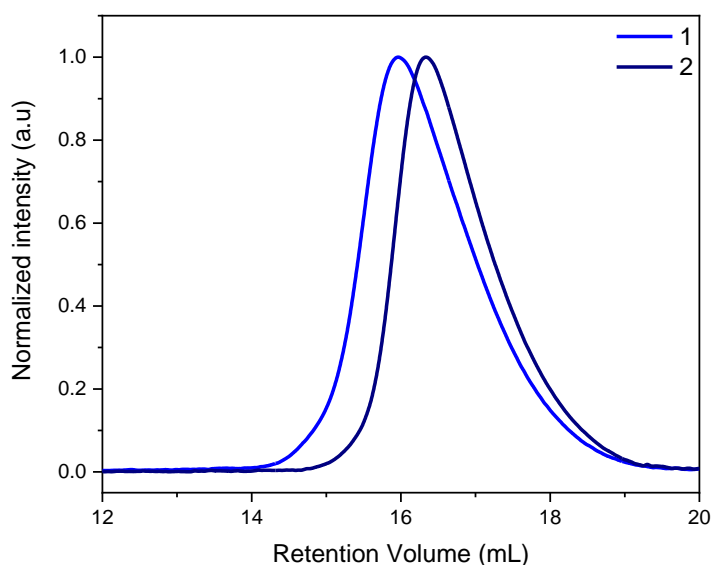


Figure 70: Evolution of SEC profiles of copolymers obtained by SARA copolymerization, entries from **Table 20**.

3.7. Developing more complex structures using SARA ATRP

The copolymers of MEMA/AZMA are the starting point of the development of supported catalysts with multi functions by clicking two, or more, different catalysts on them. However, more complex structures can be envisioned if yet another monomer is added to develop

copolymers with two functionalized monomer units and one diluting monomer, which remains MEMA. For the two functionalized monomers, the first is still AZMA, with the azide function that engages in click chemistry, and the second one could be, for instance, the (hydroxyethyl)methacrylate (HEMA).

In the last section of this chapter, the homopolymerization of HEMA, as well as the copolymerization of MEMA and HEMA, are discussed. Some preliminary copolymerization of MEMA/HEMA/AZMA were performed and more information about it is provided in the perspectives of this work at the end of this manuscript.

3.7.1. HEMA homopolymerization

Hydroxyethyl methacrylate is a well-known methacrylate, and its homopolymerization by ATRP has been already described.¹⁵⁰ Usually, the solvent used for the polymerization of HEMA are polar protic solvents such as alcohols.^{150b} However, since the optimized conditions of the copolymerization of MEMA/AZMA include already a polar mixture of solvents (acetone/DPE 5%), the homopolymerization of HEMA was first tested using this system. Using dNbpy as ligand and eBiB as initiator at r.t., the homopolymerization revealed a quick conversion of HEMA, as evidenced by a higher viscosity of the reaction media.

The ¹H-NMR spectrum showed 26% conversion after 1-hour reaction, thus, indicating that PHEMA has a low solubility in the acetone/DPE mixture. In addition, PHEMA is not well soluble in many common organic solvents, being only partially soluble in THF-d₈, which was the solvent used for the NMR analysis. The poor solubility of PHEMA in common organic solvents makes the SEC-MALS not possible. Another solvent, such as DMF, can be envisioned for the analysis of these types of polymers.

HEMA homopolymerization allows the assignment of the peaks of PHEMA in ¹H-NMR for later identification of each comonomer in the cases of copolymerization of HEMA/MEMA/AZMA. **Figure 71** shows this assignment for PHEMA.

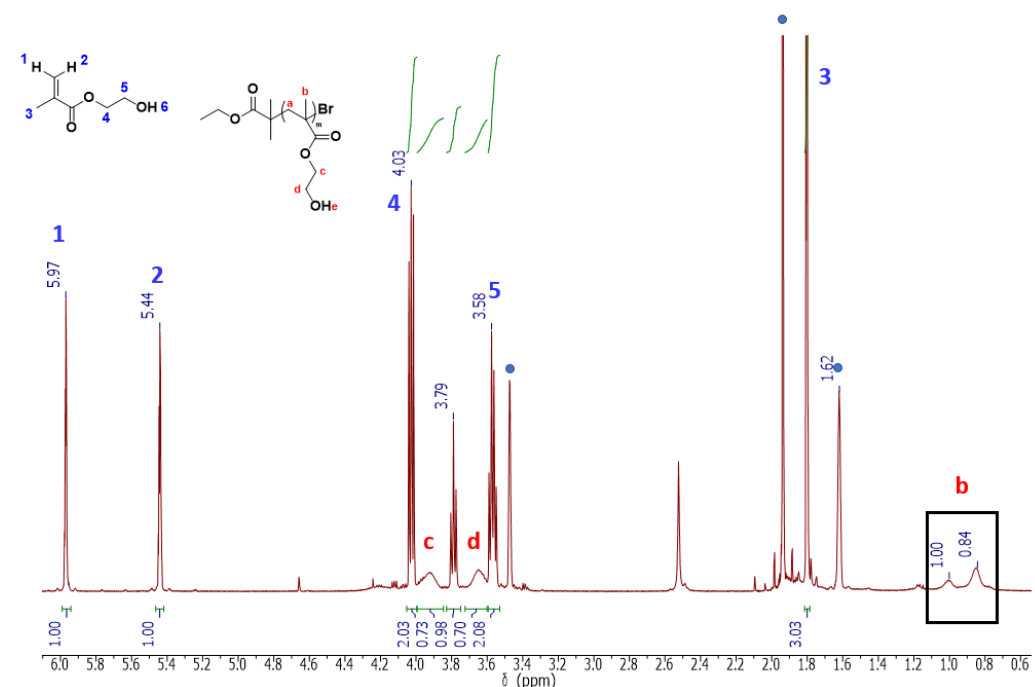
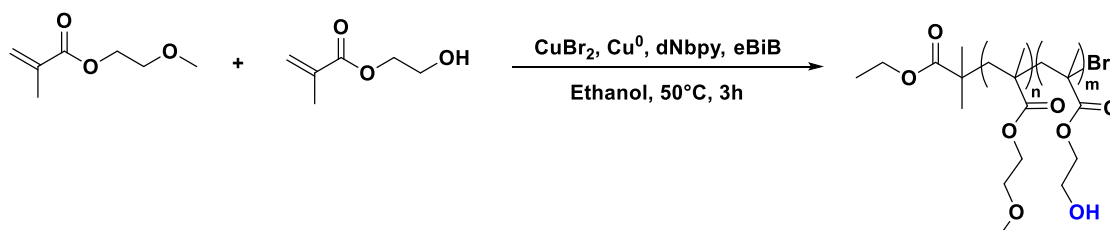


Figure 71: ^1H NMR of the reaction mixture of the polymerization of HEMA after 1h reaction in THF-d_8 . Conditions for polymerization: $[\text{HEMA}]_0:[\text{eBiB}]_0:[\text{dNbpy}]_0:[\text{CuBr}_2]_0 = 200:1:0.4:0.1$ at r.t for 1h in acetone and DPE (5% v/v). The blue circles are solvent peaks.

3.7.2. MEMA/HEMA copolymerization

Copolymers of MEMA/HEMA were also synthesized. Because the mixture acetone/DPE provides low solubility of PHEMA, preventing the further polymerization of the monomer with higher conversions, ethanol was chosen as the solvent for this copolymerization. Copolymerization reaction at room temperature showed low reproducibility as the reaction is very sensible to temperature variations. As for the SARA ATRP of MEMA/HEMA, copolymerization was then conducted at higher temperature ($50\text{ }^\circ\text{C}$). The reaction conditions for this polymerization are shown below (**Scheme 32**).



Scheme 32: SARA copolymerization conditions for MEMA and HEMA.

The copolymers were synthesized with 62% conversion of MEMA, and 50% conversion of HEMA in three hours. Although the kinetics of this copolymerization was not studied, the $^1\text{H-NMR}$ conversion suggests a lower kinetics of HEMA, providing a copolymer with lower ratio of HEMA comonomer than envisioned in the initial feed (23% real ratio x 30% initial loading). The precipitated copolymer is now soluble in THF, allowing SEC-MALS analysis. The monodispersity of the synthesized copolymers was of 1.2 using triple detection method, and fits with a value for polymers with a narrow molar mass distribution (**Table 21**).

Table 21: NMR conversion and SEC data for the SARA copolymerization of MEMA/HEMA 70/30 at 50 °C in ethanol for 3h.

Conversion M/H (%) ^a	Ratio M/H (%) ^a	M _n (g/mol) ^b	M _n SEC (g/mol) ^c	Đ ^c
62/50	77/23	16 800	23 300	1.23

^a Calculated from $^1\text{H-NMR}$ ^b with $M_{n \text{ calc}} = M_{\text{eBiB}} + p_{\text{MEMA}} \times M_{0 \text{ MEMA}} \times \text{DP}_{\text{target(MEMA)}} + p_{\text{HEMA}} \times M_{0 \text{ HEMA}} \times \text{DP}_{\text{target(HEMA)}}$. ^c Obtained from SEC-MALS analysis. M/H means MEMA/HEMA

The SEC profile of the synthesized copolymers are monomodal and shown in **Figure 72**.

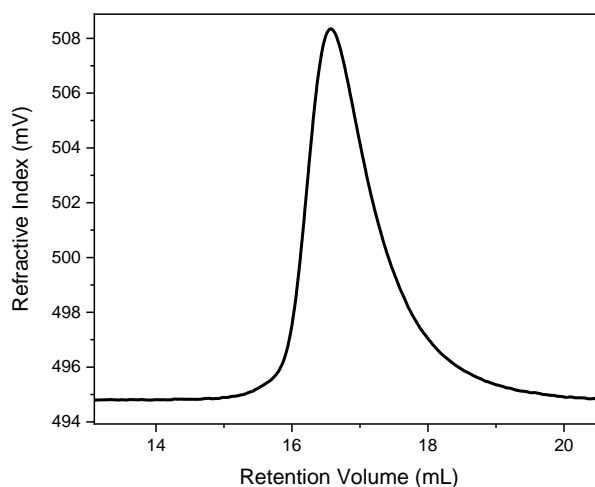


Figure 72: SEC profile of the synthesized copolymer of MEMA and HEMA (**Table 21**).

Figure 73 shows the $^1\text{H-NMR}$ of the reaction mixture after 3 hours reaction. The conversion and ratio calculation can be performed in various ways, but the simplest manner is to analyze the methylene hydrogens from the monomers and compare them with the CH_2 from the polymers (region between 3.7 to 6.3 ppm).

Therefore, the $\text{Conv}_{\text{HEMA}} = \frac{\text{Integral Hd}}{\text{Integral Hd} + (\text{integral H8} \times 2)}$. The same is applied for MEMA,
 with $\text{Conv}_{\text{MEMA}} = \frac{\text{Integral Hi,c} - \text{Integral Hd}}{(\text{Integral H2} \times 2) + (\text{Integral Hi,c} - \text{Integral Hd})}$. The ratio for HEMA is given with
 $\text{Ratio}_{\text{HEMA}} = \frac{\text{Integral Hd}}{\text{Integral Hi,c}}$.

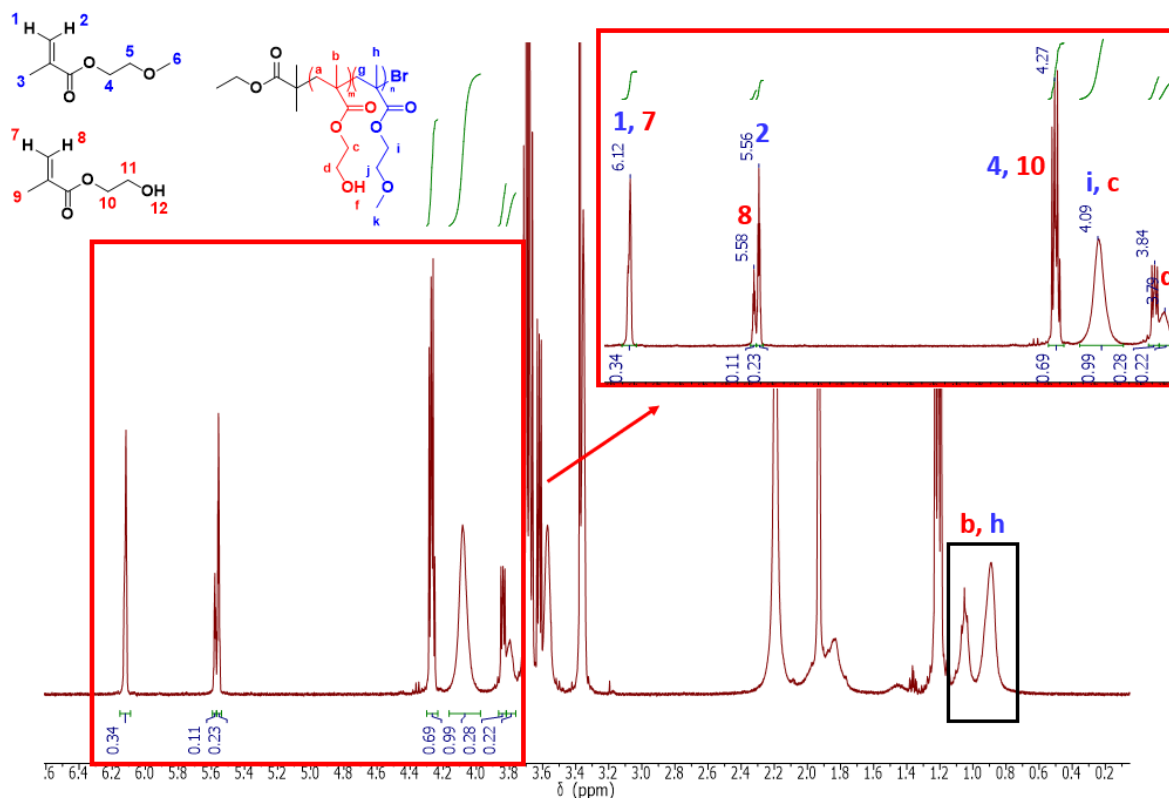


Figure 73: ¹H NMR (CDCl₃) of the reaction mixture of the polymerization of MEMA/HEMA in a 70/30 initial loading after 3h reaction. Conditions for polymerization: [MEMA]₀: [HEMA]₀: [eBiB]₀: [dNpby]₀: [CuBr₂]₀ = 140:60:1:0.4:0.1 at 50 °C in ethanol. Inset shows a higher magnification of the region between 3.7 to 6.3 ppm, the region used for the calculation of conversion and ratio of polymers.

3.8. Conclusions

This chapter delved into the synthesis and characterization of copolymers of methacrylate employing both classical ATRP and SARA ATRP methodologies. The methodologies for synthesis were developed in solution, and later applied on surface. The copolymers of MEMA/AZMA usually provide higher dispersities due to the reactive azide group presented in the AZMA comonomer, however, these copolymers were synthesized with dispersities usually lower than 1.5

SI-ATRP of MEMA and of copolymers of MEMA/AZMA were developed using crystalline and macroporous silicon surfaces. Through a comparative analysis, it was observed that SI-ATRP of MEMA using different imitator layers provides precise control over surface-bound polymerization with DP ranging from 50 to 200, and polymer brushes up to 10 nm. However, XPS data suggests a non-homogeneity of the polymer brushes in the case of SiOBr1-PMEMA even if its AFM images shows a homogenous layer. Nevertheless, when the polymerization time is increased, the thickness and the density of monomer units on surface also increases, allowing the development of polymer brushes with different thickness that can be applied in different applications.

Then, a copolymer, now based on MEMA and HEMA monomers, were studied using SARA ATRP to afford more complex polymer structures. The last stage of this study lays on the SARA copolymerization of HEMA/MEMA/AZMA for the development of a copolymer constituting of two functional comonomers. Nevertheless, this chapter sheds light on the versatility and potential applications of surface-initiated polymerization, offering insights for further development of functionalized surfaces.

CHAPTER 4

Synthesis of salen catalysts and post-functionalization of copolymers

“All truths are easy to understand once they are discovered; the point is to discover them.”

Galileo Galilei

SUMMARY

4.1. Contextualization	129
4.1.1. Synthesis of salen ligands	129
4.1.2. Sonogashira Pd/Cu cross-coupling reactions.....	130
4.1.3. Functionalization using click chemistry	131
4.2. Synthesis of enantiopure salen ligands	132
4.3. Synthesis of salen complexes	135
4.3.1. Chromium-salen complexes	135
4.3.2. Cobalt-salen complexes	136
4.3.3. Characterization of metal-salen complexes	136
4.4. Synthesis of FTIR markers for click chemistry	138
4.4.1. Synthesis of aryl-1	139
4.4.2. Synthesis of aryl-2.....	140
4.4.3. Synthesis of aryl-4.....	140
4.4.4. Characterization of aryl products by ATR-FTIR.....	141
4.5. Click chemistry with copolymers in solution	142
4.5.1. Using FTIR markers	142

4.5.2. Using salen complexes	145
4.6. Click chemistry with copolymers on surface	149
4.6.1. Using FTIR markers on crystalline silicon	149
4.6.2. Using salen complexes on macroporous silicon	153
4.7. Conclusions	156

In the last two chapters, it was discussed the grafting of initiators on surface, and their further polymerization. Copolymers of MEMA/AZMA were grown both on surface and in solution. This chapter discuss the post-functionalization of these copolymers with 1) FTIR markers to develop the methodology, and 2) salen complexes so to obtain the supported catalysts envisioned in this project.

First, the synthesis of the salen ligands and complexes will be discussed, together with the synthesis of the FTIR markers by means of Sonogashira cross-coupling, to then go over to the post-functionalization of copolymers. The salen complexes were clicked in both copolymers in solution and also on surface. In the first case, two different salen complexes based on chromium and cobalt were engaged in a click reaction in a 50/50 loading of each catalyst to afford a multipurpose supported salen catalysts. In the second case, chromium-salen catalyst were clicked on the copolymers on surface to perform silicon-supported monocatalysis.

The main techniques to characterize the post-functionalized copolymers are ATR-FTIR and XPS. A general contextualization is given before going into the details of the results.

4.1. Contextualization

4.1.1. Synthesis of salen ligands

The term salen is generally used to describe primarily bis-Schiff bases ligands derived from the condensation of salicylaldehyde derivatives with diamines.^{2, 151} The prototype salen, *N,N'*-bis-(salicylaldehydo)ethylenediamine (4) (**Figure 74**), was first synthesized in 1889 by Combes from condensation of salicylaldehyde with ethylenediame.¹⁵²

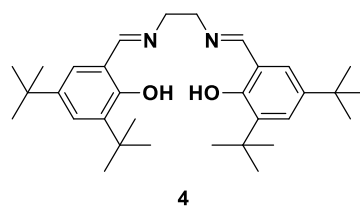


Figure 74: First synthesized salen prototype.

Since then, the salen ligand was modified enabling the development of an entire field of chemistry in which these tetradentate bis-Schiff bases act as ligands for a large number of metal ions. In fact, chiral salen-type metal complexes are known for their catalytic activity, allowing the preparation of scalemic building blocks. If associated with metals (Cr, Cu, Co, Mn, Fe, etc.), they promote the enantioselective catalytic formation of carbon–carbon or carbon–heteroatom bonds with excellent efficiency both in terms of activity and selectivity.^{2, 151}

In this context, this project aims to develop supported asymmetric catalysts based on salen complexes for the study of functionalization of surfaces using these complexes, and their catalytic activity.

4.1.2. Sonogashira Pd/Cu cross-coupling reactions

Sonogashira palladium/copper cross-coupling is an effective method to form new C–C bonds and has been applied in organic chemistry since its discovery in 1975. In fact, preceding the Sonogashira reaction, Heck and Diek¹⁵³, and Cassar¹⁵⁴ reported the arylation and alkenylation of alkenes via phosphane-palladium complexes. However, these procedures used harsh conditions with elevated temperatures. Then, in 1975, Sonogashira and coworkers¹⁵⁵ reported the cross-coupling of iodobenzene with acetylene in the presence of palladium and copper catalysts. Since then, Sonogashira reaction remains one of the most popular reactions for the formation of C(sp²)-C(sp) bonds.

The mechanism for the Sonogashira cross-coupling is shown in **Figure 75**. The Pd/Cu-catalysed Sonogashira reaction includes oxidative addition, transmetalation and reductive elimination and proceeds along two catalytic cycles.

In **Cycle A**, Pd(0) undergoes oxidative addition (**OA**) with the aryl or vinyl halide substrate to produce Pd(II) species A. Then, it reacts with copper acetylide in the transmetalation I step, yielding complex B and regenerating the copper catalyst. The copper acetylide reagent is produced from the alkyne derivative in the second reaction sequence shown

in **Cycle B**. Finally, the complex undergoes reductive elimination (**RE**) releasing the targeted coupling product and regenerating the starting Pd(0) species.

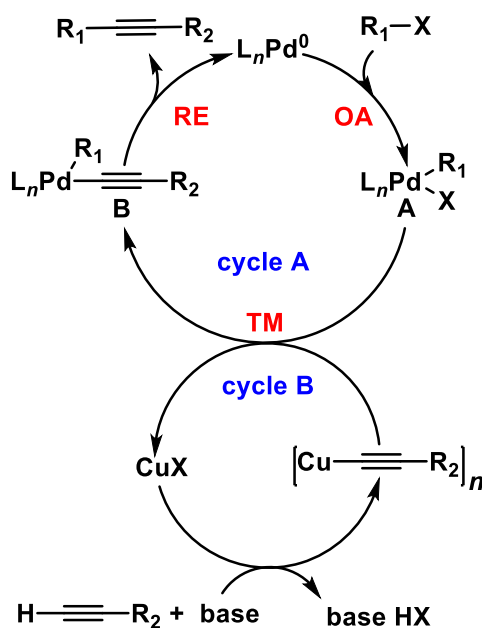
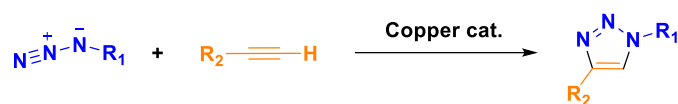


Figure 75: Proposed mechanism for the Pd/Cu catalyzed Sonogashira cross-coupling reaction that is synergistically catalyzed by Pd and Cu.¹⁵⁶

4.1.3. Functionalization using click chemistry

Click chemistry represents a practical and well-understood method to form C–N bonds to develop complex, mixed structures. It was first discovered by Huisgen in the 1960s¹⁵⁷, but Sharpless consolidated the term “click-chemistry” and defined highly efficient synthetic conditions.¹⁵⁸ Since then, click chemistry has been commonly used by the scientific community. The Cu-catalyzed click chemistry involves the coupling of a terminal alkyne with a terminal azide to exclusively form the 1,2,3-triazole unit (**Scheme 33**), which catalyzed by copper provides the regioselectivity shown below. However, Rh-catalyzed click cycloaddition of alkynes with azides provides isomeric triazoles.¹⁵⁹ Nevertheless, this thesis focuses on copper catalyzed click chemistry. This reaction has been of great importance in the modern society, in applications ranging from plastics to pharmaceuticals and biorthogonal chemistry.¹⁶⁰ Carolyn Bertozzi, Morten Meldal and Barry Sharpless received the Nobel Prize in 2022 for their contributions to this chemistry.



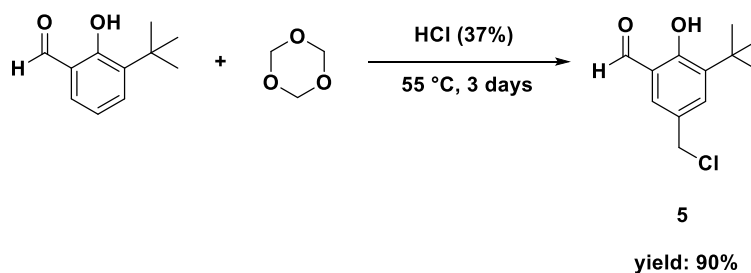
Scheme 33: General representation of the click chemistry reaction between an azide and a terminal alkyne to form a triazole ring.

The use of click chemistry for the modification of molecules on surface has emerged as a pivotal approach in diverse areas of surface functionalization, such as for applications in biomedicine.⁷ It offers advantages that includes high selectivity and efficiency, while using mild conditions. This technique enables the modification of surfaces to design complex structures with tailored properties. In our case, we use click chemistry for the direct functionalization of copolymers on surface with catalysts to design supported asymmetric catalysts.

4.2. Synthesis of enantiopure salen ligands

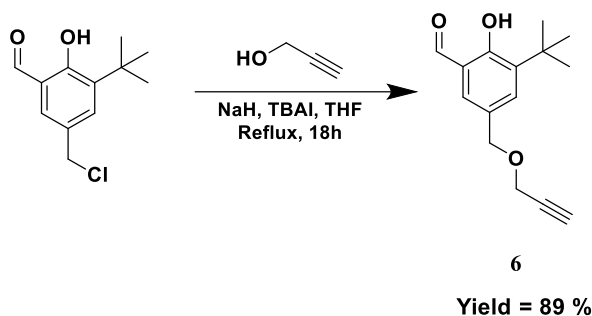
For the synthesis of salen ligands, a condensation between an enantiopure 1,2-diamine and two equivalents of a salicylaldehyde derivative is usually employed using standard methodologies in good yields.^{2, 161} The modification of the salen structure to obtain asymmetric salen ligands is thus possible by modifying the structure of the aldehyde and/or the diamine backbones.

The first step to obtain the unsymmetrical salen ligand used in this project is the synthesis of 3-(*tert*-butyl)-5-(chloromethyl)-2-hydroxybenzaldehyde. Based on the procedure described by Salunke and coworkers,¹⁶² the aldehyde, product 5, is obtained from a chloromethylation reaction between the commercially available 3-(*tert*-butyl)-2-hydroxybenzaldehyde and 1,3,5-trioxane (2.5 eq.) in the presence of an excess of hydrochloric acid HCl (37%), over 3 days at 55 °C. After simple workup, the desired chloromethyl salicylaldehyde is obtained with 90% yield with no further purification (**Scheme 34**).



Scheme 34: Synthesis of 3-(*tert*-butyl)-5-(chloromethyl)-2-hydroxybenzaldehyde, product 5.

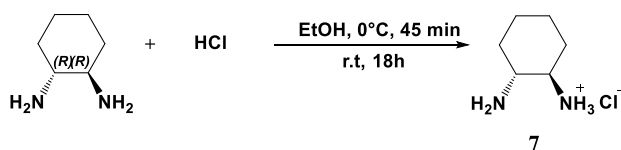
The following step involves the nucleophilic substitution of the chloride group with a propargyl alcohol for the formation of the desired salicylaldehyde **6** (**Scheme 35**). The alcohol is first deprotonated with NaH in THF with a clear visual representation of the reaction turning the solution from clear white to yellow. Then the aldehyde, product 5, is added together with tetrabutylammonium iodide (TBAI) to catalyze the reaction by forming the product in high yield.



Scheme 35: Synthesis of 3-(*tert*-butyl)-2-hydroxy-5-((prop-2-yn-1-yloxy)methyl)benzaldehyde, product 6.

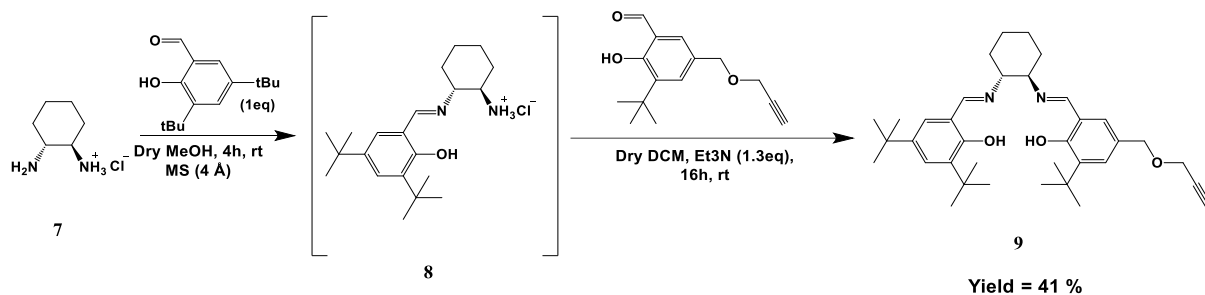
While the synthesis of symmetrical salen ligands is obtained by the condensation of 1 equivalent of diamine and 2 equivalents of a salicylaldehyde providing high yields, the synthesis of unsymmetrical salen ligands is more challenging. Because the condensation of the two amino groups frequently occurs at equal rates, the reaction results in a statistical combination of an aimed unsymmetrical salen and two undesired symmetrical salen.¹⁰⁶ Then, in 2006, Holbach and coworkers¹⁶³ demonstrated a feasible one-pot synthesis of enantiopure unsymmetrical salen ligands with good yields (60-85%) using 1:1:1 molar ratio of a chiral diamine and two distinct salicylaldehydes.

Therefore, by using the same concept, the chirality of the salen ligand used in this project comes from the monoprotected-cyclohexane diamine. Thus, one amine group of the enantiopure (1*R*,2*R*)-cyclohexane-1,2-diamine was protected using HCl solution, as described by S. T. Nguyen and coworkers (**Scheme 36**).¹⁶⁴



Scheme 36: Synthesis of mono protected diamine, product 7.

The final step involves the two-step synthesis of the unsymmetrical salen ligand bearing a propargyl moiety. This propargyl moiety is highly important in the structure of the salen complexes since this functional group is responsible for reacting with the azide moiety in the copolymer by means of click chemistry to afford the supported catalysts. As described before, the formation of unsymmetrical salen ligands is usually more difficult than the formation of the symmetrical ligands because of the formation of bis-imine products.¹⁶³ Nevertheless, by reacting the protected diamine with one salicylaldehyde to obtain intermediate 8 (**Scheme 37**) and then further with the modified benzaldehyde, affords the desired product 9 in 70% NMR yield. Further purification of the product is complicated with the other symmetrical ligands having retention factors very close to the desired product. The incomplete separation led to poor yield of pure product, but it could potentially be increased with better separation conditions.



Scheme 37: Two step synthesis of the salen ligand bearing a propargyl moiety, product 9.

The salen ligand was analyzed by ^1H -NMR, ^{13}C -NMR, ATR-FTIR, UV-vis and mass spectroscopy. The ^1H -NMR provides a simple and rapid method for verifying the successful condensation of the aldehydes with the diamine (**Figure 76**). Characteristics peaks of the imines are seen at 8.3 ppm together with the alkyne hydrogen at 2.45 ppm.

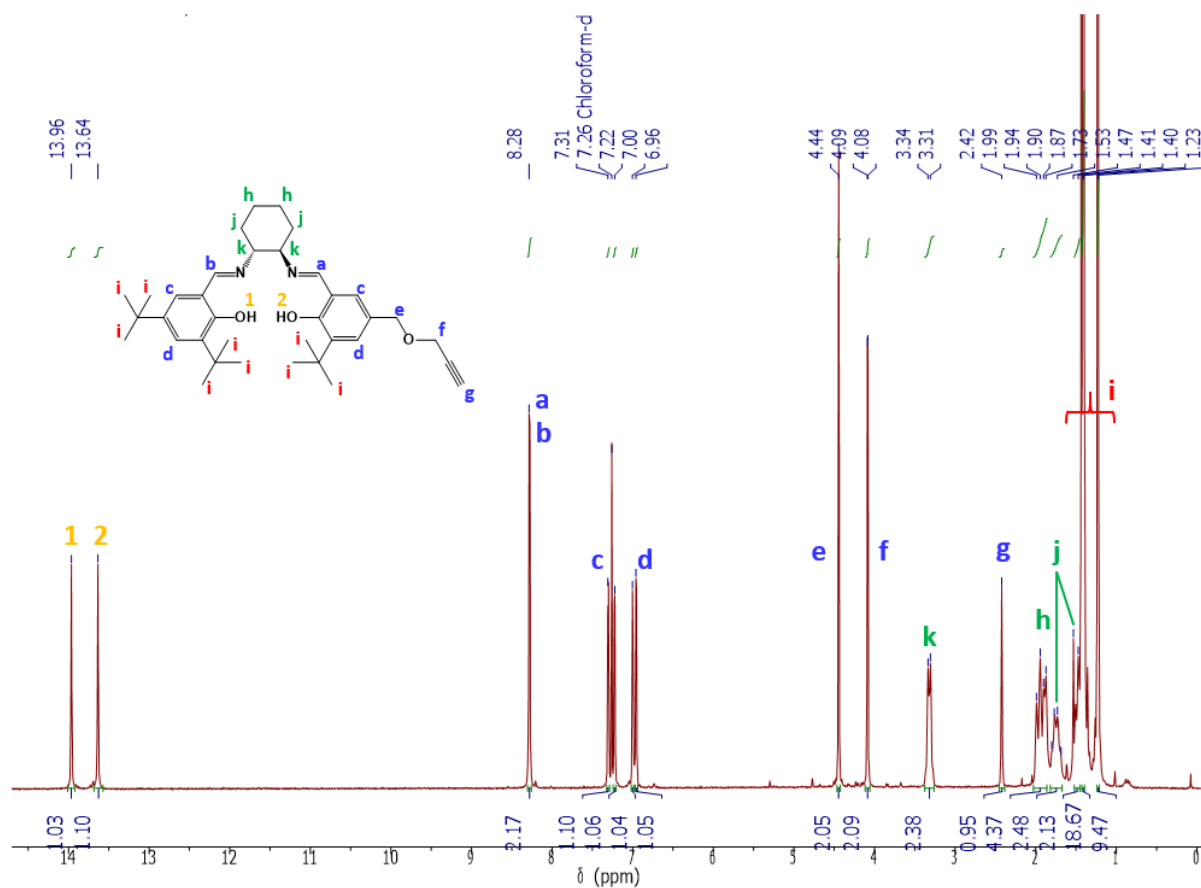


Figure 76: ¹H-NMR of the salen ligand bearing a propargyl moiety and its assigned peaks.

The other techniques used for the characterization of this product are provided in **Chapter 7**, experimental section.

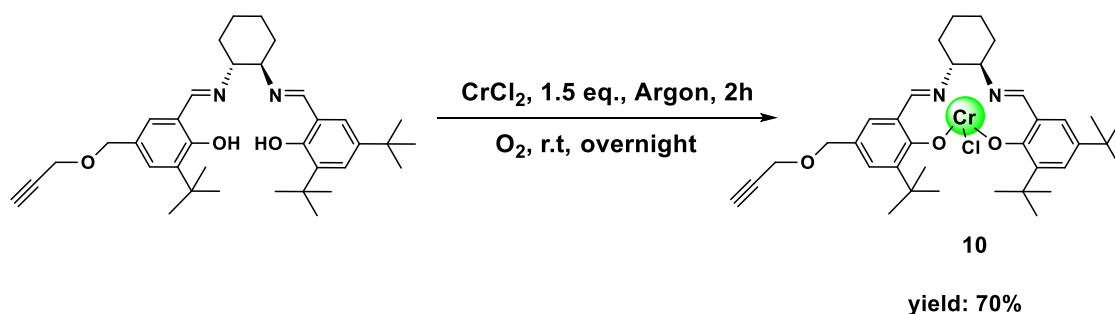
4.3. Synthesis of salen complexes

4.3.1. Chromium-salen complexes

Chromium salen complexes are well-known in the literature for their efficient catalysis for several chemical transformations, such as the asymmetric ring opening reaction (ARO) of epoxides,¹⁶⁵ the aminolytic kinetic resolution of epoxides,¹⁶⁶ the Henry reaction,^{107b, 167} the Nazarov cyclization,¹⁶⁸ and others. In most cases, the reactions using chiral Cr-salen catalysts deliver good conversions and high enantiomeric excesses for the desired products.

In typical procedures, the CrCl₂ is reacted with the chosen salen ligands under inert atmosphere to afford the resulting chromium(II) complex, which is later oxidized by the addition of air in the reaction overnight yielding the chromium (III) complex. The product is

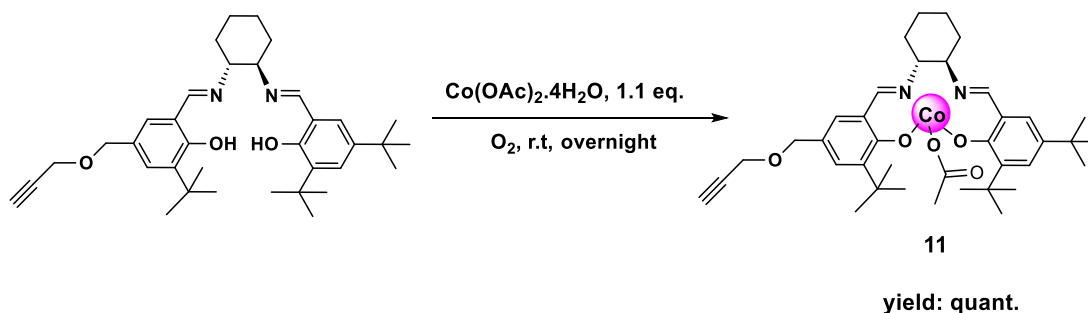
obtained after various washings with saturated NH_4Cl and brine as a brown powder in good yield (70%). The reaction conditions for this transformation is summarized in **Scheme 38**.



Scheme 38: Synthesis of chromium salen complexes, product 10.

4.3.2. Cobalt-salen complexes

Similarly, cobalt complexation was carried out from $\text{Co}(\text{OAc})_2 \cdot 4 \text{H}_2\text{O}$ in degassed DCM and methanol, followed by oxidation in air.¹⁶⁹ The product was then obtained as a brown powder in quantitative yield (**Scheme 39**).



Scheme 39: Synthesis of cobalt salen complexes, product 11.

4.3.3. Characterization of metal-salen complexes

The UV-vis analyses of the ligand and the synthesized complexes are shown in **Figure 77**. The salen ligand leads to the spectrum with the characteristic bands for this structure with typical absorptions at around 262 and 330 nm attributable to ligand $n-\pi^*$ and $\pi-\pi^*$ charge transfer bands,¹⁷⁰ and the two cobalt and chromium complexes showed the expected bathochrome effect, proof that metal complexation had been achieved.

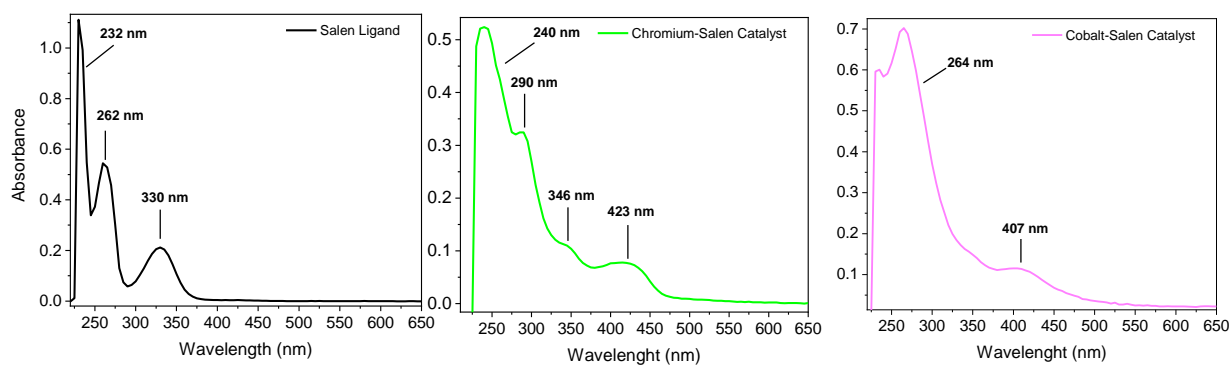


Figure 77: UV-vis spectra of salen ligand and the complexes of salen with chromium and cobalt.

The complexes were also characterized by ATR-FTIR, and **Figure 78** shows the spectra for the ligand and its complexes. Characteristics bands at 3300 cm^{-1} from $\text{C}\equiv\text{C}-\text{H}$ stretching mode attest the stability of the propargyl moiety after complexation. Besides, there is also an obvious shift in the stretching vibration mode of the imine ($\text{C}=\text{N}$) from 1627 to 1616 cm^{-1} after complexation with chromium metal, and to 1612 cm^{-1} after complexation with cobalt. This reflects the change in the electron density in the imine moiety, which after complexation, the nitrogen gives electron density to the metal, thus reducing its force constant, and therefore, its wavenumber.

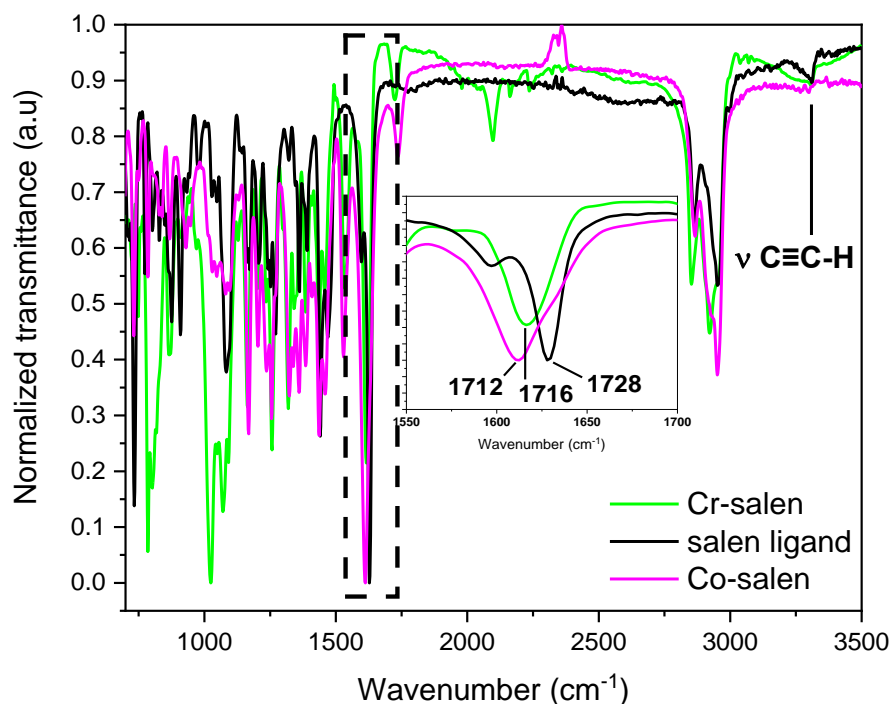


Figure 78: ATR-FTIR of the salen ligand and its complexes with cobalt and chromium. Inset in the picture shows an enlargement in the region from 1561 to 1680 cm⁻¹.

The other techniques used for the characterization of these complexes are provided in **Chapter 7**, experimental section.

4.4. Synthesis of FTIR markers for click chemistry

This section has been performed by engineering students at Ecole Polytechnique working on a project under my supervision from January to March 2023 and from November 2023 to February 2024.

The final goal of this thesis is to develop a supported salen catalyst based on silicon surface. The steps for grafting and modification on surface is usually followed by ATR-FTIR since other common techniques, such as NMR, are not possible with this support. However, before using the salen complexes to click on the copolymers, and because the salen complexes do not have many characteristics and strong FTIR bands to follow during the reaction, click reactions using the copolymer were first studied using simple molecules containing specific functional groups to be used as FTIR markers.

To this end, these FTIR markers were synthesized to be studied in the click chemistry reaction with the copolymers first in solution, then on a surface. It is important to note that all

reactions in this thesis are first evaluated in solution, and then applied on surface, because, if the reaction does not work in solution, the probability that it will work on the surface is even lower.

Therefore, to undergo the click reactions on the copolymers, four different alkynes (**Figure 79**) were envisioned. They are aryl-based compounds, with different functional groups. Furthermore, aryl-1, 2 and 3 have similar reactivities since all of them have mesomeric and inductive withdrawing effect, besides similar electronegativity properties. A fourth product very different from the first three, aryl-4 was also studied. The final goal of this study is to understand if there are any preferences/competitive behaviors between the molecules when using a mixture of aryl products to be clicked on the copolymers. This will help understand whether the same can be expected when using different salen complexes.

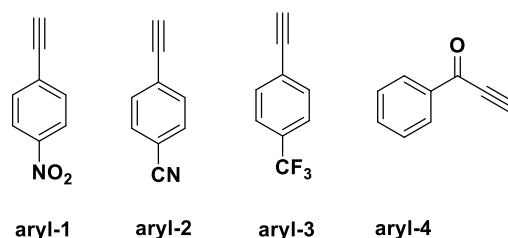
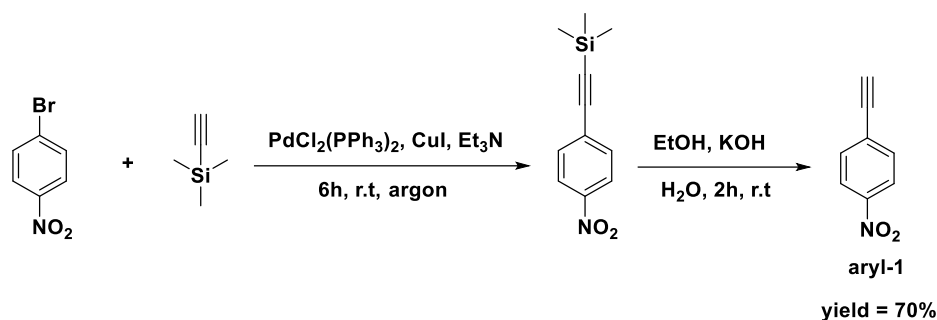


Figure 79: Aryl compounds used for the click chemistry with copolymers of MEMA and AZMA.

Aryl-1 and aryl-2 were synthesized using Sonogashira Pd/Cu cross coupling reactions, whereas aryl-4 was synthesized via an organomagnesium strategy. Aryl-3 was commercially available and used without any further purification.

4.4.1. Synthesis of aryl-1

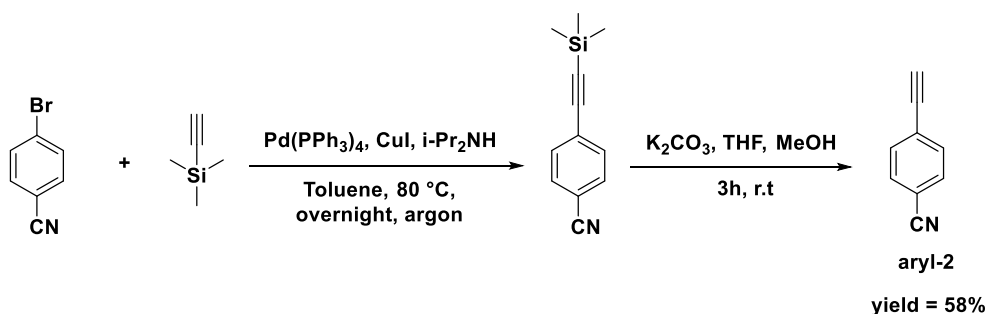
Aryl-1 was synthesized in a two-step reaction using classical Sonogashira Pd/Cu cross coupling conditions starting from 1-bromo-4-nitrobenzene and ethynyltrimethylsilane, with a palladium catalyst, a copper(I) cocatalyst, and an amine as base (**Scheme 40**). The base is necessary to neutralize the hydrogen halide produced as byproduct in this transformation. Inert atmosphere and deoxygenated conditions are usually employed because the Pd(0) complexes are unstable in air; besides, oxygen can promote the homocoupling of acetylenes.¹⁷¹ After removal of the trimethylsilyl (TMS) group, the desired product was obtained with a 70% yield.



Scheme 40: Reaction conditions for the synthesis of 1-ethynyl-4-nitrobenzene (aryl 1).

4.4.2. Synthesis of aryl-2

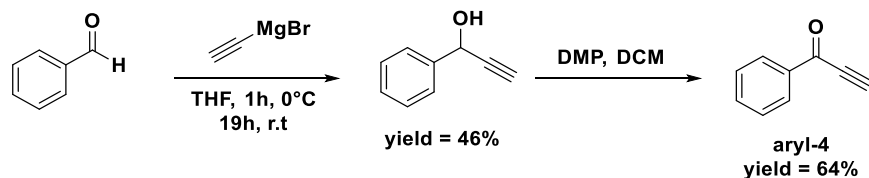
Similarly, aryl 2 was synthesized using the Sonogashira Pd/Cu cross coupling reaction conditions, but with a slight modification from aryl 1 synthesis procedure, as it was not very effective for the formation of aryl 2. Therefore, 4-bromobenzonitrile was reacted with ethynyltrimethylsilane using $\text{Pd}(\text{PPh}_3)_4$ and CuI as catalyst at $80\text{ }^\circ\text{C}$ overnight using toluene as solvent and diisopropylamine as base (**Scheme 41**). The elimination of the silane group was achieved by using potassium carbonate in methanol for over 3h at room temperature. After column chromatography, the product was obtained in 58% yield as a white powder.



Scheme 41: Reaction conditions for the synthesis of 1-ethynyl-4-benzonitrile (aryl 1).

4.4.3. Synthesis of aryl-4

Aryl-4, 1-phenyl-2-propyn-1-one, was synthesized in two steps starting from benzaldehyde (**Scheme 42**). The first step involves the nucleophilic reaction of the carbanion in the organometallic reagent with the electrophilic carbon in the carbonyl of the aldehyde to form an alcohol. Then, the alcohol is oxidized with Dess-Martin Periodinane (DMP), a hypervalent iodine compound that offers selective and mild oxidation of alcohols to ketones. After column chromatography, the aryl-4 is obtained as a white powder with a 30% overall yield.



Scheme 42: Reaction conditions for the formation of 1-phenyl-2-propyn-1-one (aryl-4).

4.4.4. Characterization of aryl products by ATR-FTIR

Since the major technique to characterize and evaluate the post-functionalized copolymers is by ATR-FTIR, it is important to check the main characteristics vibrations modes in each aryl product. **Figure 80** shows the infrared spectrum of the four products; aryl-1 has νNO_2 at 1502 and 1340 cm^{-1} , aryl-2 has $\nu \text{C}\equiv\text{N}$ at 2230 cm^{-1} , aryl-3 has νCF_3 at 1483, 1086 and 823 cm^{-1} and aryl-4 has $\nu \text{C}=\text{O}$ at 1633 cm^{-1} . The $\nu \text{C}\equiv\text{C}-\text{H}$ at 3230 cm^{-1} are seen for all cases attesting the correct synthesis of the aryl compounds. Concerning the $\nu \text{C}\equiv\text{C}$ at $\sim 2095 \text{ cm}^{-1}$, it is well observed in the cases of aryl-1 and aryl-4, however, much weaker for aryl-2 and aryl-3, illustrating the variability of the intensity of this band. However, in all cases, $^1\text{H-NMR}$ also confirms the structure of the synthesized products.

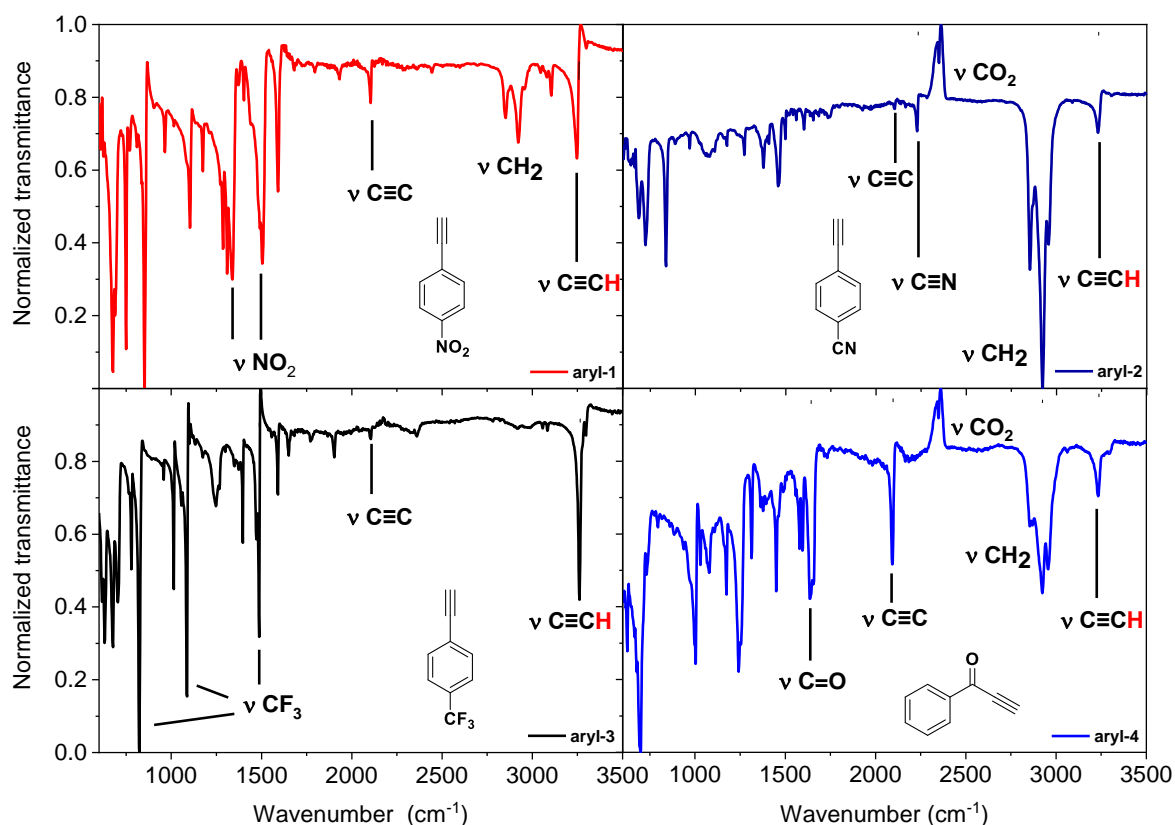


Figure 80: ATR-FTIR of the aryl compounds used as FTIR markers and their assigned peaks.

The CH₂ stretching modes appearing in all synthesized compounds, aryl-1, 2 and 4, are probably from remaining residual solvents.

4.5. Click chemistry with copolymers in solution

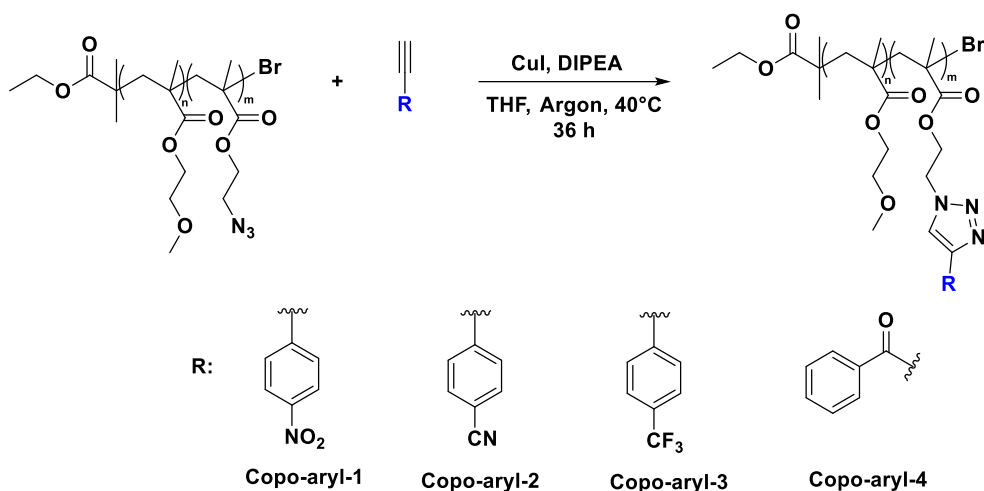
Once the products were synthesized, together with the copolymers of MEMA and AZMA, the click reaction between the azide from the copolymer and the alkyne from the synthesized products is performed. Firstly, the click reaction was studied in solution using FTIR markers, and then, applied to the catalysts to develop multipurpose catalysts. On surface, FTIR markers were also reacted with the copolymers to evaluate the efficiency of the reaction on surface; then, the same methodology was applied to Cr-salen catalyst to obtain silicon supported monocatalysts.

4.5.1. Using FTIR markers

This section has been performed by engineering students at Ecole Polytechnique working on a project under my supervision from January to March 2023 and November 2023 to February 2024.

A copolymer of MEMA/AZMA synthesized by means of SARA copolymerization in a 50/50 ratio was used for the click reactions – see **Chapter 3** for ATR-FTIR of copolymer (**Figure 59**). It is the azide function from the AZMA comonomer that it is engaged in the click reaction. All four aryl compounds were first clicked separately, and then in an equimolar quantity with another aryl compound. The click reaction of each aryl compound separately sets the expected intensity of their characteristic peak if a 100% click reaction is obtained.

The reaction conditions for the click of these molecules onto the copolymers are shown in **Scheme 43**, which is carried out either with two alkynes in equimolar quantities or with only one alkyne, together with the copolymer and *N,N*-Diisopropylethylamine (DIPEA) as base. Copper(I) iodide is used as the catalyst for this transformation. Then, the post-functionalized copolymers are filtered on an Al₂O₃ column for removal of copper catalyst and then precipitated in cold petroleum ether. The powders, usually having a yellow to orange color, were dried under vacuum and analyzed by ATR-FTIR.



Scheme 43: Reaction conditions for the click reaction of FTIR markers with a copolymer synthesized by SARA ATRP with an initial feed of 50/50 of MEMA/AZMA.

The spectra of the obtained functionalized copolymers using one aryl compound each is shown in **Figure 81**. In all cases, the azide function from the AZMA comonomer disappears, except for Copo-aryl-1 where there is still some remaining νN_3 but much less intense than the initial copolymers, showing that almost all azide function was reacted. This disappearing/diminishing of the azide band is a clear indication of the successful click of the compounds. Besides, the characteristics peaks of each aryl compound are also found in the products, and since nearly no $\nu \text{C}\equiv\text{C}-\text{H}$ is observed, it is certain that the products are covalently linked to the copolymers via a triazole bond. The characteristic peaks of aryl-3 are in the same region as the bulk and broad peaks from the copolymer in the fingerprint region; thus, complicating the analysis of Copo-aryl-3.

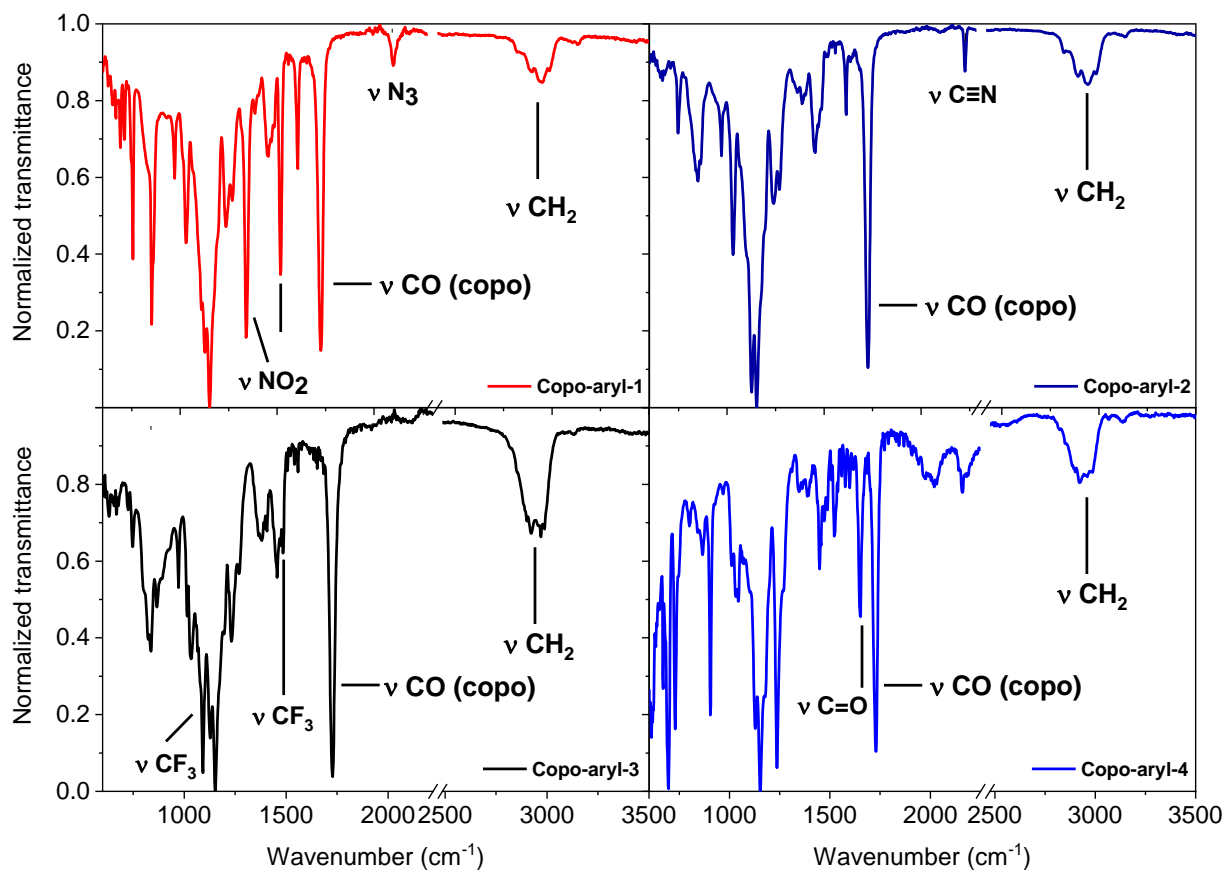


Figure 81: ATR-FTIR spectra of the post-functionalized copolymers using the aryl compounds. Added break in the spectrum between 2200 to 2400 cm^{-1} to remove the CO_2 contribution. Copo-aryl-4 was synthesized using a copolymer in a 50/50 ratio obtained by classical ATRP.

Then, the aryl compounds were clicked in an equimolar quantity using 2 aryl compounds. To show one example, **Figure 82** brings the case in which the peaks have the best resolution and are easy to analyze. The other examples using the other compounds are provided in the **Appendix B**.

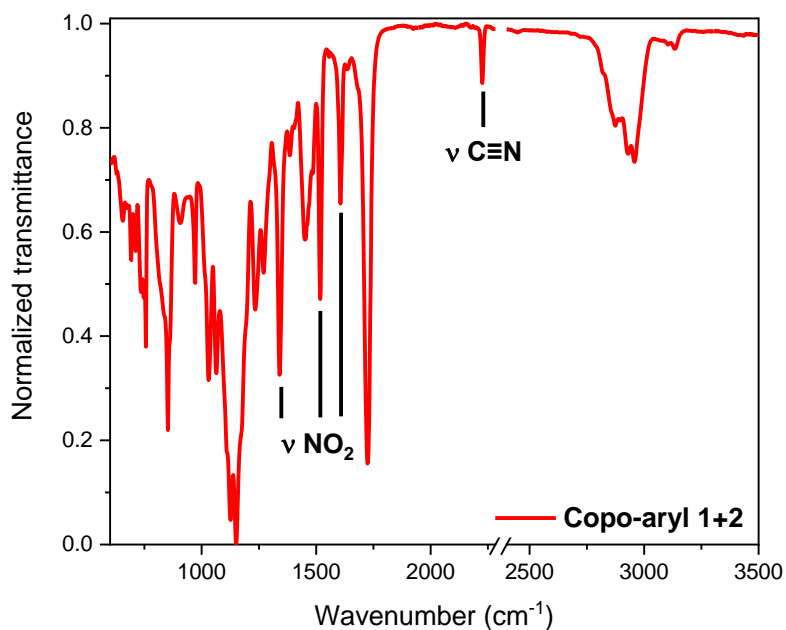


Figure 82: ATR-FTIR spectrum of the post-functionalized copolymer with aryl 1 and aryl 2 in an equimolar mixture. Added break in the spectrum between 2200 to 2400 cm^{-1} to remove the CO_2 contribution.

As a reminder, it is not possible to quantitatively analyze these spectra because the infrared technique used (ATR-FTIR for powders) is not suitable for quantitative analysis. Although it is not possible to accurately quantify the percentage of each molecule on the functionalized copolymer, we observe the peaks of both molecules and with an approximately equal intensity as in cases where they were clicked alone. This is an indication that the compounds are clicked respecting their initial loading.

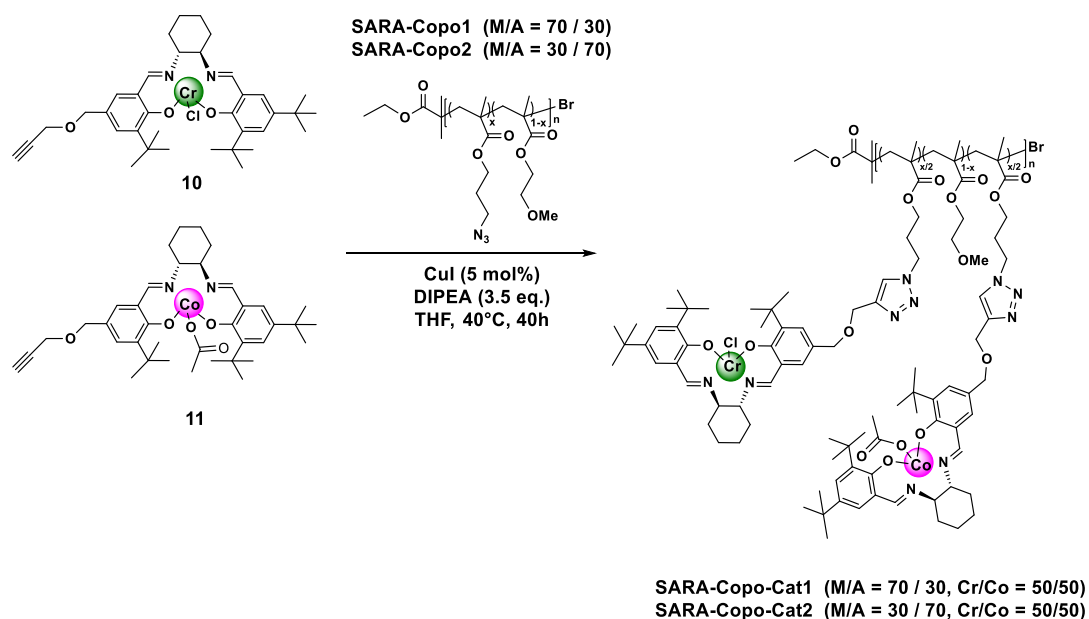
Therefore, the same strategy was applied to develop the supported catalysts using two different catalysts, which is reported in the next subsection.

4.5.2. Using salen complexes

This part has been inspired by the article by [Rafaela Bechara](#), [Philippe Roger](#), [Mohamed Mellah](#), [Nadine Barroca-Aubry](#), [François Ozanam](#), [Anne-Chantal Gouget-Laemmel](#), [Emmanuelle Schulz](#). Development of multipurpose supported asymmetric salen catalysts by SARA copolymerization. Manuscript in preparation.

Using SARA-Copo1 and SARA-Copo2 presented in **Chapter 3** (see **section 3.6.2**), subsequent copper(I)-promoted azide-alkyne Huisgen cycloadditions allowed propargyl-tagged chromium and cobalt salen complexes to react with the azide function of the

copolymers, yielding the corresponding supported catalysts as brown powders. Both catalysts were added in 0.65 eq. in relation to the available azide functional groups (calculation details in the experimental section, **Chapter 7**), so expecting a 50/50 loading of Co/Cr catalysts. The reaction conditions for this transformation is the same as described in the last section and shown in **Scheme 44**. After click reaction, the modified copolymers are solubilized in dichloromethane, filtered on an Al₂O₃ column to remove copper salts and precipitated again in cold hexanes under vigorous mixing, and dried overnight.



Scheme 44: Reaction conditions for the click reaction between the copolymers and the synthesized catalysts. M/A means MEMA/AZMA.

The click reaction for both copolymers was successful, as evidenced by the decrease in the characteristic stretching band of the azide function in IR, although it did not disappear completely, indicating that incorporation of the complexes was not complete (**Figure 83**). Considering that the composition of the modified copolymers after the click reaction is homogenous, the C=O stretching band of the copolymers can be normalized before and after the cycloaddition to estimate the approximate % of N₃ engaged in the reaction. As a result, ~40% of the azide function was reacted in SARA-Copo1 and ~35% in SARA-Copo2. It can therefore be estimated that there is around 6% of each catalyst in SARA-Copo-Cat1 and 12% of each catalyst in SARA-Copo-Cat2. In addition, a band at 1534 cm⁻¹ appears in both cases, characteristic of a deformation mode of the triazole cycle. Another peak also appears at 1622 cm⁻¹, which is attributed to the stretching of the C=N vibration mode of the salen complex.

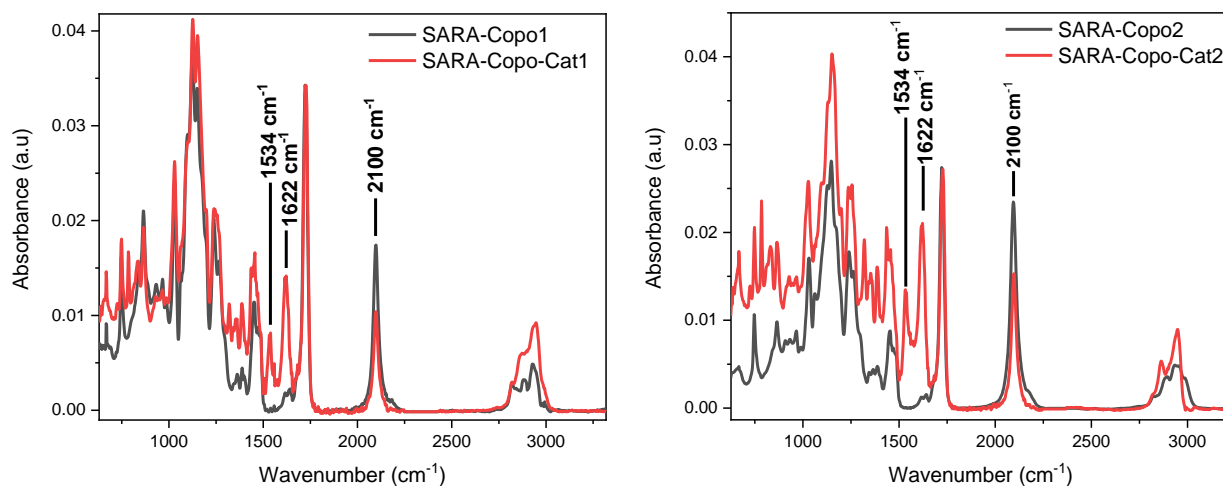


Figure 83: FTIR spectra of copolymers before (black curve) and after (red curve) click with cobalt and chromium salen catalysts.

The resulting copolymers were further analyzed by XPS. The N1s region (**Figure 84a**) SARA-Copo-Cat2 shows the characteristic $\text{N}\equiv\text{N}$ peak at 404.08 eV which corroborates with the FTIR analysis proving that there is still unreacted azide groups in the post-modified copolymers. However, the somewhat large peak $\text{C}-\underline{\text{N}}-\text{N}=\underline{\text{N}}$ at 398.59 eV clearly shows the formation of a new bond characteristic for a triazole moiety after the click reaction. The $-\text{N}-$ peak is observed at 400.4 eV contains both contribution of the formed triazole and the remaining $\underline{\text{N}}=\text{N}=\underline{\text{N}}$ from the unreacted azide. In order to verify the structure of the triazole moiety, it is necessary to first remove the contribution of the unreacted azide. Therefore, considering the ratio of $\underline{\text{N}}=\text{N}=\underline{\text{N}}/\text{N}=\underline{\text{N}}=\underline{\text{N}}$ of an unreacted copolymer of MEMA/AZMA, we obtained a value of ~ 2 . Then, by subtracting the contribution coming from the $\underline{\text{N}}=\text{N}=\underline{\text{N}}$ in the $-\text{N}-$ fit in the spectra of the clicked copolymer, the ratio $\text{C}-\underline{\text{N}}-\text{N}=\underline{\text{N}}/-\text{N}-$ is also ~ 2 , which confirms the correct structure of the triazole ring.

The Cr2p region is shown in **Figure 84b**, and its doublet falls between 570 to 590 eV, with the Cr2p_{3/2} located at 576 eV and Cr2p_{1/2} at 585 eV. As far as the chemical states of cobalt are concerned, Co2p_{3/2} (780 eV) and its doublet (796 eV) are observed both containing their satellites at a displacement of around 5-6 eV (**Figure 84c**). A satellite peak located at ~ 6 eV above the 2p_{3/2} main line is associated with Co(II) species, whereas at ~ 10 eV above the main line is associated with Co(III) species.¹⁷² Nevertheless, a mixture of the two chemical states is observed since their satellites are weak compared to satellites usually obtained for pure Co(II)

species. Besides, longer exposure to electron beam could potentially reduce the Co(III) species in the catalyst.

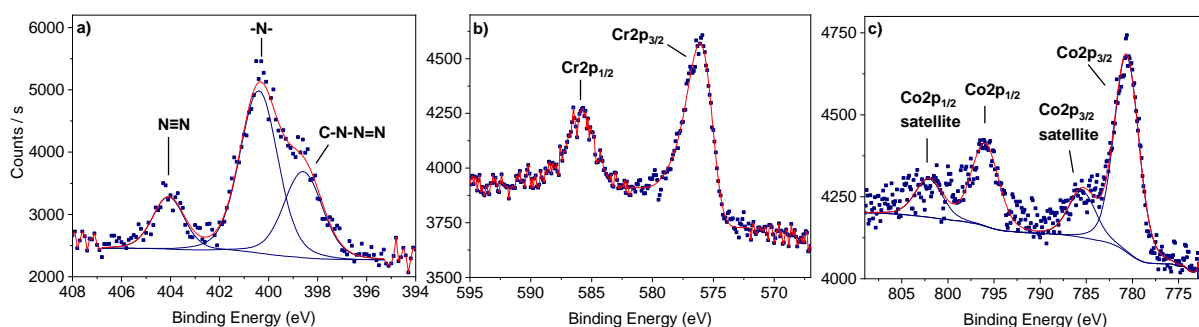


Figure 84: a) N1s b) Cr2p and c) Co2p XPS peaks for the modified supported catalyst (SARA-Copo-Cat2).

By comparing the XPS spectrum of chromium for both supported catalysts, we clearly observe an increase in counts/s in the case of SARA-Copo-Cat2 compared with the SARA-Copo-Cat1 (**Figure 85**), with approximately double the height at half-maximum. However, for cobalt, this increase is not so evident, but it is rather shown by larger contributions of the peaks, specially from the satellites. Finally, by comparing the ratio of each metal for each modified copolymer with the same carbon intensity, a ratio of $\sim 46/54$ Cr/Co for SARA-Copo-Cat1 and $\sim 60/40$ for SARA-Copo-Cat2 is obtained (values in **Appendix A**). XPS survey does not indicate any traces of copper therefore validating the purification strategy.

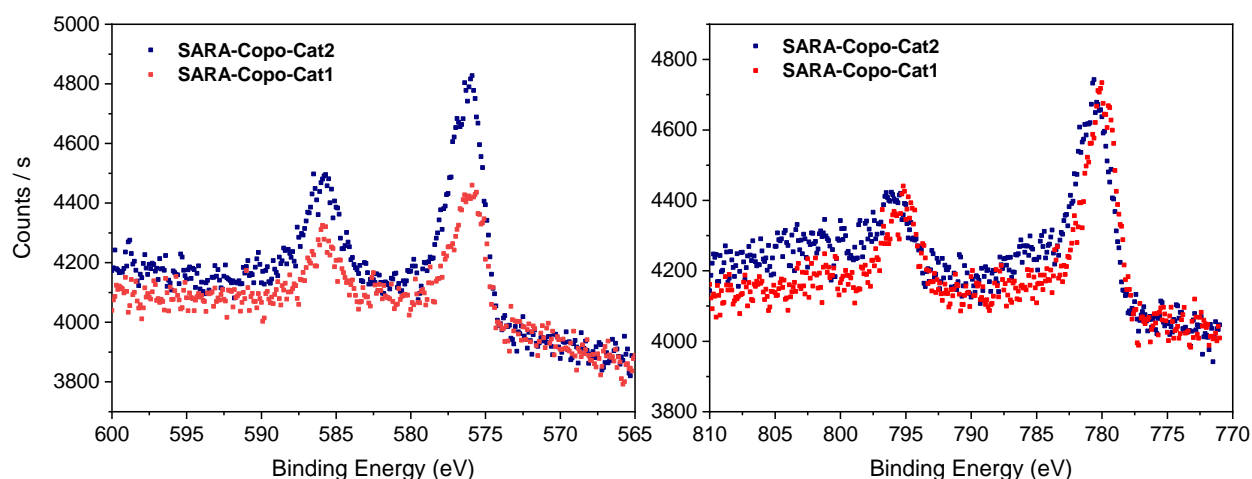


Figure 85: Comparison of XPS peaks for chromium (left) and cobalt (right) for both SARA-Copo-Cat1 and SARA-Copo-Cat2.

These supported catalysts are used as multipurpose catalysts for two different transformations, and their catalytic activity is discussed in **Chapter 5**.

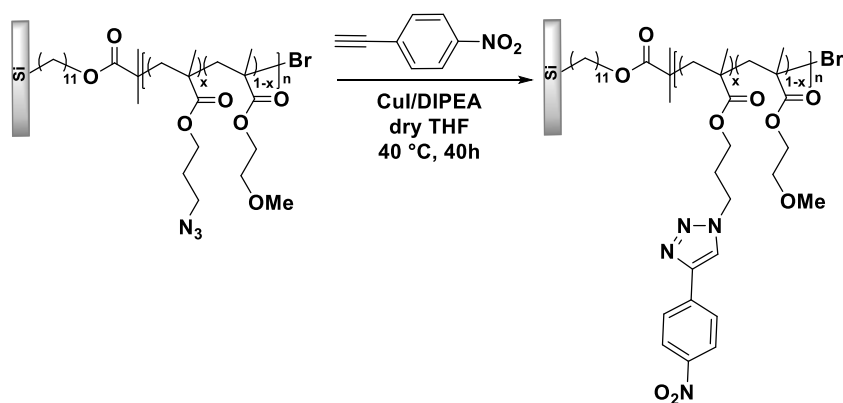
4.6. Click chemistry with copolymers on surface

After understanding the chemistry of the copolymers and the salen complexes in solution, we applied the same concepts on surface to develop the silicon-supported asymmetric catalysts. Before engaging the salen complexes on surface directly, it is however advised to test the reaction using the FTIR markers. Therefore, the next subsections discuss first the click of FTIR markers on copolymer brushes on silicon, and then the Cr-salen catalyst for the final step of the development of the supported catalysts.

4.6.1. Using FTIR markers on crystalline silicon

4.6.1.1. In the case of aryl-1

Using a Si(111) surface with copolymer brushes in a 50/50 loading of MEMA/AZMA, a click reaction was tested using aryl-1, 1-ethynyl-4-nitrobenzene, since its vibration bands are very characteristic and easy to identify by FITR. **Scheme 45** shows the conditions for this surface modification.



Scheme 45: Conditions for the click chemistry of aryl-1 with SiBr1-Copo3.

Figure 86 brings the ATR-FTIR spectrum before (a) and after (b) the click reaction of the molecule on surface. Observing the spectrum after the click, the negative peak of the azide band at 2100 cm^{-1} with a mAbs of 3.5 is found, indicating that nearly all N_3 functions disappeared (compared to the 3.7 mAbs from the start). Besides, three characteristics peaks for nitrobenzene are found at 1606 , 1520 and 1344 cm^{-1} proving the proposed structure. The $\text{C}=\text{O}$ band at 1730 cm^{-1} did not change, which attests that the copolymers were covalently bonded

on the surface through the initiator. In addition, the aryl compound is proved to be covalently attached on the surface because no peak in the region of 3250 cm^{-1} from the $\text{C}\equiv\text{C}-\text{H}$ is found. The triazole absorption mode falls approximately in the same region as the peak at 1520 cm^{-1} from the aryl compound, thus complicating the observation of this peak.

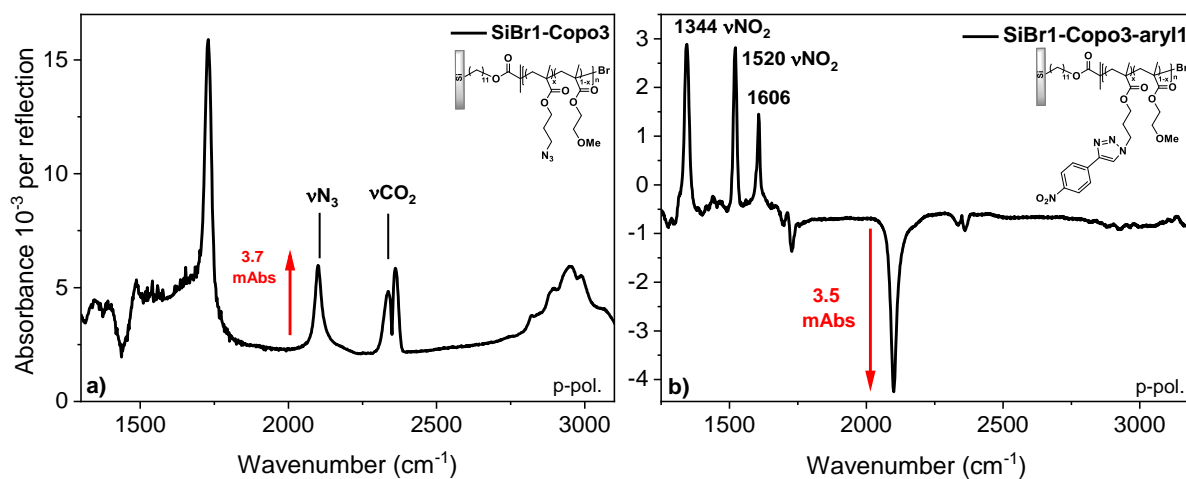


Figure 86: a) SiBr1-Copo3 on Si-(111) with reference spectrum being the SiBr1 b) SiBr1-Copo3-aryl1 with the reference spectrum being SiBr1-Copo3.

The successful click reaction of ethynyl nitrobenzene to the copolymers on surface was also evidenced by XPS. The N1s core level spectrum (**Figure 87a**) contains 3 main contributions, the first at 401.24 eV attributed to the nitrogen double linked to another nitrogen ($\text{C}-\underline{\text{N}}-\underline{\text{N}}=\underline{\text{N}}$), the second at 402.68 eV to the nitrogen in between the other two nitrogen ($-\underline{\text{N}}-$) and finally at 407.13 eV to the nitrogen linked to the oxygens (NO_2). The C1s core level is also shown in **Figure 87b** and it contains the contributions from C-C at 286.04 eV, C-O and C-N at 287.62 eV and finally the ester carbon $\text{OC}=\text{O}$ at 289.96 eV. There is charge shift observed for this sample which is not unusual when measuring insulating samples even when using charge neutralization.

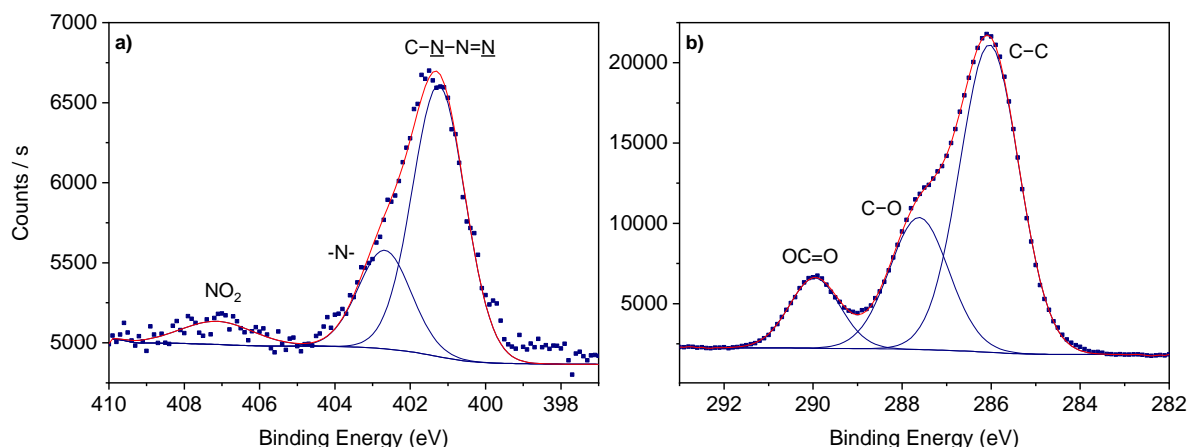
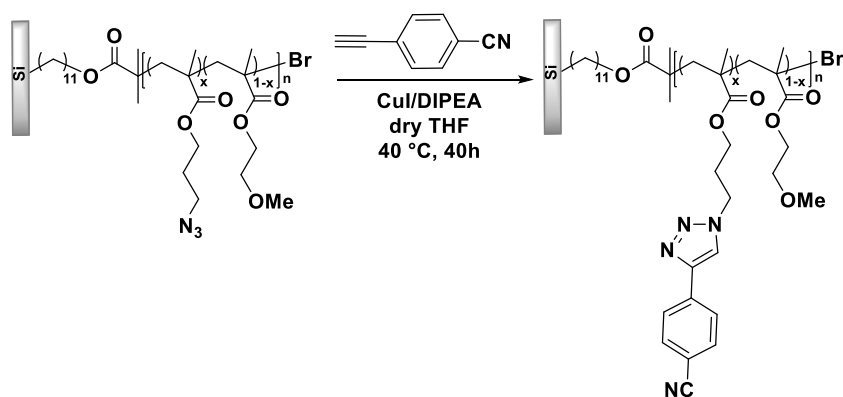


Figure 87: XPS narrow scans of the (a) N1s and (b) C1s region of the nitro functionalized surface.

The thickness of the prepared surfaces was measured before and after the click reaction and the SiBr1-Copo3 had 20.4 ± 1.2 nm using a value of 1.6 for refractive index, and then, after the click of ethynyl nitrobenzene, the surface SiBr1-Copo3-aryl1 had 22.8 ± 0.3 nm thickness. The increase in thickness of approximate 2 nm is similar to that expected for aryl-1.

4.6.1.2. In the case of aryl-2

The same methodology was applied for the click of another FTIR marker, now 4-ethynylbenzonitrile (aryl-2), with a CN function group that is also very characteristic in FTIR with a strong band at 2220 cm^{-1} . Therefore, using another SiBr1-Copo3, aryl-2 was engaged in the click reaction similarly as described before (**Scheme 46**).



Scheme 46: Conditions for the click chemistry of aryl-2 with SiBr1-Copo3.

Figure 88 shows the spectrum before and after click reaction with aryl-2, and as seen before, the azide band reacts almost to its completeness, and a new $\text{C}\equiv\text{N}$ stretching band appears at the expected wavenumber. We observe a slight removal of the $\text{C}=\text{O}$ band from the copolymer at 1730 cm^{-1} after the click reaction, indicating that some absorbed copolymer might have been rinsed off during procedure. In addition, the fingerprint region ($< 1500\text{ cm}^{-1}$) for SiBr1-Copo3-aryl2 is unfortunately not well resolved due to a FTIR reference problem.

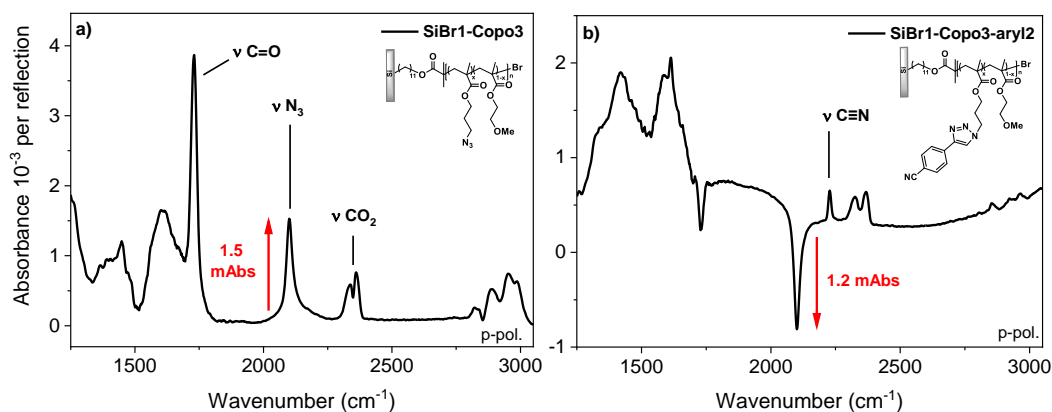


Figure 88: a) SiBr1-Copo3 on Si-(111) with reference spectrum being the SiBr1 b) SiBr1-Copo3-aryl2 with the reference spectrum being SiBr1-Copo3.

The XPS of the modified surface (**Figure 89**) does not give much different insights since the chemical environment does not change much from before and after click reaction, except by the fact that the azide peak at $\sim 405\text{ eV}$ is not present in the modified surface, attesting the efficiency of the reaction. The new nitrile bond present in the structure is close in energy with the $-\text{N}-$ and can be considered in the same component located at 402 eV .

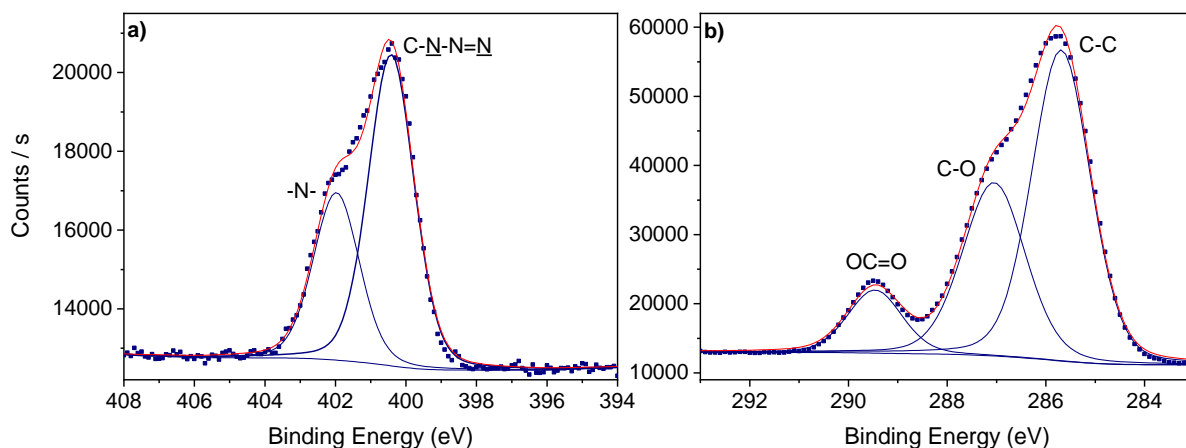
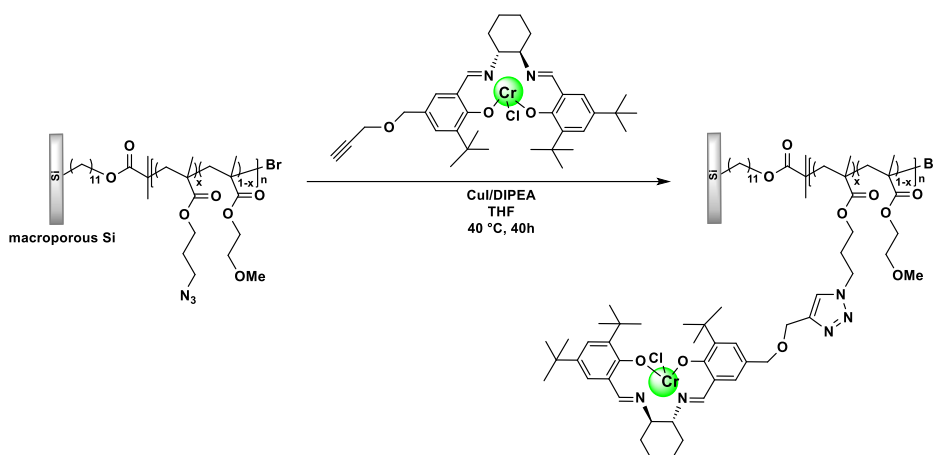


Figure 89: XPS narrow scans of the (a) N1s and (b) C2p region of the cyano-functionalized surface.

4.6.2. Using salen complexes on macroporous silicon

After studying the click reaction with the copolymers in solution and on surface, the same reaction conditions were applied using the synthesized Cr-salen complexes directly on macroporous silicon surface (**Scheme 47**).



Scheme 47: Conditions for grafting Cr-salen complex on copolymers of MEMA/AZMA on the surface of macroporous silicon.

Therefore, following the development of the catalyst, the same substrate as presented in **section 3.5.3** of **Chapter 3** (p. 114), is used for the click of the Cr-salen complex. Once more, the click appears to be almost 100% efficient coming from a ν_{N_3} intensity of 77 mAbs for the copolymer on surface to approximately 72.5 mAbs of reacted azide on the supported catalyst. This time, the triazole band is clearly visible at around 1572 cm^{-1} and the C=N from the imine

at 1629 cm^{-1} (**Figure 90**). As observed for SiBr1-Copo3-aryl2, some part of the C=O stretching band of the copolymer is negative, indicating that absorbed copolymers on surface were removed during this last step.

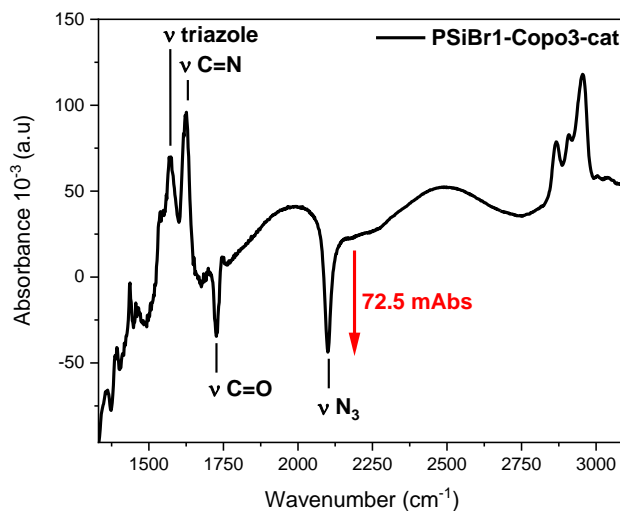


Figure 90: Transmittance IR of Cr-salen supported catalyst based on macroporous silicon.

The XPS spectrum of the supported catalyst shows no azide peak in the N1s region corroborating with the previous FTIR results. Besides, the ratio of $\text{C}-\underline{\text{N}}-\text{N}=\underline{\text{N}}/\text{-N-}$ is ~ 1.7 , close to the expected value of 2, thus validating the correct fit and atomic percentage of the structure in the N1s region after click reaction. The Cr2p region was surveyed and it is shown in **Figure 91b**. By comparing the atomic percentage of Cr2p to Cl2p (see **Appendix A**), the ratio of ~ 1.4 is obtained, also close to the expected value of 1, which suggests that chromium remains complexed in the developed structure. Residual copper is observed at 573 eV even after various rinsing in Soxhlet; however, it does not affect the envisioned reaction and therefore should not be a problem.

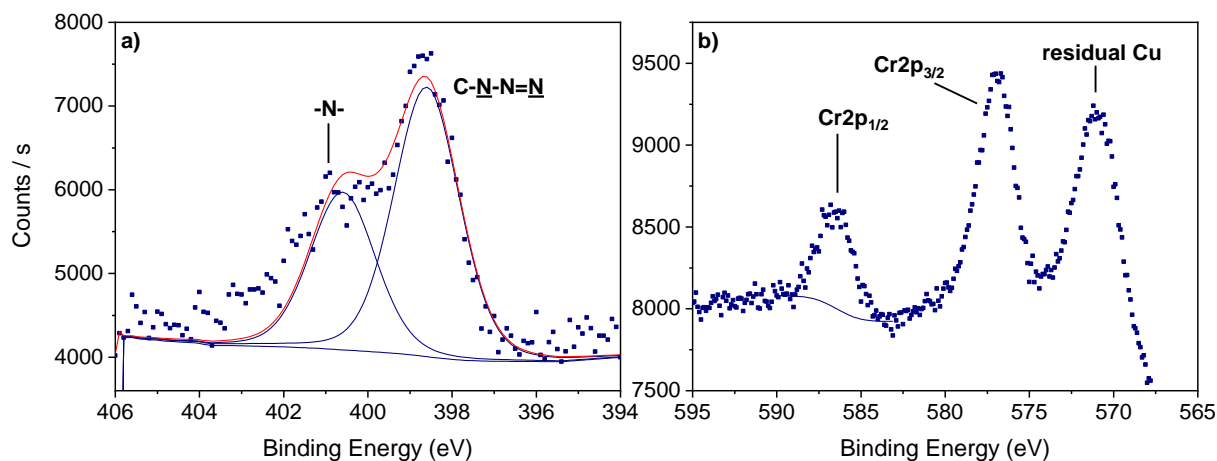


Figure 91: N1s (a) and Cr2p (b) XPS peaks for PSiBr1-Copo3-Cat.

The quantification of the density of catalysts on surface is not straightforward. As explained in **Chapter 3**, the accurate quantification of molecules on macroporous silicon is not possible since its infrared analysis is done by transmittance mode, and other techniques such as BET and TGA were not successful due to the thin layer of porous silicon. Therefore, a correlation between the mAbs and density of molecules was made for the case of crystalline silicon, and then applied to macroporous silicon (see **section 3.5.3**). Considering the azide function was clicked in almost its completeness, we estimate to have ~ 450 molecules of salen catalyst- nm^{-2} . Therefore, calculating the total number of salen complexes and dividing it by the Avogadro's number gives 1.1×10^{-7} moles of salen catalyst for this supported catalyst.

Table 22: Summary of the information regarding the number of moles for the supported catalyst PSiBr1-Copo3-Cat.

N molecules of salen catalyst/ nm^2	Length x height (mm)	Area (cm^2)	Total N of molecules ^a ($\times 10^{14}$)	Number of mol ^c
450	9×17	1.5	675	1.1×10^{-7}

^a obtained by multiplying the density of molecules/ nm^2 to the total area ^c obtained by dividing the total number of molecules by the Avogadro number (6.02×10^{23} molecules/mol).

Comparing to the crystalline surface, the copolymerization of MEMA and AZMA on SiBr1 yields a DP_{AZMA} of ~ 80 and density of AZMA comonomer units of 9 nm^{-2} (**Table 17**). This is 50 times more the value obtained for the N of reacted azide molecules (450 nm^{-2}) shown in **Table 22**. This factor is of the same magnitude as the estimated increase in surface specific area of macroporous silicon (78 cm^2 for every 1 cm^2 of crystalline silicon, see formula (1) and

(2), **section 3.5.3**). Thus, it indicates that the copolymerization on macroporous silicon essentially proceeds like on crystalline.

4.7. Conclusions

This chapter first presented the synthesis of salen catalysts and the aryl compounds. The later was synthesized by the Sonogashira Pd/Cu catalysis in good yields. Salen ligands were then complexed with chromium and cobalt metals, and they were characterized by UV-vis, ATR-FTIR and mass spectrometry.

Later, it was presented a comprehensive overview of the application of click chemistry on copolymers of MEMA/AZMA either in solution and on surface for the final aim of catalysis. The aryl compounds were first clicked on copolymers in solution in order to obtain direct information about the efficacy of this reaction using copolymers, since they are very good FTIR markers. They were also clicked on surface, attesting the efficiency of this strategy to develop the supported catalysts.

Finally, considering the salen supported catalysts, two types were developed: 1) catalysts anchored on the free copolymers and 2) anchored on the copolymer's brushes grown on the macroporous silicon surface. In the first case, two different salen catalysts were grafted in order to perform multipurpose catalysis. They were studied by ATR-FTIR and XPS and these analyzes proves the correct attachment of the catalysts. In the second case, chromium salen catalyst was attached to the surface to obtain a monocatalyst supported on macroporous silicon. It was also analyzed by IR and XPS, which confirmed the expected structure.

In all, this chapter shows that click chemistry offers a versatile platform for the functionalization of surfaces enabling the design of complex structures.

CHAPTER 5

Supported asymmetric catalysis

*“O que vale na vida não é o ponto de partida e sim a caminhada. Caminhando e semeando,
no fim, terás o que colher.”*

Cora Coralina, Brazilian writer and poet.

SUMMARY

5.1. Contextualization	158
5.1.1. Homogenous salen catalysis	158
5.1.2. Supported salen catalysis	159
5.2. Homogenous Catalysis	161
5.2.1. Asymmetric ring opening ARO of epoxides	161
5.2.2. Henry reaction	162
5.2.3. HKR of epibromohydrin.....	163
5.3. Multipurpose supported catalysis	164
5.4. Silicon supported monocatalysis	169
5.4.1. ARO of cyclohexene oxide.....	169
5.4.2. Henry reaction	171
5.5. Conclusions	172

This chapter discusses the findings for the asymmetric catalysis using supports, either with the MEMA/AZMA copolymers in suspension, or using the modified silicon surface. Two salen catalysts are studied, one based on chromium and the other based on cobalt. The reactivity

of these modified catalysts is described for three different reactions, the asymmetric ring opening (ARO) of cyclohexene oxide, the dynamic hydrolytic kinetic resolution of epibromohydrin (DKR) and the nitroaldol reaction.

5.1. Contextualization

5.1.1. Homogenous salen catalysis

Catalysis has been a pivotal technique in various industries ranging from pharmaceuticals to environmental remediation. Among many catalysts, metal complexes have emerged as prominent candidates due to their tunable selectivity and reactivity. Salen complexes play a major role in this area since they can be used for many different reactions by simply changing their metal center, or modifying their ligand structure.

The structural features of the salen complexes lay on the tetradentate ligand scaffold which gives stability for the coordination of the metal center. Chromium salen catalysts have demonstrated remarkable efficiency in the catalysis of the asymmetric epoxidation of olefins,^{98, 173} in the asymmetric Henry reactions of aldehydes with nitromethane,^{167a, 174} and the ARO of meso-epoxides with different nucleophiles.¹⁰⁰ This last reaction was found to be important in asymmetric catalysis, with the formation of valuable synthons such as chiral β -amino alcohols, using trimethylsilyl azide, TMSN₃, as the nucleophile, followed by subsequent reduction. Mechanistic studies show that this reaction involves the use of two chromium complexes in a bimetallic cooperation to obtain the desired product.¹⁰¹

The Henry reaction is commonly used to synthesize β -nitroalcohols from aldehydes or ketones. The highly acidic proton at the α -position of the nitroalkanes is easily accessible by a base, and the resulting anion is thus stable due to the nitro group. It is a very versatile process that creates carbon-carbon bonds while introducing a nitrogen functional group that is usually further modified, therefore, making this reaction a very interesting pathway to synthesize different molecules.¹⁵¹ Although this reaction can also be catalyzed by cobalt and copper derivatives, in this thesis we focused on the use of chromium salen complexes for this transformation.

Finally, cobalt salen catalysts have also found applications in many different reactions, but in this context, they are used in the dynamic hydrolytic kinetic resolution (HKR) of

epibromohydrin. According to mechanistic studies, this reaction is also governed by a bimetallic activation mechanism.¹⁶⁵

Therefore, chromium and cobalt salen complexes represent versatile catalysts with broad use in synthesis. Their structure can be modified for tunneling their reactivity and selectivity in various applications.

5.1.2. Supported salen catalysis

The grafting of enantioselective salen metal complexes on supports is advantageous as it allows the easy removal of the catalyst from the reaction mixture and their further reuse. The strategy of immobilizing salen catalysts on inorganic supports ranges from the encapsulation in the cavities of zeolites¹⁷⁵ to synthetically more demanding methodologies to afford covalent immobilization on supports.⁴ A comprehensive review on asymmetric supported catalysts is provided in **Chapter 1** of this manuscript.

The catalysts' covalently immobilization allows their recyclability for longer uses since leaching is much less possible with covalently bonded catalysts, therefore, increasing their life span. Schulz's group has made several advancements on the development of salen supported catalysts, for instance with the development of heterogeneous chromium catalysts through the anodic polymerization of a thiophene-salen that led to an insoluble polymer-salen catalyst used for the transformation of 2-methoxybenzaldehyde in a Henry reaction with enantiomeric excesses up to 77%. The polymerized catalyst was recovered and recycled maintaining good reactivity.^{107b} Yet, chromium salen complexes with pyrene-tagged groups were also immobilized on reduced graphene oxide (rGO) through π - π non-covalent interactions (**Figure 92**). The catalytic system promoted asymmetric catalysis in repeated cycles, without loss of activity or enantioselectivity, for both the cyclohexene oxide ring opening reaction and the hetero-Diels-Alder cycloaddition between various aldehydes and Danishefsky's diene.¹⁷⁶

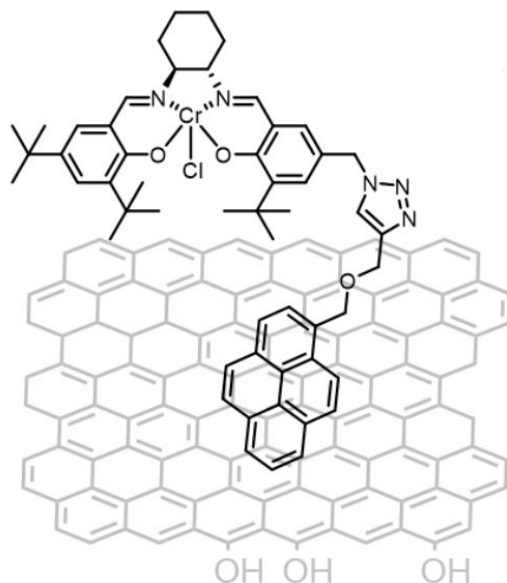


Figure 92: Pyrene-tagged salen catalysts immobilized on rGO.¹⁷⁶

In the context of this project, we also have demonstrated the successful development of salen catalysts based on polymers, such as styrene copolymers containing comonomers with a salen catalytic-active moiety with a cobalt center to promote the HKR of epibromohydrin, in which the higher concentration of salen complexes on the polymer matrix yielded better yields, probably because of the improved bimetallic cooperation.⁴

Finally, the copolymers of MEMA/AZMA were used to click chromium salen complexes for the ARO of cyclohexene oxide, yielding good conversions (> 98% over 6 h) and good enantioselectivity (74% *ee*). These modified copolymers showed good stability and recyclability up to 7 runs of the catalytic reaction.^{8b}

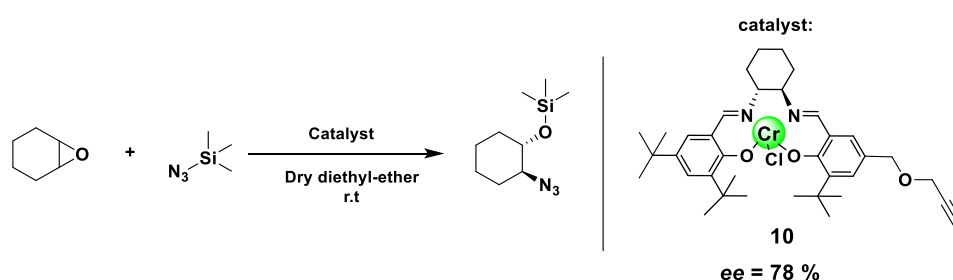
Thus, the polymer supports are of great interest because they can be recyclable and also have a higher local concentration of active centers. In fact, this proximity of active sites on the polymer matrix could increase the reactivity and selectivity of the catalysts by improving the bimetallic cooperation. In this context, this chapter is dedicated to the evaluation of immobilized salen complexes on supports, focusing on the reactions of ARO of cyclohexene oxide, the HKR of epibromohydrin and the Henry reaction.

5.2. Homogenous Catalysis

In this section, the catalysis reactions were first tested in homogenous conditions to i) get the handling of the reaction, ii) develop analytical methodologies for following the reactions before their involvement in homogeneous supported conditions. The main techniques used was gas chromatography, either with achiral (for the determination of conversion and yield) and chiral columns, or high-performance liquid chromatography (HPLC) mostly for the determination of enantioselectivity values.

5.2.1. Asymmetric ring opening (ARO) of epoxides

The prepared chromium supported catalysts are engaged to promote the ARO of cyclohexene oxide with TMSN_3 . Therefore, this reaction was first studied in homogenous conditions with the unsymmetrical Cr^* catalyst bearing a propargyl moiety (**10**) so to develop the conditions for GC analysis. The conversion of this reaction can be followed by an achiral GC, but the chiral column (chiraldex β -PM column) can also resolve all products enabling the analysis of both conversion and enantiomeric excess within the same injection. The reaction was followed up to 5h yielding 64% conversion of the substrate, and then let it continue over the weekend, delivering the product with complete conversion and enantiomeric excess of 78% (**Scheme 48**). The product is quite volatile and therefore not easy to purify as it evaporates with solvent evaporation under reduced pressure, for instance. Therefore, the main technique used to follow this reaction is by chiral GC using dodecane as internal standard. The absolute stereochemistry was assigned as *1S*, *2S* based on comparison with the literature.¹⁰⁰



Scheme 48: Reaction conditions for the ARO of cyclohexene oxide using unsymmetrical Cr-salen catalyst in homogenous media.

Compared to the chiral Jacobsen catalyst, the reaction was followed during 24h with full conversion and 81% enantioselectivity. The conversion at 5h reaction shows 42% conversion,

lower than the unsymmetrical catalyst presented before, suggesting that the kinetics is higher when using the Cr-salen 10. These results are summarized in **Table 23**.

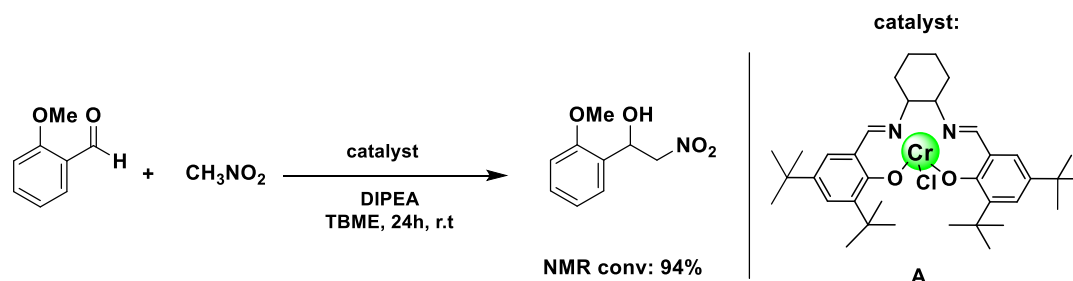
Table 23: Summary of the results obtained for the ARO of cyclohexene oxide in homogenous media.

Catalyst	Time (h)	Conversion (%)	Enantioselectivity (%)
<i>R, R</i> Cr-Ussymmetrical salen (6)	5	64	Not checked
<i>R, R</i> Cr-Ussymmetrical salen (6)	72	100	78
<i>R, R</i> Cr-Jacobsen	5	42	74
<i>R, R</i> Cr-Jacobsen	8	72	76
<i>R, R</i> Cr-Jacobsen	24	100	81

5.2.2. Henry reaction

The nitroaldol reaction of 2-methoxy benzaldehyde with nitromethane in great excess using DIPEA and methyl *tert*-butyl ether (TBME) as solvent was performed at r.t for over 24 hours (**Scheme 49**). The reaction was promoted using a racemic Cr-Jacobsen catalyst in order to understand the reactivity of this reaction and also to develop the analytical methods to follow and analyze the reaction. After 24h reaction, the crude was obtained as a brown oil, and ¹H-NMR shows 94% conversion of the product compared to the limiting reagent, the 2-methoxy benzaldehyde.

Chiral HPLC conditions resolved both enantiomers, showing that a racemic product was obtained (chromatogram in **Appendix B**). The product *R* or *S* was assigned following the literature.^{107b}

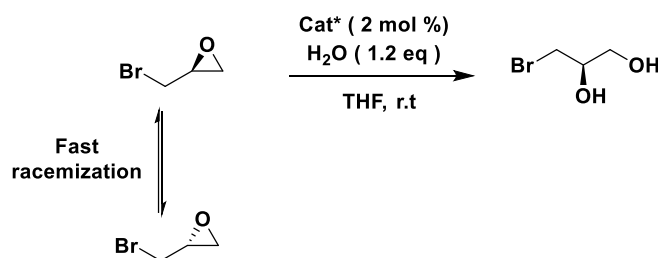


Scheme 49: Reaction conditions for the nitroaldol reaction of methoxy benzaldehyde using racemic Cr-salen catalysts in homogenous conditions.

The same reaction was performed using chiral (*R,R*) Cr-Jacobsen which yields the product with 91% NMR conversion and 44% *ee*. Since the reaction with the silicon supported catalysts usually is performed using very low quantities of reagents, it is necessary to develop a technique that can easily follow the reaction in dilute conditions. Therefore, a GC methodology was developed for the follow up of the reaction in which the two starting materials, and the internal standard tetradecane, as well as the formed product can be detected in a 20 min range, at a very low concentration.

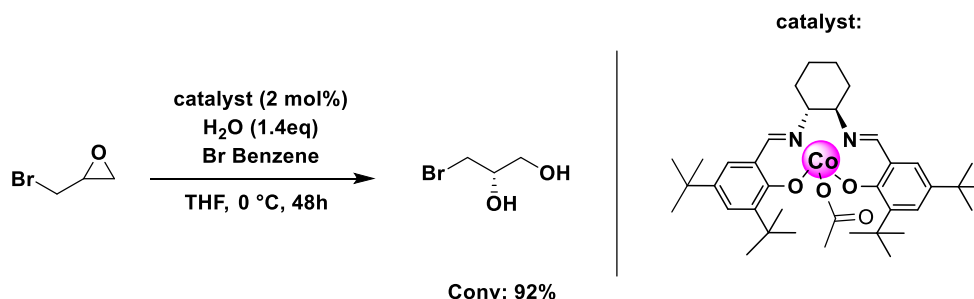
5.2.3. Hydrolytic Kinetic Resolution (HKR) of epibromohydrin

To evaluate the catalytic activity of the cobalt salen complexes, we have chosen to study the dynamic hydrolytic kinetic resolution of epibromohydrin. It can undergo dynamic splitting thanks to its rapid racemization under common reaction conditions (**Scheme 50**).¹⁷⁷



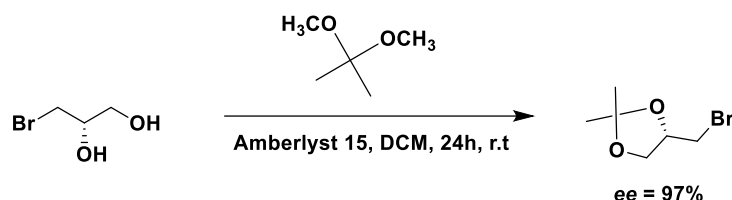
Scheme 50: Dynamic HKR of epibromohydrin.

The reaction is performed using 2 mol% of catalyst, a salen-Co(III)-OAc, in THF at 0°C (**Scheme 51**). Water is added and the reaction is followed over 24 h by GC chromatography with an achiral stationary phase (ZB 1701) using bromo-benzene as standard. The reaction is faster in concentrated solutions, and with an 8.3 M solution, the conversion reaches 92% in 48h with 97% enantioselectivity.



Scheme 51: Reaction conditions for the HKR of epibromohydrin catalyzed by (*R,R*) Co-salen catalyst.

The enantioselectivity is determined by chiral GPC (Chiraldex β -PM column), after having protected the diols formed as an acetonide (**Scheme 52**). With their high polarity, it is then possible to analyze it by chiral GC. The product can also be purified by column chromatography using pentane : diethyl ether 95 : 5 as eluent in a silica stationary phase, but in the context of this thesis, the reactions using supported catalysts were done in small batches (order of 0.1 mmol), therefore, the product was only analyzed by GC.

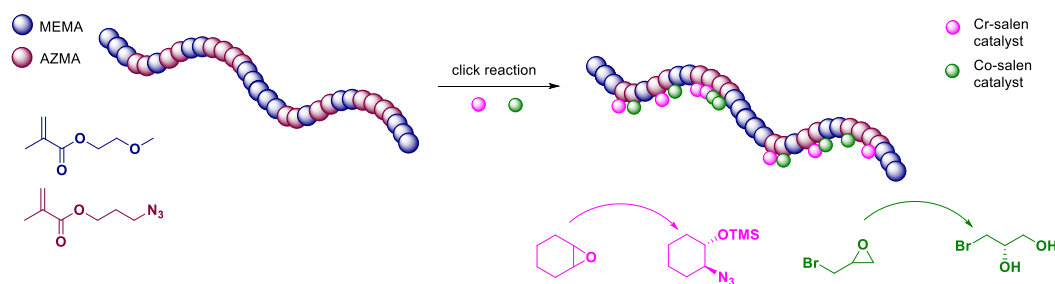


Scheme 52: Protection of diols in the form of acetonide for the enantioselectivity determination.

5.3. Multipurpose supported catalysis

This part has been inspired by the article by [Rafaela Bechara](#), Philippe Roger, Mohamed Mellah, Nadine Barroca-Aubry, François Ozanam, Anne-Chantal Gouget-Laemmel, Emmanuelle Schulz. Development of multipurpose supported asymmetric salen catalysts by SARA copolymerization. Manuscript in preparation.

Designing supported catalysts that ensure efficient recycling and reuse of the catalyst in a wide range of transformations remains a real challenge. In this section, targeted copolymers are used as supports for the development of homogeneous-supported asymmetric catalysts. They are the modified copolymers described in **Chapter 4, section 4.5.2**, p. 145. To recall, SARA-Cop1 has a loading of 70/30 MEMA/AZMA and SARA-Cop2 has 30/70. These copolymers were post-functionalized with two chiral salen catalysts, one containing a chromium center and the other a cobalt one. Their activity is evaluated in two different reactions after simple precipitation, allowing the catalyst to be reused. The first reaction involves the asymmetric ring opening of cyclohexene oxide with trimethylsilyl azide, catalyzed by the chromium sites,¹⁰⁰ and the second reaction was the asymmetric ring opening of epibromohydrin with water, promoted by the cobalt sites^{177b} (**Scheme 53**).



Scheme 53: Multipurpose catalysis using functionalized copolymers with chromium and cobalt salen complexes, SARA-Copo-Cat1 and SARA-Copo-Cat2, respectively.

The Jacobsen homogenous catalysts were also engaged in the other reaction, *i.e.* Cr-catalyst for the DKR of epibromohydrin and Co-catalyst for the ARO of cyclohexene oxide, to see whether or not the cobalt and chromium catalysts are active to promote the other reaction. To the best of our knowledge, these reactivities are not described in the literature.

After 5h of reaction, chiral (*R,R*) Co-OAc Jacobsen catalyst did not promote the ARO of cyclohexene oxide, followed by chiral GC as explained in **section 5.2.1**. In the same time, Cr catalysts usually promote around 40 – 60% conversion. However, after 24 hours of reaction, it can be observed that the chiral (*R,R*) Co-OAc Jacobsen complex catalyzes the reaction with a conversion of 70% and an *ee* of 51%. These results are summarized in **Table 24**.

Table 24: Results for the reactivity and enantioselectivity of cobalt and chromium Jacobsen catalysts for the ARO of cyclohexene oxide.

Catalyst	Time (h)	Conv. (%)	<i>ee</i> (%)
Chiral (<i>R,R</i>) Cr-Cl Jacobsen	5	42	74
Chiral (<i>R,R</i>) Cr-Cl Jacobsen	24	100	81
Chiral (<i>R,R</i>) Co-OAc Jacobsen	5	0	N/A
Chiral (<i>R,R</i>) Co-OAc Jacobsen	24	70	51

The same evaluation was done for the DKR of epibromohydrin, and the chiral Cr-Jacobsen catalyst also promoted the reaction. After 48h of reaction, the reaction is promoted with 47% conversion with an enantioselectivity of 87%. In the same conditions, the Co-Jacobsen catalyst promotes the full conversion of epibromohydrin with a 97% enantioselectivity. Therefore, the fact that Co and Cr promote both reactions, but with different enantioselectivity, we expect the enantioselectivity of the prepared multipurpose catalyst to be lower than compared to the catalyst alone.

Table 25: Results for the reactivity and enantioselectivity of cobalt and chromium Jacobsen catalysts for the DKR of epibromohydrin after 48h reaction.

Catalyst	Conv. (%)	ee (%)
Chiral (<i>R,R</i>) Co-OAc Jacobsen	92	97
Chiral (<i>R,R</i>) Cr-Cl Jacobsen	47	87

Therefore, both catalytic reactions were performed with 2 mol% of the Cr or Co active sites in the support relative to the limiting reagent used (either cyclohexene oxide or epibromohydrin), and since the modified polymer catalysts have both Cr and Co sites which are active for both reactions, the obtained *ee* is unfortunately lower due to the contribution from the species. In other words, the *ee* and conversion is thus an average of both reactivities and selectivities. The calculation of the mass of supported catalyst for the catalytic reaction is described in the experimental section.

The first catalytic reaction tested was the ring opening of cyclohexene oxide (run #1) with trimethyl silylazide in diethyl ether. Using SARA-Copo-Cat1 with an approximate density of 6% of active sites in the modified polymer matrix, the reaction reached 50% conversion after 8 hours of reaction and went to completion in 24h with 62% *ee* for the target product. The enantioselectivity is close to that obtained using a similar modified copolymer use for the ARO of cyclohexene oxide.^{8b} Then, the catalyst was precipitated using dry hexane, washed, dried and re-engaged in a second reaction. The second reaction uses the cobalt catalytic sites to perform the hydrolytic ring opening of epibromohydrin (run #2). With also ~ 6% of cobalt sites in the copolymer matrix, the supported catalyst achieved 40% conversion after 72 h of reaction, with an enantiomeric excess of 80%. This reaction usually works better in concentrated media, but as a minimum amount of solvent is required to solubilize the supported catalyst in THF, this reaction was performed under rather dilute conditions (0.24 M compared to usual 8.3 M in homogenous conditions), explaining the lower conversion for this transformation. Finally, the catalyst was once again precipitated, washed and dried to be engaged in another ring opening of cyclohexene oxide (run #3). The catalyst retained an analogous enantioselectivity value, showing only a marginal difference from 62 to 58% enantiomeric excess. However, the activity was slightly lower in the third run (88% versus total conversion in first run), which can be explained by some losses during catalyst precipitation and washing.

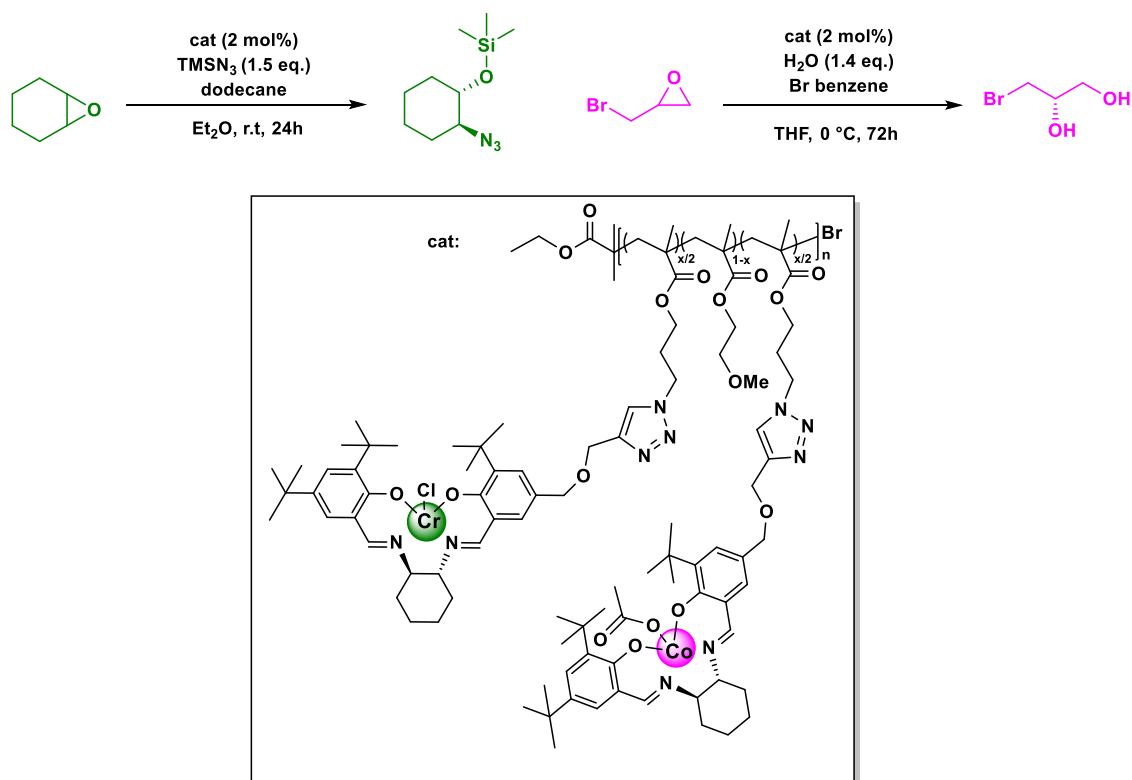
SARA-Copo-Cat2 has approximated the double density of catalytic sites as compared to SARA-Copo-1. With this catalyst, the promotion of the ARO of cyclohexene is much faster,

with 83% conversion after 8 h of reaction, reaching its completeness in 24 h. However, lower enantiomeric excess is obtained compared than its counterpart, going down to 40% *ee*. For the second reaction, the activity remained the same as observed for the SARA-Copo-Cat1, but as well with a decrease of enantiomeric excess, now at 54%. Finally, in the third run – once more the ARO of cyclohexene oxide – this catalyst showed an activity of 98% conversion after 24h, but a 48% enantiomeric excess. These results are summarized in **Table 26** and **Scheme 54**.

Table 26: Summary results of the ARO of cyclohexene oxide (24 h reaction) and DKR of epibromohydrin (72 h reaction) using the supported catalysts.

	SARA-Copo-Cat1		SARA-Copo-Cat2	
	Conv (%)	<i>ee</i> (%)	Conv (%)	<i>ee</i> (%)
1st run – ARO cyclohexene oxide	99	62	>99	40
2nd run – DKR epibromohydrin	42	80	40	54
3rd run – ARO cyclohexene oxide	88	58	98	48

The recycling of the catalysts performed on different transformations proved to be effective, demonstrating both the robustness and the versatile application of the procedure.



Scheme 54: ARO of cyclohexene oxide and DKR of epibromohydrin using the supported catalysts.

The enantioselectivity found for SARA-Copo-Cat1 (62% *ee*) follows the expected value for the ARO of cyclohexene oxide when using a catalyst with a 70/30 loading of MEMA/AZMA as described by Bakangura and coworkers.^{8b} The *ee* found for the DKR of epibromohydrin (80%) is lower than the values obtained for this reaction in homogeneous media, but explainable considering that supported catalysts have usually lower selectivity due to the hindered catalysts, for instance.

However, the enantioselectivity found for SARA-Copo-Cat2 for both reactions is much lower than compared to SARA-Copo-Cat1. With the catalytic sites more closely packed together, the chromium sites could hinder the promotion of DKR of epibromohydrin by the cobalt sites, and vice-versa, therefore lowering the enantioselective values.

This study showed the versatility of the prepared multipurpose catalysts. Nevertheless, it is necessary to test these supported catalysts on truly orthogonal reactions in order to better evaluate their efficacy.

5.4. Silicon supported monocatalysis

Following the development of silicon supported catalysts for multi-step catalysis, first it is necessary to understand rather the silicon support is adequate for this application. Therefore, before developing a support catalyst with two catalysts that engage in sequential catalysis, a simpler case was developed. In **Chapter 4**, the design of silicon supported catalyst was described in **section 4.6.2**, namely PSiBr1-Cop3-Cat. It is a supported catalyst based on macroporous silicon containing chromium sites that were reacted with the azide function of a 50/50 MEMA/AZMA copolymer on surface. After quantification of the catalytic sites, we obtained approximately 1.1×10^{-7} mol of catalyst for this specific sample (**Table 22**).

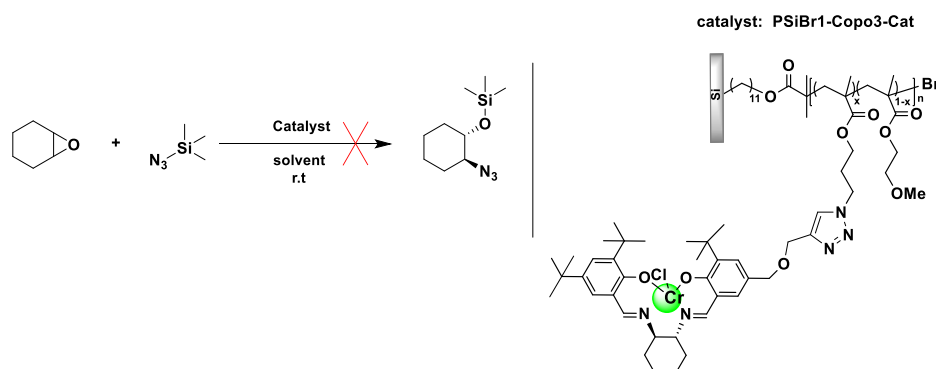
Therefore, catalysis trials using macroporous silicon were performed in two different reactions, first the ARO of cyclohexene oxide and then the nitroaldol reaction of methoxy benzaldehyde.

5.4.1. ARO of cyclohexene oxide

The reaction was performed in a special Schlenk for prisms in which the depth of the material is much smaller than usual Schlenk, providing it a square shape with approximate dimensions of 20 mm × 15 mm × 4 mm. This enables the reaction to use less solvent than a normal Schlenk. However, since the number of mol of catalyst is very low (10^{-7} range), a first trial using 0.5 mol% of the catalyst was tried. Since a minimum quantity of solvent is needed to immerse the supported catalyst, the concentration of the reaction was 0.05M compared to the usual 1M in the homogenous case. The reaction was performed in diethyl ether, using dodecane as standard and followed after 6 h, 24 h and 72 h by chiral-GC (as explained in **section 5.2.1**), but no product was formed. However, the amount of the substrate decreased in relation to the standard (dodecane) after 24 h, meaning that either the starting material, as being quite volatile, evaporated from the media, or that the product was formed but was not stable enough and possibly transformed into another sub product.

In a second trial, the catalyst was engaged in a 2 mol% equivalence, but in order to do so, less reagent was used, and therefore, the reaction was less concentrated (0.007 M) than compared to first trial. No reaction was observed until 72 h in which the starting material decreased in proportion in relation to the standard accounting for approximately 10% of starting material reacted, but no peak was observed for the product.

In yet another trial, the solvent of the reaction was changed to THF, since the copolymers are soluble in THF, and insoluble in diethyl ether, it was thought that by well solubilizing the copolymers chain on the surface it would help the catalysis. However, after 8 days, no catalysis was observed with no change in the proportion of the starting material, neither the appearance of new peaks. The reaction conditions and summary of these findings is shown in **Table 27** and **Scheme 55**.



Scheme 55: ARO of cyclohexene oxide using the silicon supported Cr catalyst.

Table 27: Summarized results for the catalysis trials using silicon supported Cr-catalyst for the ARO of cyclohexene oxide.

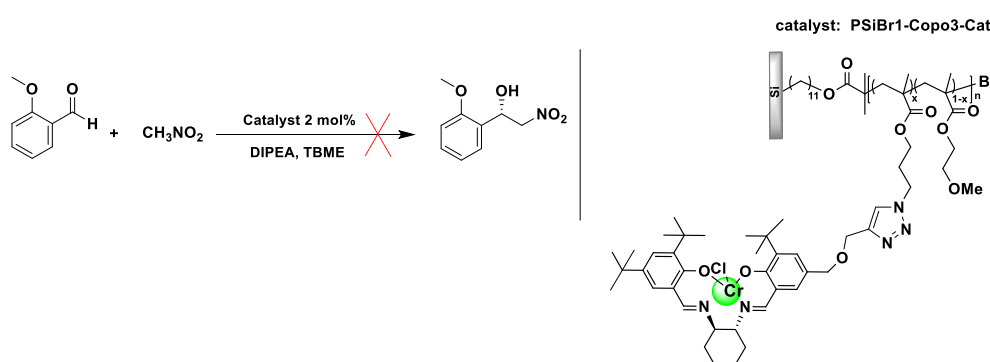
Trial #	Solvent	Catalyst loading (mol %)	Concentration (mol/L) ^a	Comments
1	Diethyl ether	0.5	5×10^{-2}	No peak from product. Decrease of starting material.
2	Diethyl ether	2	7×10^{-3}	No peak from product. Decrease of starting material.
3	Tetrahydrofuran	2	1×10^{-2}	No sign of reaction after 8 days.

^a using moles of cyclohexene oxide

These trials made it clear that this reaction is not the best reaction to be tested in such hard conditions as these, *i.e.* diluted solutions, long reaction times, poor stability of product etc. Therefore, another reaction was proposed, for which the product is more stable and should help resolving these problems observed in the ARO of cyclohexene oxide. The nitroaldol reaction (Henry reaction) of orthomethoxy benzaldehyde with nitromethane is thus described in the next section.

5.4.2. Henry reaction

The nitroaldol reaction of 2-methoxy benzaldehyde yields a product, the 1-(2-methoxyphenyl)-2-nitroethan-1-ol, which should be more stable than the product for the ARO cyclohexene oxide, the azidocyclohexyl oxy trimethylsilane, as it is less volatile and has less reactive functional groups. Therefore, this reaction was tested using the same conditions as the one performed in homogeneous conditions, using 2 mol% of catalyst, and using DIPEA as a base and methyl *tert*-butyl ether (TBME) as solvent (**Scheme 56**). The reaction was performed at a 0.021 M concentration, and followed by achiral GC (as explained in **section 5.2.2**), but no product was observed even after 2 weeks of reaction.



Scheme 56: Nitroaldol reaction of methoxy benzaldehyde using the silicon supported Cr catalyst.

Unfortunately, the silicon supported catalyst did not work in the reactions tested under the conditions thereafter mentioned. Perhaps the catalyst loading on the support is still very low and therefore it does not promote the reactions even if respecting the mol% of the reaction. As the conditions are very diluted, the access of the reagents to the catalytic sites might be compromised. Still, it is possible that the catalysts are hindered/not accessible on the surface; therefore, unable to promote the reaction.

To the best of our knowledge, silicon supports were never used as supports for applications in asymmetric catalysis. Still, we have shown the development of the silicon supported catalyst and its characterization by XPS and ATR-FTIR. Improvements such as increasing the copolymer density on surface by prolonging the polymerization reaction time, as well as increasing the surface area of the macroporous silicon could be viable solutions for subsequent supported asymmetric catalysis using silicon supports.

5.5. Conclusions

The final aim of this thesis project is to develop silicon supported catalysis to undergo multi-step catalysis. This is a very challenging goal since no catalysts using silicon for asymmetric catalysis are described in the literature. In this chapter, the reactivity and enantioselectivity of the developed catalysts were discussed, either using the free copolymers as supports or using the copolymers on macroporous silicon as supports.

Regarding the catalysts using free copolymers as supports, they have shown a proof of concept in which the same supported catalyst can promote two reactions, which were at first ideally orthogonal, but showed to be promoted by both catalytic sites. However, this is a first step towards the sequential multi-catalysis using the copolymers of MEMA/AZMA, and the results show that the copolymers are suitable supports for these applications. Although the enantiomeric excess was lower than envisioned, this study validates the strategy and gives insights for the further development of the supported catalysts for truly orthogonal and/or tandem catalysis.

Considering the silicon supported catalysts, they have not been effective for the reactions tested and under the conditions analyzed. This could mean that either the catalysts sites on surface are not available for the reaction or that the conditions tested are not yet optimized considering this support. In the first case, the catalysts sites could be hindered or cluttered with other catalytic sites inside the pores, making it hard to promote the reaction in confined spaces, for instance.

As perspectives, a way to improve the catalysis trials using silicon supported catalysts is to first increase the surface area of the support. This can be done by simply using bigger samples of the studied macroporous silicon, or increasing the pore thickness of the samples. Also, longer polymerization time for the copolymerization of MEMA/AZMA using this support could potentially increase the number of azide sites, to finally have more catalytic sites available for the reaction.

Nevertheless, this development of supported catalysts using copolymers on silicon brings the very first steps towards asymmetric salen catalysis using silicon as support.

CHAPTER 6

General conclusions and perspectives

6.1. General conclusions

This thesis focused on developing salen-supported asymmetric catalysis on silicon surfaces using controlled radical polymerization techniques. Silicon is chosen for its well-established surface chemistry and the ability to form robust Si–C bonds, enhancing the stability of the attached catalyst and preventing metal contamination in the reaction mixture. This thesis objective was to develop salen-supported catalysts on silicon, initially focusing on studying the hydrosilylation of different initiators for Atom Transfer Radical Polymerization (ATRP) on silicon surfaces through microwave-assisted reactions. Then, these initiated-surfaces were engaged in the polymerization of methacrylates by Surface-Initiated ATRP (SI-ATRP), followed by the final step of grafting with the attachment of salen catalysts using click chemistry. The supported catalyst based on silicon has an advantage over other common supports as it can be removed from the reaction media with a tweezer without filtration. The ultimate goal is to obtain good reactivity and selectivity using these supported salen catalysts based on macroporous silicon, marking the first contribution of salen catalysts supported on silicon.

In chapter 2, the grafting of initiators onto crystalline and macroporous silicon surfaces using microwave activation was investigated. The modified surfaces were characterized using ATR-FTIR, XPS, AFM, and contact angle measurements. A comprehensive study of the microwave grafting of three distinct initiators both on oxidized and hydrogenated silicon surfaces showed that the best case is that of grafting initiator 1 on SiH_x surface. This surface was obtained with good reproducibility under the optimized conditions providing a grafting

density of ~ 0.7 molecules $\cdot\text{nm}^{-2}$. Even though XPS analysis show no clear proof of Si–C bond formation, and therefore a possible grafting of the initiator 1 via Si–O–C for SiBr1 is considered, it does affect the final application of these supported catalysts. In fact, since all further reactions are in common organic solvents, there is no risk of hydrolysis. Besides, despite AFM imaging indicating the formation of agglomerates and disorganized molecular grafting, microwave activation proved to be an effective method for grafting sensible molecules such as the initiator thereafter studied for SI-ATRP.

As seen in chapter 3, the development of methacrylate-type copolymers in solution was explored using both classical and SARA ATRP methodologies. The copolymers of MEMA/AZMA typically provided higher dispersities than compared to the homopolymerization of MEMA or the copolymerization of MEMA/HEMA due to potential side reactions that are known to occur with azide moieties via either thermal or photochemical pathways. Nevertheless, these copolymers were obtained typically with dispersities lower than 1.5. SI-ATRP of MEMA and copolymers of MEMA/AZMA were developed using crystalline and macroporous silicon surfaces. Comparative analysis showed that SI-ATRP of MEMA provides precise control over surface-bound polymerization, with DP ranging from 50 to 200 and polymer brushes with thickness up to 10 nm. Longer polymer brushes of thickness ~ 23 nm were also obtained with prolonged polymerization reaction, thus allowing the development of polymer brushes with different thicknesses. The SI-ATRP of the copolymers of MEMA/AZMA respected the initial feed of monomers, consequently allowing the development of polymer brushes with different ratios of comonomers, evidenced by quantitative ATR-FTIR. Comparing the crystalline to the macroporous silicon, the later has ~ 80 times more the area of crystalline silicon, which was also evidenced by the semi-quantification of comonomer units/ nm^2 grafted in both cases.

Later, the study of click chemistry using the developed copolymers was presented in chapter 4. It explores the synthesis of salen catalysts and FTIR markers. Salen ligands were coordinated with chromium and cobalt metals and characterized using UV-vis, ATR-FTIR, and mass spectrometry. The use of click chemistry on MEMA/AZMA copolymers, both in solution and on the surface, was then investigated. Initially, the aryl compounds (FTIR markers) were subjected to click reactions with copolymers in solution to assess the effectiveness of the reaction. Then, two categories of salen-supported catalysts emerged: those tethered to free copolymers and those attached to the brushes of copolymers grown on the macroporous silicon

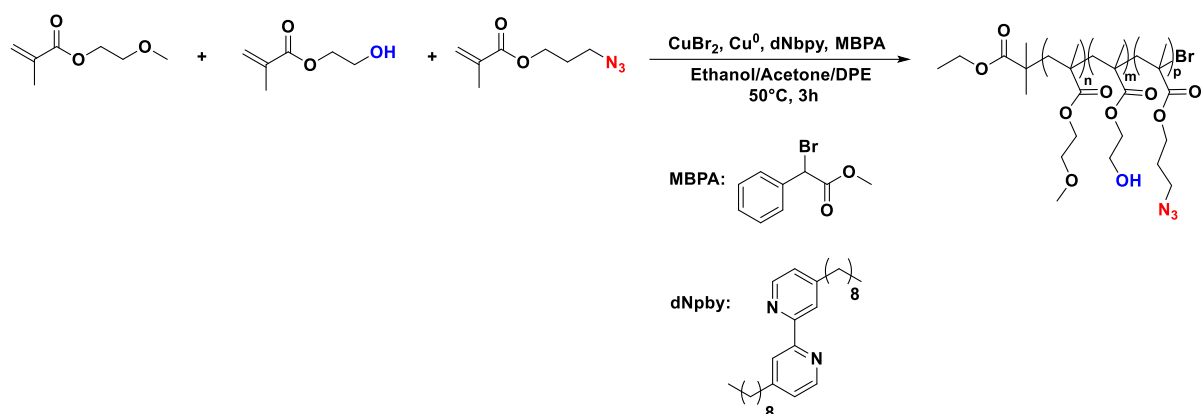
surface. In the first scenario, two distinct salen catalysts were employed for the use of multipurpose catalysis. In the latter scenario, a chromium salen catalyst was immobilized onto the surface, yielding a monocatalyst supported on macroporous silicon. These modified catalysts were studied using ATR-FTIR and XPS spectroscopy, revealing the accuracy of the constructed structures. Thus, click chemistry serves as a versatile tool for surface modification, facilitating the creation of intricate structures.

This thesis project final goal is to develop silicon-supported catalysis for multi-step catalysis, a challenging objective considering its complex chemistry. The developed catalysts were then applied, and considering the multipurpose catalysts (SARA-Copo-Cat1 and SARA-Copo-Cat2), the study demonstrated that they can promote two different reactions, evidencing that the copolymers are suitable supports for sequential multi-catalysis applications. Although the enantiomeric excess was lower than expected since the two catalysts can promote both reactions, the study validates the strategy and provides insights for further development of supported catalysts for true orthogonal and/or tandem catalysis. However, the silicon-supported catalyst has not been effective for the tested reactions and conditions, potentially due to hindered or cluttered catalytic sites, and/or low catalytic loading.

6.2. Perspectives

6.2.1. Copolymers of MEMA/HEMA/AZMA

Following with the development of the copolymers with three comonomers using SARA ATRP, preliminary trials using a mixture of three solvents (ethanol/acetone/DPE in 47.5/47.5/5 v/v proportion) was tested. Since a higher experimental M_n value than the calculated value was observed for the copolymers of MEMA/AZMA, which was then attributed to the lower initiation rate of eBiB, another initiator was tested for the copolymerization of MEMA/HEMA/AZMA. Methyl α -bromophenylacetate (MBPA) was employed since Nguyen and coworkers showed a higher initiation rate compared to eBiB (**Scheme 57**).¹⁴⁸ The preliminary results shows lack of homogeneity in the copolymers obtained, evidenced by the SEC profiles with clear polymodality of the synthesized copolymers, probably indicating the preference for homopolymerization versus the copolymerization route. The dispersity for all cases is high ranging from 2.2 to 4.



Scheme 57: Reaction conditions for the SARA copolymerization of MEMA/HEMA/AZMA.

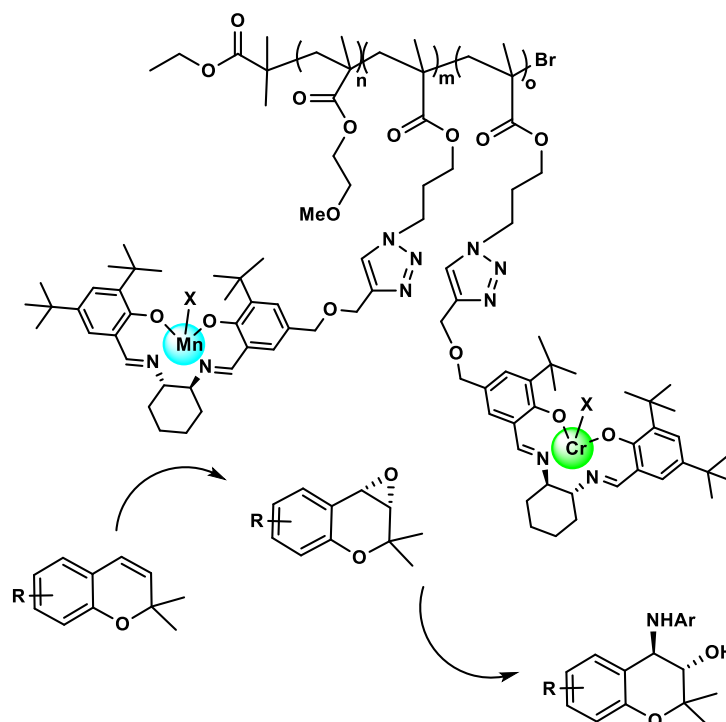
As perspectives, the reaction conditions of the copolymerization of MEMA/HEMA/AZMA should be further investigated by first changing the solvent, then the temperature, and then finally the ligand, in order to obtain copolymers with good dispersities (<1.5). The copolymers can be analyzed by ATR-FTIR since peaks associated to the functional groups N_3 (from AZMA) and OH (from MEMA) are characteristic and well visible, and thus their further post-modification can be followed by FTIR spectroscopy.

These preliminary results are promising and suggests that the strategy employing the two functional monomers to design bifunctional copolymers for multi catalysis is encouraging.

6.2.2. Supported catalysis

6.2.2.1. Using copolymers in solution

The multipurpose catalysts supported on copolymers of MEMA/AZMA described in this thesis demonstrated to be promising platforms to obtain orthogonal and/or sequential multicatalysis. Further development in this part should continue in order to test the developed catalysts in true orthogonal catalysis. The same methodology can then be applied using the chromium and manganese catalysts to finally obtain sequential multicatalysis by first transforming a chromene into an epoxide catalyzed by manganese catalysts, and then proceeding to a ring opening reaction catalyzed by chromium catalysts (**Scheme 58**).



Scheme 58: Proposed multi-step catalysis using copolymers of MEMA and AZMA.

6.2.2.2. Using macroporous silicon

Considering the tests using macroporous silicon, it is evident that a higher surface area for the substrate is needed. This can be done by simply using larger samples of the studied macroporous silicon, or by increasing the pore thickness of the samples. There are some constraints when developing the macroporous silicon for this project. In fact, a minimum of 70 – 100 nm pore size is needed to allow the growth of polymer brushes, the attachment of the salen catalysts, and the diffusion of the reagents on the pores. In the current state, macroporous silicon particles seems to be a better candidate for applications in catalysis compared to the flat macroporous silicon. The use of macroporous silicon particles is advantageous since its surface area is higher comparing to its analogous flat macroporous silicon (considering same pore size). Also, particles enable the use of higher quantity of material during the catalytic tests. The analysis can be performed with common ATR-FTIR analysis, and possible with BET and TGA analysis.

The development of these macroporous silicon particles are currently under study by our collaborators. Then, the same methodologies developed in this thesis will be applied to the macroporous silicon particles and those will be tested in the catalysis trials. We believe that

these new substrates will be a better fit for the envisioned application, bringing the very first steps towards asymmetric salen catalysis using silicon as support.

CHAPTER 7

Experimental section

Equipment

Atomic Force Microscopy (AFM)

AFM images were obtained using an Agilent 5500 SPM microscope, AC-mode, with silicon probes (μ Masch, resonance frequency ~ 180 kHz) and under N_2 atmosphere. The scratches on surface to determine the thickness of the polymer brushes were done with a needle on the perpendicular sense to the scanning probe.^{8a}

Attenuated Total Reflection Fourier Transform Infrared Spectroscopy

ATR-FTIR spectra were recorded on a Bruker Equinox FTIR spectrometer or on a Bomem MB100 FTIR spectrometer, both coupled inert (N_2) ATR, and a liquid nitrogen cooled MCT detector. All spectra were recorded in *s*- and *p*- polarization in the spectral range of 900 to 4000 cm^{-1} (200 scans, 4 cm^{-1} resolution). The dimensions of the prism limited the infrared path length in silicon, providing access to observable vibrations as low as 1000 cm^{-1} . The spectra are presented in absorbance (computed using natural logarithm) and are normalized to the reflection number (around 22). The reference spectra are that of the previously modified surface, being either SiO_x or SiH_x for the grafting of the initiators, or the $SiBr$ for the polymer brushes on surface, or the Si-polymers for the modification of polymers. The IR calibration was performed in a home-made PTFCE IR cell of ~ 2 mL volume. A PTFE tube (0.8 mm diameter) is connected on the top and the bottom of the cell to allow the addition of different

solutions without breaking the spectrometer purge. On the side there is a 9 mm diameter opening against which the Si prism (sample) is pressed via a nitrile O-ring seal.

The detector for measurement in ATR geometry is an MCT (Mercury Cadmium Telluride) detector, which is a p-n junction made from a small-gap semiconductor that must be cooled with liquid nitrogen before use. The compartment containing the detector, the parabolic mirrors as well that the sample is purged with nitrogen to avoid the absorption of atmospheric water molecules.

Chiral High-Performance Liquid Chromatography (HPLC)

Analyzes were performed on a Chromatograph composed of Jasco PU-2089 Pump, Hitachi oven column selector column, and TSP UV-100 UV detector

Ellipsometry

Thickness measurements were carried out using an Accurion nanofilm EP3 ellipsometer. The thickness was obtained by measuring the change in the polarization of light (at fixed $\lambda = 658$ nm) as it was reflected off the surface over a range of angles (from 50° to 75° with 1 step number). Thicknesses were obtained with an accuracy up to a fraction of nanometer.

Infrared Spectroscopy for powders

Synthesized powders were deposited on the diamond crystal of an ATR module from Pike Technologies and the infrared spectrum was recorded using a Bruker IFS 66 spectrometer. Two hundred scans of resolution 4 cm^{-1} were recorded between 600 cm^{-1} and 4000 cm^{-1} . Spectra visualization and treatment were done using OPUS software.

Gas Chromatography (GC)

Achiral and chiral gas chromatography analyses were performed on a GC Shimadzu 2010 Plus, FID, SSL using hydrogen as a carrier gas. For the HKR of epibromohydrin, the conversion was determined by using an achiral column ZB-1701 15 m x 0.25 mm x 0.25 μm with a ramp of temperature starting at 50°C for one minute, and then increasing $10^\circ\text{C}/\text{min}$ until 250°C , with a constant pressure of 26.2 kPa. The enantioselectivity was determined with a Chiraldex column B-PM with dimensions of 50 m x 0.25 mm x 0.12 μm at a constant temperature of 110°C for 35 minutes. The pressure was constant at 112.6 kPa. The same chiral column, and same

methodology was applied for obtaining the conversion and enantioselectivity for the ARO reaction of cyclohexene oxide. The conversion of the nitroaldol reaction was analyzed in an achiral column ZB5-MS of dimensions 15 m x 0.25 mm x 0.25 μ m with a ramp of temperature starting at 100 °C for one minute, and then increasing 5 °C/min until 160 °C and then 10 °C/min until 250 °C, with a constant pressure of 32.1 kPa.

Size Exclusion Chromatography (SEC)

SEC analysis of polymers was carried out at 35 °C, using THF as an eluent. Typically, the polymer solution was prepared at 4 mg/mL and then filtered through a 0.45 μ m PTFE filter to remove insoluble residues. The separation system included one guard column (Malvern TGuard, Malvern, UK) and two separation columns: (1) Viscotek LC3000L (Malvern, UK) (300 \times 8.0 mm) and (2) ViscoGEL™ GMHH r-H (300 \times 7.8 mm, Malvern, UK). The intensities were recorded using a refractive index (RI) detector (Walter 410; Tübingen, Germany) and a multi-angle light scattering (MALS) detector (Viscotek SEC-MALS 20, Malvern, UK). Absolute number and weight-average molar masses were calculated using OmniSec™ 5.12.467 software, distributed by Malvern Panalytical (Malvern, UK). The refractive index increment (dn/dc) of 0.078 mL/g, determined by Stejskal *et al.*¹⁷⁸ for polyMEMA in THF at 546 nm, was also used for polyAZMA based on their roughly similar chemical structures.

Mass spectrometry

ESI-HRMS was detected on a Bruker MicroTOF-Q daltonics spectrometer (Billerica, MA, USA) by electrospray ionization (ESI).

Nuclear Magnetic Resonance (NMR)

¹H and ¹³C spectra were recorded on a Bruker (Bruker AM 400 (400 MHz), 360 (360 MHz), 300 (300 MHz)) instrument with samples dissolved in CDCl₃. Chemical shifts (δ) are given in parts per million (ppm) with the signal of the residual CHCl₃ of the solvent as reference (7.24 ppm for ¹H NMR). The following abbreviations were used to describe the multiplicities: s (singlet), d (doublet), t (triplet), q (quadruplet), quint (quintet), m (multiplet), brs (broad singlet). All multiplicities were approximated to the first order; coupling constants, *J*, are reported in Hz and with an accuracy of 0.5 unit of the last digit.

Scanning electron microscopy (SEM)

The SEM pictures were taken in a Hitachi S-4800, with a field effect gun (FEG) which allows a resolution of a couple of ~2 nm at 5 keV energy. Secondary electrons for acquiring the images were used.

Ultraviolet–Visible Spectroscopy (UV-vis)

The UV-visible analysis was performed using a Bio-TEK UNIKON XL spectrometer with scanning from 200 to 500 nm.

Water contact angle

Static contact angle measurement was performed using a DSA100 Kruss analyser. The water contact angle was measured by depositing a 5 μ L droplet of UPW on surface, and five measurements were made for each droplet. The contact angle was calculated as an average of 4 droplets on each side of the prism.

X-Ray Photoelectron Spectroscopy (XPS)

These measurements were performed on a 2500 Xi spectrometer from ThermoFisher, equipped with a monochromatic X-ray Source (Al Ka, 1486.6 eV). For all measurements, a spot size of 900 μ m was employed. The hemispherical analyzer was operated in CAE (Constant Analyzer Energy) mode, with a pass energy of 100 eV and a step of 1 eV for the acquisition of surveys spectra, and a pass energy of 20 eV and a step of 0.1 eV for the acquisition of high-resolution spectra. A “dual beam” flood gun was used to neutralize the charge build-up. The recorded spectra were processed by means of Avantage software provided by Thermo Fisher using a peak fitting routine with Smart background (optimized Shirley background) and symmetrical Gaussian-Lorentzian line shapes. The quantification was performed after normalization of the peak areas with Scofield sensitivity factors.

Safety Practices

General Information and Handling of Hydrofluoric Acid (HF)

Anyone that works with hydrofluoric acid must adhere to the guidelines and procedures followed by its own institution. The goal of this guide is to advise people who would like to reproduce the experiments described in this thesis to safely handle hydrofluoric acid.

Information and training

The Principal Investigator (PI) is required to train employees on how to handle hydrofluoric acid, besides its potential hazards, and emergency practices. A Safety Data Sheet (SDS) of hydrofluoric acid must always be kept in the immediate work area.

Description

Hydrofluoric acid (HF) is a highly corrosive inorganic acid. Therefore, it must be handled with extreme caution. It can penetrate the skin and decalcifies bones leading to tissue necrosis, which may result in amputation and death. The level of severity depends on the concentration of the solution, the duration of exposure and whether it was exposed on skin, lungs, eyes, etc.

Symptoms of exposure may be delayed in less concentrated solutions; therefore, immediate medical attention is necessary even in the absence of any symptoms.

Handling

Before starting any work with HF, you should do the following:

1. Read the entire Safe Handling, Storage, and Disposal of hydrofluoric acid provided by your institution. If there is no such document, one must be prepared.
2. Read the whole Safety Data Sheet (SDS) for hydrofluoric acid.
3. Review the Standard Operating Procedure (SOP) from your laboratory. If an SOP does not exist, one must be prepared.
4. Locate the HF Specific First Aid Kit for your lab containing Calcium Gluconate Gels in case of spills.

You must always work inside a functioning chemical fume hood. Even manipulation involving small quantities of diluted HF solutions must be performed inside the hood. Keep the acid deep

inside the fume hood and as far away as possible from the user. You must dedicate a fume hood only for handling HF.

Place plastic trays the work surface before starting HF procedures to prevent contamination of the work surfaces. Use plastic beakers and containers for HF manipulations, and ensure that there are neither cracks nor brittleness.

Also, wash your hands thoroughly with soap and water after handling HF.

You must never work alone with HF and should limit all HF manipulations to regular office hours. Only trained personnel are allowed to work with HF.

Personal Protective Equipment (PPE)

Gloves

Neoprene or nitrile rubber gloves are the recommended gloves for working with HF, but their increased thickness reduces agility. Thus, wear two (or three) pairs of nitrile exam gloves, and change them often. After manipulating with HF, remove them without touching your skin and then wash your hands immediately.

When working with larger quantities of HF in procedures that do not require agility, wear heavy nitrile or neoprene rubber gloves, with a nitrile exam glove underneath.

Body

You should wear a long-sleeved shirt, long pants, and closed toed-shoes. Always wear a lab coat with sleeves. The recommended is also to use a chemical resistant apron.

Eye

When handling HF, the proper eye protection is approved safety goggles and a face shield.

!! Further information about safety practices, handling and emergencies related to HF, please refer to this reference.¹⁷⁹

Handling of azido-3-propyl methacrylate

Description

Azides constitute a highly reactive and versatile class of chemicals that are commonly used in chemical synthesis. They possess toxic properties and can be potentially explosive and shock sensitive under certain conditions (high temperature, for instance).

Safety of azides

There are two methods that may give you an insight about the safety of the azide you are working with: the C/N ratio and the Rule of 6. However, always consult with the laboratory supervisor before working with any organic azide.

Carbon to Nitrogen Ratio (C/N): with rare exceptions, the number of nitrogen atoms must not exceed the number of carbon atoms in an organic azide. Usually, the azide should also be quenched as soon as possible. The azides should be stored at -18 °C, and in the absence of light (preferably in plastic amber containers).¹⁸⁰

Rule of Six: there should be no less than six carbons per energetic functional group. Six carbons (or other atoms of about the same size) per energetic functional group provides sufficient dilution to yield the compound relatively safe. Less than six carbons per functional group can result in the material being explosive.^{158a}

Storage and handling of azido-3-propyl methacrylate

AZMA should be kept in the freezer (-10 °C) and used soon as it is synthesized (2 weeks maximum) to avoid the product to be degraded. While synthesizing AZMA, the workup solution with HCl should not be higher than 10 % v/v as azides may be reactive with acids. For the distillation of AZMA under vacuum, ensure to know the pressure of your vacuum pump to correctly set the maximum temperature of distillation. In our hands, a pump of 0.4 mbar was enough to purify half of the brut material at 80 °C under vigorous stirring and for a period of 20 minutes maximum. For better safety, start your first distillations at lower temperature such as 75 °C as AZMA can be shock sensitive at temperatures higher than 80 °C.⁸⁸

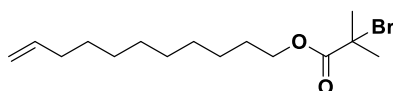
CHAPTER 2: Preparation of a surface-initiated layer on silicon

Materials

The cleaning agents for silicon prisms (hydrogen peroxide, H₂O₂, 30%; sulfuric acid, H₂SO₄ 96%) and etching agent (hydrofluoric acid, HF, 50%) were of RS grade and supplied by Carlo Erba. 10-undecen-1-ol (97%), α -bromoisobutyryl bromide (98%), 2-hydroxyethyl 2-bromoisobutyrate (95%), and triethylamine were purchased from Sigma Aldrich and used with no further purification. Mesitylene (98%) was purchased from Sigma Aldrich and filtered by an Al₂O₃ column before use (Al₂O₃ neutral, Brockmann I, 40-300 μ m, 60 Å). The solvents (tetrahydrofuran, ethanol, dichloromethane, toluene) were of RS quality and they were supplied by Carlo Erba. Ultrapure water (MilliQ, 18.2 M Ω ·cm, at 25°C) was used to prepare aqueous solutions and for rinsing the prisms. The silicon samples were cleaved from double-side polished p-type silicon with orientation (111) \pm 0.02°, FZ process, 5 – 6 Ω cm, 475 – 525 μ m, from Siltronic, France.

Methods

Synthesis of 10-undecylenic-2-bromoisobutyrate (1)



Chemical Formula: C₁₅H₂₇BrO₂
Exact Mass: 318,12
Molecular Weight: 319,28

To a solution 10-undecen-1-ol (1 eq., 30.75 mmol, 6.16 mL) in 50 mL of dry THF, 2-bromoisobutyrate bromide (1.1 eq., 33.75 mmol, 4.17 mL) was added, followed by addition of triethylamine (1.1 eq., 33.75 mmol, 4.7 mL) at 0 °C. The reaction mixture was allowed to stir for 3h under argon at room temperature. The white precipitates formed during the reaction were filtered using a small plug of silica. The solvent was removed under reduced pressure, and 50 mL of hexanes was added, which was then washed 3 times with deionized water. The organic phase was dried over anhydrous MgSO₄. The solvent was removed under reduced pressure to give the product as a colorless liquid (9.7 g, 98%).

¹H NMR (300 MHz, Chloroform-d) δ 5.81 (ddt, J = 16.9, 10.1, 6.6 Hz, 1H), 5.07 – 4.86 (m, 2H), 4.16 (t, J = 6.6 Hz, 2H), 2.04 (q, J = 6.6 Hz, 2H), 1.93 (s, 6H), 1.74 – 1.57 (m, 2H), 1.39 – 1.23 (m, 12H).

Preparing the silicon prisms for grafting

i. Polishing

The silicon wafer used for this project were produced by Siltronix, a (111) orientation silicon with a diameter of 4" (100 mm), p-doped (boron), with a resistivity of 5-6 Ωcm^{-1} and a thickness of 475-525 μm . The process of fabrication was of FZ (Float Zone). Rectangular pieces of $1.6 \times 1.8 \text{ cm}^2$ were cut using diamond pen and then glued in an aluminum support using bee wax for polishing the edges (**Figure 93**).



Figure 93: left) Silicon wafer pieces of $1.6 \times 1.8 \text{ cm}^2$ and right) pieces placed in the support for polishing.

The silicon pieces were then polished using 6 polishing papers of different grit sizes starting from the roughest to the softest paper: P120 \rightarrow P240 \rightarrow P400 \rightarrow P600 \rightarrow P800 \rightarrow P1200 and then using 3 polishing disks (SAT.S) of 6 μm , 3 μm and 1 μm . After having an evenly polished bevel, as shown in **Figure 94**, right picture, the prisms are cleaned by various washings of technical acetone, trichloroethylene and ultra sound washes using trichloroethylene, acetone SDS, ethanol RS and milli-Q water (10 min each). Later, the prisms are left in Piranha solution ($\text{H}_2\text{SO}_4/\text{H}_2\text{O}_2$, 3/1) at 100 $^\circ\text{C}$ overnight at the least.

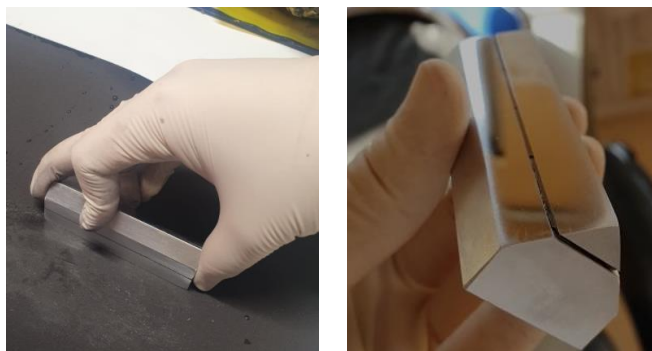


Figure 94: left) Polishing procedure and right) visually polished surface.

ii. Measuring angle of bevels and number of reflections

The silicon angle bevels are measured by measuring the difference in value of a reflected laser on each extremity of the bevel. The difference between the two values is the angle of the bevel. Knowing the exact angle of the bevels is important for the accurate calculation of the number of internal reflections during an ATR FTIR measurement. The ATR technique has its main advantage of increasing the sensitivity of the analysis. The principle relies on the propagation of the infrared beam inside the silicon prism, whose index is higher than the adjacent medium (N₂ atmosphere), by different reflections on the internal walls of the silicon crystal (**Figure 95**). A first parabolic mirror allows the entrance of the infrared beam on one of the beveled edges of the prism, and after various internal reflections, the beam gets out from the silicon and it is focused by other two parabolic mirrors leading to the detector.

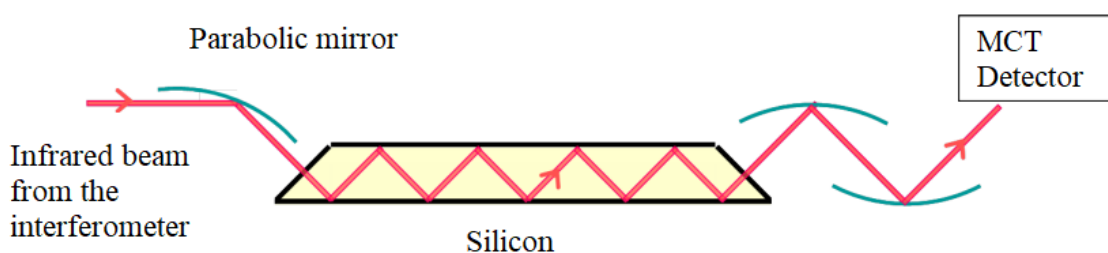


Figure 95: Diagrams of a silicon prism for Fourier Transform Infrared in an ATR geometry. Adapted from Douarche thesis.¹³

The number of reflections inside the prism is given by the following formula:

$$\mathbf{n} = \frac{\mathbf{L}}{\mathbf{e \tan \phi}} \quad (3)$$

where L is the length of the prism, e is the thickness of the silicon sample and φ is the angle of the bevel of the silicon prisms.

The value of the angles of the prisms used in this work and the total number of reflections for each one is shown in **Table 28**. For the calculation of total number of reflections when using the Bruker equipment, the side A is to be used. If the Bomen equipment is used, side B is to be used.

Table 28: Angle of the prisms used in the project and their respective total number of reflections. Side A is the entrance side on the Bruker Spectrometer.

Prims name	Angle ($^{\circ}$), Side A	Angle ($^{\circ}$), Side B	Length (mm)	Total Number of Reflections
P1	47	46.5	12	22.4
P2	47,5	46,5	12	22
P3	46,5	47	12	22.7
P4	46,5	47,5	12	22
P5	47	45	12	22.4
P6	48	46	12	21.6
P7	47	44	12	22.4
P8	48	46	12	22.4
P9	45	48	12	24
P10	45	48	12	24
P12	48	45	12	21.6
PACG	47	50	12	20.1
PH1	48	48	10.5	19

Synthesis of macroporous samples

The macroporous were synthesized from (100)-oriented, highly-doped n-type Si ($\rho = 0.01 - 0.015 \Omega \cdot \text{cm}$) in an electrolyte composed of HF 5 wt. % - CTAC 100 ppm. In order to obtain macropores in highly-doped silicon, high current density must be injected to the

electrochemical circuit (for a given HF concentration).¹⁸¹ In the present study, a three-step current command was set: (1) high current density (80 mA/cm²) was injected for 10 s to ensure the formation of large pores at the silicon/electrolyte interface. Then (2), a decreasing ramp from 80 to 30 mA/cm² at 2 mA/cm²/s ensured the stable growth of the pores. Finally, (3) galvanostatic etching conditions were set (30 mA/cm² for 4 min 25 s) to obtain mechanically stable macropores.

Preparation of oxidized silicon surface

The polished silicon (111) prisms were immersed in piranha solution (H₂SO₄/H₂O₂, 3/1) at 100°C overnight. Piranha solution is a strong oxidizing agent and removes organic pollutions on the surface. Later, the piranha solution was refreshed with a new solution, and continuing heating at 100 °C was allowed for more 30 min. Afterwards the wafer was carefully rinsed with ultra-pure water to avoid any possible contaminations during the etching.

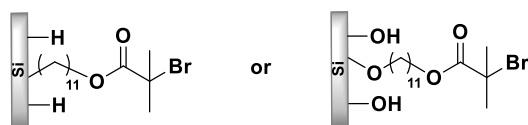
This procedure was the same when using macroporous silicon.

Preparation of hydrogenated silicon surface

The oxidized layer is removed by immersing the freshly prepared prims by immersing it for either 5 seconds in a polytetrafluoroethylene (PTFE) beaker filled with hydrofluoric acid solution HF (50%) for 5 seconds. Then, the prims are immersed for 5 seconds in milli-Q water and dried using N₂ flow. The same hydrogenated surface can be obtained by either immersing the prism in 5% HF solution for 2 min or in a 2% HF solution for 4 min. The solutions at lower concentration were preferred to use as a principle of safety.

When using macroporous silicon, the etching was performed with ethanolic HF 25% for 1 min, and then rinsed in ethanol for another minute, with a final rinse in running DI water for 5 seconds. It was then dried using N₂ flow.

Grafting of 10-undecylenic-2-bromoisobutyrate (SiBr1 or SiOBr1)



A 10% (v/v) solution of 10-undecylenic-2-bromoisobutyrate (0.4 mL) in filtered mesitylene (3.6 mL) over alumina was degassed using Argon flow in a Schlenk for 30 min. Then, a freshly prepared prism with hydrogenated surface was added to a micro-wave (MW) reactor, followed by the addition of the degassed mixture. The air of the MW reactor was flushed out using Argon flow before closing the reactor. The reactor was placed in the microwave chamber and the reaction was proceeded following the pre-defined MW conditions. The same procedure was also performed using a 5%, 30%; 50% (v/v) solution of the initiator in mesitylene.

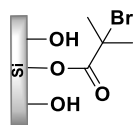
Different MW conditions were tested, and they were usually the following:

- i. Temperature: 75, 100, 125, 147 or 170°C
- ii. Time: 20, 50 or 120 minutes
- iii. Power: 10, 30 or 50 Watts
- iv. Pressure safe limit: 5 bar

The power is not constant throughout the experiment because it is needed to 1) achieve the set temperature, 2) maintain a constant temperature during the experiment. In addition, the pressure is a safety parameter and does not influence the reaction. In other words, no pressure was applied during the experiment, but instead, it was assessed during the whole period so to not surpass the safety setup. In fact, in all experiments, 1 bar was the maximum pressure achieved.

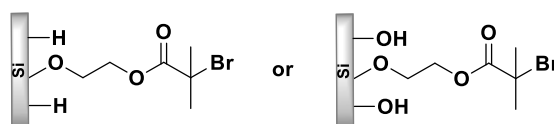
The procedure was the same when using macroporous silicon. The same procedure was performed from an oxidized (SiO_x) surface to obtain SiOBr1.

Grafting of α -bromoisobutyryl bromide (SiOBr₂)



A 10% (v/v) solution of α -bromoisobutyryl bromide (0.4 mL) in filtered mesitylene over alumina (3.6 mL) was degassed using Argon flow in a Schlenk for 30 min. Then, a freshly prepared prism with an oxidized surface was added to a micro-wave (MW) reactor, followed by the addition of the degassed mixture. The air of the MW reactor was flushed out using Argon flow before closing the reactor. The reactor was placed in the microwave chamber and the reaction was proceeded following the pre-defined MW conditions using dynamic settings: 125 °C, 50 W, 50 min, 5 bar.

Grafting of 2-hydroxyethyl 2-bromoisobutyrate (SiBr₃ or SiOBr₃)



A 10% (v/v) solution of 2-hydroxyethyl 2-bromoisobutyrate (0.4 mL) in filtered mesitylene over alumina (3.6 mL) was degassed using Argon flow in a Schlenk for 30 min. Then, a freshly prepared prism with hydrogenated, or oxidized, surface was added to a micro-wave (MW) reactor, followed by the addition of the degassed mixture. The air of the MW reactor was flushed out using Argon flow before closing the reactor. The reactor was placed in the microwave chamber and the reaction was proceeded following the pre-defined MW conditions using dynamic settings: 125 °C, 50 W, 50 min, 5 bar.

The same procedure was performed from an oxidized (SiO_x) surface to obtain SiOBr₃.

Rinsing

The rinsing step is a very crucial step to remove all physisorbed molecules on surface. After the reaction, the grafted silicon prism was removed from the reactor and rinsed twice with toluene for 2 min using a rinsing glassware. Then, two cycles of 15 min each in ultra-sound bath using toluene were done, followed by another two rinses with dichloromethane using the rinsing glassware. The samples were dried N₂ flow and stored in inert atmosphere. This

cleaning methodology showed to be efficient for the rinsing of the prism, but further Soxhlet extraction overnight was potentially performed (stated in the text if it is case).

When using macroporous silicon, Soxhlet rinsing was always employed since molecules could be trapped inside the pores.

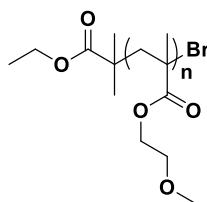
CHAPTER 3: ATRP of methacrylates in solution and on surface

Materials

Dichloromethane, methanol, ethanol and diethyl ether were dried before use. Copper (I) bromide was purified by treating it with glacial acetic acid and washed several times with ethanol absolute and diethyl ether. Copper (II) bromide (99%) was purchased from Sigma Aldrich and used without further purification. Copper wire (Rowan Cable, 1 mm, ½ kg) was cleaned overnight with a HCl conc./Methanol 50/50 v/v solution overnight, then rinsed with acetone and diethyl ether and further dried overnight on a desiccator. MEMA was purified in an Al₂O₃ column to remove inhibitors.

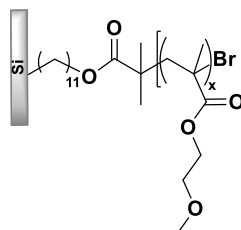
Methods

General procedure for the homopolymerization of MEMA using classical ATRP



Polymerizations were performed using a mix of [MEMA]₀/[CuBr]₀/[eBiB]₀/[bpy]₀ = 200/1/1/2 molar ratio in acetone and DPE (5% volume) in a Schlenk tube at 50 °C for 5 hours. Therefore, a mixture of dry acetone (3 mL), diphenyl ether (DPE) (0.2 mL), MEMA (1 eq, 30.00 mmol, 4.3 g), CuBr (0.005 eq, 0.15 mmol, 21.4 mg) and 2,2'-bipyridine (bpy) (0.01 eq, 0.30 mmol, 46.8 mg) was deoxygenated in a Schlenk tube by 3 freeze–pump–thaw cycles. In a frozen mixture, and under positive argon atmosphere, ethyl 2-bromoisobutyrate (eBiB) (0.005 eq, 0.15 mmol, 22 µL) was added, followed by another 3 freeze–pump–thaw cycles. The mixture was put in a preheated oil bath at 50 °C and allowed to stir for 5 hours. Samples were taken during reaction and analyzed by ¹H-NMR for kinetics study. After completion of the reaction, the mixture was dissolved in DCM and filtered through a short column of Al₂O₃. The solvent was then removed under reduced pressure and the polymer was precipitated in petroleum ether under stirring and then dried in a desiccator overnight. The following proton NMR description only describes the signals for the polymer: ¹H NMR (360 MHz, CDCl₃) δ 4.09 (s, 2H), 3.58 (s, 2H), 3.36 (s, 3H), 1.84 (s, 2H), 1.09 and 0.91 (2 bs, 3H).

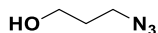
General procedure for the surface-initiated polymerization of MEMA on surface using either crystalline or macroporous silicon



Polymerizations were performed using a mix of [MEMA]₀/[CuBr]₀/[CuBr₂]₀/[bpy]₀ = 200/1/0.05/2 molar ratio in acetone and DPE (5% volume) in a Schlenk tube at 50 °C for 5 hours. In a typical experiment for the preparation of PMEMA brushes, the following amounts were used: MEMA (200 eq., 17.3 mmol, 2.5 mL), CuBr (1 eq., 0.0865 mmol, 12.5 mg), CuBr₂ (0.05 eq., 0.00432 mmol, 0.96 mg), bpy (2 eq., 0.173 mmol, 27.29 mg), acetone (2.5 mL) and DPE (0.25 mL). The initiator-modified surface (SiBr) was placed in a special Schlenk for prisms and then acetone, DPE and MEMA were added. The solution was frozen and air was purged out using vacuum. Then, under positive argon atmosphere, CuBr, CuBr₂ and bpy were added and high vacuum was applied for ~ 5 min. The resulting solution was deoxygenated by 5 freeze-pump-thaw cycles and back-filled with argon in the last step. The solution was put in a preheated oil bath at 50 °C for 5h. After polymerization, the silicon prism was purified by multiple washings with acetone, toluene, THF, and a Soxhlet was carried out for 6 hours in THF, then the prism was dried under N₂ flow.

When using macroporous silicon, the macroporous silicon sample was put in a special Schlenk for prisms together with CuBr and CuBr₂, and then 3 cycles of vacuum-argon was applied. In parallel, the solution containing MEMA, acetone, DPE and bpy was deoxygenated by 5 freeze-pump-thaw cycles and then transferred to the Schlenk containing the macroporous silicon using inert syringe techniques. Then the reaction was put in a preheated oil bath at 50 °C for 5h and the following steps were the same as stated before. The procedure for macroporous silicon is slightly different because it is quite sensible and can easily break during the process of degassing of liquids.

Synthesis of 3-azidopropanol (2)



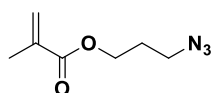
Chemical Formula: C₃H₇N₃O

Exact Mass: 101,06

Molecular Weight: 101,11

To a mixture of acetone (60 mL) and deionized water (10 mL), 3-bromo-1-propanol (1 eq., 36 mmol, 5 g) and sodium azide (2 eq., 72 mmol, 4.7 g) were added. The mixture was allowed to reflux overnight at 80 °C. Acetone was removed under reduced pressure followed by the addition of deionized water (50 mL). The product was extracted from the aqueous layer by diethyl ether extraction (3 × 50 mL). The organic phase was combined and dried over MgSO₄, filtered, and evaporated to dryness under reduced pressure yielding a colorless liquid (3.2 g, 89% yield). ¹H NMR (360 MHz, CDCl₃) δ 3.72 (t, *J* = 6.4 Hz, 2H), 3.43 (t, *J* = 6.4 Hz, 2H), 2.13 (s, 1H), 1.81 (q, *J* = 6.4 Hz, 2H).

Synthesis of 3-azidopropyl methacrylate (3)



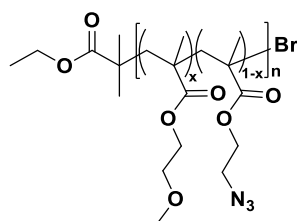
Chemical Formula: C₇H₁₁N₃O₂

Exact Mass: 169,09

Molecular Weight: 169,18

To a 500 mL round-bottom flask, 3-azido-1-propanol (1 eq., 0.077 mmol, 7.8 g) was dissolved in 68 mL distilled diethyl ether. Then, distilled triethylamine (1.2 eq., 0.0926 mmol, 12.9 mL), DMAP (0.03 eq., 0.0023 mmol, 0.2818 g) and hydroquinone (0.015 eq., 0.001155 mmol, 0.12 g) were added. The reaction mixture was cooled with an ice-bath and methacryloyl chloride (1.2 eq., 0.0926 mmol, 9.7 mL) was added dropwise during 5 minutes. The reaction mixture was allowed to stir at r.t for 16 h. After completion of the reaction, 10 mL of diethyl ether was added and then the solution was washed with HCl (1M) (2 × 25 mL), deionized water (2 × 25 mL), NaOH (10% v/v) (2 × 25 mL) and again with deionized water (2 × 25 mL). The organic solution was dried over anhydrous Na₂SO₄, filtered and evaporated to dryness under reduced pressure yielding a colorless liquid. ¹H NMR (360 MHz, CDCl₃) δ 6.11 (m, 1H), 5.59 (q, 1H), 4.24 (t, 2H), 3.42 (t, *J* = 6.8 Hz, 2H), 1.96 (m, *J* = 6.8 Hz, 5H, overlapping CH₃C and CCH₂C). Impurities in the region of 4.3, 4.2, 2.3 and 1.8 ppm. Additional 0.015 eq of hydroquinone was added and further purification of the product was done by distillation under vacuum at 80 °C. Special attention must be taken into consideration to not heat the product higher than 80 °C as it can be shock sensitive. Yield after distillation: 6g, 46%.

General procedure for the copolymerization of MEMA/AZMA in solution using classical ATRP



Polymerizations were performed using a mix of [MEMA]₀/[AZMA]₀/[CuBr]₀/[eBiB]₀/[bpy]₀ = X/200-X/1/1/2 molar ratio in acetone and DPE (5% volume) in a Schlenk tube at 50 °C for 6 hours. Thus, a mixture of dry acetone (3 mL) and DPE (0.5 mL) was degassed in a Schlenk tube by 5 freeze–pump–thaw cycles. Then, a mixture of MEMA (see quantity indicated below) and 3-azidopropyl methacrylate (AZMA) (see quantity indicated below) was degassed in a Schlenk tube by 4 freeze–pump–thaw cycles. Over the acetone/DPE mixture, CuBr (see quantity indicated below) and the ligand (see quantity indicated below) were added under an argon atmosphere. The MEMA and AZMA mixture was subsequently added using inert syringe techniques. Over a frozen mixture, eBiB (see quantity indicated below) was added. Four new freeze–pump–thaw cycles were applied to the mixture, and then it was placed in a preheated oil bath at the desired temperature during 6 h. At the end of the reaction, the solution was solubilized in 20 mL of THF and passed through a short Al₂O₃ column. The solvent was then removed under reduced pressure and the copolymer was precipitated in cold hexane/methanol 50/50 v/v mixture under rapid stirring followed by various rinsings with cold hexanes to afford a white solid. The copolymers were dried out under vacuum and analyzed by SEC-MALS. The following proton NMR description only describes the signals for the copolymer: ¹H NMR (360 MHz, CDCl₃) δ 4.09 (s, 2H), 3.96 (s, 2H), 3.52 (s, 2H), 3.42 (s, 2H), 3.37 (s, 3H), 1.92 – 1.84 (2 bs, 6H), 1.09 and 0.91 (2 bs, 6H).

MEMA70-co-AZMA30

2-methoxyethyl methacrylate (0.70 eq., 9.5 mmol, 1.368 g), 3-azidopropyl methacrylate (0.30 eq., 4 mmol, 0.676 g), CuBr (0.005 eq., 0.065 mmol, 0.0095 g), bpy (0.01 eq., 0.3 mmol, 0.021 g), and eBiB (0.005 eq., 0.065 mmol, 9.8 μL).

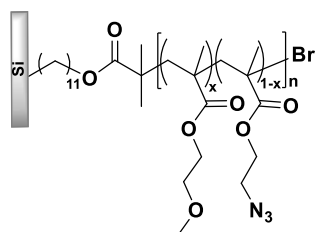
MEMA50-co-AZMA50

2-methoxyethyl methacrylate (0.50 eq., 5.5 mmol, 0.79 g), 3-azidopropyl methacrylate (0.50 eq., 5.5 mmol, 0.93 g), CuBr (0.005 eq., 0.055 mmol, 0.0075 g), bpy (0.01 eq., 0.11 mmol, 0.017 g), and eBiB (0.005 eq., 0.055 mmol, 8 μ L).

MEMA25-co-AZMA75

2-methoxyethyl methacrylate (0.25 eq., 5.5 mmol, 0.792 g), 3-azidopropyl methacrylate (0.75 eq., 16.5 mmol, 2.78 g), CuBr (0.005 eq., 0.11 mmol, 0.016 g), bpy (0.01 eq., 0.22 mmol, 0.035 g), and eBiB (0.005 eq., 0.11 mmol, 15.9 μ L).

General procedure for the surface-initiated copolymerization on surface using either crystalline or macroporous silicon



Polymerization were performed using [monomers]₀/[CuBr]₀/[CuBr₂]₀/[bpy]₀ = 200/1/0.05/2 molar ratio in a Schlenk tube at 50°C for 6h. In a typical experiment for the preparation of MEMA-co-AZMA brushes, 2 Schlenks are used: the first one containing the modified surface (SiBr1), bpy, CuBr and CuBr₂, and the second containing MEMA, AZMA, acetone and DPE (see quantities below). Except in the case of **Figure 61b** and **Figure 86a** in which the experiment was performed without the addition of CuBr₂. In the first, three cycles of vacuum-argon are applied, and for the second, the solution is deoxygenated by 8 freeze-pump-thaw cycles. Then, the latter mixture is transferred to the first Schlenk using inert syringe techniques, followed by another 3 fast cycles of vacuum-argon. The reaction was allowed to proceed for 6 h. After polymerization, the silicon film was purified by multiple washings with acetone, toluene, and Soxhlet extraction with THF for 6 to 8 h.

SiBr1-Copo1

2-methoxyethyl methacrylate (0.90 eq., 10 mmol, 1.44 g), 3-azidopropyl methacrylate (0.10 eq., 1.1 mmol, 0.18 g), CuBr (0.005 eq., 0.055 mmol, 0.008 g), CuBr₂ (5 mol%, 0.00275 mmol, 0.6 mg), bpy (0.01 eq., 0.11 mmol, 0.017 g), acetone (1.5 mL) and DPE (0.25 mL).

SiBr1-Copo2

2-methoxyethyl methacrylate (0.70 eq., 7.7 mmol, 1.1 g), 3-azidopropyl methacrylate (0.30 eq., 3.3 mmol, 0.55 g), CuBr (0.005 eq., 0.055 mmol, 0.0075 g), bpy (0.01 eq., 0.11 mmol, 0.017 g), and eBiB (0.005 eq., 0.055 mmol, 8 μ L).

SiBr1-Copo3 or PSiBr1-Copo3

2-methoxyethyl methacrylate (0.5 eq., 5.17 mmol, 0.74 g), 3-azidopropyl methacrylate (0.5 eq., 5.17 mmol, 0.87 g), CuBr (0.005 eq., 0.0517 mmol, 0.0074 g), CuBr₂ (5 mol%, 0.0258 mmol, 0.5 mg), bpy (0.01 eq., 0.10 mmol, 0.016 g), acetone (1.5 mL) and DPE (0.25 mL).

General Procedure for Cu(0) SARA ATRP

i. Homopolymerization of HEMA

Cu(0)-mediated SARA ATRP of HEMA, where $[\text{HEMA}]_0/[\text{eBiB}]_0/[\text{dNpby}]_0/[\text{CuBr}_2]_0 = 200/1/0.4/0.1$, dNpby (0.4 eq., 0.022 mmol, 0.009 g), CuBr₂ (0.1 eq., 0.0055 mmol, 0.0012 g), HEMA (200 eq., 11 mmol, 1.43 g), acetone (1.5 mL) and DPE (0.16 mL) were put in a Schlenk tube then purged with a moderate flow of argon for 15 min. The initiator eBiB (1 eq., 0.055 mmol, 8 μ L) was introduced into the reaction tube followed by the addition of a 2 cm pre-cleaned Cu(0) wire. The Schlenk was sealed and let stir for one hour at room temperature. The reaction mixture was diluted in 10 mL of ethanol and passed through an Al₂O₃ column. The solvent was then removed under reduced pressure and PHEMA was precipitated in cold petroleum ether under rapid stirring followed by various rinsing with cold petroleum ether to afford white pellets. PHEMA was dried out under vacuum in a desiccator overnight. Insolubility of PHEMA in common organic solvents did not allow its analysis by SEC-MALS. The following proton NMR description only describes the signals for the polymer: ¹H NMR (360 MHz, CDCl₃) δ 4.01 (s, 2H), 3.74 (s, 2H), 1.08 and 0.94 (2 bs, 3H).

ii. Homopolymerization of MEMA

Cu(0)-mediated SARA ATRP of MEMA, where $[\text{MEMA}]_0/[\text{eBiB}]_0/[\text{dNpby}]_0/[\text{CuBr}_2]_0 = 200/1/0.4/0.1$, dNpby (0.4 eq., 0.022 mmol, 0.009 g), CuBr₂ (0.1 eq., 0.0055 mmol, 0.0012 g), MEMA (200 eq., 11 mmol, 1.58 g) and acetone (1.5 mL) were put in a Schlenk tube then purged with a moderate flow of argon for 15 min. The initiator eBiB (1 eq., 0.055 mmol, 8 μL) was introduced into the reaction tube followed by the addition of a 2 cm pre-cleaned Cu(0) wire. The Schlenk was sealed and put in a pre-heated oil bath at 50 °C for 2h30. Samples were taken during reaction and analyzed by ¹H-NMR for kinetics study. The reaction mixture was diluted in 10 mL of dichloromethane and passed through an Al₂O₃ column. The solvent was then removed under reduced pressure and PMEMA was precipitated in cold petroleum ether under rapid stirring followed by various rinsings with cold petroleum ether to afford white powder. PMEMA was dried out under vacuum in a desiccator overnight and analyzed by SEC-MALS.

iii. Copolymerization of MEMA/AZMA

Cu(0)-mediated SARA ATRP of MEMA and AZMA, where $[\text{monomers}]_0/[\text{eBiB}]_0/[\text{dNpby}]_0/[\text{CuBr}_2]_0 = 200/1/0.4/0.1$, dNpby (0.4 eq., 0.022 mmol, 0.009 g), CuBr₂ (0.1 eq., 0.0055 mmol, 0.0012 g), MEMA and AZMA (see quantity below), acetone (1.5 mL) and DPE (0.16 mL) were put taken in a Schlenk tube then purged with a moderate flow of argon for 15 min. The initiator eBiB (1 eq., 0.055 mmol, 8 μL) was introduced into the reaction tube followed by the addition of a 2 cm pre-cleaned Cu(0) wire. The Schlenk was sealed and placed in a pre-heated oil bath at 50 °C for 2h30. Samples were taken during reaction and analyzed by ¹H-NMR for kinetics study. At the end of the reaction, the reaction mixture was diluted in 10 mL of THF and passed through an Al₂O₃ column. The solvent was then removed under reduced pressure and the copolymers precipitated in cold hexane/methanol 50/50 v/v mixture under rapid stirring followed by various rinsings with cold hexanes to afford a white solid. The copolymers were dried out under vacuum and analyzed by SEC-MALS.

SARA-Cop1: MEMA (0.70 eq., 7.7 mmol, 1.1 g), AZMA (0.30 eq., 3.3 mmol, 0.55 g).

SARA-Cop2: MEMA (0.30 eq., 3.3 mmol, 0.47 g), AZMA (0.70 eq., 7.7 mmol, 1.3 g).

CHAPTER 4: Synthesis of Salen Catalysts and Post-Functionalization of Copolymers

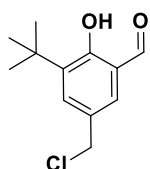
Materials

Dichloromethane, toluene, tetrahydrofuran, methanol, ethanol and diethyl ether were dried before use. Copper bromide was purified by treating it with glacial acetic acid and washed several times with ethanol absolute and diethyl ether. Trimethylsilyl acetylene, 1-bromo-4-nitrobenzene, 4-bromobenzonitrile, triethylamine, tetrakis(triphenylphosphine)palladium(0), Bis(triphenylphosphine)palladium(II) dichloride, diisopropylamine, benzaldehyde, ethylmagnesium bromide solution 3.0 M in diethyl ether, Dess–Martin periodinane (DMP), *N,N*-diisopropyléthylamine (DIPEA), 1-ethynyl-4-(trifluoromethyl)benzene, 3-*tert*-butyl-2-hydroxybenzaldehyde, trioxane, (1*R*,2*R*)-1,2-cyclohexanediamine, tetrabutylammonium iodide (TBAI), sodium hydride (NaH), sodium hydroxide (KOH) and potassium carbonate (K₂CO₃) were purchased from Aldrich. DIPEA and triethylamine were distilled before use.

Methods

Synthesis of catalysts

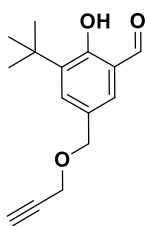
- i. Synthesis of 3-*tert*-butyl-5-(chloromethyl)-2-hydroxybenzaldehyde (5)



Chemical Formula: C₁₂H₁₅ClO₂
Exact Mass: 226,08
Molecular Weight: 226,70

In a 250 mL round bottom flask, 3-(*tert*-butyl)-2-hydroxybenzaldehyde (1 eq., 28 mmol, 4.8 mL) was added followed by the addition of 1,3,5-trioxane (2.5 eq., 70 mmol, 6.32 g). 110 mL of concentrated HCl (37%) was added slowly and then placed the solution in a pre-heated oil bath at 55 °C for 3 days under stirring. The reaction mixture was diluted with 80 mL of DI water and the product was extracted with diethyl ether (3 × 80 mL). The organic phase was washed with concentrated NaHCO₃ (2 × 80 mL) and then with brine solution (3 × 80 mL). The combined organic layer was dried with MgSO₄ and the solvent was removed under reduced pressure. The product was obtained as a yellow solid (5.7 g, 90% yield). ¹H NMR (360 MHz, CDCl₃) δ 11.86 (s, 1H), 9.87 (s, 1H), 7.53 (s, 1H), 7.44 (s, 1H), 4.59 (s, 2H), 1.43 (s, 9H).

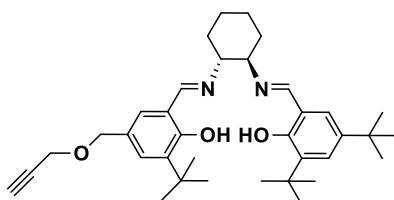
ii. Synthesis of 3-tert-butyl-2-hydroxy-5-((prop-2-ynoxy)methyl) benzaldehyde (6)



Chemical Formula: $C_{15}H_{18}O_3$
Exact Mass: 246,13
Molecular Weight: 246,31

In a three-necked bottom flask, sodium hydride (60% dispersion in mineral oil, 1.5 eq., 7.96 mmol, 0.316 g) was washed with dry hexanes (3×5 mL) and dried under vacuum. Then, under positive argon atmosphere, 15 mL of dry THF was added. The solution was cooled down at 0 °C using an ice bath. Propargyl alcohol (1.5 eq., 7.96 mmol, 463 μ L) in 15 mL of dry THF was added dropwise, and the mixture was stirred at ambient temperature for 2 h. The reaction mixture was cooled at 0 °C and then 3-(tert-butyl)-5-(chloromethyl)-2-hydroxybenzaldehyde (1 eq., 5.30 mmol, 1.18 g) in 15 mL of dry THF was added dropwise and TBAI (0.03 eq., 0.16 mmol, 0.058 g) was added under an argon atmosphere. The reaction mixture was allowed to stir while refluxing (80 °C) for 16 h and was then cooled down at 0 °C. Deionized water (6 mL) was slowly added. Solvents were removed under reduced pressure. The product was partitioned in dichloromethane (50 mL) and deionized water (50 mL). The aqueous layer was extracted two times by DCM (50 mL). The organic phase was combined and washed with brine solution (3×50 mL) and dried over $MgSO_4$. After filtration and removal of solvents under reduced pressure, the product was obtained as a brown viscous liquid (1.15 g, 89% yield). 1H NMR (360 MHz, $CDCl_3$) δ 11.82 (s, 1H), 9.90 (s, 1H), 7.53 (d, 1H, $J = 2.0$ Hz), 7.44 (d, 1H, $J = 2.0$ Hz), 4.59 (s, 2H), 4.23 (s, 2H), 2.52 (s, 1H), 1.42 (s, 9H).

iii. Synthesis of the salen ligand bearing a propargyl moiety (9)

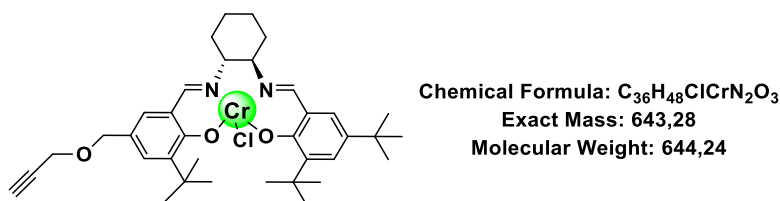


Chemical Formula: $C_{36}H_{50}N_2O_3$
Exact Mass: 558,38
Molecular Weight: 558,81

First, (1*R*,2*R*)-1,2-cyclohexanediamine mono(hydrogen chloride) (1 eq., 1 mmol, 150 mg), 3,5-di-tert-butyl-2-hydroxybenzaldehyde (1 eq., 1 mmol, 234 mg) and a molecular sieve (4 Å, 0.83 g) were charged into a Schlenk tube. The tube was then evacuated three times and filled with argon. Under the argon atmosphere, 9 mL of anhydrous methanol was added, and the

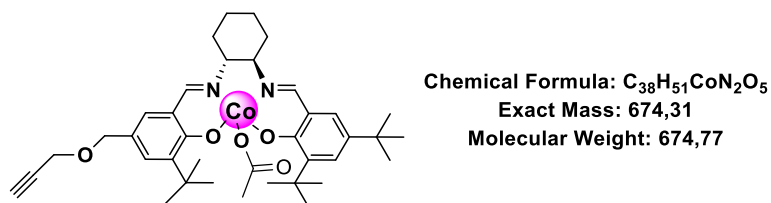
mixture was stirred at room temperature for 4 h. The solution had a turve and yellow aspect. A solution of 3-tert-butyl-2-hydroxy-5-((prop2-ynyloxy) methyl)benzaldehyde (1 eq., 1 mmol, 246 mg) in 9 mL of dried dichloromethane and 0.42 mL of anhydrous triethylamine (3 eq., 3 mmol) was added to the above mixture and was stirred at room temperature for 18 h. The reaction mixture was filtered through a short pad of celite and flushed with anhydrous dichloromethane. After removal of the solvent under reduced pressure, the crude product was purified by column chromatography on silica gel (cyclohexane/AcOEt/Et₃N: 99/0.9/0.1) to afford the product as a yellow powder (234 mg, 41% yield). ¹H NMR (300 MHz, CDCl₃) δ 14.00 (s, 1H), 13.68 (s, 1H), 8.31 (s, 1H), 8.30 (s, 1H), 7.32 (d, *J* = 2.5 Hz, 1H), 7.25 (d, *J* = 2.2 Hz, 1H), 7.02 (d, *J* = 2.2 Hz, 1H), 6.98 (d, *J* = 2.5 Hz, 1H), 4.46 (s, 2H), 4.10 (d, *J* = 2.4 Hz, 2H), 3.36 (m, 2H), 2.46 (t, *J* = 2.4 Hz, 1H), 2.01 – 1.87 (m, 4H), 1.81 – 1.69 (m, 2H), 1.53 – 1.45 (m, 2H), 1.44 (s, 9H), 1.43 (s, 9H), 1.25 (s, 9H). ¹³C NMR (101 MHz, CDCl₃) δ 166.04, 165.42, 160.46, 158.07, 140.05, 137.47, 136.50, 130.12, 129.92, 126.95, 126.17, 126.07, 118.43, 117.91, 79.93, 74.61, 72.54, 72.49, 71.57, 56.79, 35.09, 34.90, 34.15, 33.28, 31.55, 29.58, 29.45, 24.45. FTIR (cm⁻¹): 3311, 2952, 2862, 1628, 1597, 1469, 1441, 1390, 1361, 1321, 1270, 1252, 1205, 1173, 1163, 1084, 1047, 909. HRMS (M + H⁺): calc for C₃₆H₅₁N₂O₃; 559.3894 found for C₃₆H₅₁N₂O₃: 559.3878.

iv. Synthesis of the chromium salen complex bearing a propargyl moiety (10)



A solution of the salen ligand (1 eq., 0.23 mmol, 130 mg) in dry, degassed THF (2 mL) was assessed with a solution of anhydrous CrCl₂ (1,1 eq., 0.26 mmol, 32 mg) in dry, degassed THF (4 mL). The resulting brown solution was stirred under argon for 2 h and then in air for an additional 18 h. The solution was then diluted with dichloromethane (50 mL) and washed with saturated NH₄Cl and brine. The organic phase was dried over anhydrous MgSO₄ and filtered. The solvent was removed under reduced pressure to afford the salen complex as a brown powder (112 mg, 73% yield). ATR-FTIR (cm⁻¹): 2951, 2865, 2093, 1619, 1534, 1436, 1389, 1342, 1320, 1256, 1204, 1166, 1078, 1026, 969, 924, 865, 830, 785, 746, 734, 701, 668, 649, 639, 624. HRMS (M-Cl): calc for C₃₆H₄₈CrN₂O₃: 608.3070; found for C₃₆H₄₈CrN₂O₃: 608.3037.

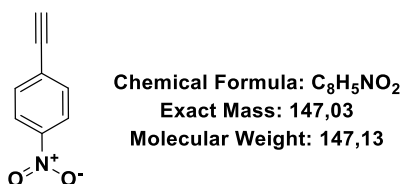
v. Synthesis of the cobalt salen complex bearing a propargyl moiety (11)



A solution of the salen ligand (1 eq., 0.179 mmol, 100 mg) in dry and degassed dichloromethane (1 mL) was transferred to a solution of $Co(OAc)_2 \cdot 4H_2O$ (1 eq., 0.179 mmol, 44.6 mg) in methanol (1 mL). The resulting dark red solution was stirred under argon for 4 h. Acetic acid (100 eq., 17.9 mmol, 1 mL) was added and then the solution was stirred in air for another 18 h. The resulting dark brown solution had its solvent removed under pressure and then rinsed with toluene three times (120 mg, quantitative yield). ATR-FTIR (cm^{-1}): 2951, 2867, 1736, 1612, 1529, 1459, 1436, 1385, 1360, 1323, 1256, 1234, 1203, 1168, 1081, 1045, 1029, 930, 868, 839, 786, 731, 696, 665, 638, 624. HRMS ($M-C_2H_3O_2$): calc for $C_{36}H_{48}CoN_2O_3$: 615.2997; found for $C_{36}H_{48}CoN_2O_3$: 615.2956.

Synthesis of FTIR markers by Sonogashira Pd/Cu cross-coupling

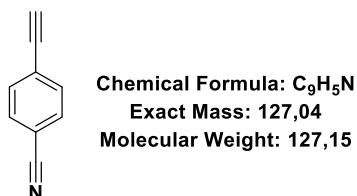
i. Synthesis of 1-ethynyl-4-nitrobenzene (aryl-1)



To a mixture of trimethylsilylacetylene (1.2 eq., 2.4 mmol, 0.236 g) and 1-bromo-4-nitrobenzene (1 eq., 2 mmol, 0.404 g) in distilled triethylamine (8 mL) bis(triphenylphosphine)palladium dichloride (0.02 eq., 0.04 mmol, 0.028 g) and copper(I) iodide (0.005 eq., 0.01 mmol, 0.002 g) were added. The reaction mixture was stirred at room temperature for 6 h under nitrogen followed by solvent evaporation. The residue was filtered in a small pad of silica plug using dichloromethane as solvent, followed by solvent evaporation. The crude was pure as evidenced by NMR with a quantitative yield (437 mg). 170 mg of the crude intermediate was dissolved in 10 mL ethanol, and aqueous potassium hydroxide (0.5 mL, 1.0 M) was added, and the mixture was stirred at room temperature for 2 h. After solvent removal, the residue was extracted with dichloromethane and washed with water 3 times. The

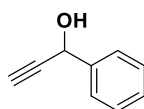
solvent was finally removed by rotary evaporation. The crude product was purified by silica column chromatography using petroleum ether:ethyl acetate 95:5 as eluent. Yield: 83 mg (71%). ^1H NMR (360 MHz, CDCl_3) δ 3.37 (s, 1H), 7.65 (d, $J = 12.0$ Hz, 2H), 8.21 (d, $J = 12.0$ Hz, 2H).

ii. Synthesis of 4-ethynylbenzotrile (aryl -2)



In a round-bottom flask filled with toluene (10 mL), 4-bromobenzotrile (1 eq, 5.0 mmol, 910 mg) and trimethylsilylacetylene (1.2 eq, 6.0 mmol, 589 mg) were added using inert atmosphere techniques. The catalysts $\text{Pd}(\text{PPh}_3)_4$ (0.05 eq, 0.25 mmol, 288 mg) and CuI (0.02 eq, 0.1 mmol, 48 mg), together with $i\text{-Pr}_2\text{NH}$ (8 eq, 0.04 mol, 5.0 mL) were added. The reaction was allowed to stir at 80°C for a week, in which the solution turned brown. The solvent was evaporated under pressure, and the metals were removed using a silica plug with dichloromethane as solvent. The solvent was evaporated under reduced pressure and the product was purified by column chromatography (stationary phase: silica, eluent: petroleum ether). The product was obtained pure as a white powder (484 mg, 50% yield). Then, 484 mg of the synthesized intermediate (1 eq, 2.43 mmol, 484 mg) was put in a flask with 5.6 mL of THF, 5.6 mL of MeOH and H_2CO_3 (10 eq, 24.5 mmol, 3.38 g). The reaction mixture was allowed to stir at room temperature for 3 hours. TLC conditions for following reaction: eluent PE / AcOEt: 85/15, UV revealing. The product was extracted three times with DCM, and the combined organic layers were then washed with a saturated aqueous solution of NH_4Cl , dried over Na_2SO_4 and then filtered. The solvent was removed under reduced pressure, and the crude product was further purified by column chromatography (stationary phase: silica, eluent: hexane/dichloromethane, 60/40) yielding the product as a white powder (179 mg, 58% yield). ^1H NMR (400 MHz, CDCl_3) in ppm: δ 7.64 - 7.61 (m, 2H), 7.59 - 7.56 (m, 2H), 3.30 (s, 1H).

iii. Synthesis of α -ethynylbenzenemethanol



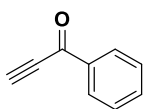
Chemical Formula: C_9H_8O

Exact Mass: 132,06

Molecular Weight: 132,16

Benzaldehyde (1 eq, 3.94 mmol, 0.4 mL) was treated in dry THF (2 mL) with ethylmagnesium bromide (1.27 eq, 5 mmol, 10 mL). The mixture was stirred at 0°C for 1 hour and then for 19 hours at room temperature. TLC conditions to follow the reaction: petroleum ether / ethyl acetate : 95 / 5, UV revealing. The reaction mixture was treated with a saturated aqueous solution of NH_4Cl and then extracted three times with Et_2O . The combined organic layers were washed three times with brine, dried over Na_2SO_4 and then filtered. The solvent was removed under reduced pressure and the crude was purified by column chromatography (stationary phase: silica, eluent: petroleum ether / ethyl acetate : 95 / 5)..yielding the product as a yellowish liquid (241 mg, 46% yield). 1H NMR (400 MHz, $CDCl_3$) δ 7.58 – 7.55 (m, 2H), 7.43 – 7.32 (m, 3H), 5.47 (s, 1H), 2.67 (s, 1H), 2.2 (s, 1H).

iv. Synthesis of 1-phenyl-2-propyn-1-one (aryl-4)



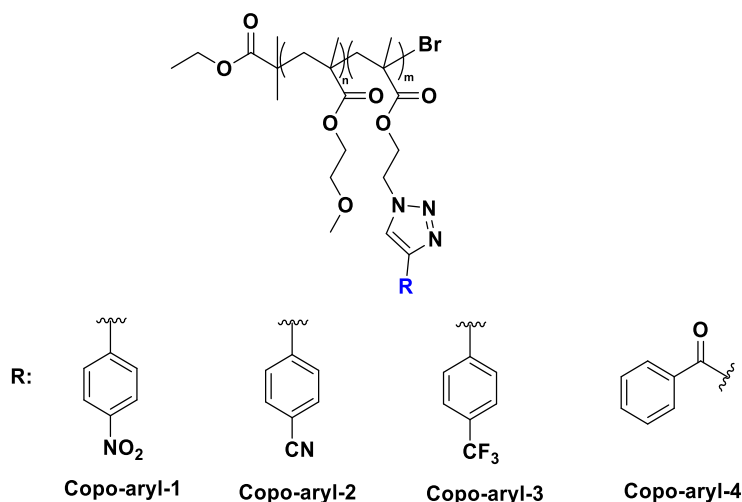
Chemical Formula: C_9H_6O

Exact Mass: 130,04

Molecular Weight: 130,15

Dess-Martin oxydant (1.1 eq, 2.02 mmol, 848 mg) was added to a solution α -ethynylbenzenemethanol (1 eq., 1.8 mmol, 242 mg) and dichloromethane (50 mL) at 0°C. The reaction was allowed to stir at room temperature for 30 minutes. TLC conditions to follow the reaction: pentane / EtOAc: 20/1, UV revealing. The product was filtered using a pad of celite using dichloromethane as solvent, which was then washed twice with concentrated solution of sodium bicarbonate, then twice with brine. The organic phase was dried over $MgSO_4$, then filtered. The solvent was evaporated under pressure and the crude was purified by column chromatography (stationary: silica, eluent: petroleum ether / ethyl acetate : 20/1) yielding the product as a yellowish solid (152 mg, 64% yield). 1H NMR (400 MHz, $CDCl_3$) δ 8.17 (m, 2H), 7.64 (m, 1H), 7.51 (m, 2H), 3.44 (s, 1H)

Click chemistry with FTIR markers in solution



In a general procedure, 2 mL of dry THF was introduced in a tube under Argon atmosphere. Aryl compound (1.5 eq, 0.18 mmol) and the copolymer (50.0 mg) were added with the catalyst CuI (5 mol%, 6.1×10^{-6} mol, 1.2 mg), followed by the addition of 77 μ L of DIPEA. The reaction was allowed to stir at 40 °C during 36 h in an oil bath. The reaction mixture was diluted in 20 mL of THF and passed through a small Al₂O₃ column. The solvent was evaporated under pressure and the modified polymer was precipitated in cold hexane under high stirring. The modified polymer was isolated, dried in a desiccator overnight.

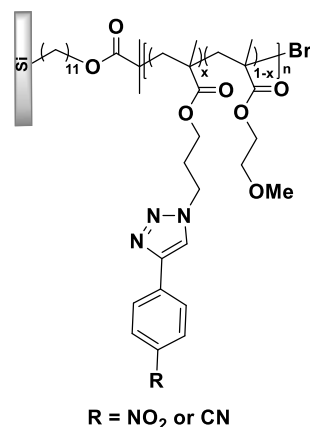
The quantity of aryl compound was calculated as following:

$$n_{\text{aryl}} = (1.5 \times DP_{\text{AZMA}} \times m_{\text{Copo}}) / M_{\text{wCopo}}$$

where M_{wCopo} is 10 240 g·mol⁻¹, and $DP_{\text{AZMA}} = 25$.

In the reactions where 2 aryl compounds were used, the quantity n_{aryl} was divided so to have an equimolar quantity of each aryl compound (0.18 mmol / 2).

Click chemistry with FTIR markers on silicon surface



SiBr1-Copo3, aryl compound (see quantity below) and CuI (see quantity below) were placed inside a Schlenk designed for reactions with silicon substrates. Vacuum was applied for 5 min and then back filled with argon. This step was repeated another 2 times. Then, dried and degassed THF (4 mL) and distilled DIPEA (see quantity below) were added using inert syringe technique. The Schlenk was placed in a preheated oil bath at 40 °C for 44 h, under constant stirring. Then, the prism was removed from the reaction mixture and thoroughly rinsed with THF, followed by rinsing in THF in an ultra sound bath for 15 min twice. Finally, it was further rinsed using Soxhlet extraction overnight with THF as solvent. The prism was dried using N₂ flow and stored under argon.

For aryl 1: 1-ethynyl-4-nitrobenzene (0.1 mmol, 0.012 g), CuI (0.007 mmol, 1.3 mg), DIPEA (0.245 mmol, 45 μL).

For aryl 2: 4-ethynylbenzonitrile (0.0065 mmol, 0.8 mg), CuI (0.007 mmol, 1.3 mg), DIPEA (0.245 mmol, 45 μL).

Click chemistry with salen complexes in solution

General procedure for the post-modification by azide–alkyne Huisgen cycloaddition of SARA-Copo1 and SARA-Copo2 with Cr and Co salen ligands.

Copolymer of MEMA/AZMA, a 50/50 molar ratio of salen Cr-Cl and Co-OAc, and CuI were added in a Schlenk tube and various vacuum argon cycles were performed. In parallel, 5 mL of dry THF and distilled *N,N*-diisopropylethylamine (DIPEA) were degassed by 3 freeze-pump-thaw cycles. Under argon atmosphere and using inert canula, the degassed solvent was

transferred in the Schlenk containing the solids. The mixture was placed in a preheated oil bath at 40 °C for 36 h, under constant stirring. Then, 20 mL of dry THF was added to the mixture, and it was filtered through Al₂O₃ column chromatography. The solvent was removed under reduced pressure and the product was precipitated in excess of petroleum ether. The product was washed with petroleum ether and then dried in a desiccator under vacuum.

The method for calculating the quantity of each species to be introduced is detailed below. These reactions were performed with SARA-Copo1 and SARA-Copo2.

The molar mass of copolymers ($M_w\text{Copo}$) was calculated according to the conversion obtained by NMR data, namely, DP_{AZMA} states for the degree of polymerization of AZMA monomer; the salen unit which was introduced in a 1.3 equivalence compared to the azido unit contained in the copolymers. Therefore,

$$n_{\text{salen}} = (1.3 \times DP_{\text{AZMA}} \times m\text{Copo}) / M_w\text{Copo}$$

Where $m\text{Copo}$ is the mass of copolymer used for the click reaction, and set as 50 mg for each reaction.

Thus,

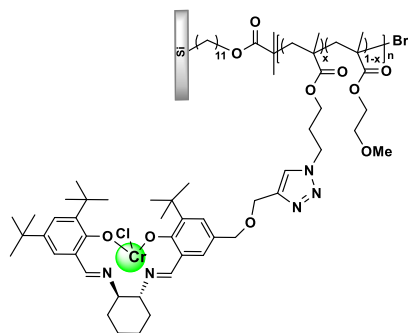
SARA-Copo1: $M_w\text{Copo} = 18200 \text{ g}\cdot\text{mol}^{-1}$, with 58 % conversion of AZMA, and $DP_{\text{AZMA}} = 32$;

SARA-Copo2: $M_w\text{Copo} = 16900 \text{ g}\cdot\text{mol}^{-1}$, with 52 % conversion of AZMA, and $DP_{\text{AZMA}} = 70$;

Preparation of SARA-Copo-Cat1: SARA-Copo1 (1 eq., 0.087 mmol, 50 mg), Salen-Co ((1.3/2 eq.), 0.055 mmol, 38 mg), Salen-Cr ((1.3/2 eq.), 0.055 mmol, 36 mg), CuI (10 %, 0.0087 mmol, 1.6 mg), DIPEA (3.5 eq., 0.3 mmol, 55 μL).

Preparation of SARA-Copo-Cat2: SARA-Copo2 (1 eq., 0.2 mmol, 50 mg), Salen-Co ((1.3/2 eq.), 0.13 mmol, 90 mg), Salen-Cr ((1.3/2 eq.), 0.13 mmol, 86 mg), CuI (10 %, 0.02 mmol, 3.81 mg), DIPEA (3.5 eq., 0.7 mmol, 120 μL).

Click chemistry with Cr-salen complex on surface



PSiBr1-Copo3, Cr-salen complex (0.0065 mmol, 4.2 mg) and CuI (0.007 mmol, 1.3 mg) were placed inside a Schlenk designed for reactions with silicon. Vacuum was applied for 5 min and then back filled with argon. This step was repeated another 2 times. Distilled THF (4 mL) and distilled DIPEA (45 μ L, 0.245 mmol) were degassed by 3 freeze-pump-thaw cycles, and then transferred to the Schlenk reaction using inert syringe technique. The Schlenk was placed in a preheated oil bath at 40 $^{\circ}$ C for 40 h, under constant stirring. Then, the prism was removed from the reaction mixture and thoroughly rinsed with THF, followed by rinsing in THF in an ultra sound bath for 15 min twice. Finally, it was further rinsed using Soxhlet apparatus overnight with THF as solvent. The prism was dried using N₂ flow and stored under argon.

CHAPTER 5: Supported asymmetric catalysis

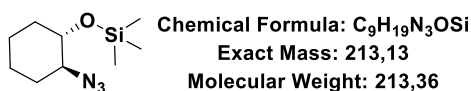
Materials

Tetrahydrofuran and diethyl ether were dried before use. Methyl tert-butyl ether was used as received. Cyclohexene oxide, dodecane, trimethylsilyl azide, epibromohydrin, bromobenzene, 2,2-dimethoxypropane, Amberlyst 15, 2-methoxybenzaldehyde and nitromethane were purchased from Aldrich and used without further purification. DIPEA was distilled before use. Cr and Co Jacobsen catalysts were synthesized by group members.

Methods

Homogenous catalysis

ARO of cyclohexene oxide to form (((1*S*,2*S*)-2-azidocyclohexyl)oxy)trimethylsilane



A Schlenk was charged with catalyst (2 mol%), and three vacuum-argon cycles was applied, and it was then maintained under argon. Solvent (230 μ L), cyclohexene oxide (1 eq., 0.25 mmol, 25 μ L), and dodecane as internal standard (0.28 eq., 0.07 mmol, 16 μ L) were then added. The reaction mixture was stirred for 10 minutes at 25 °C before adding the trimethylsilyl azide (1.5 eq., 0.375 mmol, 50 μ L), and then stirred for the corresponding amount of time. Samples were taken and diluted in ether for the calculation of conversion and *ee* by GC analysis (cf. **Appendix B**).

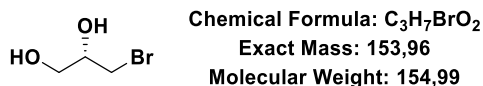
Using Cr-Jacobsen: catalyst (2 mol%, 0.005 mmol, 3.16 mg).

Using Cr-unsymmetrical salen: catalyst (2 mol%, 0.005 mmol, 3.22 mg).

Using Co-Jacobsen: catalyst (2 mol%, 0.005 mmol, 3.3 mg).

The *ee* was determined by chiral GC on a Shimadzu GC 2010 plus using a chiraldex β -PM column (50m \times 0.25mm \times 0.12 μ m) and hydrogen as a carrier gas (isothermal 110 °C), which resolved both enantiomers (t_{R} = 10.57 min, t_{S} = 10.89 min). The absolute stereochemistry was assigned as 1*S*,2*S* based on comparison with the literature.¹⁰⁰

DKR of epibromohydrin to form (*S*)-3-bromopropane-1,2-diol



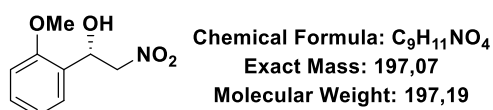
A Schlenk was charged with catalyst (2 mol%) and solubilized in THF (0.145 mL). Racemic epibromohydrin (1 eq., 1.2 mmol, 0.103 mL), bromobenzene (0.14 eq., 0.17 mmol, 40 μ L), and deionized water (1.4 eq., 1.7 mmol, 30 μ L) were added and the reaction was stirred at 0 °C for the desired time. Samples were taken and diluted in ether for the calculation of conversion by GC analysis using a ZB-1701 column (15 m \times 0.25 mm \times 0.25 μ m) (cf. **Appendix B**).

Using Cr-Jacobsen: catalyst (2 mol%, 0.024 mmol, 15.17 mg).

Using Co-Jacobsen: catalyst (2 mol%, 0.024 mmol, 15.89 mg).

Then, to obtain enantioselectivity results, DCM (5.4 mL), Amberlyst 15 (16 mg) and 2,2-dimethoxypropane (2 eq., 2.4 mmol, 0.29 mL) were added. The resulting mixture was stirred at r.t. overnight, and then analyzed by chiral GC. The enantioselectivity was determined using a chiraldex β -PM column (50m \times 0.25mm \times 0.12 μ m) and hydrogen as a carrier gas (isothermal 110 °C), which resolved both enantiomers (t_{R} = 4.69 min, t_{S} = 4.73 min) (cf. **Appendix B**).

Henry reaction to form (*S*)-1-(2-methoxyphenyl)-2-nitroethan-1-ol



A Schlenk tube was charged with the catalyst (2 mol %, 0.02 mmol, 0.0126 g) and 2-methoxybenzaldehyde (1 eq., 1 mmol, 0.136 g) and maintained under an argon atmosphere by three successive vacuo-argon cycles. Nitromethane (37.5 eq., 37.5 mmol, 2 mL) was introduced with 4 mL of MTBE, followed by the addition of a solution of diisopropylethylamine (1 eq., 1 mmol, 0.17 mL) in MTBE (4 mL). The resulting solution was stirred for 24 h. TLC conditions for following the reaction: petroleum ether / ethyl acetate, 9 / 1. The solvents were then removed under reduced pressure, and the product was analyzed by NMR to give NMR yield (94 %). ¹H NMR (300 MHz, CDCl₃) δ 7.45 (dd, J = 7.5, 1.8 Hz, 1H), 7.33 (td, J = 7.5, 1.8 Hz, 1H), 7.02 (dd, J = 7.5, 0.75 Hz, 1H), 6.91 (d, J = 8.3 Hz, 1H), 5.64

(ddd, $J = 9.2, 6.0, 3.4$ Hz, 1H), 4.66 (dd, $J = 13.1, 3.4$ Hz, 1H), 4.58 (dd, $J = 13.1, 9.2$ Hz, 1H), 3.88 (s, 3H), 3.12 (d, $J = 6.0$ Hz, 1H).

The *ee* was determined by HPLC analysis using an IB column (flow rate: 1.0 mL·min⁻¹; 90% hexane, 10% isopropanol, $\lambda = 254$ nm), which resolved both enantiomers ($t_{R} = 11.16$ min, $t_{S} = 12.33$ min). The absolute stereochemistry was assigned as **S** based on comparison of the measured rotation with the literature value (cf. **Appendix B**).^{107b}

Supported catalysis

- Ring opening of cyclohexene oxide

A Schlenk tube was charged with the appropriate SARA-Copo-Cat (2 mol%) and three vacuum argon cycles were performed by finally maintaining it under argon. Diethyl ether (500 μ L), cyclohexene oxide (0.122 mmol) and dodecane as an internal standard (8 μ L) were then added. The reaction mixture was stirred for 10 min at 25 °C before adding the trimethylsilyl azide (24 μ L, 0.183 mmol), and then stirred for 24 h. A sample was prepared to calculate conversion and enantiomeric excess by GC. The supported catalyst was precipitated with hexanes and washed 3 times with hexanes (3 \times 2 mL) and dried in the tube for its reuse.

The conversion and *ee* was determined by chiral GC on a Shimadzu GC 2010 plus using a chiraldex β -PM column (50m \times 0.25mm \times 0.12 μ m) and hydrogen as a carrier gas (isothermal 110 °C). Conversion was calculated using dodecane as an internal standard. Enantiomers retention time: ($t_{R} = 10.57$ min, $t_{S} = 10.89$ min).

The amount of weighted SARA-Copo-Cat ($m_{\text{SARA-Copo-Cat}}$) to be introduced in the reaction mixture was calculated as follows. The molar mass of SARA-Copo-Cat ($M_{\text{WSARA-Copo-Cat}}$) was calculated according to the NMR data, considering the conversion of each monomer and the molar mass of MEMA and of the monomer unit resulting from the click reaction of the salen-Cr complex with AZMA, and DP_{AZMA} states for the degree of polymerization of AZMA monomer.

$$M_{\text{SARA-Copo-Cat}} = (0.02 \times n_{\text{epoxide}} \times M_{\text{WSARA-Copo-Cat}}) / DP_{\text{AZMA}}$$

Thus, for

SARA-Copo-Cat1: $M_{\text{WSARA-Copo-Cat1}} = 39240$ g·mol⁻¹, $DP_{\text{AZMA}} = 32$, $DP_{\text{MEMA}} = 88.5$;

SARA-Copo-Cat2: $M_{wSARA-Copo-Cat2} = 63028 \text{ g}\cdot\text{mol}^{-1}$, $DP_{AZMA} = 70$, $DP_{MEMA} = 35.2$;

However, some corrections should be done since:

- 1) There are two different catalysts clicked;
- 2) Not all of the azide functions were reacted.

Therefore, assuming that the supported catalyst has half of chromium and half of cobalt catalysts (as the loading for the Azide–Alkyne Huisgen cycloaddition was 50/50), we thus need to double the quantity of catalyst used. Then, the new formula is:

$$M_{SARA-Copo-Cat} = 2 \times [(0.02 \times n_{\text{epoxide}} \times M_{wSARA-Copo-Cat}) / DP_{AZMA}]$$

Considering that $n_{\text{epoxide}} = 0.305 \text{ mmol}$, thus we obtain:

SARA-Copo-Cat1 (2 mol %) 14.8 mg

SARA-Copo-Cat2 (2 mol %) 10.8 mg

Regarding point two, in fact, it has been observed by FTIR that the click reaction was not completed, and that ~ 40% of the azide functions were reacted, therefore, the quantity of each reagent has to respect that only 40% of the azide functions in the copolymers have the desired catalysts, ending with the following proportions:

Catalytic test with SARA-Copo-Cat1 (2 mol %) 14.8 mg, cyclohexene oxide (12.4 μL , 0.122 mmol), Et_2O (500 μL), dodecane (8 μL), trimethylsilyl azide (24 μL , 0.183 mmol).

Catalytic test with SARA-Copo-Cat2 (2 mol %) 10.8 mg, cyclohexene oxide (12.4 μL , 0.122 mmol), Et_2O (500 μL), dodecane (8 μL), trimethylsilyl azide (24 μL , 0.183 mmol).

- *Ring opening of epibromohydrin*

After washing and drying the SARA-Copo-Cat from the first reaction, it was kept under argon atmosphere. Tetrahydrofuran (500 μL), epibromohydrin (1 eq., 0.122 mmol, 0.0103 mL), water (1.4 eq., 0.17 mmol, 3 μL) and bromobenzene as internal standard (0.017 mmol, 4 μL) were then added. The reaction mixture was stirred for 72 h at 0 °C. A sample was taken to calculate conversion by achiral GC (ZB-1701 column (15 m \times 0.25 mm \times 0.25 μm)). The supported catalyst was precipitated with hexane and washed 3 times with hexane (3 \times 2 mL) and dried in

the tube for its reuse. The supernatant was then engaged in another reaction by adding 2,2-dimethoxypropane (2 eq., 0.24 mmol, 30 μ L) and Amberlyst 15 (1.6 mg), and then a sample was taken to determine the enantiomeric excess by chiral GC (isothermal 110 $^{\circ}$ C), which resolved both enantiomers (t_{R} = 4.69 min, t_{S} = 4.73 min). The absolute stereochemistry was assigned as (*S*) based on comparison with the literature.¹⁸²

Monocatalysis using silicon supported catalysts

- *Ring opening of cyclohexene oxide*

The silicon supported catalyst, which contains $\sim 1.1 \times 10^{-4}$ mmol of salen catalyst attached on surface, was put in a special Schlenk for prisms. High vacuum was applied and it was then maintained under argon atmosphere after 3 successive vacuum-argon cycles. Dry diethyl ether or THF (see quantity below) was added, followed by the addition of dodecane (see quantity below) and cyclohexene oxide (see quantity below). The reaction was let to mix over 10 min, followed by the addition of TMSN₃ (see quantity below). Various samples were taken over time and analyzed by GC.

The reaction was followed by chiral GC on a Shimadzu GC 2010 plus using a chiraldex β -PM column (50m \times 0.25mm \times 0.12 μ m) and hydrogen as a carrier gas (isothermal 110 $^{\circ}$ C).

Trial at 0.5 mol%: supported catalyst (0.5 mol%, $\sim 1.1 \times 10^{-4}$ mmol), cyclohexene oxide (1 eq., 0.025 mmol, 2.5 μ L), dodecane (1.6 μ L), TMSN₃ (1.5 eq., 0.0375 mmol, 5 μ L) in 500 μ L of diethyl ether.

Trial at 2 mol% in diethyl ether: supported catalyst (2 mol%, $\sim 1.1 \times 10^{-4}$ mmol), cyclohexene oxide (1 eq., 6.3×10^{-3} mmol, 0.617 μ L) was added using a stock solution in dry diethyl ether (0.3 mL of a 0.021 mol/L solution), dodecane (0.001 mmol, 0.24 μ L) was added using a stock solution in dry diethyl ether (0.3 mL of a 0.003 mol/L solution), TMSN₃ (1.5 eq., 9.45×10^{-3} mmol, 1.2 μ L) was added using a stock solution (0.3 mL of a 0.031 mol/L solution).

Trial at 2 mol% in THF: supported catalyst (2 mol%, $\sim 1.1 \times 10^{-4}$ mmol), cyclohexene oxide (1 eq., 6.3×10^{-3} mmol, 0.617 μ L), dodecane (0.001 mmol, 0.24 μ L), TMSN₃ (1.5 eq., 9.45×10^{-3} mmol, 1.2 μ L) were added using a 1 μ L syringe in 500 μ L of dry THF.

- *Henry reaction*

The silicon supported catalyst (2 mol%), which contains $\sim 1.1 \times 10^{-4}$ mmol of salen catalyst attached on surface, and 2-methoxybenzaldehyde (1 eq., 6.3×10^{-3} mmol, 0.856 mg) were put in a special Schlenk for prisms. High vacuum was applied and it was then maintained under argon atmosphere after 3 successive vacuum-argon cycles. Under positive argon atmosphere, nitromethane (37.5 eq., 0.23 mmol, 12.6 μ L), tetradecane (0.5 eq., 3.15×10^{-3} mmol, 8 μ L) and DIPEA (1 eq., 6.3×10^{-3} mmol, 1.1 μ L) were added in 300 μ L of MTBE. Various samples were taken over time and analyzed by achiral GC column ZB5-MS of dimensions 15 m x 0.25 mm x 0.25 μ m.

Appendix A

X-ray Photoelectron Spectroscopy (XPS): atomic information tables from presented spectra

Chapter 2

SiBr1

Name	Peak BE	FWHM eV	Area (P) CPS.eV	Area (N) TPP-2M	Atomic %	Correction factor
Br3d5 C-Br	69.29	1.01	915.66	0.01	0.49	1.68
Br3d3 C-Br	70.34	1.01	604.24	0	0	1.16
Br3d5 Br-O	70.43	1.16	413.58	0.01	0.22	1.68
Br3d3 Br-O	71.48	1.16	272.96	0	0	1.16
Si2p3 Si-Si	99.33	0.54	22324.28	0.82	34.17	0.596
Si2p1 Si-Si	99.95	0.55	11145.76	0	0	0.304
Si2p3 SiO ₂	102.64	1.62	4248.19	0.16	6.51	0.596
Si2p1 SiO ₂	103.26	1.62	2124.1	0	0	0.304
Si2p3 Interface	99.73	0.7	4156.82	0.15	6.36	0.596
Si2p1 Interface	100.35	0.7	2077.2	0	0	0.304
C1s C-C	284.96	1.42	22899.03	0.52	21.69	1
C1s C-O	286.49	1.42	4447.02	0.1	4.21	1
C1s C=O	288.93	1.5	654.65	0.01	0.62	1
O1s	532.66	1.69	73153.62	0.62	25.72	2.881

SiOBr1

Name	Peak BE	FWHM eV	Area (P) CPS.eV	Area (N)	Atomic %	Correction factor
O1s	533.71	1.61	218225.80	1.85	43.28	2.881
C1s C-C	286.02	1.33	29080.38	0.66	15.54	1.000
C1s C-O	287.71	1.33	5108.89	0.12	2.73	1.000
C1s C=O	290.10	1.33	538.31	0.01	0.29	1.000
O1s Scan A	534.48	1.30	3365.75	0.03	0.67	2.881
O1s Scan B	532.24	0.89	4114.66	0.03	0.82	2.881
Br3d	70.02	2.19	589.86	0.00	0.12	2.729
Si2p	99.60	1.03	63967.47	1.56	36.57	0.900

SiOBr3

Name	Peak BE	FWHM eV	Area (P) CPS.eV	Area (N) TPP-2M	Atomic %	Correction factor
Br3d5 Br-O	71.1	1	484.32	0.01	0.16	1.68
O1s	533.2	1.51	133876.59	1.13	28.11	2.881
Br3d3 Br-O	72.14	1	319.65	0	0	1.16
Br3d5 C-Br	69.22	1.16	746.59	0.01	0.24	1.68
Br3d3 C-Br	70.26	1.16	492.77	0	0	1.16
O1s Scan A	534.49	1.54	23222.8	0.2	4.88	2.881
Si2p3 Si-Si	99.68	0.54	30944.73	1.14	28.29	0.596
Si2p1 Si-Si	100.3	0.54	15473.81	0	0	0.304
Si2p3 SiO ₂	103.53	1.34	7959.99	0.29	7.28	0.596
Si2p1 SiO ₂	104.15	1.34	3980.02	0	0	0.304
Si2p3 Interface	100.08	0.79	2850.28	0.1	2.61	0.596
Si2p1 Interface	100.7	0.79	1425.16	0	0	0.304
C1s C-C	285.92	1.38	26264.88	0.6	14.86	1
C1s C-O	287.55	1.38	12928.24	0.29	7.32	1
C1s C=O	289.81	1.38	8476.39	0.19	4.8	1
O1s Scan B	532.11	1	6991.91	0.06	1.47	2.881

SiBr3

Name	Peak BE	FWHM eV	Area (P) CPS.eV	Area (N) TPP-2M	Atomic %	Correction factor
Br3d5 C-Br	68.64	1.5	787.31	0.01	0.4	1.68
Br3d3 C-Br	69.69	1.5	519.65	0	0	1.16
C1s C-C	284.62	1.43	8194.56	0.19	7.28	1
C1s C-O	286.2	1.43	6368.92	0.15	5.66	1
C1s C=O	288.6	1.14	1972.78	0.04	1.75	1
O1s	532.06	1.65	71875.6	0.61	23.7	2.881
O1s SiO ₂	533.55	1.65	3893.69	0.03	1.28	2.881
Si2p3 Si-Si	98.8	0.58	35837.12	1.32	51.46	0.596
Si2p1 Si-Si	99.42	0.58	17907.9	0	0	0.304
Si2p3 SiO ₂	102.29	1.3	3647.1	0.13	5.24	0.596
Si2p3 Interface	99.2	0.72	2178.3	0.08	3.13	0.596
Si2p1 Interface	99.82	0.72	1088.87	0	0	0.304
Si2p1 SiO ₂	102.91	1.3	1823.55	0	0	0.304
Br3d5 Br-O	70.03	1	156.48	0	0.08	1.68
Br3d3 Br-O	71.08	2.05	103.28	0	0	1.16

SiOBr2

Name	Peak BE	FWHM eV	Area (P) CPS.eV	Area (N) TPP-2M	Atomic %	Correction factor
C1s	285.43	1.70	10655.10	0.24	6.68	1.000
O1s	533.16	1.62	160465.52	1.36	37.37	2.881
Si2p SiO ₂	103.74	1.51	14740.13	0.36	9.90	0.900
Si2p Si-Si	99.71	1.01	68594.07	1.67	46.05	0.900

PSiBr1 macroporous Si

Name	Peak BE	FWHM eV	Area (P) CPS.eV	Area (N) TPP-2M	Atomic %	Correction factor
Br3d	69.74	1.97	2934	0.02	1.44	2.729
C1s C-C	285.19	1.29	26559.34	0.6	37.03	1
O1s	532.87	1.79	40469.76	0.34	20.94	2.881
Si2p SiO ₂	103.3	1.53	2844.61	0.07	4.25	0.9
Si2p Si-Si	99.7	1.11	21633.81	0.53	32.27	0.9
C1s C-O	286.72	1.29	2642.84	0.06	3.69	1
C1s C=O	289.65	0.77	284.02	0.01	0.4	1

Chapter 3

SiOBr1-PMEMA

Name	Peak BE	FWHM eV	Area (P) CPS.eV	Area (N) TPP-2M	Atomic %	Correction factor
O1s Scan A	534.49	1.75	20441.98	0.17	4.54	2.881
Si2p3 Si-Si	99.38	0.54	4595.56	0.17	4.44	0.596
Si2p3 SiO ₂	103.51	1.68	8781.27	0.32	8.5	0.596
Si2p1 Si-Si	100	0.54	2299.67	0	0	0.304
Si2p3 Interface	99.69	0.78	986.43	0.04	0.95	0.596
Si2p1 Interface	100.31	0.78	493.21	0	0	0.304
Si2p1 SiO ₂	104.13	1.68	4390.59	0	0	0.304
C1s C-C	285.83	1.33	50927.59	1.16	30.48	1
C1s C-O	287.44	1.33	26822.58	0.61	16.06	1
C1s C=O	289.77	1.23	10272.5	0.23	6.15	1
O1s Scan B	533.42	1.75	128448.43	1.09	28.53	2.881
Br3d	70.29	2.19	1719.97	0.01	0.35	2.84

SiBr1-PMEMA

Name	Peak BE	FWHM eV	Area (P) CPS.eV	Area (N) TPP-2M	Atomic %	Correction factor
O1s Scan A	532.52	1.69	60720.92	0.51	21.59	2.881
O1s Scan B	533.66	1.69	29666.97	0.25	10.55	2.881
Si2p3 Si-Si	99.16	0.54	9417.76	0.35	14.58	0.596
Si2p1 Si-Si	99.78	0.54	4715.35	0	0	0.304
Si2p3 SiO ₂	102.83	1.33	2751.42	0.1	4.26	0.596
Si2p3 Interface	99.38	0.78	2247.47	0.08	3.48	0.596
Si2p1 Interface	100	0.78	1123.81	0	0	0.304
Si2p1 SiO ₂	103.45	1.33	1375.68	0	0	0.304
C1s C-C	285.19	1.33	21447.84	0.49	20.55	1
C1s C=O	289.07	1	6714	0.15	6.44	1
C1s C-O	286.78	1.33	19211.61	0.44	18.41	1
Br3d	69.61	2.28	432.13	0	0.14	2.84

SiOBr3-PMEMA

Name	Peak BE	FWHM M eV	Area (P) CPS.eV	Area (N) TPP-2M	Atomic %	Correction factor
C1s C-C	285.6	1.33	44031.45	1	27.86	1
C1s C=O	289.43	1.06	15129.17	0.34	9.58	1
C1s C-O	287.11	1.33	43093.46	0.98	27.28	1
O1s Scan A	532.95	1.75	68127.6	0.58	16	2.881
O1s Scan B	533.98	1.75	62334.37	0.53	14.64	2.881
Si2p3 Si-Si	99.3	0.53	3178.18	0.12	3.25	0.596
Si2p3 Interface	99.8	0.78	275.52	0.01	0.28	0.596
Si2p3 SiO ₂	102.83	1.34	922.66	0.03	0.94	0.596
Si2p1 Si-Si	99.92	0.53	1588.38	0	0	0.304
Si2p1 Interface	100.42	0.78	137.74	0	0	0.304
Si2p1 SiO ₂	103.45	1.34	461.32	0	0	0.304
Br3d	69.95	2.28	729.74	0.01	0.16	2.84

SiBr3-PMEMA

Name	Peak BE	FWHM eV	Area (P) CPS.eV	Area (N) TPP-2M	Atomic %	Correction factor
O1s Scan A	531.89	1.75	94738.45	0.8	24.7	2.881
O1s Scan B	532.85	1.75	30188.32	0.26	7.87	2.881
Si2p3 Si-Si	98.83	0.54	15211.65	0.56	17.27	0.596
Si2p1 Si-Si	99.45	0.54	7593.97	0	0	0.304
Si2p3 SiO ₂	102.15	1.51	4517.11	0.17	5.13	0.596
Si2p1 SiO ₂	102.77	1.51	2258.62	0	0	0.304
Si2p3 interface	99.21	0.78	1301.38	0.05	1.48	0.596
Si2p1 interface	99.83	0.78	650.54	0	0	0.304
C1s C-C	284.42	1.33	29433.04	0.67	20.68	1
C1s C-O	286	1.33	22520.23	0.51	15.83	1
C1s C=O	288.27	1.14	9930.37	0.23	6.98	1
Br3d	68.46	2.21	308.48	0	0.07	2.84

MEMA₅₀-co-AZMA₅₀ (entry 2 Table 16)

Name	Peak BE	FWHM eV	Area (P) CPS.eV	Area (N) KE ^{0.6}	Atomic %	Correction factor
O1s	531.59	2.39	73478.16	0.6	22.65	2.93
C1s C-C	284.15	1.38	43051.76	0.99	37.76	1
Br3d	67.06	1.89	553.46	0	0.17	2.84
C1s C=O	288.06	0.97	8593.74	0.2	7.54	1
C1s C-O	285.64	1.4	26454.92	0.61	23.21	1
N1s <u>N=N=N</u>	400.04	1.37	11554.67	0.15	5.7	1.8
N1s N= <u>N=N</u>	403.69	1.01	5229.39	0.07	2.58	1.8
N1s C-N	398.53	0.8	790.03	0.01	0.39	1.8

SiBr1-Cop3

Name	Peak BE	FWHM eV	Area (P) CPS.eV	Area (N) TPP-2M	Atomic %	Correction factor
Br3d	70.57	2.72	443.27	0	0.11	2.729
C1s C-C	286.02	1.43	40178.46	0.92	28.64	1
C1s C=O	289.9	1	9119.7	0.21	6.51	1
C1s C-O	287.53	1.43	26718.46	0.61	19.05	1
N1s <u>N=N=N</u>	401.44	1.5	12877.53	0.18	5.64	1.676
N1s N= <u>N=N</u>	405.18	1.2	5877.15	0.08	2.57	1.676
O1s	533.54	2.61	95056.69	0.8	25.15	2.881
Si2p	99.73	0.57	14666.66	0.39	12.32	0.817

PSiBr1-Cop3

Name	Peak BE	FWHM eV	Area (P) CPS.eV	Area (N) KE ^{0.6}	Atomic %	Correction factor
Br3d	69.72	2.3	1368.88	0.01	0.25	2.84
Si2p SiO ₂	103.89	1.77	13627.84	0.38	8.55	0.817
Si2p Si-Si	99.93	1.16	11399.59	0.32	7.15	0.817
C1s C-C	285.96	1.43	58102.61	1.34	30.18	1
C1s C-O	287.55	1.53	28622.65	0.66	14.87	1
C1s C=O	289.9	1.33	9455.07	0.22	4.91	1
O1s	533.51	1.9	164125.04	1.33	29.96	2.93
N1s <u>N=N=N</u>	401.73	1.69	9660.9	0.13	2.82	1.8
N1s N= <u>N=N</u>	405.46	1.14	3168.33	0.04	0.93	1.8
N1s C-N	400.32	1.1	1301.57	0.02	0.38	1.8

Chapter 4.

SARA-Copo-Cat1

Name	Peak BE	FWHM eV	Area (P) CPS.eV	Area (N) TPP-2M	Atomic %	Correction factor
C1s C-C	284.23	1.51	30249.9	0.69	49.04	1
N1s -N-	400.29	1.88	3206.89	0.04	3.19	1.676
O1s	532.08	2.46	31020.36	0.26	18.67	2.881
C1s C-O	285.81	1.51	12334.72	0.28	20	1
C1s C=O	288.35	1.51	3240.2	0.07	5.26	1
N1s N=N=N	404.05	1.74	1045.4	0.01	1.04	1.676
N1s C-N-N=N	398.51	1.7	2017.51	0.03	2.01	1.676
Cl2p	196.77	0.66	89.32	0	0.09	1.51
Co2p	779.93	2.55	3451.91	0	0.34	19.16
Cr2p	575.99	2.76	2334.59	0	0.35	11.67

SARA-Copo-Cat2

Name	Peak BE	FWHM eV	Area (P) CPS.eV	Area (N) TPP-2M	Atomic %	Correction factor
C1s C-C	284.25	1.59	30563.42	0.7	50.91	1
O1s	531.75	1.65	11754.54	0.1	7.27	2.881
N1s -N-	400.4	1.82	5287.33	0.07	5.41	1.676
C-O	285.7	1.59	11427.83	0.26	19.04	1
C=O	288.36	1.59	2595.35	0.06	4.33	1
O1s Scan A	533.06	1.65	7840.71	0.07	4.85	2.881
O1s Scan B	530.39	1.52	4366.57	0.04	2.7	2.881
N1s N=N=N	404.08	1.53	1428.29	0.02	1.46	1.676
N1s C-N-N=N	398.59	1.85	2860.34	0.04	2.92	1.676
Co2p	780.52	2.66	3845.62	0.01	0.39	19.16
Cr 2p1	585.91	2.47	1076.41	0	0	3.98
Cr 2p3	576.01	2.39	2058.34	0.01	0.48	7.69
Cl2p	196.96	1.32	220.85	0	0.24	1.51

SARA-Copo-Cat1 comparison of atomic % of Cr and Co

Name	Peak BE	FWHM eV	Area (P) CPS.eV	Area (N) TPP-2M	Atomic %	Correction factor
Co2p	779.93	2.56	3843.62	0.01	53.66	18.235
Cr2p	575.95	2.75	2326	0	46.34	11.765

SARA-Copo-Cat2 comparison of atomic % of Cr and Co

Name	Peak BE	FWHM eV	Area (P) CPS.eV	Area (N) TPP-2M	Atomic %	Correction factor
Co2p	780.52	2.66	3849.6	0.01	40.2	18.235
Cr2p	576.08	2.58	4013.5	0.01	59.8	11.765

SiBr1-Copo3-aryl1

Name	Peak BE	FWHM eV	Area (P) CPS.eV	Area (N) KE ^{0.6}	Atomic %	Correction factor
C1s C-C	286.03	1.47	32865.46	0.76	37.08	1
N1s C-N-N=N	401.35	1.73	3261.66	0.04	2.07	1.8
O1s	533.59	2.05	70031.38	0.57	27.78	2.93
Si2p SiO ₂	103.35	1.77	4908.5	0.14	6.69	0.817
Si2p Si-Si	99.32	0.55	1517.45	0.04	2.07	0.817
C1s C=O	289.93	1.46	6461.07	0.15	7.29	1
C1s C-O	287.55	1.47	14436.16	0.33	16.29	1
N1s -N-	402.81	1.73	859.12	0.01	0.54	1.8
N1s NO ₂	407.16	1.73	287.58	0	0.18	1.8

SiBr1-Copo3-aryl2

Name	Peak BE	FWHM eV	Area (P) CPS.eV	Area (N) KE ^{0.6}	Atomic %	Correction factor
C1s	285.69	1.4	72167.64	1.66	33.3	1
C1s Scan A	289.46	1.3	13645.77	0.31	6.3	1
C1s Scan B	287.05	1.5	43140.08	0.99	19.91	1
N1s C-N-N=N	400.42	1.53	13891.02	0.19	3.87	1.676
N1s -N-	401.97	1.53	7477.68	0.1	2.08	1.676
O1s	532.89	2.7	151066.21	1.22	24.5	2.93
Si2p SiO ₂	103.04	1.57	3094.07	0.09	1.73	0.817
Si2p Si-Si	99.34	0.58	14932.36	0.42	8.33	0.817

PSiBr1-Copo3-Cat

Name	Peak BE	FWHM eV	Area (P) CPS.eV	Area (N) KE ^{0.6}	Atomic %	Correction factor
C1s C-C	284.62	1.73	37619.01	0.87	48.73	1
C1s C-O	286.12	1.73	15718.25	0.36	20.36	1
C1s C=O	288.77	1.73	2371.79	0.05	3.07	1
O1s	532.4	2.84	33798.81	0.27	15.39	2.93
N1s -N-	400.6	1.84	3955.67	0.05	2.88	1.8
N1s C-N-N=N	398.6	1.84	6749.85	0.09	4.91	1.8
Cl2p	198.52	2.85	679.95	0.01	0.38	2.285
Cr2p1	586.43	2.56	1572.77	0.01	0.53	3.98
Si2p3 SiO ₂	102.34	2.06	878.13	0.04	2.08	0.541
Si2p3 Si-Si	99.17	1.01	700.48	0.03	1.66	0.541
Si2p1 Si-Si	99.74	1.02	357.92	0	0	0.276
Si2p1 SiO ₂	102.95	2.06	448.1	0	0	0.276

Appendix B

Supporting information (tables, figures and chromatograms)

Chapter 2: Preparation of a surface-initiated layer on silicon

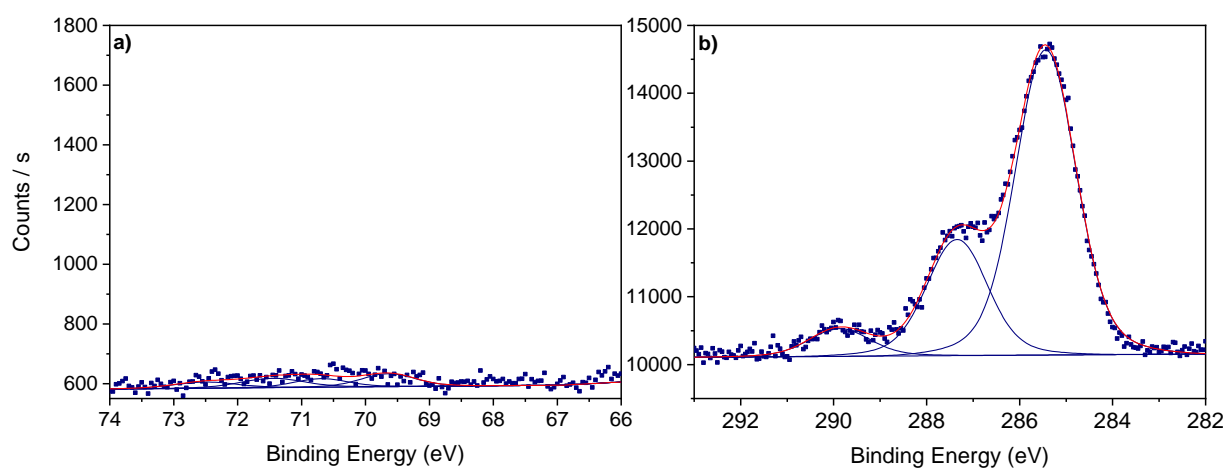


Figure 96: XPS graphs for SiOBr₂. a) Br3d region and b) C1s region.

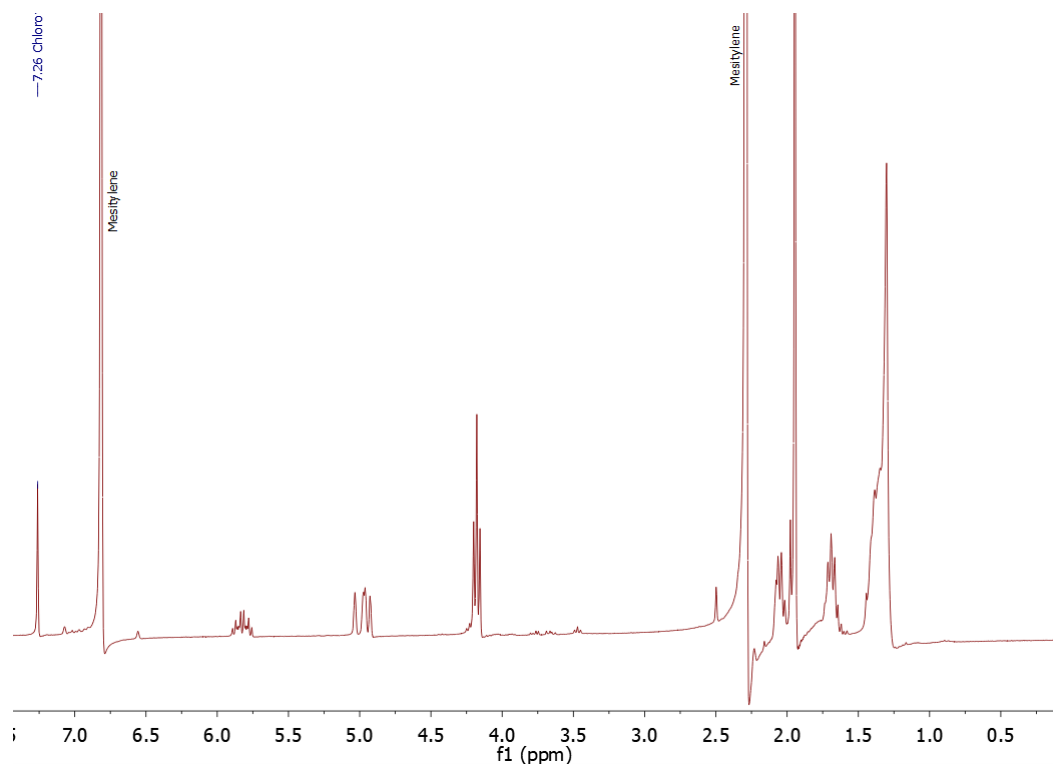


Figure 97: ^1H NMR of reaction mixture of initiator 1 in mesitylene after microwave grafting showing no sign of chemical degradation in solution.

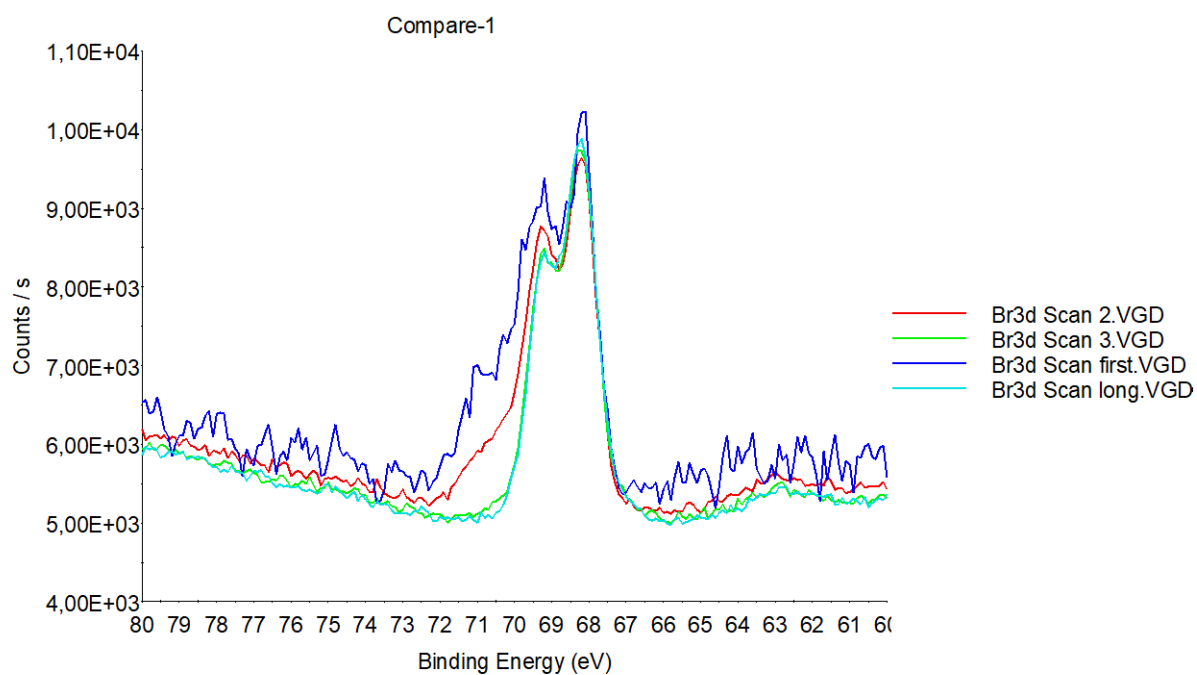


Figure 98: Br3d spectra of initiator 1 drop coated on silver showing only one Br contribution (C–Br) at 68.2 eV and its doublet at 69.2 eV.

Chapter 3: ATRP of methacrylates in solution and on surface

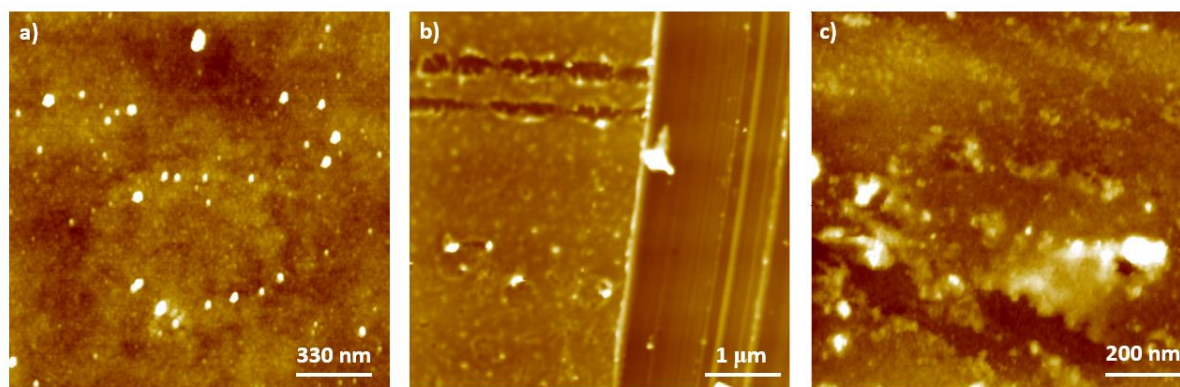


Figure 99: AFM images of a) SiBr1-PMEMA, b) SiOBr3-PMEMA and c) SiBr3-PMEMA.

Table 29: Number of monomer units per nm^2 to mAbs correlation to obtain slope for estimation of number of molecules on macroporous silicon.

Sample	Monomer units / nm^2	mAbs
SiOBr1-PMEMA	9.1	2.4
SiOBr1-PMEMA*	42	12.2
SiBr1-PMEMA	10	3.4
SiOBr3-PMEMA	62	17.2
SiBr3-PMEMA	13	3.8

*Polymerization reaction performed overnight.

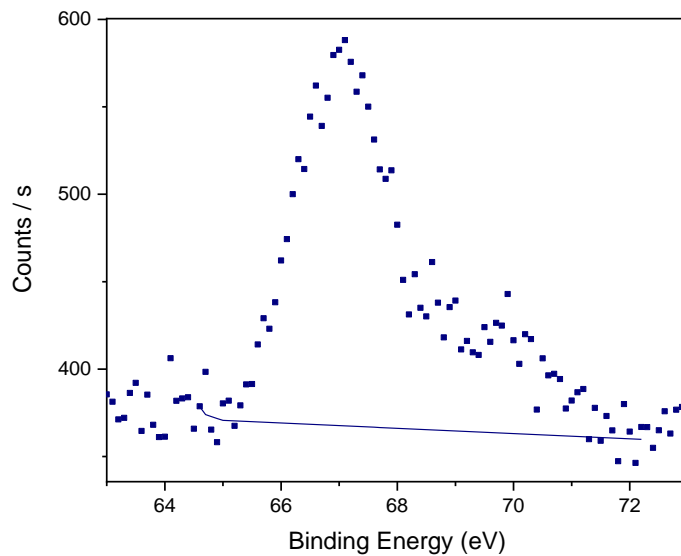


Figure 100: Br3d spectrum of copolymers of MEMA and AZMA synthesized with a 50/50 initial feed (entry 2 of **Table 16**).

Table 30: Number of molecules per nm² to mAbs correlation to obtain slope for estimation of vN₃ density on macroporous silicon.

Sample	Molecules/ nm ²	mAbs
SiBr1-Copo1	1.31	0.3
SiBr1-Copo2	2.81	0.9
SiBr1-Copo3	9.09	3

Chapter 4: Synthesis of salen catalysts and post-functionalization of copolymers

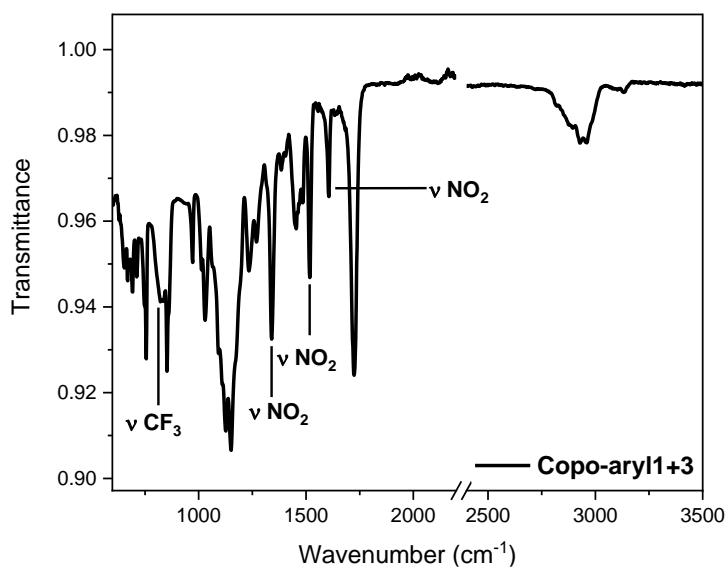


Figure 101: ATR-FTIR spectra of the post-functionalized copolymer using the aryl 1 and 3 in an equimolar quantity. Added break in the spectrum between 2200 to 2400 cm⁻¹ to remove the CO₂ contribution. Characteristics CF₃ bands overlap with copolymer bands in fingerprint region.

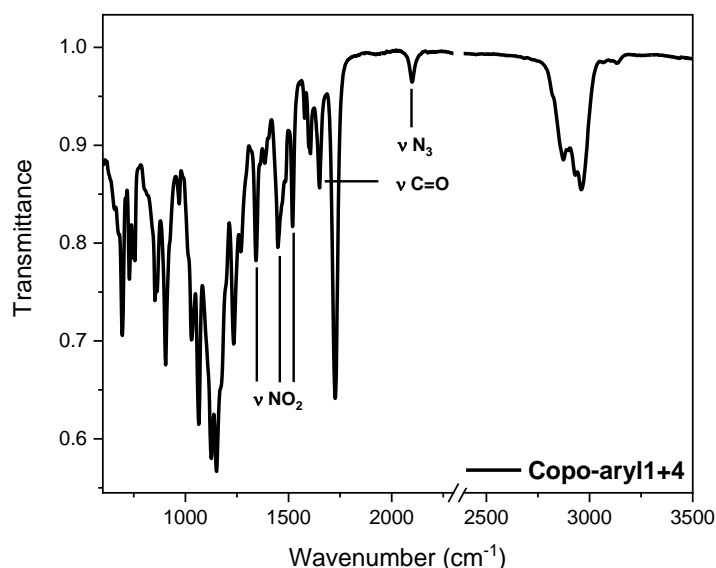


Figure 102: ATR-FTIR spectra of the post-functionalized copolymer using the aryl 1 and 4 in an equimolar quantity. Added break in the spectrum between 2300 to 2390 cm⁻¹ to remove the CO₂ contribution.

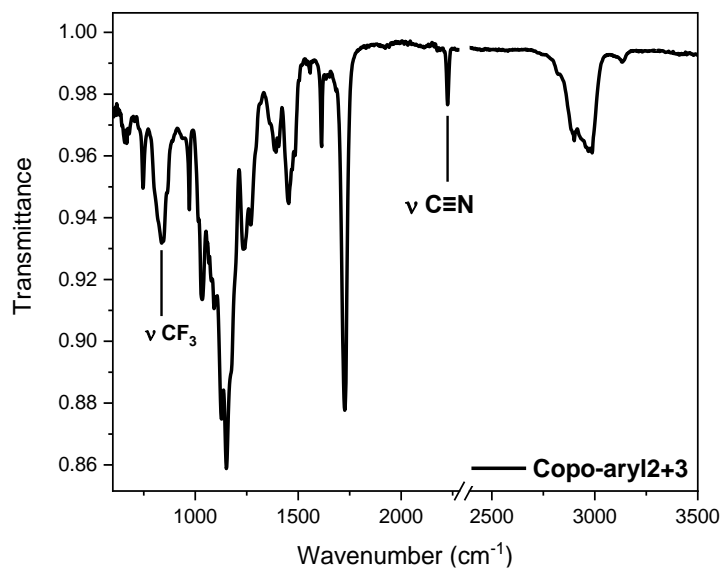


Figure 103: ATR-FTIR spectra of the post-functionalized copolymer using the aryl 2 and 3 in an equimolar quantity. Added break in the spectrum between 2280 to 2390 cm⁻¹ to remove the CO₂ contribution. Characteristics CF₃ bands overlap with copolymer bands in fingerprint region.

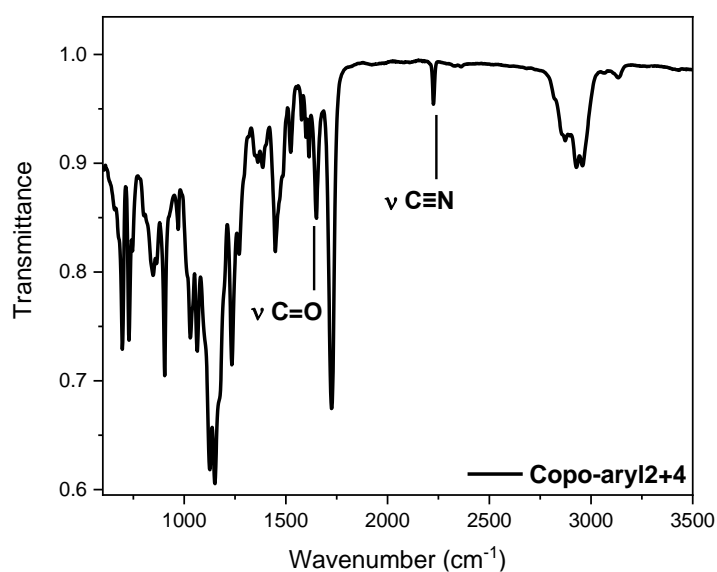


Figure 104: ATR-FTIR spectra of the post-functionalized copolymer using the aryl 2 and 4 in an equimolar quantity.

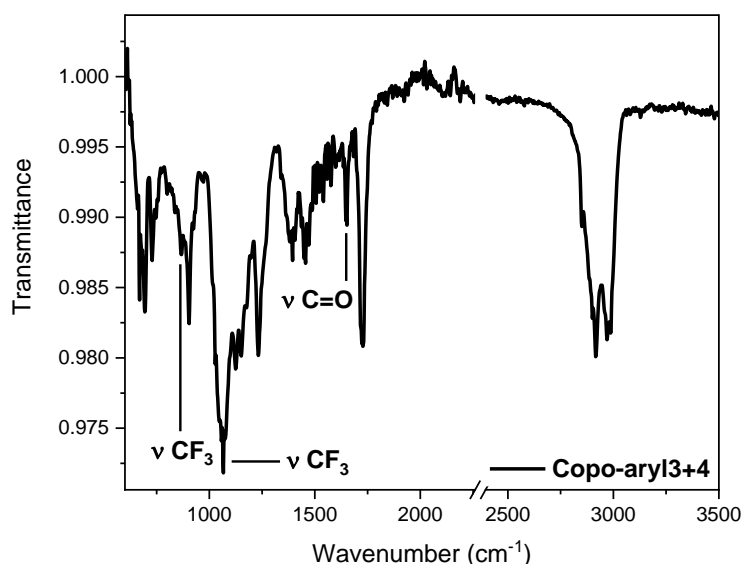


Figure 105: ATR-FTIR spectra of the post-functionalized copolymer using the aryl 3 and 4 in an equimolar quantity. Added break in the spectrum between 2260 to 2400 cm^{-1} to remove the CO_2 contribution. Characteristics CF_3 bands overlap with copolymer bands in fingerprint region. Poor quality spectra due to low quantity of analyzed material.

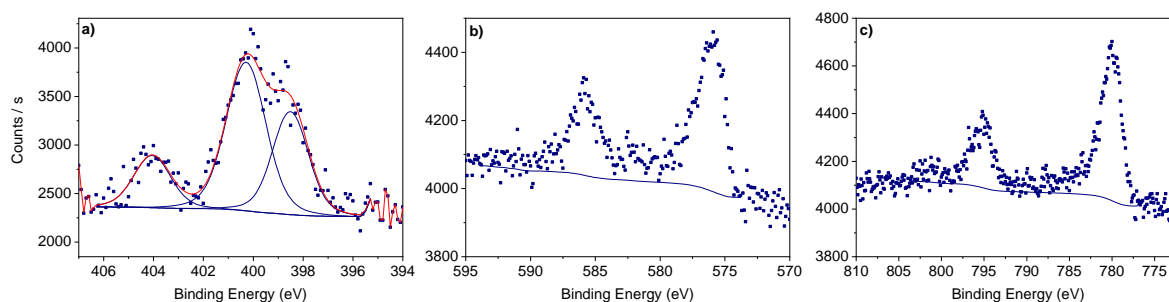


Figure 106: a) N1s b) Cr2p and c) Co2p XPS peaks for the modified supported catalyst (SARA-Copo-Cat1).

Chapter 5: Supported asymmetric catalysis

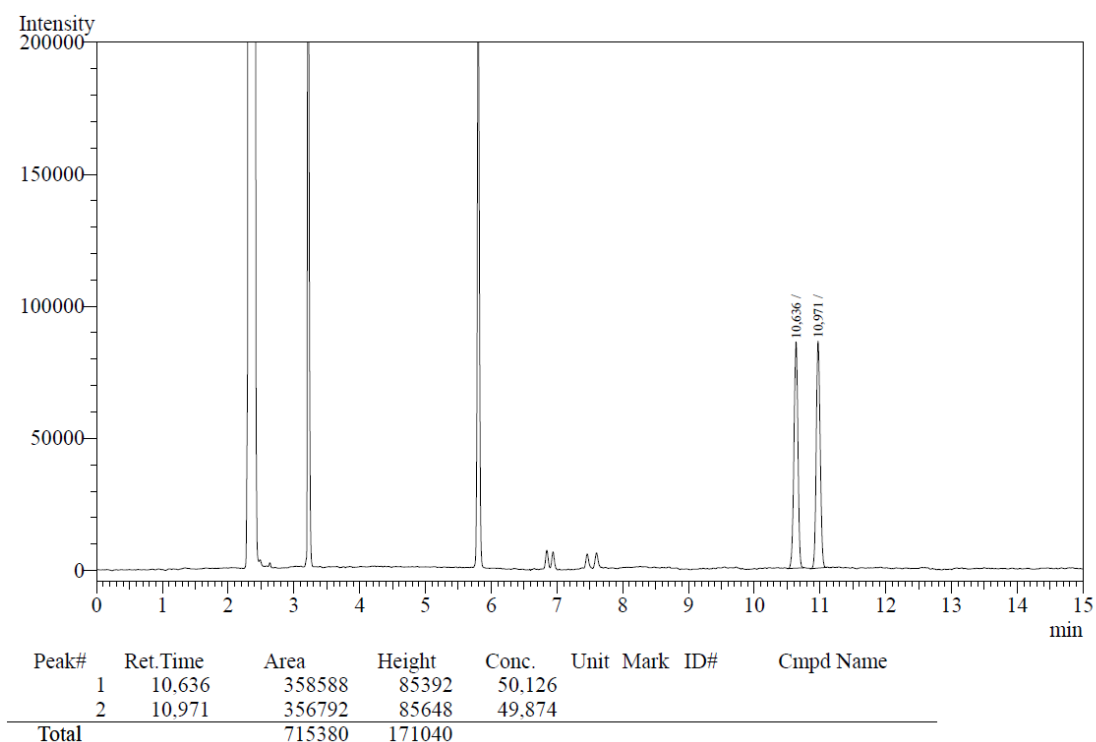


Figure 107: GC spectrum of a racemic sample of ((2-azidocyclohexyl)oxy)trimethylsilane. GC spectrum shown by Bakangura and coworkers.^{8b}

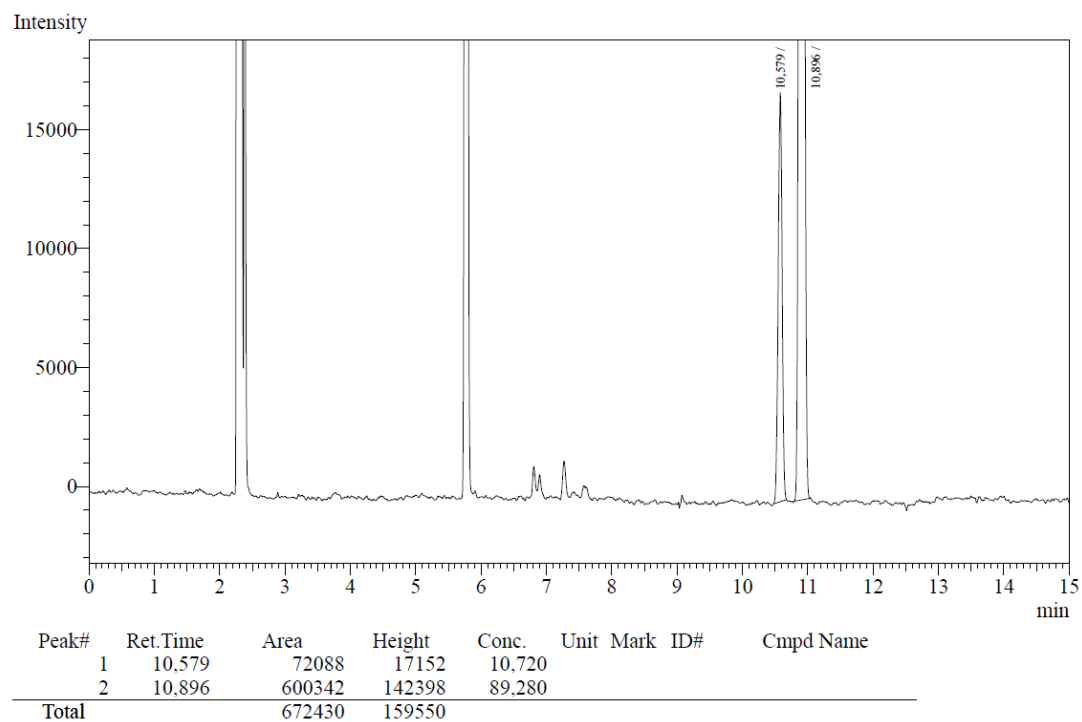


Figure 108: GC spectrum of a 78% *ee* sample of (((1*S*,2*S*)-2-azidocyclohexyl)oxy)trimethylsilane.

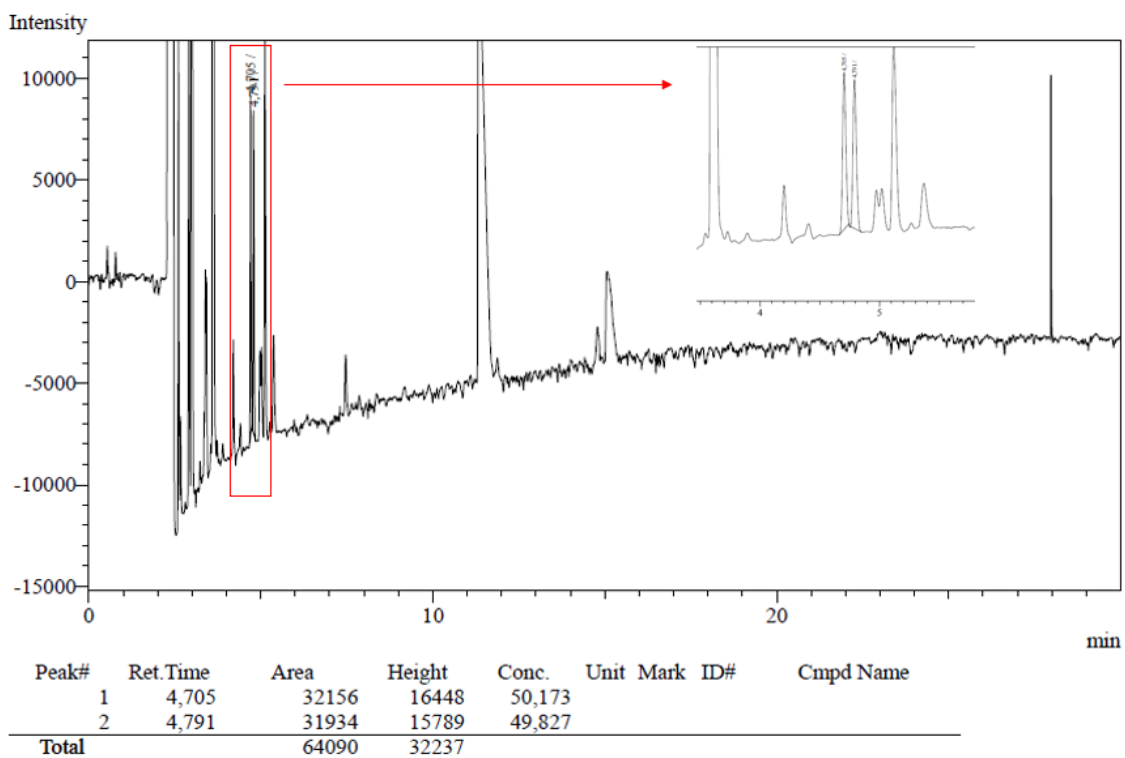


Figure 109: GC spectrum of a racemic sample of 3-bromopropane-1,2-diol. Inset shows the enlargement of the concerned peaks.

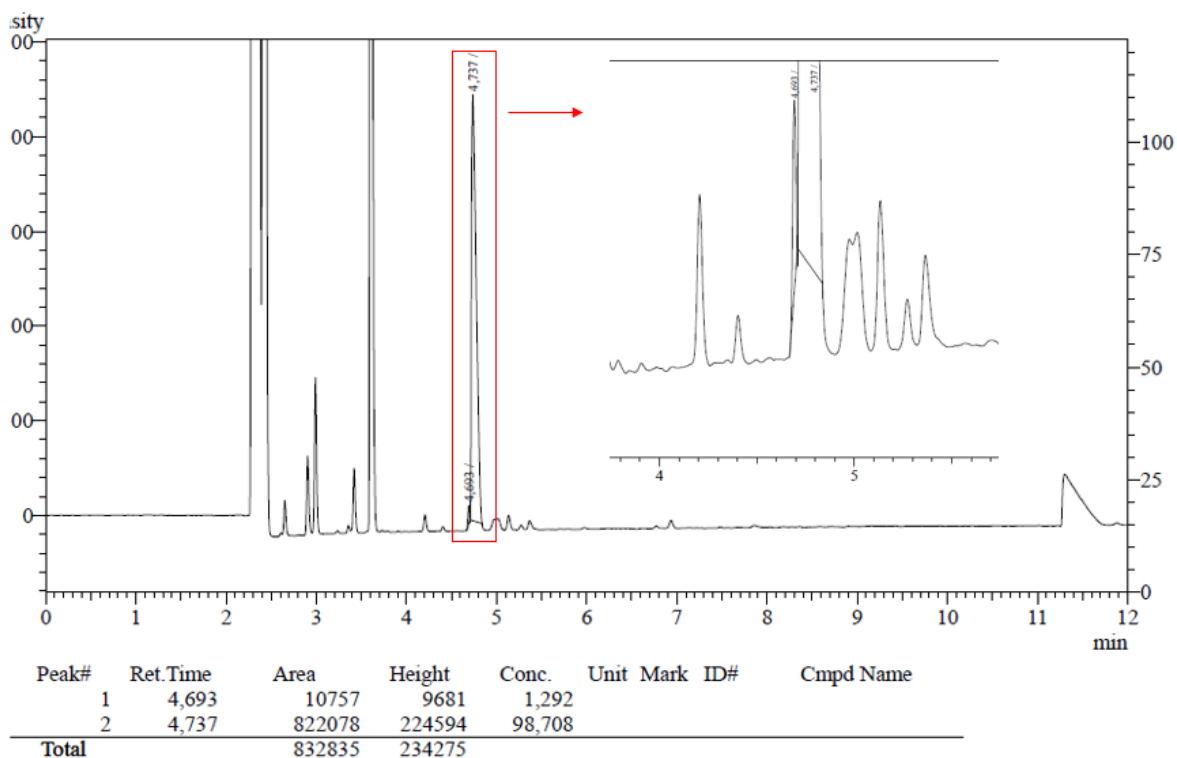


Figure 110: GC spectrum of a 97% *ee* sample of (*S*)-1-bromo-2,3-dimethoxypropane. Inset shows the enlargement of the concerned peaks.

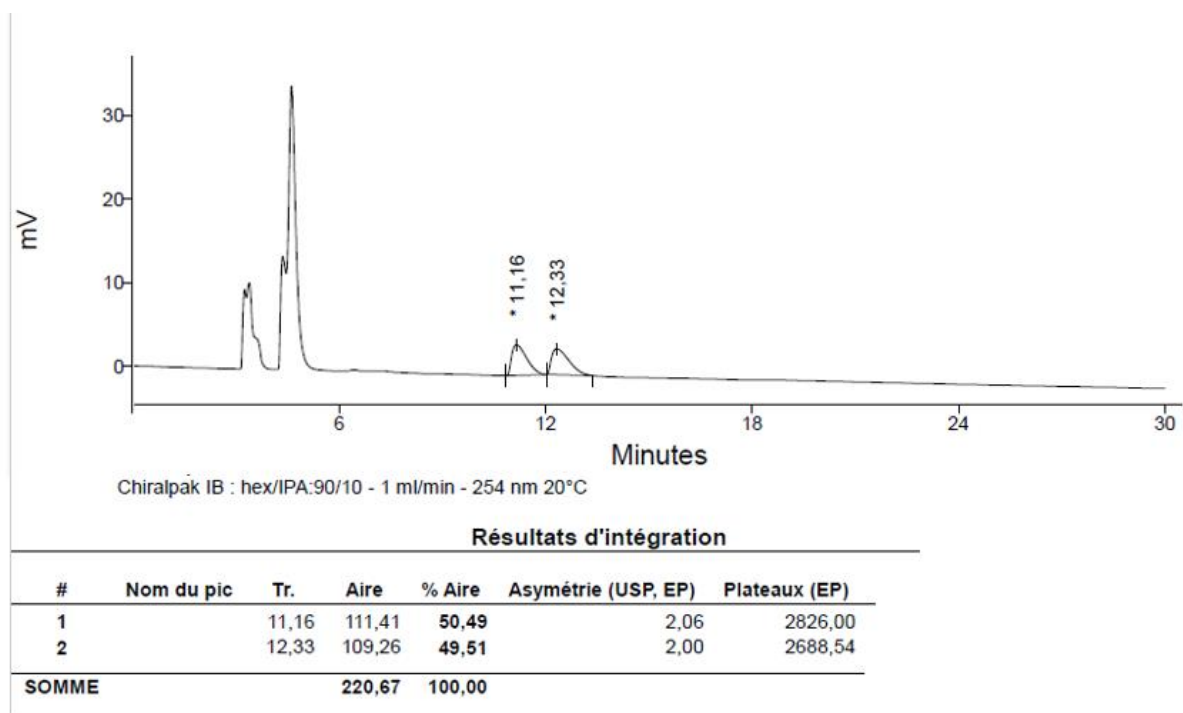


Figure 111: HPLC spectrum of a racemic sample of 1-(2-methoxyphenyl)-2-nitroethan-1-ol.

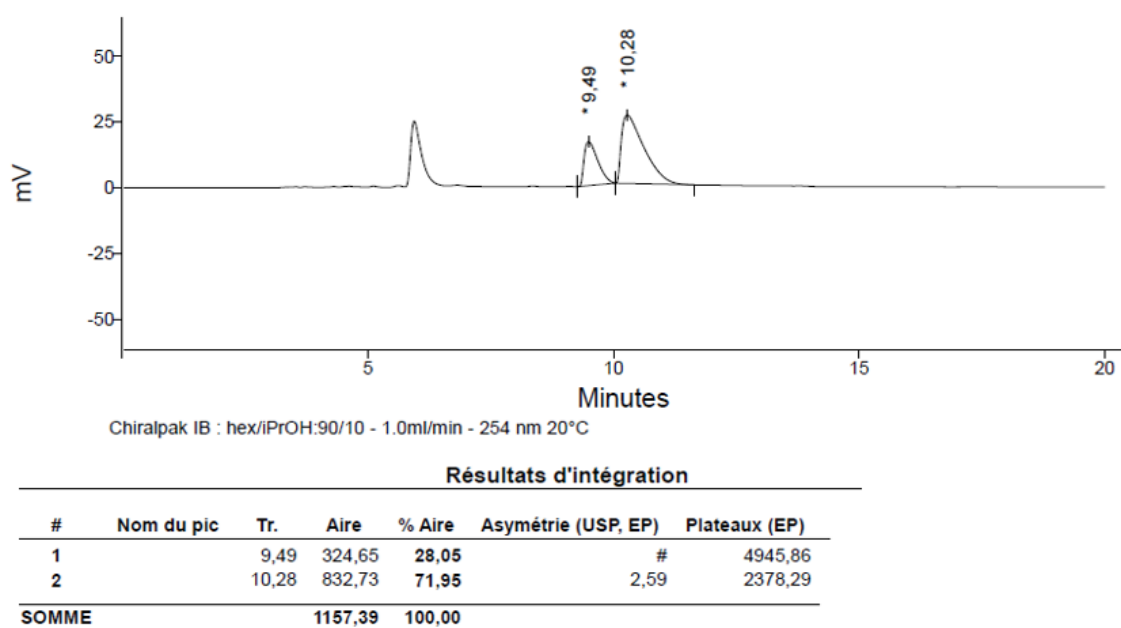


Figure 112: HPLC spectrum of a 44% *ee* sample of (*S*)-1-(2-methoxyphenyl)-2-nitroethan-1-ol.

Appendix C

IR quantification of the chemical groups on crystalline Si

To determine the molecules density grafted on the surface, it is necessary to know the infrared adsorption per molecule. The principle is to measure the infrared absorption intensity of a solution with a known concentration. Then, by analyzing the integral of the absorption peaks on the spectrum of a surface, the density of grafted molecules can be estimated.⁴¹

The geometry of the experiment is that described in **Figure 113**.

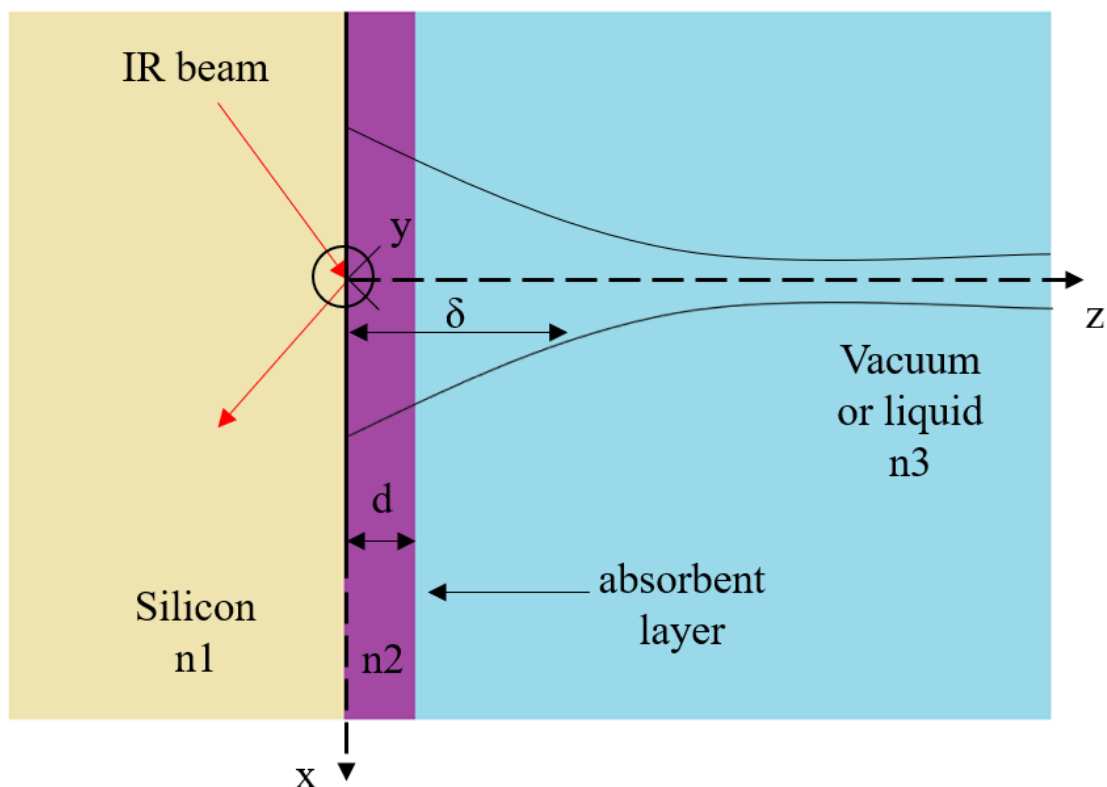


Figure 113: Diagram of the ATR geometry experiment: the infrared beam is propagating in silicon with refractive index $n_1 = 3.42$. The evanescent wave that is formed at the interface produces no loss of beam intensity unless the medium in which it is formed is absorbent. This is the case in the presence of a molecular layer of thickness d and whose dielectric function is n_2 . In this case, the adjacent medium of refractive index n_3 is assumed to be non-absorbent. During the calibration experiments, there is no interfacial layer ($d = 0$), but the medium adjacent (of complex index $n_3 - ik_3$) is absorbing. Figure recreated from Douarche thesis.¹³

The calibration of the C=O functional group of initiator 1 is carried out using a solution of 10-undecylenic-2-bromoisobutyrate in CDCl_3 with different known concentrations. Similarly, the calibration of the C=O functional group of 2-methoxy methyl methacrylate (MEMA) is carried out using a solution of MEMA in CDCl_3 with different known concentrations. And finally, the calibration of 3-azidopropyl methacrylate (AZMA) is carried out using a solution of AZMA in CDCl_3 with different known concentrations. The refractive index of the liquid medium considered is that of CDCl_3 , $n_3=1.44$.

In case of a grafted surface

The infrared absorption of a grafted layer can be analyzed by describing the layer as a slice of thickness δ and effective dielectric function $\varepsilon = \varepsilon' + i\varepsilon''$ at the interface between the solid with refractive index n_1 (3.42 for silicon) and a homogeneous medium with refractive index n_2 (1 for air). The absorbance can then be expressed at the wavelength λ in s and p polarization (the formulas are always written for a single reflection):

$$abs_s = \frac{2\pi}{\lambda} \frac{1}{n_1 \cos \varphi} I_y(\varepsilon''_y d) \quad (1)$$

$$abs_p = \frac{2\pi}{\lambda} \frac{1}{n_1 \cos \varphi} \left(I_x(\varepsilon''_x d) + I_z \frac{n_2^4}{\varepsilon'_z{}^2 + \varepsilon''_z{}^2} (\varepsilon''_z d) \right) \quad (2)$$

With φ the angle of the incident beam and I_x , I_y and I_z corresponding to the intensities of the electromagnetic field in the three directions of space (dimensionless). I_x , I_y and I_z are given by the following expressions:

$$I_x = \frac{4n_1^2 \cos^2 \varphi (n_1^2 \sin^2 \varphi - n_2^2)}{n_2^4 \cos^2 \varphi + n_1^4 \sin^2 \varphi - n_1^2 n_2^2} \quad (3)$$

$$I_y = \frac{4n_1^2 \cos^2 \varphi}{n_1^2 - n_2^2} \quad (4)$$

$$I_z = \frac{4n_1^4 \cos^2 \varphi \sin^2 \varphi}{n_2^4 \cos^2 \varphi + n_1^4 \sin^2 \varphi - n_1^2 n_2^2} \quad (5)$$

In most of the measurements of a layer grafted on silicon reported in this work, the angle of incidence φ was 46.5° . The following coefficients are then obtained: $I_x=1.88$, $I_y=2.07$ and $I_z=2.24$.

The $abs_{p,s}$ values are measured by adjustment of the characteristic bands (ν CO of the surface initiated, ν CO or νN_3 of the polymerized surface) by Voigt functions.

In case of a liquid measurement (calibration)

In order to calibrate the intensity of the desired band, the calibration was done using different concentrations of the initiator in CDCl_3 .

The calibration measurement makes it possible to determine the absorption of the liquid defined by the loss of reflected intensity (for a reflection) compared to the total reflection without absorption. In this case, the configuration is simpler than in **Figure 113** because there is no interfacial layer. On the other hand, this liquid is absorbent and its refractive index is complex $\tilde{n}_2 = n_2 + i k_2$. In internal reflection, at the interface between a high index medium and a low index medium, the field is evanescent: the electric field associated with the electromagnetic wave decreases exponentially in the second low index medium from the surface $z = 0$, following a profile of type $\exp(-z/d)$. If k_2 is sufficiently low ($k_2 \ll 0.1$), the penetration depth δ of the electric field is little affected by adsorption, and the value of δ is:

$$\delta_i = \frac{\lambda_i}{2\pi\sqrt{n_1^2 \sin^2(\phi) - n_2^2}} \quad (6)$$

where λ is the absorption wavelength of the considered vibrational mode. In this project, the elongation modes of the carbonyls of the ester is at 1730 cm^{-1} for initiator 1 and 1715 cm^{-1} for MEMA. The elongation mode of the azide is at 2100 cm^{-1} for AZMA.

In this case, the liquid absorption in s and p polarization are:

$$abs_s^0 = \frac{2\pi}{\lambda} \frac{1}{n_1 \cos \varphi} I_y^0 2n_2 k_2 \frac{\delta}{2} \quad (7)$$

$$abs_p^0 = \frac{2\pi}{\lambda} \frac{1}{n_1 \cos \varphi} (I_x^0 + I_z^0) 2n_2 k_2 \frac{\delta}{2} \quad (8)$$

I_y^0 , I_x^0 and I_z^0 are the normalized coefficients of the intensity of the electric field in the case of the silicon/liquid interface. They can be deduced from equations (3), (4) and (5). **Table 31** summarizes the main values of n_2 , φ , δ , C and abs^0 . The values $abs_{p,s}$ are measured by numerical integration in a specific range using Origin software.

Range for νCO of initiator 1: $1698 - 1765 \text{ cm}^{-1}$

Range for ν_{CO} of MEMA: $1683 - 1746 \text{ cm}^{-1}$

Range for ν_{N_3} for AZMA: $2051 - 2179 \text{ cm}^{-1}$

Figure 114 shows the regression lines for the calibrations thereafter mentioned:

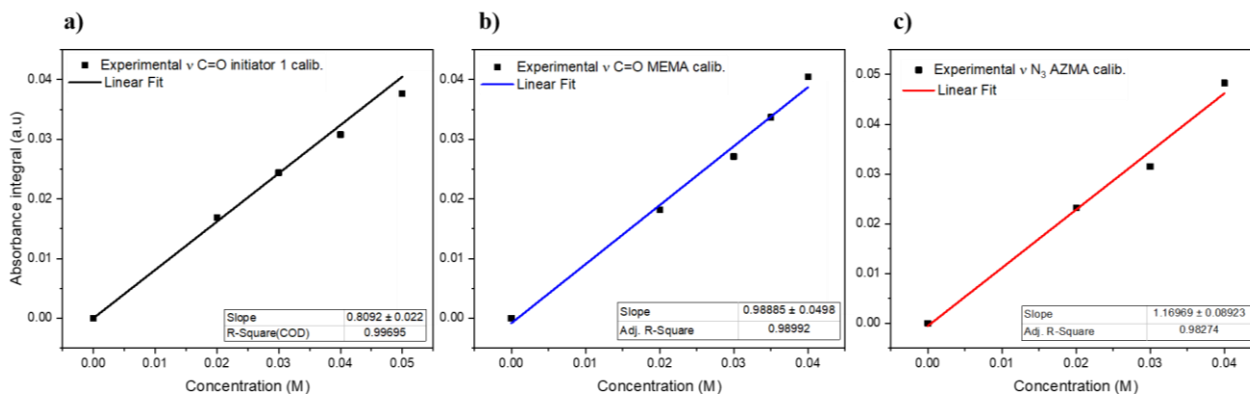


Figure 114: Calibration curves of a) initiator 1 ($\nu_{\text{C=O}}$) b) MEMA ($\nu_{\text{C=O}}$) and b) AZMA (ν_{N_3}).

Table 31: Values of n_2 , φ , λ , δ , I_y^0 , C and abs^0 for the calibration of initiator 1, MEMA and AZMA in CDCl_3

Solution	n_2	φ	λ (cm^{-1})	δ (cm)	I_y^0	C (molecules/ cm^3)	abs^0
Initiator 1 in CDCl_3 20, 30, 40, 50 mM	1.44	44	1730	4.87×10^{-5}	2.52	1.20×10^{19}	0.01618
MEMA in CDCl_3 20, 30, 35, 40 mM	1.44	48	1715	4.44×10^{-5}	2.18	1.20×10^{19}	0.01977
AZMA in CDCl_3 20, 30, 40 mM	1.44	48	2100	3.61×10^{-5}	2.17	1.20×10^{19}	0.02339

Relationship between liquid measurement and grafted surface

N is defined as the number of chemical groups per cm^2 of the band studied. To characterize the orientation of dynamic dipoles with respect to the surface, two populations can be defined: $N_{//}$ and N_{\perp} . $N_{//}$ is the equivalent number of oscillators corresponding to the projection of the dynamic dipoles in the plane of the surface, and N_{\perp} is perpendicular to the surface. If N is the total number of vibrators per unit area, as the infrared absorption is proportional to the square of the dynamic dipole, we have: $N = N_{//} + N_{\perp}$.

For an isotropic medium, we have the relation $N_{\perp} = \frac{N_{//}}{2} = \frac{N}{3}$, as there is no preferential orientation of the molecules.

Now, by making the following assumptions:

- 1) the absorption coefficient of the mode considered is proportional to the volume concentration (C) of the vibrators in the grafted layer as in the liquid. The proportionality coefficient is the same in the grafted layer and in the solution (same absorption cross section).
- 2) the actual dielectric response of the grafted layer is isotropic and identical to that of the liquid:

$$n_2 \approx \sqrt{\varepsilon'_x} \approx \sqrt{\varepsilon'_y} \approx \sqrt{\varepsilon'_z}$$

And with this we can write that:

$$\frac{N_{\perp} / \delta}{C/3} = \frac{\varepsilon''_z}{k_2 \sqrt{\varepsilon'_z}} \quad (9)$$

$$\frac{N_{//} / 2\delta}{C/3} = \frac{\varepsilon''_x}{2k_2 \sqrt{\varepsilon'_x}} = \frac{\varepsilon''_y}{2k_2 \sqrt{\varepsilon'_y}} \quad (10)$$

And in case of s polarization, the monolayer absorption is

$$abs_s = \frac{2\pi}{\lambda} \frac{1}{n_1 \cos \varphi} I_y \frac{6n_2 k_2}{C} \frac{N_{//}}{2} \quad (11)$$

The ratio of equations (11) and (7) gives:

$$\frac{abs_s}{abs_s^0} = \frac{I_y}{I_y^0} \frac{3}{C} \frac{N_{//}}{2} \quad (12)$$

In which

$$N_{//} = \frac{I_y^0}{I_y} \times \frac{C}{3} \times \frac{abs_s}{abs_s^0} \times \delta \quad (13)$$

The information on $N_{//}$ is contained in the p -polarized spectrum. By a similar calculation, it is possible to obtain N_{\perp} from equation (2), which allows us to obtain the following expression of the absorption of the layer:

$$abs_p = \frac{2\pi}{\lambda} \frac{1}{n_1 \cos \varphi} \left(I_x \frac{N_{//}}{2} + I_z \frac{1}{\varepsilon_z'^2} N_{\perp} \right) \frac{6n_2 k_2}{C} \quad (14)$$

When we consider the fact that the imaginary part ε'' of the dielectric constant of the layer is negligible compared to the real part, we can write that $\varepsilon_z'^2 + \varepsilon_z''^2 \approx \varepsilon_z'^2 \approx n_2^4$. Then, it is

possible to remove the term $\frac{N_{//}}{2}$, and then we have the following expression:

$$I_y abs_p - I_x abs_s = \frac{2\pi}{\lambda} \frac{1}{n_1 \cos \varphi} \frac{6n_2 k_2}{C} \left(I_y N_{\perp} \times I_z \frac{1}{\varepsilon_z'^2} \right) \quad (15)$$

Which can be rewritten as:

$$\frac{I_y abs_p - I_x abs_s}{abs_0} = \frac{I_y \times I_z \times \frac{1}{\varepsilon_z'^2} \times N_{\perp}}{I_y^0 \times \frac{C}{3} \times \frac{\delta}{2}} \quad (16)$$

Where

$$N_{\perp} = \frac{C}{6} \times \frac{I_y^0}{I_y} \times \frac{n_2^4}{I_z} \times \frac{[I_y \times A_p - I_x \times A_s]}{A_s^0} \times \delta \quad (17)$$

Then, for an angle φ , we can infer the total number of chemical groups on the surface per cm^2 considering $N = N_{//} + N_{\perp}$:

Appendix D

Atomic Force Microscopy

After inventing the scanning tunneling microscope, Binnig and Rohrer developed point the atomic force microscope (AFM for the English acronym of Atomic Force Microscopy) in 1986.¹⁸³ This technique makes it possible to observe the surface of several microns or several tens of square microns with a vertical resolution of a few nanometers. The concept consists of sweeping the surface using a tip with submicron resolution; therefore, enabling the study of a surface topography.

The principle of AFM is the detection of the bending of this cantilever spring as a response to external forces. In the case of interaction between the tip and the surface, it provides a force of the order 0.1 – 1 nN. In order to detect such low forces, we must obtain sensitive ways of measuring its bending. Therefore, a laser beam is focused on the back of the cantilever, and then the beam is reflected towards a position-sensitive photodetector. Therefore, depending on the cantilever deflection, the position of the reflected beam changes, and then, the photodetector converts it into an electrical signal (**Figure 115**).¹⁸⁴

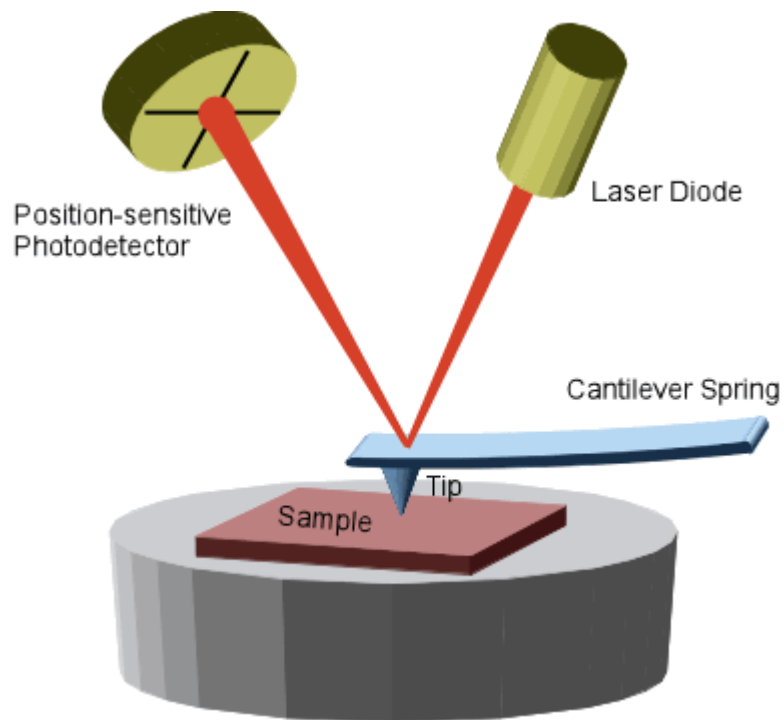


Figure 115: Schematic representation of AFM technique. Retrieved from Universität Greifswald website.¹⁸⁴

Different modes are available for the survey of the surface's topography. The simplest measurement method is the contact mode, which means that it scans the information while the end of the tip is in mechanical contact with the sample. An electronic feedback control keeps the deflection by adjusting the z position. However, this mode has a disadvantage of damaging the sensible surfaces with the pressure of the tip. Therefore, another measurement technique is used in these cases, the tapping mode. The cantilever is then stimulated to vibrations near the resonance frequency ($\sim 300\text{kHz}$), and when approaching the surface, the vibration amplitude of the cantilever decreases as the interaction force with the surface changes the resonance frequency. Therefore, the tip is not mechanically in contact with the surface.¹⁸⁴

In this thesis, we have used tapping mode techniques to observe the surfaces topographies.

Synthèse de Thèse de Doctorat en Français

Introduction et motivation

La catalyse est au cœur de la recherche fondamentale et appliquée et constitue un des aspects les plus importants de la chimie verte, avec une augmentation du rendement de la réaction et la réduction de la consommation énergétique, des déchets et des produits secondaires. Les catalyseurs homogènes dissous dans le milieu réactionnel ont généralement une activité plus élevée; cependant, leur énorme inconvénient est leur séparation compliquée du mélange réactionnel afin de pouvoir les réutiliser/recycler.¹ La catalyse homogène supportée est la solution à ce problème car le catalyseur peut être incorporé dans des supports solides insolubles, tels que des particules fines, des poudres ou des films, puis être récupéré et réutilisé très facilement. Les substrats de silicium macroporeux sont des candidats stratégiques pour le développement de catalyseurs supportés en raison de leur chimie bien connue et robuste et de leur très grande surface spécifique. Pour construire les catalyseurs, les ligands de salen ont été choisis car associés avec des métaux de transition, ils forment des complexes chiraux connus pour former un seul produit en excès énantiomérique.² L'autre avantage de ces catalyseurs est qu'ils peuvent être engagés dans des multiples réactions catalytiques différentes par simple changement de la nature du centre métallique. Le fait d'accrocher des complexes chiraux organométalliques sur substrats permettra une récupération plus aisée pour étudier leur recyclage, en parfait accord avec les concepts de la chimie éco-compatible.

Méthodologie et résultats

Le projet de recherche vise la préparation de silicium poreux fonctionnalisé par des complexes métalliques chiraux de type salen. L'utilisation du silicium est intéressante car sa

surface hydrogénée permet le greffage d'espèces organiques via des liaisons covalentes Si-C extrêmement robustes. La polymérisation radicalaire contrôlée amorcée en surface (*eg*, SI-ATRP) a été envisagée afin de former des brosses de copolymères fonctionnalisées de type méthacrylate qui vont servir de point d'ancrage aux catalyseurs.⁴⁻⁵ Nous avons ainsi une grande quantité de catalyseurs nécessaire pour la réaction catalytique. Ces copolymères sont modifiés par post-fonctionnalisation avec des complexes salen de sels métalliques identiques et/ou différents (tels que Mn et Cr) pour être testés en catalyse asymétrique (**Schéma 59**).

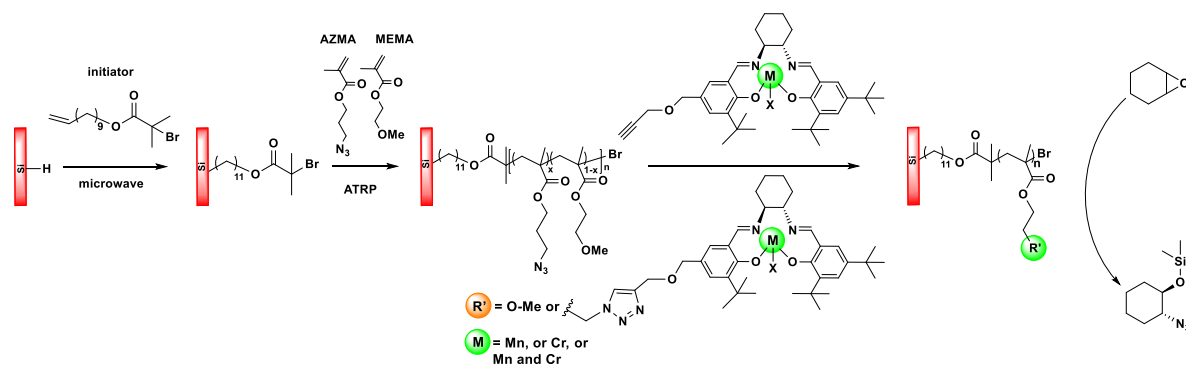


Schéma 59 : Proposition de greffage en plusieurs étapes à partir d'une surface de silicium hydrogéné.

Dans le chapitre 2, on a démontré comment l'activation micro-onde permet le greffage des amorceurs sur une surface de silicium cristallin et macroporeux. Les techniques d'analyse comme ATR-FTIR, XPS, AFM et des mesures d'angle de contact ont été utilisés pour étudier les surfaces modifiées. La surface hydrogénée greffée avec l'amorceur 1 (**Schéma 59**) a une densité de $0,7 \text{ nm}^{-2}$ déterminé par analyse ATR-FTIR. Par exemple, la **Figure 116** montre un spectre d'une surface greffée (SiBr1). La bande à 1730 cm^{-1} est caractéristique du mode de vibration d'élongation de la liaison C=O d'un ester, et les bandes à 2858 et 2931 cm^{-1} correspondent aux modes de vibration d'élongation symétriques et antisymétriques des groupes CH_2 . Une bande plus petite à 2967 cm^{-1} peut également être observée, attribuée à un mode de vibration CH_3 . Comme le spectre d'une surface hydrogénée est utilisé comme référence, nous observons un pic négatif de SiH_x , cohérent avec l'hypothèse selon laquelle l'initiateur 1 est greffé via une liaison Si-C.

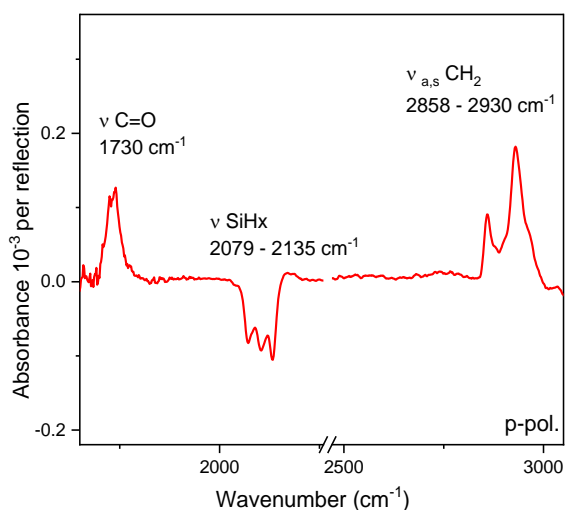


Figure 116: Spectre ATR-FTIR de la couche obtenue après greffage de l'amorceur 1 sur c-Si(111). Le spectre de référence est celui de la surface SiH_x. Conditions de gravure : HF (50%) pendant 5 s. Conditions de greffage : MW 125 °C, 50 min, 50 W, 10 vol%. Les données de ce spectre correspondent à l'entrée 2 du **Tableau 2**.

Les analyses de spectre XPS et des images AFM de SiBr1 suggère que le processus de greffage MW entraîne un attachement désordonné de molécules à la surface, ainsi que la formation d'agrégats. Néanmoins, l'activation MW reste une méthode efficace pour greffer la couche d'amorceur pour réaliser SI-ATRP, à cause de sa simplicité de mise en œuvre. De plus, le greffage de l'amorceur 1 pourrait être reproduit dans les conditions étudiées.

La polymérisation par SI-ATRP des surfaces modifiées avec les amorceurs a été réalisée ultérieurement avec un monomère méthyl (MEMA). Les brosses de polymères ont été quantifiées par spectroscopie ATR-FTIR et XPS, et leur épaisseur a été déterminée par ellipsométrie et imagerie AFM. Puis, en utilisant différents ratios de monomères, la réaction de copolymérisation de MEMA a été réalisée avec un monomère azido (AZMA) en surface. La **Figure 117** montre les spectres IR de trois surfaces fonctionnalisées par des brosses de copolymères de MEMA et d'AZMA à différents ratios, avec la présence des pics caractéristiques de l'azoture de l'AZMA (2100 cm⁻¹) et du carbonyle de l'ester des deux polymères (1730 cm⁻¹).

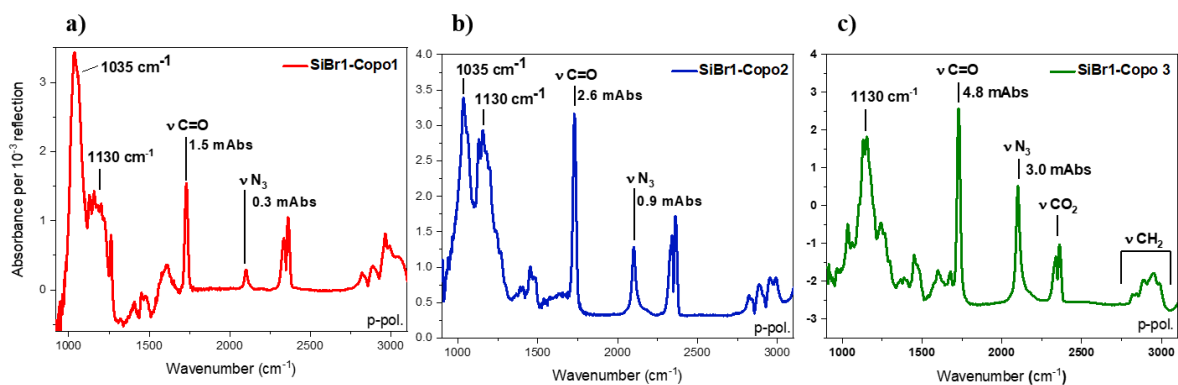


Figure 117: Spectre ATR-FTIR des copolymères sur surface en utilisant [MEMA]:[AZMA]:[CuBr]:[CuBr₂]:[bpy] = X:200-X:1:0.05:2 dans l'acétone et DPE (5%) pendant 6h à 50 °C où a) SiBr1-Copo 1 avec X = 180 b) SiBr1-Copo2 avec X = 140 et c) SiBr1-Copo 3 avec X = 100. Dans tous les cas, le spectre de la surface greffée avant polymérisation est utilisé comme référence.

Ensuite, la chimie click avec des molécules modèles a été réalisée sur les surfaces copolymère et a démontré la très grande efficacité de leur accrochage par ATR-FTIR et XPS. Les ligands salen ont ensuite été complexés avec des métaux chrome et cobalt, et ils ont été caractérisés par UV-Vis, ATR-FTIR et spectrométrie de masse. La chimie click sur des copolymères de MEMA/AZMA en solution et en surface a été réalisée afin de développer des catalyseurs supportés. Deux types de catalyseurs supportés ont été développés. Le premier concerne de catalyseur ancré sur les copolymères libres (**Schéma 60**).

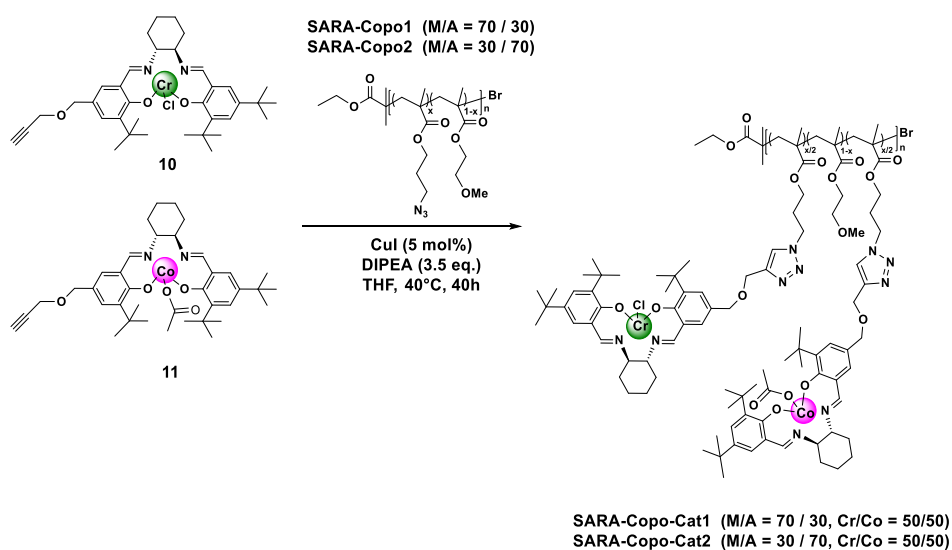


Schéma 60: Conditions de réaction pour la réaction click entre les copolymères et les catalyseurs synthétisés. M/A = MEMA/AZMA.

Le second concerne des catalyseurs ancrés sur les brosses des copolymères sur la surface macroporeuse du silicium (**Schéma 61**).

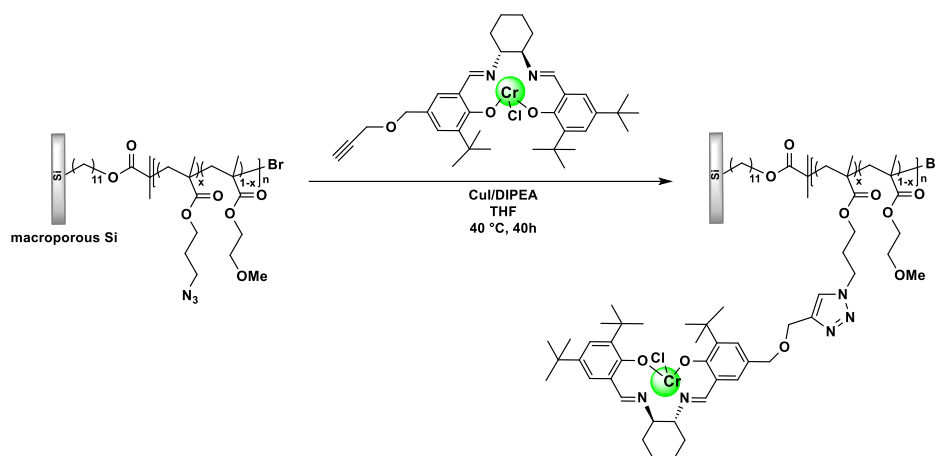


Schéma 61: Conditions de greffage du complexe Cr-salen sur des copolymères de MEMA/AZMA à la surface du silicium macroporeux.

L'objectif final de ce projet de thèse est de développer une catalyse supportée sur silicium pour une catalyse multi-étapes. Il s'agit d'un objectif très ambitieux car aucun catalyseur utilisant le silicium pour la catalyse asymétrique n'est décrit dans la littérature. Dans ce manuscrit, la réactivité et l'énantiosélectivité des catalyseurs développés ont été étudiés. En ce qui concerne les catalyseurs utilisant des copolymères libres comme supports (**Schéma 60**), ils ont montré une preuve de concept dans laquelle le même catalyseur supporté peut favoriser deux réactions, qui étaient au départ idéalement orthogonal, mais se sont révélées favorisées par les deux sites catalytiques. Cependant, il s'agit d'un premier pas vers la multi-catalyse séquentielle utilisant les copolymères de MEMA/AZMA, et les résultats montrent que les copolymères sont des supports adaptés à ces applications. En résumé, les catalyseurs développés ont permis l'ouverture de l'oxyde de cyclohexène catalysé par les sites de chrome avec des conversions supérieures à 99 % lors de la première utilisation, et supérieures à 88 % lors de sa réutilisation. Leur excès énantiomérique est satisfaisant, avec un excès de 60 %. Pour la résolution cinétique dynamique de l'épibromohydrine, les catalyseurs ont catalysé la réaction avec des conversions supérieures à 40 %, ce qui s'explique par une dilution plus importante des réactifs lors de l'utilisation des catalyseurs supportés. Cependant, l'excès énantiomérique reste élevé, avec un taux de 80 %.

Bien que l'excès énantiomérique soit inférieur à celui envisagé, cette étude valide la stratégie et donne des indications pour le développement ultérieur des catalyseurs supportés pour une catalyse orthogonale et/ou en tandem.

Concernant les catalyseurs supportés sur silicium (**Schéma 61**), ils ne se sont pas révélés efficaces pour les réactions testées et dans les conditions analysées. Cela pourrait signifier que soit les sites catalytiques en surface ne sont pas disponibles pour la réaction, soit que les conditions testées ne sont pas encore optimisées compte tenu de ce support. Dans le premier cas, les sites catalytiques pourraient être gênés ou encombrés par d'autres sites catalytiques à l'intérieur des pores, rendant difficile la réaction dans des espaces confinés.

En perspective, une façon d'améliorer les essais de catalyse utilisant des catalyseurs supportés sur silicium est d'abord d'augmenter la surface du support. Cela peut être fait simplement en utilisant des échantillons plus grands du silicium macroporeux étudié, ou en augmentant l'épaisseur des pores des échantillons. De plus, un temps de polymérisation plus long pour la copolymérisation de MEMA/AZMA en utilisant ce support pourrait potentiellement augmenter le nombre de sites azotures, pour finalement avoir plus de sites catalytiques disponibles pour la réaction. Néanmoins, ce développement de catalyseurs supportés utilisant des copolymères sur silicium constitue le tout premier pas vers la catalyse salen asymétrique utilisant le silicium comme support.

Conclusion

Cette thèse a portée sur le développement de catalyseurs asymétriques à base de complexes de salen supportés sur des surfaces de silicium, en utilisant des techniques de polymérisation radicalaire contrôlée. Le silicium a été choisi pour sa chimie de surface bien établie et sa capacité à former des liaisons robustes Si-C, améliorant ainsi la stabilité des catalyseurs et empêchant la contamination métallique dans le mélange réactionnel. Le travail a d'abord exploré l'hydrosilylation d'initiateurs pour la polymérisation radicalaire par transfert d'atomes (ATRP) sur des surfaces de silicium, suivie de la polymérisation de méthacrylates par ATRP amorcée en surface (SI-ATRP), puis du greffage final des catalyseurs salen via la chimie click.

Dans le chapitre 2, le greffage d'amorceurs sur des surfaces de silicium cristallin et macroporeux via l'activation par micro-ondes a été étudié et caractérisé par différentes techniques telles que l'ATR-FTIR, XPS et l'AFM. Les résultats ont montré une bonne reproductibilité du greffage de l'amorceur 1 sur une surface de silicium hydrogénée, malgré

une absence de preuve claire de liaison Si–C, suggérant aussi un greffage via Si–O–C. Le chapitre 3 s'est concentré sur le développement de copolymères de type méthacrylate en utilisant des surfaces de silicium, avec un contrôle précis de la polymérisation de surface. Le SI-ATRP a permis la création de brosses polymères d'épaisseurs variées sur silicium cristallin et macroporeux, avec des résultats démontrant que le silicium macroporeux offre une surface nettement plus grande pour le greffage.

Enfin, les chapitres 4 et 5 ont exploré la chimie de click pour fixer des catalyseurs de salen sur des copolymères en solution et sur des surfaces, et leur utilisation en catalyse. Deux catégories de catalyseurs salen ont été développées : des catalyseurs attachés à des copolymères libres et des catalyseurs greffés sur des brosses de copolymères sur silicium macroporeux. Ces catalyseurs ont montré des capacités de catalyse polyvalente, bien que certains résultats, comme l'excès énantiomérique, aient été en dessous des attentes. Cela ouvre la voie aux futures améliorations des catalyseurs supportés sur silicium pour des applications de catalyse séquentielle.

References

1. Fulgheri, T.; Della Penna, F.; Baschieri, A.; Carlone, A., Advancements in the recycling of organocatalysts: From classical to alternative approaches. *Current Opinion in Green and Sustainable Chemistry* **2020**, *25*, 100387.
2. Cozzi, P. G., Metal–Salen Schiff base complexes in catalysis: practical aspects. *Chemical Society Review* **2004**, *33*, 410-421.
3. Zulauf, A.; Mellah, M.; Hong, X.; Schulz, E., Recoverable chiral salen complexes for asymmetric catalysis: recent progress. *Dalton transactions* **2010**, *39* (30), 6911-35.
4. Zidelmal, N.; Aubry-Barroca, N.; Lepoittevin, B.; Mellah, M.; Costa, L.; Ozanam, F.; Gouget-Laemmel, A.-C.; Schulz, E.; Roger, P., Synthesis, characterization and catalytic properties of salen-containing polymers obtained by atom transfer radical polymerization. *Polymer* **2018**, *135*, 261-270.
5. Bech, L.; Elzein, T.; Meylheuc, T.; Ponche, A.; Brogly, M.; Lepoittevin, B.; Roger, P., Atom transfer radical polymerization of styrene from different poly(ethylene terephthalate) surfaces: Films, fibers and fabrics. *European Polymer Journal* **2009**, *45* (1), 246-255.
6. Tang, W.; Matyjaszewski, K., Effect of Ligand Structure on Activation Rate Constants in ATRP. *Macromolecules* **2006**, *39*, 4953-4959.
7. Gouget-Laemmel, A. C.; Yang, J.; Lodhi, M. A.; Siriwardena, A.; Aureau, D.; Boukherroub, R.; Chazalviel, J. N.; Ozanam, F.; Szunerits, S., Functionalization of Azide-Terminated Silicon Surfaces with Glycans Using Click Chemistry: XPS and FTIR Study. *The Journal of Physical Chemistry C* **2012**, *117* (1), 368-375.
8. (a) Gouget-Laemmel, A.-C.; Zidelmal, N.; Soares, R. S. B.; Barroca-Aubry, N.; Dragoe, D.; Costa, L.; Lepoittevin, B.; Salmi-Mani, H.; Mellah, M.; Henry-de-Villeneuve, C.; Ozanam, F.; Schulz, E.; Roger, P., Direct Quantitative Characterization of Polymer Brushes Obtained by Surface-Initiated ATRP on Silicon. *ACS Applied Polymer Materials* **2022**, *5* (1), 517-528; (b) Bakangura, E.; Roger, P.; Soares, R. S. B.; Mellah, M.; Barroca-Aubry, N.; Gouget-Laemmel, A. C.; Ozanam, F.; Costa, L.; Baltaze, J. P.; Schulz, E., Post-Modification of Copolymers Obtained by ATRP for an Application in Heterogeneous Asymmetric Salen Catalysis. *Molecules* **2022**, *27* (14).
9. Buriak, J. M., Organometallic Chemistry on Silicon and Germanium Surfaces. *Chemical Reviews* **2002**, *102* (5), 1271-1308.
10. Soref, R. A., Silicon-based optoelectronics. *Proceedings of the IEEE* **1993**, *81* (12), 1687-1706.

11. Neergaard Waltenburg, H.; Yates, J., Surface Chemistry of Silicon. *Chemical Reviews* **1995**, *95* (5), 1589-1673.
12. Aureau, D. Interface silicium/couche organique: Maîtrise des propriétés et fonctionnalisation. Ph.D. Thesis, Ecole Polytechnique, France, 2008.
13. Douarche, C. Étude de l'adsorption de l'ADN simple brin et double brin aux interfaces. Ph. D. Thesis, Université de Lille 1 - USTL, France, 2007.
14. Peng, W.; Rupich, S. M.; Shafiq, N.; Gartstein, Y. N.; Malko, A. V.; Chabal, Y. J., Silicon Surface Modification and Characterization for Emergent Photovoltaic Applications Based on Energy Transfer. *Chemical Reviews* **2015**, *115* (23), 12764-96.
15. G. W. Trucks, K. R., G. S. Higashi, and Y. J. Chabal, Mechanism of HF Etching of Silicon Surfaces: A Theoretical Understanding of Hydrogen Passivation. *Physical Review Letters* **1990**, *65* (4), 504-507.
16. Ciampi, S.; Harper, J. B.; Gooding, J. J., Wet chemical routes to the assembly of organic monolayers on silicon surfaces via the formation of Si-C bonds: surface preparation, passivation and functionalization. *Chemical Society Reviews* **2010**, *39* (6), 2158-83.
17. Matthew R. Linford, C. E. D. C., Alkyl Monolayers Covalently Bonded to Silicon Surfaces. *Journal of the American Chemical Society*. **1993**, *115*, 12631-12632.
18. Gooding, J. J.; Ciampi, S., The molecular level modification of surfaces: from self-assembled monolayers to complex molecular assemblies. *Chemical Society Reviews* **2011**, *40* (5), 2704-18.
19. Sieval, A. B.; Demirel, A. L.; Nissink, J. W. M.; Linford, M. R.; van der Maas, J. H.; de Jeu, W. H.; Zuilhof, H.; Sudhölter, E. J. R., Highly Stable Si-C Linked Functionalized Monolayers on the Silicon (100) Surface. *Langmuir* **1998**, *14* (7), 1759-1768.
20. (a) Terry, J.; Linford, M. R.; Wigren, C.; Cao, R.; Pianetta, P.; Chidsey, C. E. D., Alkyl-terminated Si(111) surfaces: A high-resolution, core level photoelectron spectroscopy study. *Journal of Applied Physics* **1999**, *85* (1), 213-221; (b) Terry, J.; Linford, M. R.; Wigren, C.; Cao, R.; Pianetta, P.; Chidsey, C. E. D., Determination of the bonding of alkyl monolayers to the Si(111) surface using chemical-shift, scanned-energy photoelectron diffraction. *Applied Physics Letters* **1997**, *71* (8), 1056-1058.
21. Coletti, C.; Marrone, A.; Giorgi, G.; Sgamellotti, A.; Cerofolini, G.; Re, N., Nonradical Mechanisms for the Uncatalyzed Thermal Functionalization of Silicon Surfaces by Alkenes and Alkynes: A Density Functional Study. *Langmuir* **2006**, *22* (24), 9949-9956.
22. de Almeida, L. D.; Wang, H.; Junge, K.; Cui, X.; Beller, M. A.-O., Recent Advances in Catalytic Hydrosilylations: Developments beyond Traditional Platinum Catalysts. *Angewandte Chemie* **2021**, *60* (2), 550-565.
23. Ozanam, F.; Vieillard, C.; Warntjes, M.; Dubois, T.; Pauly, M.; Chazalviel, J.-N., Greffage de molécules à la surface du silicium par voie électrochimique. *The Canadian Journal of Chemical Engineering* **1998**, *76* (6), 1020-1026.
24. (a) Bateman, J. E.; Eagling, R. D.; Horrocks, B. R.; Houlton, A., A Deuterium Labeling, FTIR, and Ab Initio Investigation of the Solution-Phase Thermal Reactions of Alcohols and Alkenes with Hydrogen-Terminated Silicon Surfaces. *The Journal of Physical Chemistry B* **2000**, *104* (23), 5557-5565; (b) Hacker, C. A.; Anderson, K. A.; Richter, L. J.; Richter, C. A., Comparison of Si-O-C Interfacial Bonding of Alcohols and Aldehydes on Si(111) Formed from Dilute Solution with Ultraviolet Irradiation. *Langmuir* **2005**, *21* (3), 882-889; (c) Boukherroub, R.; Morin, S.; Sharpe, P.; Wayner, D. D. M.; Allongue, P., Insights into the Formation Mechanisms of Si-OR Monolayers from the Thermal Reactions of Alcohols and Aldehydes with Si(111)-H1. *Langmuir* **2000**, *16* (19), 7429-7434.
25. (a) Wei, S.; Wang, J.; Guo, D.-J.; Chen, Y.-Q.; Xiao, S.-J., Grafting Organic and Biomolecules on H-Terminated Porous Silicon from a Diazirine. *Chemistry Letters* **2006**, *35*

- (10), 1172-1173; (b) Boukherroub, R.; Petit, A.; Loupy, A.; Chazalviel, J.-N.; Ozanam, F., Microwave-Assisted Chemical Functionalization of Hydrogen-Terminated Porous Silicon Surfaces. *The Journal of Physical Chemistry B* **2003**, *107* (48), 13459 - 13462; (c) Cisneros-Covarrubias, C. A.; Palestino, G.; Gómez-Durán, C. F. A.; Rosales-Mendoza, S.; Betancourt-Mendiola, M. d. L., Optimized microwave-assisted functionalization and quantification of superficial amino groups on porous silicon nanostructured microparticles. *Analytical Methods* **2021**, *13* (4), 516-525; (d) Wang, J.; Guo, D.-J.; Xia, B.; Chao, J.; Xiao, S.-J., Preparation of organic monolayers with azide on porous silicon via Si–N bonds. *Colloids and Surfaces A: Physicochemical and Engineering Aspects* **2007**, *305* (1-3), 66-75.
26. Pandit, S.; Preston, T. J.; King, S. J.; Vallance, C.; Orr-Ewing, A. J., Evidence for concerted ring opening and C-Br bond breaking in UV-excited bromocyclopropane. *The Journal of Chemical Physics* **2016**, *144* (24), 244312.
27. Petit, A.; Delmotte, M.; Loupy, A.; Chazalviel, J.-N.; Ozanam, F.; Boukherroub, R., Microwave Effects on Chemical Functionalization of Hydrogen-Terminated Porous Silicon Nanostructures. *The Journal of Physical Chemistry C* **2008**, *112* (42), 16622-16628.
28. Lee, A. W.; Gates, B. D., Rapid Covalent Modification of Silicon Oxide Surfaces through Microwave-Assisted Reactions with Alcohols. *Langmuir* **2016**, *32* (29), 7284-93.
29. García, N.; Benito, E.; Guzmán, J.; de Francisco, R.; Tiemblo, P., Microwave versus Conventional Heating in the Grafting of Alkyltrimethoxysilanes onto Silica Particles. *Langmuir* **2010**, *26* (8), 5499-5506.
30. Lu, X.; Yan, Q.; Ma, Y.; Guo, X.; Xiao, S. J., Growing Embossed Nanostructures of Polymer Brushes on Wet-Etched Silicon Templated via Block Copolymers. *Scientific Reports* **2016**, *6*, 20291.
31. Pujari, S. P.; Scheres, L.; Marcelis, A. T.; Zuilhof, H., Covalent surface modification of oxide surfaces. *Angewandte Chemie* **2014**, *53* (25), 6322-56.
32. Ulman, A., Formation and Structure of Self-Assembled Monolayers. *Chemical Reviews* **1996**, *96* (4), 1533-1554.
33. Rosso, M.; Giesbers, M.; Arafat, A.; Schroën, K.; Zuilhof, H., Covalently Attached Organic Monolayers on SiC and SixN4 Surfaces: Formation Using UV Light at Room Temperature. *Langmuir* **2009**, *25* (4), 2172-2180.
34. Roccaforte, F.; La Via, F.; Raineri, V.; Musumeci, P.; Calcagno, L.; Condorelli, G. G., Highly reproducible ideal SiC Schottky rectifiers: effects of surface preparation and thermal annealing on the Ni/6H-SiC barrier height. *Applied Physics A* **2003**, *77* (6), 827-833.
35. ter Maat, J.; Regeling, R.; Yang, M.; Mullings, M. N.; Bent, S. F.; Zuilhof, H., Photochemical Covalent Attachment of Alkene-Derived Monolayers onto Hydroxyl-Terminated Silica. *Langmuir* **2009**, *25* (19), 11592-11597.
36. Li, B.; Franking, R.; Landis, E. C.; Kim, H.; Hamers, R. J., Photochemical Grafting and Patterning of Biomolecular Layers onto TiO₂ Thin Films. *ACS Applied Materials & Interfaces* **2009**, *1* (5), 1013-1022.
37. Franking, R. A.; Landis, E. C.; Hamers, R. J., Highly Stable Molecular Layers on Nanocrystalline Anatase TiO₂ through Photochemical Grafting. *Langmuir* **2009**, *25* (18), 10676-10684.
38. Mischki, T. K.; Donkers, R. L.; Eves, B. J.; Lopinski, G. P.; Wayner, D. D. M., Reaction of Alkenes with Hydrogen-Terminated and Photooxidized Silicon Surfaces. A Comparison of Thermal and Photochemical Processes. *Langmuir* **2006**, *22* (20), 8359-8365.
39. Rosso, M.; Arafat, A.; Schroën, K.; Giesbers, M.; Roper, C. S.; Maboudian, R.; Zuilhof, H., Covalent Attachment of Organic Monolayers to Silicon Carbide Surfaces. *Langmuir* **2008**, *24* (8), 4007-4012.

40. Wallart, X.; Henry de Villeneuve, C.; Allongue, P., Truly Quantitative XPS Characterization of Organic Monolayers on Silicon: Study of Alkyl and Alkoxy Monolayers on H-Si(111). *Journal of the American Chemical Society* **2005**, *127* (21), 7871-7878.
41. Faucheux, A., Gouget-Laemmel, A. C., Henry de Villeneuve, C., Boukherroub, R., Ozanam, F., Allongue, P., Chazalviel, J-N. Well-Defined Carboxyl-Terminated Alkyl Monolayers Grafted onto H-Si(111): Packing Density from a Combined AFM and Quantitative IR Study. *Langmuir* **2006**, *22* (1), 153-162.
42. Faucheux, A.; Gouget-Laemmel, A. C.; Allongue, P.; Henry de Villeneuve, C.; Ozanam, F.; Chazalviel, J. N., Mechanisms of Thermal Decomposition of Organic Monolayers Grafted on (111) Silicon. *Langmuir* **2007**, *23* (3), 1326-1332.
43. (a) Moraillon, A.; Gouget-Laemmel, A. C.; Ozanam, F.; Chazalviel, J. N., Amidation of Monolayers on Silicon in Physiological Buffers: A Quantitative IR Study. *The Journal of Physical Chemistry C* **2008**, *112* (18), 7158-7167; (b) Sam, S.; Touahir, L.; Salvador Andresa, J.; Allongue, P.; Chazalviel, J. N.; Gouget-Laemmel, A. C.; Henry de Villeneuve, C.; Moraillon, A.; Ozanam, F.; Gabouze, N.; Djebbar, S., Semiquantitative Study of the EDC/NHS Activation of Acid Terminal Groups at Modified Porous Silicon Surfaces. *Langmuir* **2010**, *26* (2), 809-814.
44. Lorandi, F.; Fantin, M.; Matyjaszewski, K., Atom Transfer Radical Polymerization: A Mechanistic Perspective. *Journal of the American Chemical Society* **2022**, *144* (34), 15413-15430.
45. Wang, J.-S.; Matyjaszewski, K., Controlled "Living" Radical Polymerization. Atom Transfer Radical Polymerization in the Presence of Transition-Metal Complexes. *Journal of the American Chemical Society* **1995**, *117*, 5614-5615.
46. Lin, C. Y.; Coote, M. L.; Gennaro, A.; Matyjaszewski, K., Ab Initio Evaluation of the Thermodynamic and Electrochemical Properties of Alkyl Halides and Radicals and Their Mechanistic Implications for Atom Transfer Radical Polymerization. *Journal American Chemical Society* **2008**, *130*, 12762-12774.
47. Patten, T. E.; Matyjaszewski, K., Atom Transfer Radical Polymerization and the Synthesis of Polymeric Materials. *Advanced Materials* **1998**, *10* (12), 901-915.
48. Xia, K. M. a. J., Atom Transfer Radical Polymerization. *Chemicam Review* **2001**, *101*, 2921-2990.
49. Matyjaszewski, J. H. a. K., Atom Transfer Radical Polymerization of Dimethyl(1-ethoxycarbonyl)vinyl Phosphate and Corresponding Block Copolymers. *Macromolecules* **2005**, *38*, 3577-3583.
50. Rinkenauer, A. C.; Schubert, S.; Traeger, A.; Schubert, U. S., The influence of polymer architecture on in vitro pDNA transfection. *Journal of Materials Chemistry B* **2015**, *3* (38), 7477-7493.
51. Xia, J.; Zhang, X.; Matyjaszewski, K., The Effect of Ligands on Copper-Mediated Atom Transfer Radical Polymerization. In *Transition Metal Catalysis in Macromolecular Design*, American Chemical Society: 2000; Vol. 760, pp 207-223.
52. Rorabacher, D. B., Electron transfer by copper centers. *Chem. Rev.* **2004**, *104*, 651-697.
53. Tang, W.; Kwak, Y.; Braunecker, W.; Tsarevsky, N. V.; Coote, M. L.; Matyjaszewski, K., Understanding Atom Transfer Radical Polymerization: Effect of Ligand and Initiator Structures on the Equilibrium Constants. *Journal of the American Chemical Society* **2008**, *130*, 10702-10713.
54. (a) Nanda, A. K.; Matyjaszewski, K., Effect of [PMDETA]/[Cu(I)] Ratio, Monomer, Solvent, Counterion, Ligand, and Alkyl Bromide on the Activation Rate Constants in Atom Transfer Radical Polymerization. *Macromolecules* **2003**, *36* (5), 1487-1493; (b) Kwak, Y.;

- Matyjaszewski, K., Effect of Initiator and Ligand Structures on ATRP of Styrene and Methyl Methacrylate Initiated by Alkyl Dithiocarbamate. *Macromolecules* **2008**, *41* (18), 6627-6635.
55. Tang, W.; Matyjaszewski, K., Effects of Initiator Structure on Activation Rate Constants in ATRP. *Macromolecules* **2007**, *40* (6), 1858-1863.
56. Braunecker, W. A.; Tsarevsky, N. V.; Gennaro, A.; Matyjaszewski, K., Thermodynamic Components of the Atom Transfer Radical Polymerization Equilibrium: Quantifying Solvent Effects. *Macromolecules* **2009**, *42* (17), 6348-6360.
57. Matyjaszewski, K.; Coca, S.; Gaynor, S. G.; Wei, M.; Woodworth, B. E., Zerovalent Metals in Controlled/"Living" Radical Polymerization. *Macromolecules* **1997**, *30* (23), 7348-7350.
58. Xia, J.; Gaynor, S. G.; Matyjaszewski, K., Controlled/"Living" Radical Polymerization. Atom Transfer Radical Polymerization of Acrylates at Ambient Temperature. *Macromolecules* **1998**, *31*, 5958 - 5959
59. Matyjaszewski, K.; Nakagawa, Y.; Jasieczek, C. B., Polymerization of n-Butyl Acrylate by Atom Transfer Radical Polymerization. Remarkable Effect of Ethylene Carbonate and Other Solvents. *Macromolecules* **1998**, *31* (5), 1535-1541.
60. Percec, V.; Guliashvili, T.; Ladislaw, J. S.; Wistrand, A.; Stjerndahl, A.; Sienkowska, M. J.; Monteiro, M. J.; Sahoo, S., Ultrafast Synthesis of Ultrahigh Molar Mass Polymers by Metal-Catalyzed Living Radical Polymerization of Acrylates, Methacrylates, and Vinyl Chloride Mediated by SET at 25 °C. *Journal of the American Chemical Society* **2006**, *128* (43), 14156-14165.
61. Konkolewicz, D.; Wang, Y.; Krysz, P.; Zhong, M.; Isse, A. A.; Gennaro, A.; Matyjaszewski, K., SARA ATRP or SET-LRP. End of controversy? *Polymer Chemistry* **2014**, *5* (15), 4396-4417.
62. University, C. M. SARA ATRP or SET LRP? - *Matyjaszewski Polymer Group - Carnegie Mellon University*. www.cmu.edu. <https://www.cmu.edu/maty/atrp-how/procedures-for-initiation-of-ATRP/SARA-ATRP-or-SET-LRP.html>.
63. (a) Konkolewicz, D.; Wang, Y.; Zhong, M.; Krysz, P.; Isse, A. A.; Gennaro, A.; Matyjaszewski, K., Reversible-Deactivation Radical Polymerization in the Presence of Metallic Copper. A Critical Assessment of the SARA ATRP and SET-LRP Mechanisms. *Macromolecules* **2013**, *46* (22), 8749-8772; (b) Konkolewicz, D.; Krysz, P.; Matyjaszewski, K., Explaining Unexpected Data via Competitive Equilibria and Processes in Radical Reactions with Reversible Deactivation. *Accounts of Chemical Research* **2014**, *47* (10), 3028-3036; (c) Wang, Y.; Zhong, M.; Zhu, W.; Peng, C.-H.; Zhang, Y.; Konkolewicz, D.; Bortolamei, N.; Isse, A. A.; Gennaro, A.; Matyjaszewski, K., Reversible-Deactivation Radical Polymerization in the Presence of Metallic Copper. Comproportionation–Disproportionation Equilibria and Kinetics. *Macromolecules* **2013**, *46* (10), 3793-3802.
64. Boyer, C.; Corrigan, N. A.; Jung, K.; Nguyen, D.; Nguyen, T.-K.; Adnan, N. N. M.; Oliver, S.; Shanmugam, S.; Yeow, J., Copper-Mediated Living Radical Polymerization (Atom Transfer Radical Polymerization and Copper(0) Mediated Polymerization): From Fundamentals to Bioapplications. *Chemical Reviews* **2016**, *116* (4), 1803-1949.
65. Rosen, B. M.; Percec, V., Single-electron transfer and single-electron transfer degenerative chain transfer living radical polymerization. *Chem. Rev.* **2009**, *109*, 5069-5119.
66. Jones, G. R.; Whitfield, R.; Anastasaki, A.; Risangud, N.; Simula, A.; Keddie, D. J.; Haddleton, D. M., Cu(0)-RDRP of methacrylates in DMSO: importance of the initiator. *Polymer Chemistry* **2018**, *9* (18), 2382-2388.
67. Flejszar, M.; Chmielarz, P. A.-O., Surface-Initiated Atom Transfer Radical Polymerization for the Preparation of Well-Defined Organic-Inorganic Hybrid Nanomaterials. *Materials* **2019**, *12*, 3030.

68. Li, D.; Zheng, Q.; Wang, Y.; Chen, H., Combining surface topography with polymer chemistry: exploring new interfacial biological phenomena. *Polymer Chemistry* **2014**, *5* (1), 14-24.
69. de Gennes, P. G., Conformations of Polymers Attached to an Interface. *Macromolecules* **1980**, *13* (5), 1069-1075.
70. Tsujii, Y.; Ohno, K.; Yamamoto, S.; Goto, A.; Fukuda, T., Structure and Properties of High-Density Polymer Brushes Prepared by Surface-Initiated Living Radical Polymerization. In *Advanced Polymer Science*, **2006**, *197*, 1-45.
71. Zoppe, J. O.; Ataman, N. C.; Mocny, P.; Wang, J.; Moraes, J.; Klok, H.-A., Surface-Initiated Controlled Radical Polymerization: State-of-the-Art, Opportunities, and Challenges in Surface and Interface Engineering with Polymer Brushes. *Chemical Reviews* **2017**, *117* (3), 1105-1318.
72. Maaz, M.; Elzein, T.; Bejjani, A.; Barroca-Aubry, N.; Lepoittevin, B.; Dragoe, D.; Mazerat, S.; Nsouli, B.; Roger, P., Surface initiated supplemental activator and reducing agent atom transfer radical polymerization (SI-SARA-ATRP) of 4-vinylpyridine on poly(ethylene terephthalate). *Journal of Colloid and Interface Science* **2017**, *500*, 69-78.
73. Lindqvist, J.; Nyström, D.; Östmark, E.; Antoni, P.; Carlmark, A.; Johansson, M.; Hult, A.; Malmström, E., Intelligent Dual-Responsive Cellulose Surfaces via Surface-Initiated ATRP. *Biomacromolecules* **2008**, *9* (8), 2139-2145.
74. Kalelkar, P. P.; Geng, Z.; Cox, B.; Finn, M. G.; Collard, D. M., Surface-initiated atom-transfer radical polymerization (SI-ATRP) of bactericidal polymer brushes on poly(lactic acid) surfaces. *Colloids and Surfaces B: Biointerfaces* **2022**, *211*, 112242.
75. (a) Chen, J.-K.; Hsieh, C.-Y.; Huang, C.-F.; Li, P. M.; Kuo, S.-W.; Chang, F.-C., Using Solvent Immersion to Fabricate Variably Patterned Poly(methyl methacrylate) Brushes on Silicon Surfaces. *Macromolecules* **2008**, *41* (22), 8729-8736; (b) Yu, W. H.; Kang, E. T.; Neoh, K. G., Controlled Grafting of Well-Defined Epoxide Polymers on Hydrogen-Terminated Silicon Substrates by Surface-Initiated ATRP at Ambient Temperature. *Langmuir* **2004**, *20* (19), 8294-8300; (c) Xu, F. J.; Yuan, Z. L.; Kang, E. T.; Neoh, K. G., Branched Fluoropolymer-Si Hybrids via Surface-Initiated ATRP of Pentafluorostyrene on Hydrogen-Terminated Si(100) Surfaces. *Langmuir* **2004**, *20* (19), 8200-8208; (d) Vasani, R. B.; McInnes, S. J. P.; Cole, M. A.; Jani, A. M. M.; Ellis, A. V.; Voelcker, N. H., Stimulus-Responsiveness and Drug Release from Porous Silicon Films ATRP-Grafted with Poly(N-isopropylacrylamide). *Langmuir* **2011**, *27* (12), 7843-7853.
76. Huang, C.-F., Surface-initiated atom transfer radical polymerization for applications in sensors, non-biofouling surfaces and adsorbents. *Polymer Journal* **2016**, *48* (4), 341-350.
77. Fernandes, A. E.; Dirani, A.; d'Haese, C.; Deumer, G.; Guo, W.; Hensenne, P.; Nahra, F.; Laloyaux, X.; Haufroid, V.; Nysten, B.; Riant, O.; Jonas, A. M., Thicker is Better? Synthesis and Evaluation of Well-Defined Polymer Brushes with Controllable Catalytic Loadings. *Chemistry – A European Journal* **2012**, *18* (50), 16226-16233.
78. Cunningham, W. A., Sulfur. III. *Journal of Chemical Education* **1935**, *12* (3), 120.
79. Worley, S.; Sun, G., Biocidal polymers. *Trends in Polymer Science* **1996**, *11* (4), 364-370.
80. Singh, C. N. P., *Functionalized Polymers: Synthesis, Characterization and Applications*. CRC Press: 2023; p 298.
81. Günay, K. A.; Theato, P.; Klok, H. A., Standing on the shoulders of Hermann Staudinger: Post-polymerization modification from past to present. *Journal of Polymer Science Part A: Polymer Chemistry* **2012**, *51* (1), 1-28.
82. Hucul, D. A.; Hahn, S. F., Catalytic Hydrogenation of Polystyrene. *Advanced Materials* **2000**, *12* (23), 1855-1858.

83. Zuchowska, D., Polybutadiene modified by epoxidation. 1. Effect of polybutadiene microstructure on the reactivity of double bonds. *Polymer* **1980**, *21* (5), 514-520.
84. Aziz, T.; Farid, A.; Haq, F.; Kiran, M.; Ullah, A.; Zhang, K.; Li, C.; Ghazanfar, S.; Sun, H.; Ullah, R.; Ali, A.; Muzammal, M.; Shah, M.; Akhtar, N.; Selim, S.; Hagagy, N.; Samy, M.; Al Jaouni, S. K., A Review on the Modification of Cellulose and Its Applications. *Polymers* **2022**, *14* (15), 3206.
85. Aruldass, S.; Mathivanan, V.; Mohamed, A. R.; Tye, C. T., Factors affecting hydrolysis of polyvinyl acetate to polyvinyl alcohol. *Journal of Environmental Chemical Engineering* **2019**, *7* (5), 103238.
86. Li, Y.; Benicewicz, B. C., Functionalization of Silica Nanoparticles via the Combination of Surface-Initiated RAFT Polymerization and Click Reactions. *Macromolecules* **2008**, *41* (21), 7986-7992.
87. Parrish, B.; Breitenkamp, R. B.; Emrick, T., PEG- and Peptide-Grafted Aliphatic Polyesters by Click Chemistry. *Journal of the American Chemical Society* **2005**, *127* (20), 7404-7410.
88. Brent S. Sumerlin, N. V. T., Guillaume Louche, Robert Y. Lee, and Krzysztof Matyjaszewski, Highly Efficient "Click" Functionalization of Poly(3-azidopropyl methacrylate) Prepared by ATRP. *Macromolecules* **2005**, *38*, 7540-7545.
89. Agard, N. J.; Baskin, J. M.; Prescher, J. A.; Lo, A.; Bertozzi, C. R., A Comparative Study of Bioorthogonal Reactions with Azides. *ACS Chemical Biology* **2006**, *1* (10), 644-648.
90. (a) Bein, T., Asymmetric catalysis on solids. *Current Opinion in Solid State and Materials Science* **1999**, *4* (1), 85-96; (b) Heitbaum, M.; Glorius, F.; Escher, I., Asymmetric heterogeneous catalysis. *Angewandte Chemie* **2006**, *45* (29), 4732-62.
91. Zhu, L., *Surface temperature excess in heterogeneous catalysis*. Delft University of Technology, The Netherlands: 2005.
92. Schulz, E., Chiral Cobalt-Salen Complexes: Ubiquitous Species in Asymmetric Catalysis. *The Chemical Record* **2021**, *21* (2), 427-439.
93. (a) Fukuda, T.; Katsuki, T., Co(III)-Salen Catalyzed Asymmetric Cyclopropanation. *Synlett* **1995**, *1995* (08), 825-826; (b) Fukuda, T.; Katsuki, T., Highly enantioselective cyclopropanation of styrene derivatives using Co(III)-salen complex as a catalyst. *Tetrahedron* **1997**, *53* (21), 7201-7208.
94. Jacobsen, E. N.; Kakiuchi, F.; Konsler, R. G.; Larrow, J. F.; Tokunaga, M., Enantioselective catalytic ring opening of epoxides with carboxylic acids. *Tetrahedron Letters* **1997**, *38* (5), 773-776.
95. Tokunaga, M.; Larrow, J. F.; Kakiuchi, F.; Jacobsen, E. N., Asymmetric catalysis with water: efficient kinetic resolution of terminal epoxides by means of catalytic hydrolysis. *Science* **1997**, *277*, 936-938.
96. Brandes, B. D.; Jacobsen, E. N., Synthesis of enantiopure 3-chlorostyrene oxide via an asymmetric epoxidation-hydrolytic kinetic resolution sequence. *Tetrahedron: Asymmetry* **1997**, *8* (23), 3927-3933.
97. Bousquet, C.; Gilheany, D. G., Chromium catalysed asymmetric alkene epoxidation. greater selectivity for an E-alkene versus its Z-isomer. *Tetrahedron Letters* **1995**, *36* (42), 7739-7742.
98. McGarrigle, E. M.; Gilheany, D. G., Chromium- and Manganese-salen Promoted Epoxidation of Alkenes. *Chemical Reviews* **2005**, *105* (5), 1563-1602.
99. Lidskog, A.; Li, Y.; Wärnmark, K., Asymmetric Ring-Opening of Epoxides Catalyzed by Metal-Salen Complexes. *Catalysts* **2020**, *10* (6), 705.
100. Martinez, L. E.; Leighton, J. L.; Carsten, D. H.; Jacobsen, E. N., Highly Enantioselective Ring Opening of Epoxides Catalyzed by (salen)Cr(III) Complexes. *Journal of the American Chemical Society* **1995**, *117* (21), 5897-5898.

101. Hansen, K. B.; Leighton, J. L.; Jacobsen, E. N., On the Mechanism of Asymmetric Nucleophilic Ring-Opening of Epoxides Catalyzed by (Salen)Cr(III) Complexes. *Journal of the American Chemical Society* **1996**, *118* (44), 10924-10925.
102. Konsler, R. G.; Karl, J.; Jacobsen, E. N., Cooperative Asymmetric Catalysis with Dimeric Salen Complexes. *Journal of the American Chemical Society* **1998**, *120* (41), 10780-10781.
103. Schaus, S. E.; Brånalt, J.; Jacobsen, E. N., Asymmetric Hetero-Diels–Alder Reactions Catalyzed by Chiral (Salen)Chromium(III) Complexes. *The Journal of Organic Chemistry* **1998**, *63* (2), 403-405.
104. Thomas, J. M.; Thomas, W. J., *Principles and practice of heterogeneous catalysis*. John Wiley & Sons: 2014.
105. (a) Hoogenboom, R., Click chemistry in polymer science. *Chem* **2023**, *9* (9), 2416-2424; (b) Geng, Z.; Shin, J. J.; Xi, Y.; Hawker, C. J., Click chemistry strategies for the accelerated synthesis of functional macromolecules. *Journal of Polymer Science* **2021**, *59* (11), 963-1042; (c) Dohler, D.; Michael, P.; Binder, W. H., CuAAC-Based Click Chemistry in Self-Healing Polymers. *Accounts of chemical research* **2017**, *50* (10), 2610-2620.
106. Annis, D. A.; Jacobsen, E. N., Polymer-Supported Chiral Co(Salen) Complexes: Synthetic Applications and Mechanistic Investigations in the Hydrolytic Kinetic Resolution of Terminal Epoxides. *Journal of the American Chemical Society* **1999**, *121* (17), 4147-4154.
107. (a) Zulauf, A.; Mellah, M.; Guillot, R.; Schulz, E., Chromium-Thiophene-salen-Based Polymers for Heterogeneous Asymmetric Hetero-Diels–Alder Reactions. *European Journal of Organic Chemistry* **2008**, *2008* (12), 2118-2129; (b) Zulauf, A.; Mellah, M.; Schulz, E., New Chiral Thiophene–Salen Chromium Complexes for the Asymmetric Henry Reaction. *The Journal of Organic Chemistry* **2009**, *74* (5), 2242-2245; (c) Zulauf, A.; Mellah, M.; Schulz, E., Original use of the same heterogeneous chiral catalyst batch to promote different asymmetric reactions. *Chemical communications* **2009**, (43), 6574-6.
108. (a) Baleizão, C.; Garcia, H., Chiral Salen Complexes: An Overview to Recoverable and Reusable Homogeneous and Heterogeneous Catalysts. *Chemical Reviews* **2006**, *106* (9), 3987-4043; (b) McMorn, P.; Hutchings, G. J., Heterogeneous enantioselective catalysts: strategies for the immobilisation of homogeneous catalysts. *Chemical Society Reviews* **2004**, *33* (2), 108-122; (c) Vankelecom, I. F.; Jacobs, P. A., Catalyst immobilization on inorganic supports. *Chiral Catalyst Immobilization and Recycling* **2000**, 19-42.
109. Fan, Q.-H.; Li, Y.-M.; Chan, A. S. C., Recoverable Catalysts for Asymmetric Organic Synthesis. *Chemical reviews* **2002**, *102* (10), 3385-3466.
110. Frunza, L.; Kosslick, H.; Landmesser, H.; Höft, E.; Fricke, R., Host/guest interactions in nanoporous materials I. The embedding of chiral salen manganese(III) complex into mesoporous silicates. *Journal of Molecular Catalysis A: Chemical* **1997**, *123* (2), 179-187.
111. (a) Yang, H.; Zhang, L.; Su, W.; Yang, Q.; Li, C., Asymmetric ring-opening of epoxides on chiral Co(Salen) catalyst synthesized in SBA-16 through the “ship in a bottle” strategy. *Journal of Catalysis* **2007**, *248* (2), 204-212; (b) Yang, H.; Zhang, L.; Zhong, L.; Yang, Q.; Li, C., Enhanced cooperative activation effect in the hydrolytic kinetic resolution of epoxides on [Co(salen)] catalysts confined in nanocages. *Angewandte Chemie* **2007**, *46* (36), 6861-5; (c) Lee, Y.; Yu, J.; Park, K.; Kim, G. J., Superior Effect of Ultrasonic Homogenization to Mechanical Agitation on Accelerating Reaction Rates in Asymmetric Ring Opening of Epoxides. *Bulletin of the Korean Chemical Society* **2017**, *38* (7), 795-803.
112. Zhang, Y.; Zhao, J.; He, L.; Zhao, D.; Zhang, S., Manganese (III) salen complex anchored onto MCM-41 as catalyst for the aerobic epoxidation of olefins. *Microporous and Mesoporous Materials* **2006**, *94* (1-3), 159-165.

113. Syukri, S.; Sakthivel, A.; Sun, W.; Kühn, F. E., Immobilization of Ru(II)(salen)(PPh₃)₂ on Mesoporous MCM-41/SBA-15: Characterization and Catalytic Applications. *Catalysis Letters* **2008**, *128* (1-2), 18-24.
114. Baleizão, C.; Gigante, B.; Sabater, M. J.; Garcia, H.; Corma, A., On the activity of chiral chromium salen complexes covalently bound to solid silicates for the enantioselective epoxide ring opening. *Applied Catalysis A: General* **2002**, *228* (1), 279-288.
115. Ji, R.; Yu, K.; Lou, L.-L.; Gu, Z.; Liu, S., Mesoporous Silica Supported Unsymmetric Chiral Mn(III) Salen Complex: Synthesis, Characterization and Effect of Pore Size on Catalytic Performance. *Journal of Inorganic and Organometallic Polymers and Materials* **2010**, *20* (4), 675-683.
116. Gill, C. S.; Venkatasubbaiah, K.; Phan, N. T. S.; Weck, M.; Jones, C. W., Enhanced Cooperativity through Design: Pendant CoIII□Salen Polymer Brush Catalysts for the Hydrolytic Kinetic Resolution of Epichlorohydrin (Salen=N,N'-Bis(salicylidene)ethylenediamine Dianion). *Chemistry – A European Journal* **2008**, *14* (24), 7306-7313.
117. (a) Islam, M. M.; Bhanja, P.; Halder, M.; Kundu, S. K.; Bhaumik, A.; Islam, S. M., Chiral Co(III)–salen complex supported over highly ordered functionalized mesoporous silica for enantioselective aminolysis of racemic epoxides. *RSC Advances* **2016**, *6* (111), 109315-109321; (b) Shukla, M.; Barick, K. C.; Salunke, H. G.; Chandra, S., Chiral salen - Ni (II) based spherical porous silica as platform for asymmetric transfer hydrogenation reaction and synthesis of potent drug intermediate montelukast. *Molecular Catalysis* **2021**, *502*, 111367.
118. Diosa, B. M. L.; Jacobs, P. A., Cr(III)(salen) impregnated on silica for asymmetric ring opening reactions and its recovery via desorption/re-impregnation. *Tetrahedron Letters* **2003**, *44* (49), 8815-8817.
119. J. Sabater, M.; Corma, A.; Domenech, A.; Fornés, V.; García, H., Chiral salen manganese complex encapsulated within zeolite Y: a heterogeneous enantioselective catalyst for the epoxidation of alkenes. *Chemical Communications* **1997**, (14), 1285-1286.
120. Schuster, C.; Möllmann, E.; Tompos, A.; Hölderich, W. F., Highly stereoselective epoxidation of (–)- α -pinene over chiral transition metal (salen) complexes occluded in zeolitic hosts. *Catalysis Letters* **2001**, *74* (1), 69-75.
121. Lakhani, P.; Chodvadiya, D.; Jha, P. K.; Gupta, V. K.; Trzybiński, D.; Wozniak, K.; Kurzydłowski, K.; Goutam, U. K.; Srivastava, H.; Modi, C. K., DFT stimulation and experimental insights of chiral Cu(II)–salen scaffold within the pocket of MWW-zeolite and its catalytic study. *Physical Chemistry Chemical Physics* **2023**, *25* (20), 14374-14386.
122. Furukawa, H.; Cordova, K. E.; O’Keeffe, M.; Yaghi, O. M., The Chemistry and Applications of Metal-Organic Frameworks. *Science* **2013**, *341* (6149), 1230444.
123. (a) Liu, Y.; Li, Z.; Yuan, G.; Xia, Q.; Yuan, C.; Cui, Y., Chiral Cu(salen)-Based Metal–Organic Framework for Heterogeneously Catalyzed Aziridination and Amination of Olefins. *Inorganic Chemistry* **2016**, *55* (24), 12500-12503; (b) Song, F.; Wang, C.; Lin, W., A chiral metal–organic framework for sequential asymmetric catalysis. *Chemical communications* **2011**, *47* (29), 8256-8258; (c) Zhu, C.; Yuan, G.; Chen, X.; Yang, Z.; Cui, Y., Chiral Nanoporous Metal–Metallosalen Frameworks for Hydrolytic Kinetic Resolution of Epoxides. *Journal of the American Chemical Society* **2012**, *134* (19), 8058-8061; (d) Song, F.; Zhang, T.; Wang, C.; Lin, W., Chiral porous metal-organic frameworks with dual active sites for sequential asymmetric catalysis. *Proceedings of the Royal Society A: Mathematical, Physical and Engineering Sciences* **2012**, *468* (2143), 2035-2052; (e) Xia, Q.; Liu, Y.; Li, Z.; Gong, W.; Cui, Y., A Cr(salen)-based metal–organic framework as a versatile catalyst for efficient asymmetric transformations. *Chemical communications* **2016**, *52* (89), 13167-13170; (f) Yang, Z.; Zhu, C.; Li, Z.; Liu, Y.; Liu, G.; Cui, Y., Engineering chiral Fe(salen)-based metal-organic frameworks for asymmetric sulfide oxidation. *Chemical communications* **2014**, *50* (63), 8775-

- 8; (g) Song, F.; Wang, C.; Falkowski, J. M.; Ma, L.; Lin, W., Isorecticular Chiral Metal–Organic Frameworks for Asymmetric Alkene Epoxidation: Tuning Catalytic Activity by Controlling Framework Catenation and Varying Open Channel Sizes. *Journal of the American Chemical Society* **2010**, *132* (43), 15390-15398; (h) Cho, S. H.; Ma, B.; Nguyen, S. T.; Hupp, J. T.; Albrecht-Schmitt, T. E., A metal-organic framework material that functions as an enantioselective catalyst for olefin epoxidation. *Chemical Communications* **2006**, (24), 2563-5.
124. Xia, Q.; Li, Z.; Tan, C.; Liu, Y.; Gong, W.; Cui, Y., Multivariate Metal-Organic Frameworks as Multifunctional Heterogeneous Asymmetric Catalysts for Sequential Reactions. *Journal of the American Chemical Society* **2017**, *139* (24), 8259-8266.
125. Min, J.; Xia, Z.; Zhang, T.; Su, H.; Zhi, Y.; Shan, S., Recent development of magnetic nanomaterial-supported M(Salen) composites as recyclable heterogeneous catalysts. *Chemical Papers* **2021**, *75* (7), 2965-2980.
126. (a) Niakan, M.; Asadi, Z.; Masteri-Farahani, M., Fe(III)-salen complex supported on dendrimer functionalized magnetite nanoparticles as a highly active and selective catalyst for the green oxidation of sulfides. *Journal of Physics and Chemistry of Solids* **2020**, *147*, 109642; (b) Niakan, M.; Asadi, Z.; Masteri-Farahani, M., Immobilization of salen molybdenum complex on dendrimer functionalized magnetic nanoparticles and its catalytic activity for the epoxidation of olefins. *Applied Surface Science* **2019**, *481*, 394-403; (c) Rashid, Z.; Ghahremanzadeh, R.; Nejadmoghaddam, M.-R.; Nazari, M.; Shokri, M.-R.; Naeimi, H.; Zarnani, A.-H., Nickel-Salen supported paramagnetic nanoparticles for 6-His-target recombinant protein affinity purification. *Journal of Chromatography A* **2017**, *1490*, 47-53; (d) Sardarian, A. R.; Zohourian-Mashmoul, N.; Esmailpour, M., Salen complex of Cu(II) supported on superparamagnetic Fe₃O₄@SiO₂ nanoparticles: an efficient and magnetically recoverable catalyst for N-arylation of imidazole with aryl halides. *Monatshefte für Chemie - Chemical Monthly* **2018**, *149* (6), 1101-1109; (e) Dehghani, F.; Sardarian, A. R.; Esmailpour, M., Salen complex of Cu(II) supported on superparamagnetic Fe₃O₄@SiO₂ nanoparticles: An efficient and recyclable catalyst for synthesis of 1- and 5-substituted 1H-tetrazoles. *Journal of Organometallic Chemistry* **2013**, *743*, 87-96.
127. Min, J.; Song, W.; Hu, T.; Zhi, Y.; Xia, Z.; Zhang, T.; Shan, S.; Su, H., Fe₃O₄@SiO₂ nanoparticle-supported Co(III)-Salen composites as recyclable heterogeneous catalyst for the fixation of CO₂. *Ceramics International* **2021**, *47* (24), 35320-35332.
128. Gill, C. S.; Long, W.; Jones, C. W., Magnetic Nanoparticle Polymer Brush Catalysts: Alternative Hybrid Organic/Inorganic Structures to Obtain High, Local Catalyst Loadings for Use in Organic Transformations. *Catalysis Letters* **2009**, *131* (3), 425-431.
129. Tudisco, C.; Sfrassetto, G. T.; Pappalardo, A.; Motta, A.; Tomaselli, G. A.; Fragalà, I. L.; Ballistreri, F. P.; Condorelli, G. G., Covalent Functionalization of Silicon Surfaces with a Cavitand-Modified Salen. *European Journal of Inorganic Chemistry* **2011**, *2011* (13), 2124-2131.
130. Abd El Sater, M.; Jaber, N.; Schulz, E., Chiral Salen Complexes for Asymmetric Heterogeneous Catalysis: Recent Examples for Recycling and Cooperativity. *ChemCatChem* **2019**, *11* (16), 3662-3687.
131. Negi, S.; Bhandari, R., Silicon isotropic and anisotropic etching for MEMS applications. *Microsystem Technologies* **2012**, *19* (2), 203-210.
132. K. T. Queeney, M. K. W., J. P. Chang, Y. J. Chabal, A. B. Gurevich, J. Sapjeta and R. L. Opila, Infrared spectroscopic analysis of the Si/SiO₂ interface structure of thermally oxidized silicon. *Journal of Applied Physics* **2000**, *87*, 1322 - 1330.
133. da Fonseca, C.; Ozanam, F.; Chazalviel, J. N., In situ infrared characterisation of the interfacial oxide during the anodic dissolution of a silicon electrode in fluoride electrolytes. *Surface Science* **1996**, *365* (1), 1-14.

134. Sharma, M.; Roy, P. K.; Barman, J.; Khare, K., Mobility of Aqueous and Binary Mixture Drops on Lubricating Fluid Coated Slippery Surfaces. *Langmuir* **2019**, *35* (24), 7672-7679.
135. Zidelmal, N. SILIPOLYSALEN : Etude du greffage par polymérisation contrôlée de complexes de salen sur silicium pour une application en catalyse asymétrique hétérogène. Ph. D. Thesis, Université Paris-Saclay, France, 2018.
136. Sieval, A. B.; van den Hout, B.; Zuilhof, H.; Sudhölter, E. J. R., Molecular Modeling of Alkyl Monolayers on the Si(111) Surface. *Langmuir* **2000**, *16* (7), 2987-2990.
137. Sieval, A. B.; van den Hout, B.; Zuilhof, H.; Sudhölter, E. J. R., Molecular Modeling of Covalently Attached Alkyl Monolayers on the Hydrogen-Terminated Si(111) Surface. *Langmuir* **2001**, *17* (7), 2172-2181.
138. Du, H.; Williams, C. T.; Ebner, A. D.; Ritter, J. A., In Situ FTIR Spectroscopic Analysis of Carbonate Transformations during Adsorption and Desorption of CO₂ in K-Promoted HTlc. *Chemistry of Materials* **2010**, *22* (11), 3519-3526.
139. Scheres, L.; Giesbers, M.; Zuilhof, H., Organic Monolayers onto Oxide-Free Silicon with Improved Surface Coverage: Alkynes versus Alkenes. *Langmuir* **2009**, *26* (7), 4790-4795.
140. Everett, D. H., Manual of Symbol and Terminology for Physico-chemical Quantities and Units, Appendix, Definitions, Terminology and Symbols in Colloid and Surface Chemistry, Part I. *Pure Applied Chemistry*. **1971**, *31* (4), 579 - 638.
141. Pyun, J.; Matyjaszewski, K., Synthesis of Nanocomposite Organic/Inorganic Hybrid Materials Using Controlled/"Living" Radical Polymerization. *Chemistry of Materials* **2001**, *13* (10), 3436-3448.
142. Slowikowska, M.; Chajec, K.; Michalski, A.; Zapotoczny, S.; Wolski, K., Surface-Initiated Photoinduced Iron-Catalyzed Atom Transfer Radical Polymerization with ppm Concentration of FeBr₃ under Visible Light. *Materials* **2020**, *13* (22).
143. Zhao, B.; Brittain, W. J., Polymer brushes: surface-immobilized macromolecules. *Prog. Polym. Sci.* **2000**, *25*, 677-710.
144. Chabal, Y. J., Surface infrared spectroscopy. *Surface Science Reports* **1988**, *8* (5), 211-357.
145. Watts, J. F.; Wolstenholme, J., *An Introduction to Surface Analysis by XPS and AES*. Wiley: 2003.
146. Lehmann, V., *Electrochemistry of Silicon*. Wiley-VCH Verlag GmbH: 2002.
147. (a) Mendonça, P. V.; Konkolewicz, D.; Averick, S. E.; Serra, A. C.; Popov, A. V.; Guliashvili, T.; Matyjaszewski, K.; Coelho, J. F. J., Synthesis of cationic poly((3-acrylamidopropyl) trimethylammonium chloride) by SARA ATRP in ecofriendly solvent mixtures. *Polymer Chemistry* **2014**, (5), 5829-5836; (b) Nguyen, N. H.; Rosen, B. M.; Lligadas, G.; Percec, V., Surface-Dependent Kinetics of Cu(0)-Wire-Catalyzed Single-Electron Transfer Living Radical Polymerization of Methyl Acrylate in DMSO at 25 °C. *Macromolecules* **2009**, *42*, 2379-2386; (c) Harrisson, S.; Couvreur, P.; Nicolas, J., Comproportionation versus Disproportionation in the Initiation Step of Cu(0)-Mediated Living Radical Polymerization. *Macromolecules* **2012**, *45* (18), 7388-7396; (d) Konkolewicz, D.; Krys, P.; Góis, J. R.; Mendonça, P. V.; Zhong, M.; Wang, Y.; Gennaro, A.; Isse, A. A.; Fantin, M.; Matyjaszewski, K., Aqueous RDRP in the Presence of Cu₀: The Exceptional Activity of CuI Confirms the SARA ATRP Mechanism. *Macromolecules* **2014**, *47* (2), 560-570.
148. Nguyen, T. P. T.; Barroca-Aubry, N.; Costa, L.; Bourdreux, Y.; Doisneau, G.; Roger, P., Cu(0)-mediated RDRP as new alternative for controlled synthesis of poly(pentafluorophenyl methacrylate). *Polymer* **2022**, *251*, 124924.
149. (a) Costa, J. R. C.; Mendonça, P. V.; Maximiano, P.; Serra, A. C.; Guliashvili, T.; Coelho, J. F. J., Ambient Temperature "Flash" SARA ATRP of Methyl Acrylate in Water/Ionic Liquid/Glycol Mixtures. *Macromolecules* **2015**, *48* (19), 6810-6815; (b) Abreu, C. M. R.;

- Serra, A. C.; Popov, A. V.; Matyjaszewski, K.; Guliashvili, T.; Coelho, J. F. J., Ambient temperature rapid SARA ATRP of acrylates and methacrylates in alcohol–water solutions mediated by a mixed sulfite/Cu(ii)Br₂ catalytic system. *Polymer Chemistry* **2013**, *4* (23), 5629.
150. (a) Mendonça, P. V.; Lima, M. S.; Guliashvili, T.; Serra, A. C.; Coelho, J. F. J., Deep eutectic solvents (DES): Excellent green solvents for rapid SARA ATRP of biorelevant hydrophilic monomers at ambient temperature. *Polymer* **2017**, *132*, 114-121; (b) Beers, K. L.; Boo, S.; Gaynor, S. G.; Matyjaszewski, K., Atom Transfer Radical Polymerization of 2-Hydroxyethyl Methacrylate. *Macromolecules* **1999**, *32*, 5772-5776.
151. Shaw, S.; White, J. D., Asymmetric Catalysis Using Chiral Salen-Metal Complexes: Recent Advances. *Chemical Reviews* **2019**, *119* (16), 9381-9426.
152. Combes, A., Sur l'Action des Diamines sur les Diacétone. . *C. R. Acad. Fr.* **1889**, *108*, 1252–1255.
153. Dieck, H. A.; Heck, F. R., Palladium catalyzed synthesis of aryl, heterocyclic and vinylic acetylene derivatives. *Journal of Organometallic Chemistry* **1975**, *93*, 259-263.
154. Cassar, L., Synthesis of aryl- and vinyl-substituted acetylene derivatives by the use of nickel and palladium complexes,. *Journal of Organometallic Chemistry* **1975**, *93* (2), 253-257.
155. Sonogashira, K.; Tohda, Y.; Hagihara, N., A convenient synthesis of acetylenes: catalytic substitutions of acetylenic hydrogen with bromoalkenes, iodoarenes and bromopyridines. *Tetrahedron Letters* **1975**, *16* (50), 4467-4470.
156. Gazvoda, M.; Virant, M.; Pinter, B.; Kosmrlj, J., Mechanism of copper-free Sonogashira reaction operates through palladium-palladium transmetalation. *Nature communications* **2018**, *9* (1), 4814.
157. Huisgen, R., 1,3 Dipolar cycloadditions. *Proceedings of the Chemical Society* **1961**, (October), 357-396.
158. (a) Kolb, H. C.; Finn, M. G.; Sharpless, K. B., Click Chemistry: Diverse Chemical Function from a Few Good Reactions. *Angewandte Chemie International Edition* **2001**, *40* (11), 2004-2021; (b) Himo, F.; Lovell, T.; Hilgraf, R.; Rostovtsev, V. V.; Noodleman, L.; Sharpless, K. B.; Fokin, V. V., Copper(I)-Catalyzed Synthesis of Azoles. DFT Study Predicts Unprecedented Reactivity and Intermediates. *J. Am. Chem. Soc.* **2005**, *127*, 210-216; (c) Rostovtsev, V. V.; Green, L. G.; Fokin, V. V.; Sharpless, K. B., A Stepwise Huisgen Cycloaddition Process: Copper(I)-Catalyzed Regioselective “Ligation” of Azides and Terminal Alkynes. *Angewandte Chemie International Edition* **2002**, *41* (14), 2596-2599.
159. (a) Zhou, L.; Li, Y.; Li, S.; Shi, Z.; Zhang, X.; Tung, C.-H.; Xu, Z., Asymmetric rhodium-catalyzed click cycloaddition to access C–N axially chiral N-triazolyl indoles. *Chemical Science* **2023**, *14* (19), 5182-5187; (b) Zeng, L.; Zhang, F.; Cui, S., Construction of Axial Chirality via Click Chemistry: Rh-Catalyzed Enantioselective Synthesis of 1-Triazolyl-2-Naphthylamines. *Organic Letters* **2023**, *25* (2), 443-448; (c) Zeng, L.; Li, J.; Cui, S., Rhodium-Catalyzed Atroposelective Click Cycloaddition of Azides and Alkynes. *Angewandte Chemie International Edition* **2022**, *61* (28), e202205037.
160. Best, M. D., Click Chemistry and Bioorthogonal Reactions: Unprecedented Selectivity in the Labeling of Biological Molecules. *Biochemistry* **2009**, *48* (28), 6571-6584.
161. Larrow, J. F.; Jacobsen, E. N.; Gao, Y.; Hong, Y.; Nie, X.; Zepp, C. M., A Practical Method for the Large-Scale Preparation of [N,N'-Bis(3,5-di-tertbutylsalicylidene)-1,2-cyclohexanediaminato(2-)]manganese(III) chloride, a Highly Enantioselective Epoxidation Catalyst. *The Journal of Organic Chemistry* **1994**, *59* (7), 1939–1942.
162. Salunke, S. B.; Babu, N. S.; Chen, C.-T., Asymmetric Aerobic Oxidation of α -Hydroxy Acid Derivatives Catalyzed by Reusable, Polystyrene-Supported Chiral N-Salicylidene Oxidovanadium tert-Leucinates. *Advanced Synthesis & Catalysis* **2011**, *353* (8), 1234-1240.

163. Holbach, M.; Zheng, X.; Burd, C.; Jones, C. W.; Weck, M., A Practical One-Pot Synthesis of Enantiopure Unsymmetrical Salen Ligands. *The Journal of Organic Chemistry* **2006**, *71* (7), 2903-2906.
164. Campbell, E. J.; Nguyen, S. T., Unsymmetrical salen-type ligands: high yield synthesis of salen-type Schiff bases containing two different benzaldehyde moieties. *Tetrahedron Letters* **2001**, *42* (7), 1221-1225.
165. Jacobsen, E. N., Asymmetric Catalysis of Epoxide Ring-Opening Reactions. *Accounts of Chemical Research* **2000**, *33*, 421 - 431.
166. Kureshy, R. I.; Singh, S.; Khan, N.-u. H.; Abdi, S. H. R.; Agrawal, S.; Jasra, R. V., Enantioselective aminolytic kinetic resolution (AKR) of epoxides catalyzed by recyclable polymeric Cr(III) salen complexes. *Tetrahedron: Asymmetry* **2006**, *17* (11), 1638-1643.
167. (a) Kowalczyk, R.; Kwiatkowski, P.; Skarzewski, J.; Jurczak, J., Enantioselective Nitroaldol Reaction Catalyzed by Sterically Modified Salen-Chromium Complexes. *The Journal of Organic Chemistry* **2008**, *74*, 753-756; (b) Didier, D.; Magnier-Bouvier, C.; Schulz, E., Charge-Transfer Interactions: An Efficient Tool for Recycling Bis(oxazoline)-Copper Complexes in Asymmetric Henry Reactions. *Advanced Synthesis & Catalysis* **2011**, *353* (7), 1087-1095.
168. Xia, Q.; Liu, Y.; Li, Z.; Gong, W.; Cui, Y., A Cr(salen)-based metal-organic framework as a versatile catalyst for efficient asymmetric transformations. *Chemical Communications* **2016**, *52* (89), 13167-13170.
169. Furrow, M. E.; Schaus, S. E.; Jacobsen, E. N., Practical Access to Highly Enantioenriched C-3 Building Blocks via Hydrolytic Kinetic Resolution. *The Journal of Organic Chemistry* **1998**, *63*, 6776-6777.
170. (a) Joseph, T.; Sajanikumari, C. S.; Deshpande, S. S.; Gopinathan, S., Oxidation of p-cresol catalyzed by neat and zeolite encapsulated cobalt salen complexes. *Indian Journal of Chemistry* **1999**, *38A*, 792-796; (b) Gao, T.; Yang, Y.; Sun, W.-B.; Li, G.-M.; Hou, G.-F.; Yan, P.-F.; Li, J.-T.; Ding, D.-D., Syntheses, structure and near-infrared (NIR) luminescence of Er²⁺, Yb²⁺, ErYb of homodinuclear and heterodinuclear lanthanide(III) complexes based on salen ligand. *CrystEngComm* **2013**, *15* (31), 6213.
171. Evano, G.; Blanchard, N.; Toumi, M., Copper-Mediated Coupling Reactions and Their Applications in Natural Products and Designed Biomolecules Synthesis. *Chemical Reviews* **2008**, *108*, 3054-3131.
172. (a) Wei, W.; Chen, W.; Ivey, D. G., Rock Salt-Spinel Structural Transformation in Anodically Electrodeposited Mn-Co-O Nanocrystals. *Chemistry of Materials* **2008**, *20* (5), 1941-1947; (b) Kim, K. S., X-ray-photoelectron spectroscopic studies of the electronic structure of CoO. *Physical Review B* **1975**, *11* (6), 2177-2185.
173. McGarrigle, E. M.; Murphy, D. M.; Gilheany, D. G., Ligand tuning in the chromium-salen-mediated asymmetric epoxidation of alkenes. *Tetrahedron: Asymmetry* **2004**, *15* (8), 1343-1354.
174. Kowalczyk, R.; Sidorowicz, Ł.; Skarzewski, J., Asymmetric nitroaldol reaction catalyzed by a chromium(III)-salen system. *Tetrahedron-asymmetry* **2007**, *18*, 2581-2586.
175. Corma, A.; Garcia, H., Supramolecular Host-Guest Systems in Zeolites Prepared by Ship-in-a-Bottle Synthesis. *European Journal of Inorganic Chemistry* **2004**, *2004* (6), 1143-1164.
176. Abd El Sater, M.; Mellah, M.; Drago, D.; Kolodziej, E.; Jaber, N.; Schulz, E., Chiral Chromium Salen@rGO as Multipurpose and Recyclable Heterogeneous Catalyst. *Chemistry* **2021**, *27* (36), 9454-9460.
177. (a) Schaus, S. E.; Brandes, B. D.; Larrow, J. F.; Tokunaga, M.; Hansen, K. B.; Gould, A. E.; Furrow, M. E.; Jacobsen, E. N., Highly Selective Hydrolytic Kinetic Resolution of Terminal Epoxides Catalyzed by Chiral (salen)Co(III) Complexes. Practical Synthesis of

- Enantioenriched Terminal Epoxides and 1,2-Diols. *Journal of the American Chemical Society* **2002**, *124* (7), 1307-1315; (b) Furrow, M. E.; Schaus, S. E.; Jacobsen, E. N., Practical Access to Highly Enantioenriched C-3 Building Blocks via Hydrolytic Kinetic Resolution. *The Journal of Organic Chemistry* **1998**, *63* (20), 6776-6777.
178. Stejskal, J.; Janca, J.; Kratochvíl, P., Solution Properties of Poly(2-methoxyethyl methacrylate). *Polymer Journal* **1976**, *8* (6), 549-555.
179. *HF Acid User's Guide Safe Handling, Storage, and Disposal of Hydrofluoric Acid. User's Guide Presented y UAB Occupational Health and Safety (OH&S)*. <https://www.uab.edu/ehs/images/docs/chem/HFUserGuide-2016-09-29.pdf>.
180. University, S.; Stanford; Complaints, C. 94305 C. *Information on Azide Compounds – Stanford Environmental Health & Safety*. <https://ehs.stanford.edu/reference/information-azide-compounds>.
181. Lehmann, V.; Stengl, R.; Luigart, A., On the morphology and the electrochemical formation mechanism of mesoporous silicon. . *Materials Science and Engineering: B* **2000**, *69*, 11-22.
182. Hong, X. Nouveaux catalyseurs hétérogènes chiraux pour le dédoublement cinétique hydrolytique des époxydesTERMINAUX. Université Paris-Saclay, France, 2012.
183. Binnig, G. K.; Quate, C. F.; Gerber, C., Atomic force microscope. *Physical Review Letters* **1986**, *56* 9, 930-933.
184. *AFM (Atomic Force Microscope) - University of Greifswald*. physik.uni-greifswald.de. <https://physik.uni-greifswald.de/en/research-groups/soft-matter-and-biophysics-prof-christiane-helm/methods/afm-atomic-force-microscope/>.

Titre : Greffage de complexes de salen sur silicium par polymérisation radicalaire par transfert d'atomes pour une application en catalyse asymétrique

Mots clés : complexes métalliques chiraux, salen, polymérisation contrôlée, greffage, silicium, catalyse asymétrique

Résumé : Le projet de thèse a pour objectif de préparer du silicium macroporeux (PSi) fonctionnalisé par des complexes métalliques de type salen chiraux, suite à des procédés de greffage multi-étapes robustes qui permettent leur récupération et réutilisation pour des applications en catalyse asymétrique tandem. L'immobilisation des complexes métalliques salen est proposée par ingénierie macromoléculaire pour maîtriser la composition et la longueur des chaînes greffées. La stratégie vise donc la copolymérisation, par polymérisation radicalaire par transfert d'atomes amorcée en surface (SI-ATRP), de monomères de type méthacrylate fonctionnalisés. Dans un premier temps, le greffage de différents amorceurs sur la surface oxydée et hydrogénée du silicium cristallin a été étudié par activation micro-onde puis l'influence

de la densité d'amorceurs sur l'efficacité de la polymérisation SI-ATRP du méthacrylate de méthoxyméthyle (MEMA) a été déterminée quantitativement par spectroscopie FTIR-ATR, XPS et imagerie AFM. Des brosses de polymères de différents degrés de polymérisation ont été obtenues. Ensuite, la copolymérisation du MEMA avec différents pourcentages d'un méthacrylate azoture a été réalisée en solution et à la surface du silicium. Les copolymères en solution ont été fonctionnalisés avec deux catalyseurs salen différents par chimie click qui ont montré le potentiel de cette stratégie pour la multi-catalyse. Enfin, les copolymères sur silicium macroporeux ont été fonctionnalisés avec un catalyseur salen, cependant les premiers tests catalytiques montrent la nécessité d'augmenter la surface spécifique du substrat.

Title : Grafting of salen complexes on silicon by means of Atom Transfer Radical Polymerization for applications in asymmetric catalysis

Keywords : chiral metal complexes, salen, controlled polymerization, grafting, silicon, asymmetric catalysis

Abstract : The PhD project aims at the preparation of porous silicon functionalized by enantiopure metallic complexes of salen type, following robust, multi-step grafting processes, which will allow their easy recovery and reuse for applications in tandem asymmetric catalysis. The immobilization of salen metal complexes is proposed by macromolecular engineering to control the composition and the length of the grafted chains. The strategy therefore consists in the copolymerization, by surface-initiated atom transfer radical polymerization (SI-ATRP), of functionalized methacrylate-type monomers. First, microwave activation was used to study the grafting of different initiators on the oxidized and hydrogenated surfaces of crystalline silicon. Then, the effect of initiator density on the efficiency of SI-

ATRP polymerization of methoxymethyl methacrylate (MEMA) was quantitatively determined using ATR-FTIR spectroscopy, XPS, and AFM imaging. Polymer brushes with different degrees of polymerization were obtained. Then, the copolymerization of MEMA with different percentages of a methacrylate azide monomer was performed in solution and on silicon surfaces. The copolymers in solution were functionalized with two different salen catalysts by click chemistry, which showed the potential of this strategy for multi-catalysis. Finally, the copolymers on macroporous silicon were functionalized with a salen catalyst; nevertheless, the first catalytic trials show the necessity to increase the specific surface area of the substrate.